Confining Functional Materials in Protein-Based Assemblies

Melanie Brasch

Confining Functional Materials in Protein-Based Assemblies

Melanie Brasch

The research described in this thesis was performed at the Biomolecular Nanotechnology (BNT) group within the MESA+ Institute for Nanotechnology and the Faculty of Science and Technology at the University of Twente. This research was financial supported from the Netherlands Organization for Science (NWO) and the European Science Foundation (ESF-EURYI).

Committee members:

Chairman:	Prof. dr. G. van der Steenhoven	University of Twente
Promotor:	Prof. dr. J. J. L. M. Cornelissen	University of Twente
Assistant Promotor:	Dr. M. S. T. Koay	University of Twente
Members:	Dr. A. de la Escosura Navazo	Universidad Autónoma de Madrid
	Prof. dr. Ir. J. Huskens	University of Twente
	Prof. dr. Ir. D. N. Reinhoudt	University of Twente
	Prof. dr. R. J. M. Nolte	University of Nijmegen
	Prof. dr. D. Hilvert	Eidgenössische Technische Hochschule Zürich (Hönggerberg)
	Prof. dr. S. J. G. Lemay	University of Twente

Title: Confining Functional Materials in Protein-Based Assemblies

Author: Melanie Brasch

ISBN: 978-90-365-0009-8

DOI: 10.3990./1.9789036500098

Cover art: Photography from Markus Hochstetter

Publisher: Ipskamp Drukkers B. V., Enschede

Confining Functional Materials in Protein-Based Assemblies

PROEFSCHRIFT

ter verkrijging van

de graad van doctor aan de Universiteit Twente,

op gezag van de rector magnificus,

Prof. Dr. H. Brinksma,

Volgens besluit van het College voor Promoties

in het openbaar te verdedigen

op vrijdag 30 augustus 2013 om 12.45 uur

door

Melanie Brasch

geboren op 6 juni 1984

te Wuppertal, Duitsland

Dit proefschrift is goedgekeurd door:

Promotor: Prof. dr. J. J. L. M. Cornelissen

Assistent-promotor: Dr. M. S. T. Koay

To Alberto Gomez-Casado and my family

Table of Contents

Chapter 1

General Introduction

Nature uses bottom-up approaches for the controlled assembly of highly-ordered hierarchical structures with defined functionality, from DNA, proteins and membranes to more complex organelles, molecular motors and trans-membrane pumps.[1] The field of bionanotechnology draws inspiration from nature by utilizing biomolecular building blocks for the (self-)assembly of new structures, devices and systems for applications in biomedicine,[2] optics or electronics.[3, 4] However, the ability to gain precise control on the nanometer scale over their assembly, monodispersity, size and morphology still remains a significant challenge.[5]

Amongst the toolbox of available building blocks, viruses and virus-like particles (VLPs) have emerged as promising candidates for applications in nanotechnology.[6, 7] The outer shell of virus-like particles is typically composed of multiple copies of identical virus coat proteins and their self-assembly is often induced by electrostatic interactions between the virus coat protein and its molecular cargo.

The aim of this thesis is to explore and understand the interplay between the self-assembly of Cowpea Chlorotic Mottle Virus (CCMV) with templates of functional materials. The ability to tune and control the self-assembly of viruses into well-defined structures is essential for the fabrication of new devices with enhanced properties.

Chapter 2 provides an overview of the different protein and non-protein based compartments currently reported in the literature. Particular attention is given to virus-based assemblies. The different functional materials and templates used for encapsulation into virus-like assemblies are described, together with their potential applications in the future.

In **Chapter 3,** two different strategies for the encapsulation of zinc phthalocyanines (ZnPcs) inside CCMV capsids are presented. Light-absorbing Pcs have been used for applications in photodynamic therapy (PDT). The superior light-absorbing properties of ZnPcs combined with the biocompatible nature of virus-based assemblies led to a significant improvement in PDT-induced cell-death upon irradiation, demonstrating their potential applications in biomedicine.

In **Chapter 4** the encapsulation of a two-component enzyme pathway in CCMV is described. Detailed kinetic studies were performed to study the influence of molecular confinement on enzyme efficiency. Here, CCMV was used as a model system to understand and mimic the confined environment inside biological compartments, (*i.e.* eukaryotic organelles and prokaryotic protein-based microcompartments).

Chapter 5 describes an investigation of the encapsulation of a conjugated polyelectrolyte poly[(2-methoxy-5-propyloxy sulfonate)-phenyl-ene vinylene] (MPS-PPV) and the influence of the rigid polymer with different chain lengths towards the assembly of CCMV capsids. Furthermore, the effects of encapsulation, in particular the ability of the capsid shell to shield molecular cargo from the surrounding environment are reported.

In **Chapter 6**, the encapsulation of a stimuli-responsive self-immolative polymer (SIP) in CCMV is reported. The triggered release of smaller oligomer or monomer units from the capsid interior upon photo-irradiation is studied and described in detail and the consequences of cargo release from capsid assemblies are also investigated and detailed.

Due to their superior luminescent and self-assembly properties, platinum(II) complexes have gained significant attention in recent years. In **Chapter 7**, two different Pt(II) complexes were used to direct the self-assembly of CCMV into well-defined rod-like and spherical structures. In both cases, the transition between rod-like and spherical assemblies could be controlled depending on the concentration and equilibration time. Here, the unique combination of highly luminescent Pt(II) assemblies encased in a protective protein shell opens up new possibilities for applications in biomolecular imaging and molecular optics.

References

1. P. Iqbal, J. A. Preece and P. M. Mendes, in *Supramol Chem*, John Wiley & Sons, Ltd, 2012.
2. Y. Liu, J. Tan, A. Thomas, D. Ou-Yang and V. R. Muzykantov, *Ther Deliv*, 2012, 3, 181-194.
3. H. Acar, R. Genc, M. Urel, T. S. Erkal, A. Dana and M. O. Guler, *Langmuir*, 2012, 28, 16347-16354.
4. A. Albanese, P. S. Tang and W. C. W. Chan, *Annu Rev Biomed Eng*, 2012, 14, 1-16.
5. M. T. Smith, A. K. Hawes and B. C. Bundy, *Curr Opin Biotechnol*, 2013, 24, 1-7.
6. R. Singh and J. W. Lillard, *Exp Mol Pathol*, 2009, 86, 215-223.
7. S. Choudhary, M. B. Quin, M. A. Sanders, E. T. Johnson and C. Schmidt-Dannert, *PLoS One*, 2012, 7, e33342, 1-11.

Chapter 2

Confining Functional Materials in Protein-Based Assemblies

Inspired by Nature, the self-assembly of highly ordered structures, architectures and systems, using simple molecular building blocks has been of increasing interest and importance for applications in nanotechnology. At the interface of chemistry, biology and engineering, there are increasing efforts to understand and control the self-assembly and self-organization of molecules on the nanometer scale. In recent years, proteins and other biomolecules that can reversibly assemble into highly symmetrical, monodisperse structures have proven to be extremely useful as molecular building blocks for the assembly of molecular wires, nanocompartments and nanomachines. This chapter provides a detailed overview of the different types of protein-based compartments currently used for applications in nanotechnology, and where known, the assembly and disassembly properties are described. Following the overview, this chapter focuses on the use of virus-based assemblies, particularly the Cowpea Chlorotic Mottle Virus (CCMV), their potential applications and what the future may hold for such protein cages in nanotechnology.

This chapter has been submitted:
*M. Brasch, M. S. T. Koay, J. J. L. M. Cornelissen; Synthetic Biology**;** Volume;* ***2013***

2.1 Introduction

In Nature, the eukaryotic cell contains multiple membrane-bound organelles that separate their internal contents from the external surroundings. These organelles allow multiple biological pathways to occur simultaneously without interfering or inhibiting each other.[1] The ability of cells to regulate biological pathways with precise temporal and spatial control has been a constant source of inspiration for scientists. Over the past years, there has been growing interest in designing and mimicking the interior of a living cell, more specifically the packaging of proteins and enzymes into sub-cellular compartments, using biosynthetic building blocks. In particular, the development of compartments that can confine and store molecules (similar to peroxisomes in Nature), or that can perform enzymatic reactions (similar to mitochondria) are highly interesting. The design and implementation of a synthetic system of a complexity comparable to a living cell, still remains a great challenge.

Although DNA, peptides, lipids and proteins have been explored extensively as templates and scaffolds, the development of complex systems still requires the understanding of how Nature uses these molecules to assemble highly organized cellular compartments in living cells. Here, an overview of the different biological compartments found in Nature and their loading with non-natural and natural cargos is presented. More specifically, the first part focuses on different compartments originating from protein cages, bacterial microcompartments (BMCs) to bacteriophages and virus-based assemblies. The second part focuses first on the use of different templates to achieve different shapes and morphologies of the protein-based compartments, followed by examples where the protein compartment influences the properties of the template.

2.2 Non-protein based compartments

The main building blocks of organelles are lipids, which spontaneously self-assemble into bilayered vesicles of 10 – 100 nm in diameter.[1-4] Synthetic compartments have been studied based on this class of amphiphilic molecules. The detailed discussion of lipid-based assemblies is beyond the scope of this chapter. In water, lipids forms aggregates whereby the hydrophilic head groups of the single-chain amphiphiles are directed towards the outer surface and the hydrophobic tail groups are directed towards the center. While micelles have been used as membrane mimics, one of the major limitations of micelles is their restricted internal space.[5]

The discovery of liposomes by Bangham led to an improvement in both the loading capacity and the variety of cargo that can be packaged compared to micelles.[6] Liposomes are composed of either a single bilayer (unilamellar) enclosing an internal water core, or multiple bilayers that have a thin water film between each

bilayer. The average diameter for unilamellar liposomes varies from 50 to 250 nm whereas multilamellar liposomes vary in size from 500 to 5000 nm.[7]
Although lipid-based compartments have been explored extensively as organelle mimics and biological cargo carriers, some of the major disadvantages of lipid-based assemblies are: 1) their concentration-dependent stability, 2) the polydispersity of the assemblies, 3) the lack in controlled cargo loading, and 4) targeted cell uptake and biocompatibility.[8-10] In recent years, many of these issues have been addressed by using protein-based compartments which self-assemble into well-defined structures.[11]

2.3 Protein based compartments

Protein-based compartments are composed of multiple copies of one or more types of monomeric building blocks, which self-assemble into highly-organized, monodisperse structures. The different protein-based compartments found in Nature cover a broad range of shape (spheres or rods) and length scales (10 – 1000 nm) (Figure 2.1). Unlike micelles, which undergo reversible self-assembly depending on concentration, the assembly and disassembly of protein-based compartments is based on multiple non-covalent interactions (and hence much less concentration-dependent),[12-15] which can be triggered under certain conditions (such as changes in ionic strength or pH). Interestingly, the outer shell of many protein-based compartments contains pores, which may allow substrates and molecules to cross the shell barrier.

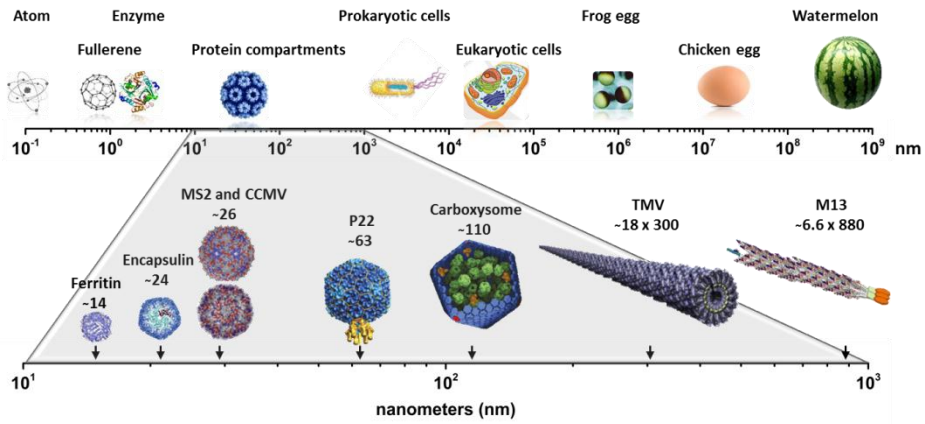

Figure 2.1. Nanometer scale for size comparison of protein based compartments with other biological objects.

2.3.1 Cage-like proteins

There are two major classes of cage-like proteins in Nature, the chaperonins and ferritins. These small protein assemblies which are ubiquitous play important roles in protein folding (chaperonins),[16] or in the storage of small molecules, in the case of ferritins.[17] An overview of the main properties of cage-like proteins is provided in Table 2.1.

Table 2.1. Overview of the main properties of cage-like proteins

Protein based compartment	Size outer/ inner diameter (nm)	Number of CPs	Different CP subunits
Chaperonin (group I)	---	14	1
Chaperonin (group II)	---	16-18	1-3
Ferritin (maxi)	12 / 8	24	1
Ferritin (mini)	9 / 5	12	1

Chaperonins are classified in two groups (Group I and II) depending on their origin and their molecular arrangement. The overall structure of chaperonins is composed of a double-ring assembly that is stacked in a back-to-back formation with a hydrophilic cavity in the center (Figure 2.2).[18] In Group I chaperonins, each ring is composed of seven identical protein subunits, whereas Group II chaperonins are composed of up to three different protein subunits that assemble with eight or nine proteins per ring.[19] For example, in the "open-lid" conformation, chaperonins such as Group II GroEL encapsulate unfolded proteins within their central cavity (Figure 2.2). Upon encapsulation of the unfolded protein, GroES is recruited to cap the assembly, forming the GroEL-GroES complex. In an ATP-driven mechanism, the unfolded protein is carefully folded into its active state before being released from the chaperonin core.[20- 22]

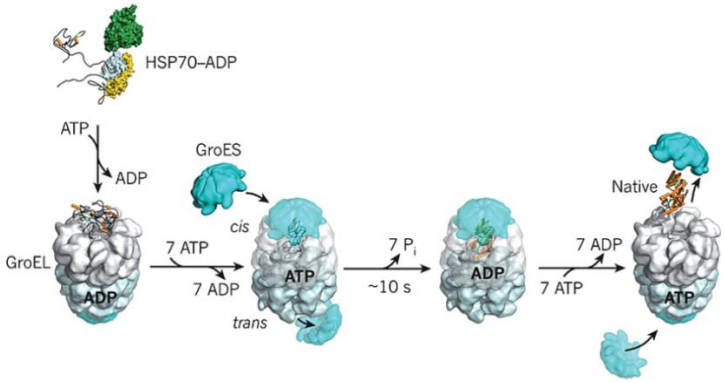

Figure 2.2. Schematic representation of the encapsulation of an unfolded protein inside the GroEL-GroES chaperonin cage. In an ATP driven mechanism, the unfolded protein is folded into its native state before its subsequent release, adapted from reference 22. Copyright © 2011, Rights Managed by Nature Publishing Group.

In contrast to chaperonins, ferritins are spherical cage-like structures composed of either twelve or twenty-four protein subunits, referred to as mini-ferritins or maxi-ferritins (Figure 2.3).[11] Ferritins are found in all living organisms and play an important role in maintaining and regulating intracellular iron concentrations to ensure the presence of sufficient iron levels whilst minimizing the formation of oxidative radicals (via Fenton redox chemistry).[23] One of the most accepted explanations for the storage of iron inside ferritin is based on the diffusion of Fe^{2+} ions through the hydrophilic pores towards the ferritin center. As soon as these Fe^{2+} ions pass the protein barrier they interact with protein chains providing a catalytic ferroxidase activity, which induces the oxidation from Fe^{2+} ions to Fe^{3+} ions under the consumption of either O_2 or H_2O_2. In a final step the formation of a mineral core composed of Fe^{3+} ions is completed, when the entire cavity of the ferritin cage is filled.

Mini-ferritins have an outer diameter of ca. 9 nm and a hollow cavity of ca. 5 nm in diameter (Figure 2.3A), which can accommodate and store up to 500 Fe^{3+} ions.[24] In comparison, maxi-ferritins have an outer diameter of around 12 nm and an inner diameter of 8 nm (Figure 2.3B) and are able to store up to 4500 Fe ions, forming a core of hydrous ferric oxide mineral in the central cavity.[25] The self-assembly process of the protein subunits to form maxi- and mini-ferritins is not entirely understood, however, the proposed pathway of maxi-ferritin assembly involves the stepwise formation of dimers, tetramers and hexamers. In the next step, four hexamers assemble into two dodecamers before forming the final maxi-ferritin cage.[17, 26] For mini-ferritins, there are two proposed pre-assembly steps, involving either the initial formation of dimers, or the initial formation of trimers. In both cases, the intermediate multimers subsequently assemble into the final dodecamer.

The maxi-ferritin (dis)-assembly is dependent on the salt concentration and/or pH.[27] More specifically, at pH 6.7 and at ionic strength below 200 mM NaCl, the protein shell of the maxi-ferritin disassembles into dimers and can be reassembled when the ionic strength is raised above 600 mM NaCl.[28] Alternatively, ferritins can be reversibly disassembled into their dimers by lowering the pH below 2, and reassembled by increasing the pH to 7.5.[27] Owing to their reversible assembly, there is much interest in the use of ferritins in nanotechnology for the encapsulation and delivery of metal-based nanoparticles[29, 30] or for applications in mineralization and storage.[28, 31]

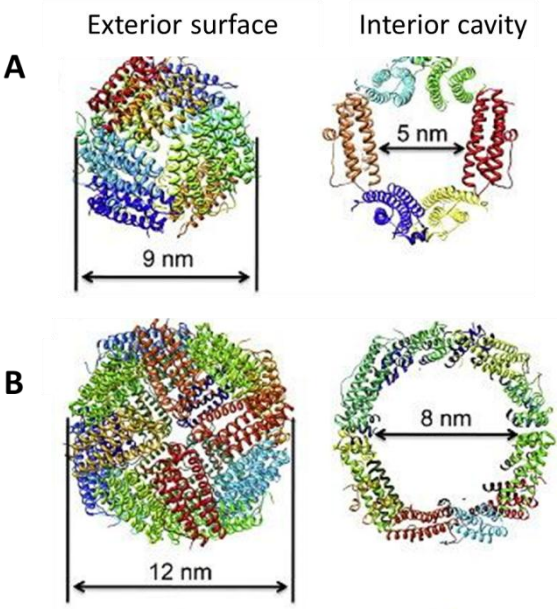

Figure 2.3. Structure of (A) mini-ferritin and (B) maxi-ferritin (adapted from reference 11). Copyright © 2010, Elsevier.

2.3.2 Bacterial microcompartments (BMCs)

Recently, large protein-based assemblies, named bacterial microcompartments (BMCs), have been discovered in prokaryotic cells.[14, 32, 33] Composed entirely of proteins, BMCs are designed to confine specific metabolic pathways by encapsulating multiple enzymes and substrates within their 20 – 150 nm interior (Table 2.2). There are currently three types of BMCs that are known: carboxysomes, metabolosomes and encapsulins.

Table 2.2. Overview of the main properties of BMCs

Protein-based compartments	Outer diameter (nm)	Inner diameter (nm)	Different CP subunits	Pore size (nm)
Carboxysomes	80-140	72-132	6-10	0.4-0.7
Metabolosomes (Pdu)	100-150	92-142	8	0.8
Metabolosomes (Eut)	100-150	92-142	5	0.8
Encapsulins	20-24	18-22	1	0.5

Carboxysomes

Carboxysomes are found in cyanobacteria and chemolithoautotrophs and are currently the best studied class of microcompartments. The carboxysomes are divided into two main groups, namely α- and β-carboxysomes (depending on the

encapsulated ribulose biphosphate carboxylase oxygenase (RuBisCO) species and the gene organization of the carboxysome) and are involved in CO_2 fixation.[34, 35] Carboxysomes are composed of multiple shell proteins, which self-assemble into an icosahedral-like structure with an average diameter around 80 – 140 nm.[32, 36, 37] The protein shell, with an estimated mass of 115 – 355 MDa is composed of six to ten different protein subunits,[38] and is around 3 – 4 nm thick with pores of around 0.4 – 0.7 nm.[36, 39] Carboxysomes encapsulate two metabolic enzymes, carbonic anhydrase (CA) and RuBisCO. Interestingly, around 250 molecules of RuBisCO per carboxysome have been reported to be encapsulated.[38] Carbonic anhydrase catalyses the production of carbon dioxide (CO_2) which, together with ribulose-1,5-biphosphate (RuBP), is consumed by RuBisCO to produce 3-phosphoglycerate (3PGA), a precursor for the Calvin cycle (Figure 2.4). The role of carboxysomes remains unclear, however, it has been proposed that carboxysomes evolved to either enhance the catalytic efficiency of RuBisCO or to protect it from competing substrates, such as oxygen.[34]

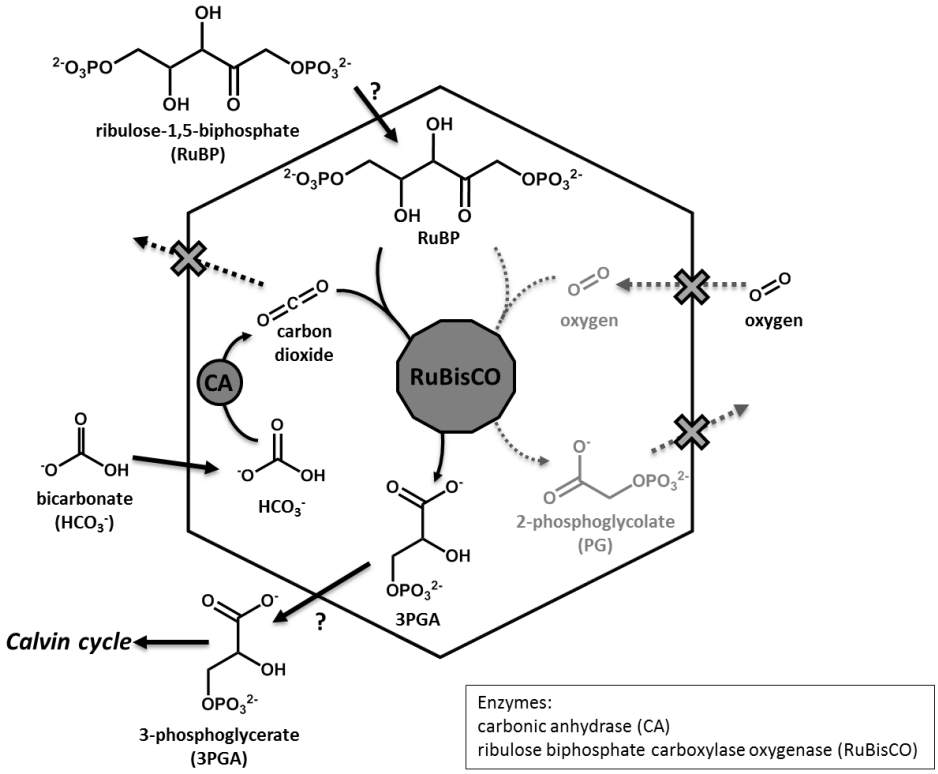

Figure 2.4. Schematic representation of the metabolic pathway inside carboxysomes. The enzymes, carbonic anhydrase (CA) and RuBisCO, are involved in CO_2 fixation (shown by solid lines, adapted from reference 34).

Metabolosomes

Since the discovery of carboxysomes, other bacterial microcompartments involved in specific metabolic pathways, namely propanediol utilization (Pdu, Figure 2.5) and ethanolamine utilization (Eut, Figure 2.6) metabolosomes, have been identified in prokaryotes. The outer shell of metabolosomes is composed of up to five different shell proteins to form a 3 – 4 nm thick shell with pores of 0.8 nm in diameter and an internal space of approximately 100 – 150 nm in diameter.[14, 40, 41] The interior of the Pdu and Eut metabolosome accommodates specific enzymes, substrates and cofactors that are involved in the catabolism of 1,2-propanediol (Pdu) and ethanolamine (Eut), respectively. It is currently believed that the shell of metabolosomes serves to either protect the cell from toxic intermediates (propionaldehyde or acetaldehyde for Pdu and Eut, respectively) and/or avoiding the loss of a carbon source by confining the enzymes and substrate intermediates.[42]

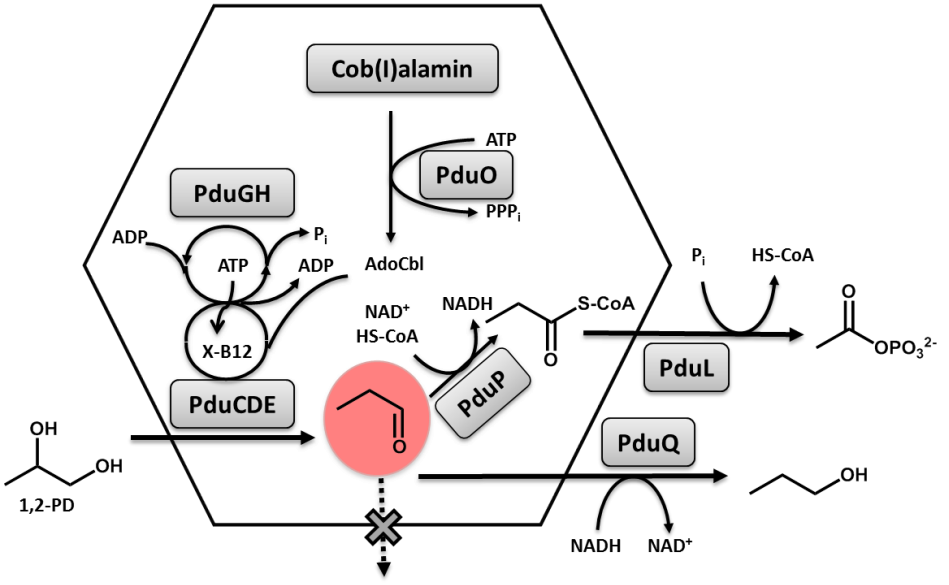

Figure 2.5. Schematic representation of the metabolic pathway of propanediol utilization (Pdu), (adapted from reference 9).

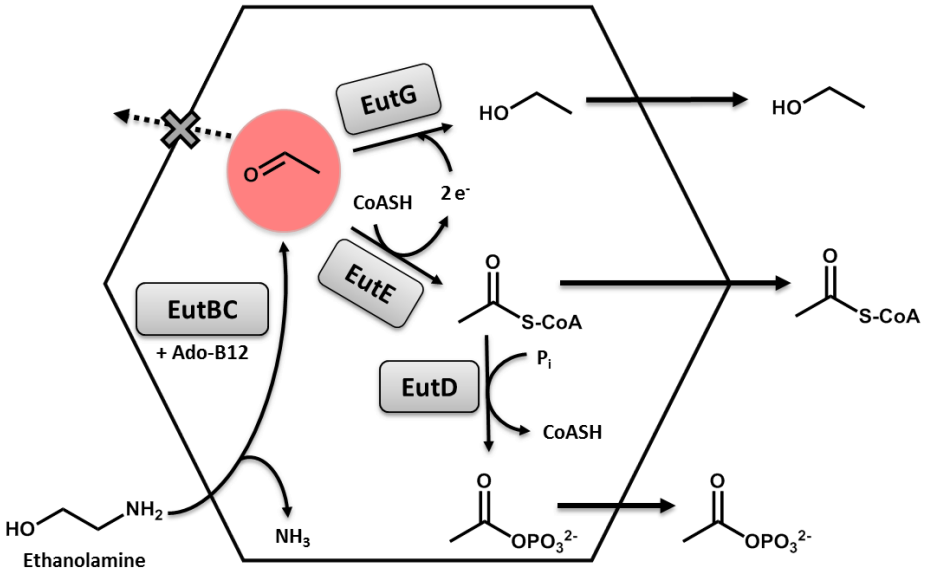

Figure 2.6. Schematic representation of the metabolic pathway of ethanolamine utilization (Eut) (adapted from reference 9).

Compared to ferritins and other protein cages, there is currently little known about the *in vitro* (or *in vivo*) disassembly and assembly of metabolosomes. For this reason, the use of metabolosomes for the encapsulation of functional materials has not been reported. Nonetheless, owing to their large size and their proposed role in Nature, bacterial microcompartments hold much promise in future applications in nanotechnology.

Encapsulins

One of the smallest reported bacterial microcompartments are the encapsulins (also called linocin-like proteins) isolated from *Thermotoga maritima* and *Brevibacterium linens*. The protein shell is composed of 60 monomers (with an average mass of 31 kDa) that is assembled *in vivo* into an icosahedron of approximately 20 – 24 nm in diameter. The pores in the protein shell are around 0.5 nm in diameter.[43] Encapsulins contain either dye-decolorizing peroxidase, DyP (*B. linens*) or a ferritin-like protein, Flp (*T. maritima*) within their internal cavity. Similar to ferritins and metabolosomes discussed in the previous section, it is thought that encapsulins confine Flps or DyPs to either store ferrous ions or to prevent the formation and release of toxic intermediates.[43] A conserved C-terminal peptide sequence (GSLxIGSLKG, Glycine-Serine-Leucine-x-Isoleucine-Glycine-Serine-Leucine-Lysine-Glycine, where x is any amino acid) was found for both DyP and Flps enzymes and is thought to be required for the directed encapsulation of the native enzymes inside the protein shell. However, until recently, the potential

applications of encapsulins were somewhat limited since the *in vitro* assembly/disassembly pathway was unknown. In 2013, Bugg and coworkers reported the *in vitro* disassembly and reassembly of the encapsulin from *Rhodococcus jostii RHA1*.[44, 45] Disassembly of empty encapsulins into their dimeric proteins was achieved by dialyzing against acetate buffer at pH 3. Subsequent dialysis back to pH 7.0 against 50 mM phosphate buffer induced the re-assembly of empty encapsulins. In order to obtain filled encapsulins, the protein dimers were mixed with peroxidase DyB and incubated at 100 mM phosphate buffer, 100 mM NaCl at pH 7.4. Here, the authors showed the controlled *in vitro* encapsulation of DypB in *R. jostii* encapsulin, which opens up new opportunities for their use as self-assembling building blocks for applications in nanotechnology.[44]

2.3.3 Virus-like-particles (VLPs)

Unlike ferritins and bacterial microcompartments, which are non-infectious assemblies involved in storage and metabolic pathways, viruses are renowned for their infectious nature and their ability to evade detection from host immune cells to effectively and efficiently deliver genetic cargo. Over the last years, more than 100 virus-like particles (VLPs) have been isolated and characterized.[12] The most common and simplest viruses are composed of genomic RNA/DNA, surrounded by an outer protein shell that serves to protect and disguise the genetic cargo. The outer protein shell is composed of multiple copies of one or more different virus coat proteins that assemble into highly symmetrical structures. Although the overall morphology varies between different viruses, the two most common geometries are icosahedral and rod-like structures (Table 2.3).
Icosahedral capsids are assembled according to the Caspar-Klug *quasi*-equivalence theory in which $60N$ subunits (where N is the triangulation (T) number) are symmetrically arranged as pentamers and hexamers to form the final icosahedron. The smallest icosahedral virus is composed of 60 protein subunits arranged as 12 pentamers to form a $T = 1$ capsid assembly. Elongated capsid assemblies can be achieved by inserting a cylindrical section between two half-icosahedral capsids, leading to rod-like structures.[46] Owing to their robust nature, stability and versatility, viruses have been used extensively for the encapsulation of functional materials for applications in nanotechnology.

Table 2.3. Overview of the main properties of VLPs

Protein based compartment	Outer/ inner diameter (nm)	Number of CPs / different CP subunits	*T* Nr.	Pore size (nm)
MS2	27 / 23	180 / 1	3	1.6-1.8
Qβ	27 / 23	180; 60 / 1	3; 1	1.3-1.4; 0.7
P22	58-64	415-420 / 1	7; 3	2; 10
M13	6.5-7 and 880-930 (length)	2700-2800 / 1	rods	---
TMV	18 / 4 and 300 (length)	2100 / 1	rods	---
CCMV	18; 22; 27 / 10; 14; 19	60; 90; 180 / 1	1; 2; 3	-; -; 2

MS2 - bacteriophage

The MS2 bacteriophage forms capsids to encapsulate single-stranded genomic RNA. The MS2 virion is composed of 90 virus coat protein dimers that form an icosahedral *T* = 3 capsid with an outer diameter of 27 nm. The protein shell is 2-3 nm thick and has 32 pores about 1.6 - 1.8 nm in diameter.[15, 47-52] Each capsid shell contains a single copy of a so-called A-protein, which is thought to be essential for the packing of RNA inside the capsid.[53] Interestingly, when expressed recombinantly in *E. coli*, MS2 can still self-assemble in the absence of the A-protein into intact icosahedral *T* = 3 virus-like particles encapsulating the viral RNA at their interior.[15, 47-52] Furthermore, MS2 can be self-assembled *in vitro* at pH 4 in the presence of peptide-based or nucleic acid cargo.[49, 54] The ability to control the assembly/disassembly process under *in vitro* conditions opens up many opportunities for the controlled cargo encapsulation inside MS2 capsids, thus making them potential candidates for applications in drug delivery and material science.

Qβ – bacteriophage

In a similar example to MS2, the Qβ bacteriophage is assembled from 90 dimers to form non-enveloped capsids of 27 nm in diameter, surrounding a 4.2 kb single-stranded RNA to form icosahedral capsids with *T* = 3 symmetry.[55-57] Furthermore, the capsid has 20 pores located in the protein shell.[56, 58] The pores have a diameter of 1.3 - 1.4 nm at the threefold axis and a diameter of 0.7 nm at the fivefold axis.[51] Unlike the native MS2, which requires a single A-protein for assembly, Qβ requires two helper proteins for the formation of infectious virus particles (A1 protein)[59] and a maturation protein (A2 protein).[60] Structurally, the assembly of the Qβ bacteriophage involves the formation of disulfide bonds, which are crucial for covalently linking the monomeric Qβ protein subunits. The morphology of the Qβ capsid can be tuned and adapted by replacing the cysteine residues and its

neighboring amino acid residues, leading to the formation of rod-like and smaller icosahedral Qβ VLPs.[61, 62] Owing to their ability to be assembled either *in vivo* or *in vitro*, Qβ is a highly attractive scaffold for applications in nanotechnology, such as molecular delivery vehicles and has been used for the encapsulation of various foreign materials.[54, 56]

P22 – bacteriophage

One of the most studied bacteriophages is the P22 bacteriophage. Whilst MS2 and Qβ bacteriophages encapsulate single-stranded RNA, P22 encapsulates a double stranded DNA genome and the assembly is performed in three steps. In the first step, 300 scaffolding proteins (33.6 kDa) are coassembled with 420 monomeric coat proteins (44.6 kDa), forming the $T = 7$ procapsid equipped with 12 – 20 copies of three different proteins necessary for the injection of DNA into the host cell.[63] In the second step, the viral dsDNA is packaged inside the procapsid and simultaneously releases the scaffold proteins through large pores located within the procapsid shell. In the third step, the procapsid undergoes a 10% volume expansion.[63, 64] Empty $T = 7$ procapsids can be isolated under *in vitro* conditions either by extraction with guanidine HCl or by heating the procapsid for 10 min at 65 °C, causing an expansion of the capsid shell from 58 nm to 64 nm by simultaneous release of the scaffold proteins.[65, 66] By further heating the procapsid to 75 °C, subunits of the protein shell are released, leaving 10 nm holes in the procapsid assembly.[65] Interestingly, by conserving the C-terminal residues of the scaffold protein, the remaining N-terminal sequence can be substituted with the protein of interest and that has been shown to be highly efficient for the directed encapsulation of guest proteins inside P22.[67] An alternative strategy involves the introduction of a single cysteine point mutation on the interior of the P22 coat protein, to which functional materials can be coupled via thiol coupling chemistry.[66] Overall, although there is no disassembly and reassembly pathway known for the P22 bacteriophage, the conformational changes induced upon heating make the P22 bacteriophage an interesting tool for nanotechnology.

M13 – bacteriophage

The filamentous M13 bacteriophage is a member of the *Inoviridae* family.[91] Unlike the Qβ, MS2 and P22 bacteriophages which encapsulate linear RNA/DNA, the native M13 bacteriophage contains a single-stranded circular DNA genome of around 6400 nucleotides (nt). The genome is encapsulated in a 1.5 – 2 nm thick flexible protein shell that is stable in the pH range between 6 and 9 and at temperatures up to 37 °C.[68] The shell is composed of five different coat proteins and forms an α-helical assembly of 6.5 – 7 nm in diameter and around 880-930 nm in length.[69] The major coat protein (gene VIII protein: gpVIII) is composed of 50

amino acids (5.2 kDa), of which approximately 2700 – 2800 copies are assembled around the genome. This assembly of gpVIII leads to the formation of a hydrophobic core, whereby the positively charged C-terminus interacts with the genome and the negatively charged N-terminus is exposed to the outside of the helical structure. The end caps of the helical structure are formed by five copies of each minor coat protein: gpVII, gpIX, gpIII and gpVI (Figure 2.7). The distal end cap is composed of gpVII and gpIX and is necessary for the formation of the M13 bacteriophage, whereas gpIII and gpVI form the proximal end cap and is responsible for the host recognition and infection.[69-71]

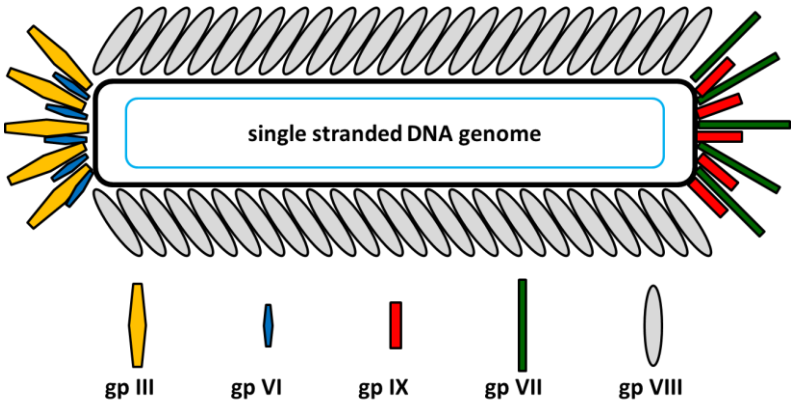

Figure 2.7. Schematic representation of the structure of the M13 bacteriophage.

The M13 phage has proven to be a very important tool in the fields of genetic engineering and biotechnology, since functional peptides can be readily attached to the N-terminus of the gpIII or gpVIII, leading to the expression of five to several thousand copies of the foreign peptide at the M13 surface, respectively.[72] However, at the same time, the coat protein function can be disrupted and can lead to inefficient representation of the foreign peptide at the phage surface. Therefore, two different methods have been developed to display foreign material at the phage surface. The first approach involves the engineering of a hybrid phage, which encodes for the five wild-type coat proteins as well as the foreign peptide fused to either gpIII or gpVIII. The second approach involves a phagemid-based system including a helper phage.[73] Here, the gene coding for the foreign material is engineered in a plasmid containing the M13 origin for replication, but lacks the genes encoding for the virus production. Instead, these genes are located on a second plasmid, encoding the viral coat protein necessary for the viral assembly. When these two plasmids are expressed together, the foreign material is incorporated in the coat protein assembly. Both methods provide a strategy to only express a few copies of the foreign material at the surface of the M13 phage and have since been shown to be suitable for applications in the fields of nanotechnology and tumor targeting.[74, 68, 75-79]

Tobacco Mosaic Virus

The tobacco mosaic virus (TMV) is a plant virus from the *virgaviridae* family forming helical rod-like particles and was discovered in the late 1800s.[80] These assemblies are composed of approximately 2100 identical 17.6 kDa coat proteins, which self-assemble in a right-handed helix around the genomic single stranded RNA of around 6300 – 6500 nt.[81] The helical rods are, on average, 300 nm long with an outer diameter of 18 nm and an inner diameter of 4 nm.[82, 83] In contrast to the M13 bacteriophage, no end caps have been observed during and after the assembly of the TMV rods. The TMV coat protein can be expressed in plants but also in bacteria, which allows them to be genetically engineered.[82, 84-87] The self-assembly process involves two major steps: 1) the binding of a specific stem-loop of the ssRNA with a disk, which is composed of a two-ring sub-assembly of the TMV coat proteins, 2) the assembly of the TMV coat protein around the RNA. The elongation step to form the TMV rod structure occurs in both directions. However the elongation in the direction towards the 5'-terminus is faster and involves the preformation of disk structures (20S), which then assemble around the RNA, whereas the elongation process towards the 3'-terminus is slower and involves the formation of smaller CP aggregates, which then bind to the RNA. Although TMV show a high stability in a pH range of 3.5 - 9 and temperatures up to 90 °C, several forms of aggregates have been observed during *invitro* expression.[20] Depending on the pH and the ionic strength, these assemblies form several structures ranging from double disks to rods of different lengths.

Cowpea Chlorotic Mottle Virus

The Cowpea chlorotic mottle virus (CCMV), from the bromovirus group of the *Bromoviridae* family, is a single-stranded RNA plant virus that forms $T = 3$ icosahedral capsids with an outer diameter of 28 nm and an internal cavity of 550 nm^3 (5.5×10^6 $Å^3$).[88, 89] The capsid is assembled from 90 dimeric coat protein subunits (20.3 kDa) to form a 2 - 4 nm thick protein layer with 60 pores.[90] The C-terminal residues (186-190) are essential during capsid assembly for the formation of non-covalent interactions between individual coat proteins (CCMV-CP). The N-terminus (residues 1-26) contains nine arginine residues and one lysine residue, and provides a net positive charge that interacts with the negatively charged viral RNA.[88, 91] The viral RNA of CCMV is composed of three genomic species (RNA 1 – RNA 3) and RNA 4, a subgenomic RNA expressed from RNA 3 and serves as the mRNA for the CCMV-CP.[92, 93] RNA 1 (3200 nt) and RNA 2 (2800 nt), which encode for proteins involved in RNA-dependent replication, are packaged in separate CCMV capsids. RNA 3 (2100 nt) and RNA 4 (900 nt) are copackaged into a third CCMV capsid in an approximate 1:1 molar ratio.[94] CCMV exhibits a well-studied *in vitro* assembly and disassembly pathway that is similar to other

icosahedral viruses, such as bromo mosaic virus (BMV) or cowpea mosaic virus (CPMV).[95-97] Depending on the pH and salt conditions, the native *T* = 3 CCMV capsid swells about 10% forming pores of up to 2 nm, which allow the release of the viral RNA. Upon further raising the pH, the CCMV capsid disassembles into the 90 coat protein dimers (Figure 2.8A).

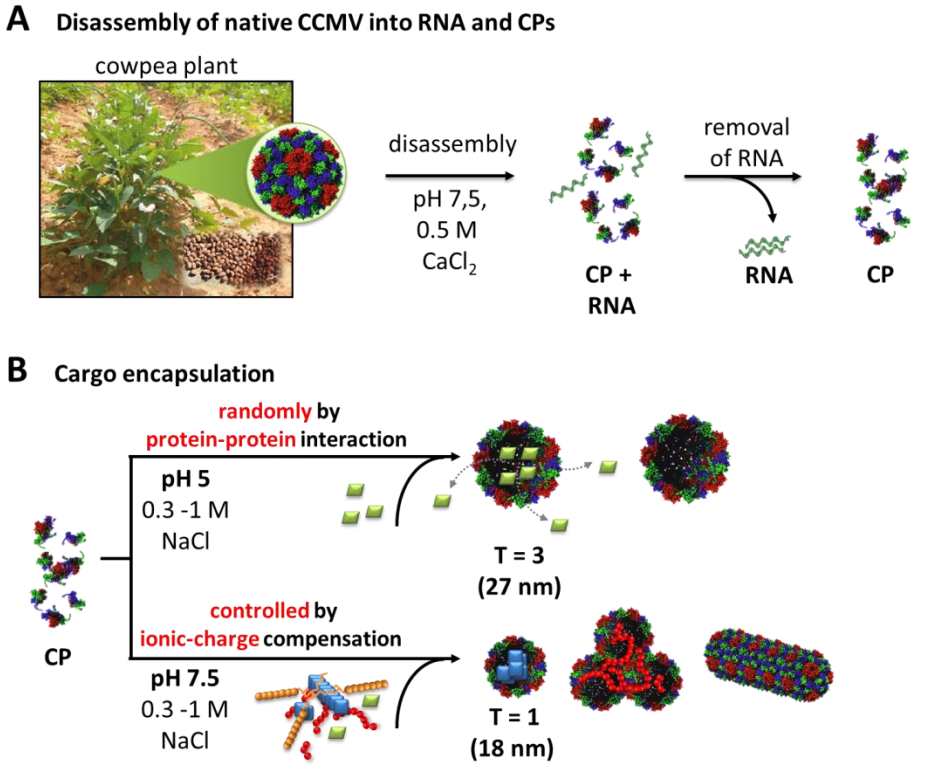

Figure 2.8. (A) The native cowpea chlorotic mottle virus (CCMV) is a plant virus that forms icosahedral T = 3 capsids, (B) Under in-vitro conditions, CCMV displays reversible that can be controlled by pH and ionic strength.

Two different *invitro* self-assembly strategies enable the disassembly of the CCMV capsid into CP dimers and the reassembly back into virus-like particles, while encapsulating non-natural cargos. The first strategy to form *T* = 3 VLPs is based on protein-protein interactions at slightly acidic pH (pH 5.0) and high ionic strength (I > 1 M). In this case the cargo does not need to provide any surface charges and is instead randomly encapsulated. The assemblies resulting from this method are typically a mixture of empty and filled VLPs. In the second strategy, the CP at slightly basic pH (pH 7.5) and an ionic strength of I > 0.3 M assembles to form VLPs in the presence of negatively charged cargo, hence only filled VLPs are formed. Depending on the size and flexibility of the cargo different sizes and shapes of VLPs have been observed, ranging from *T* = 1 VLPs (30 dimeric CP, around 18 nm in

diameter), *T* = 2 (60 dimeric CP, around 22 nm in diameter) VLPs, *T* = 3 VLPs (180 dimeric CP, around 27 nm in diameter) and rod-like CCMV assemblies. In the latter case, a double stranded DNA of high molecular mass was used as cargo.[98, 99] Note that these VLP assemblies, which are driven by ionic-charge compensation result in VLPs that always encapsulate a cargo (Figure 2.8B).[91, 100-102] CCMV VLPs that are formed by ionic-charge compensation are stable against temperatures up to 65 °C, pH values between 5.0 and 7.5 and in MilliQ water in the absence of salts.[102, 103] Furthermore, they present also pores which allow substrate exchange with the surrounding solution.[102, 104] The versatile morphology, reversible assembly and stability of CCMV makes them particularly attractive scaffolds for the encapsulation of functional materials for applications in nanotechnology.[105, 106]

2.4 Functionalization of the protein shell

In general, one of the major advantages of protein-based compartments is that they are composed entirely of protein building blocks, which enables the outer (and inner) surface to be modified genetically or by chemical labeling with small molecules.[107, 108] Furthermore, since they are composed of multiple copies of identical proteins that assemble into highly symmetrical structures, functionalization at a single amino acid position is translated over the entire cage assembly, (*i.e.* for a *T* = 3 virus capsid, one mutation of the monomer leads to 180 identical mutations that are positioned symmetrically over the entire icosahedron). This can be highly advantageous for applications in cell-recognition and molecular targeting since a single modification can introduce multivalency effects. For example, the interior of the MS2 bacteriophage was functionalized with porphyrins for applications in photodynamic therapy, while the exterior was functionalized with an aptamer to improve cell selectivity. After photoirradiation only 20 min, the functionalized capsids showed 76% efficiency in the selective targeting and killing of Jurkat cells compared to non-functionalized or (targeted) empty capsids. This impressive example demonstrates the potential applications of virus-based assemblies in targeted therapeutics. However, in general, many protein cage compartments are highly sensitive to structural modification and surface functionalization. A single modification can disrupt the subtle interactions that are crucial for protein cage assembly. For these reasons, this area still remains highly challenging and there are only a few strategies currently used to functionalize protein cage assemblies. To date, most examples are based on virus assemblies, however since the same functional groups are present on most protein cage compartments, the same strategies can be applied. An overview of the different strategies for the chemical modification of amino acids is given in Figure 2.9, and have been used for the conjugation of small molecules,[78, 106, 109] polymers,[110] nanoparticles[111] or enzymes[112] to the surface of spherical virus-like particles.

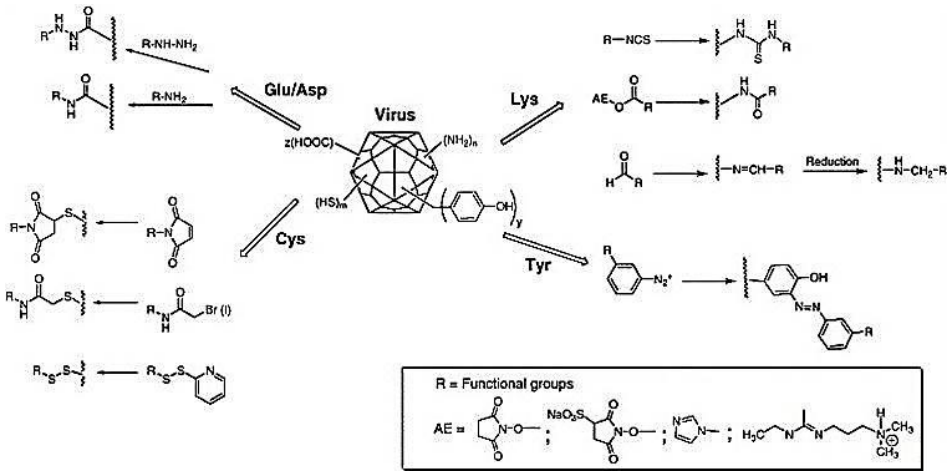

Figure 2.9. Surface modification of virus-based assemblies based on chemical functionalization (adapted from reference 113). Copyright © 2006, Elsevier.

Covalent attachment can be achieved via the a) amino (NH_2), b) carboxylic acid (COOH) and c) thiol (SH) groups present in amino acid residues. The amino groups can react with N-hydroxysuccinimide esters or isothiocyanates, the carboxylic acid groups react with amines when pre-activated using *e.g.* carbodiimides and the thiol groups can be alkylated using maleimide or bromo/iodo acetamides. In addition, the amino acid tyrosine provides a phenol group, which can be functionalized via diazonium-coupling reactions.[113] Another method to introduce functional residues, such as cysteines, can be achieved by genetic engineering using site-directed mutagenesis.[114] The specific type of amino acid and the subsequently formed bioconjugates for several viruses have been described in detail by Lee *et al.* and Cardinale *et al*.[113, 115, 116]

As an alternative or complementary strategy, protein-based compartments can be modified at the amino group of the N-terminus or the carboxylic acid group of the C-terminus. These modifications can contain peptide coils or protein binding motifs.[117] For example, CCMV was genetically modified for the controlled encapsulation of proteins inside the capsid. In this case, the positively charged N-terminus of the CCMV-CP was extended with a K-coil $(KIAALKE)_3$ peptide motif. Modification of the desired protein cargo with the complementary negatively charged E-coil $(EIAALEK)_3$ peptide motif promotes the formation of the heterodimeric CCMV-K and cargo-E coiled-coil at pH 7.5. Upon lowering to pH 5.0, CCMV assembles into T = 3 VLPs and the protein cargo is encapsulated.[118, 119] A similar strategy has been reported for the controlled assembly of empty T = 1 VLPs at pH 7.5 and 2.5 M NaCl by modification with a thermally responsive elastin-like polypeptide (ELP). These ELPs can switch between an extended water-soluble state and a hydrophobic collapsed state depending on the temperature and salt concentration.[120]

2.5 Functional cargos

In native virus assemblies, the interplay between the viral genome (DNA or RNA) and the coat proteins plays a crucial role in determining the size and shape of the capsids. Although foreign RNA or DNA can be encapsulated to form capsids that are identical to their native viruses,[87, 94, 121-123] the encapsulation of synthetic materials can manipulate the size and morphology of virus-based assemblies, leading to entirely new structures.

2.5.1 Template directing self-assembly of protein compartments

Template-induced self-assembly of spherical VLPs

As described above, depending on the properties of the cargo template, different sizes of icosahedral virus-like particles can be achieved. In particular, the self-assembly of BMV or CCMV coat proteins has been directed to form either $T = 1$, $T = 2$ or $T = 3$ assemblies by using different templates (Table 2.4) For example, de la Escosura and coworkers showed that the self-assembly of $T = 1$ CCMV based capsids can be induced upon encapsulation of short oligomers. Here, they used an oligothymine sequence composed of 40 thymine units to form monodisperse $T = 1$ CCMV particles.[99]

Polystyrene sulfonate (PSS) has been used extensively to demonstrate the tuneable self-assembly of CCMV-CP into monodisperse virus-like particles of different sizes. By using PSS of different molecular masses of 38 kDa, 300 – 900 kDa and 1900 – 3300 kDa self-assembly of CCMV-CP into $T = 1$, 2 and 3 virus-like particles, respectively, was achieved. In this work, the authors attributed the apparent size selection to charge compensation requirements between the negatively charged PSS template and the positively charged N-terminus of CCMV.[94, 98] In all of the examples described so far, anionic templates (*i.e.* polymers, nanoparticles, DNA, micelles) have been used to drive self-assembly of virus-based assemblies. In an unusual example, the bromomosaic virus (BMV) was used to encapsulate gold nanoparticles functionalized with a PEG layer (Au-PEG). Although these nanoparticles were uncharged, virus-like particles of $T = 1$, 2 and 3, respectively, were obtained depending on the diameter of the gold core (6, 9 or 12 nm) (Figure 2.10). In this unprecedented example, it was proposed that the CCMV N-terminus intercalated between the PEG layer, however no detailed description was given.[96] This example demonstrates that, in some cases, although charge compensation requirements are not fulfilled, the nature of the template can still enforce the self-assembly of virus-like particles to occur.

Table 2.4. Shape and size overview of cargos inducing spherical VLPs with different T-numbers

Origin of CP	Cargo	Diameter or molecular mass of cargo	Diameter of VLPs (nm)	*T*-number	Ref.
BMV		6 nm	~ 21	*T* = 1	
BMV	gold nanoparticles functionalized with PEG (Au-PEG)	9 nm	~ 26	*T* = 2	96
BMV		12 nm	~ 28	*T* = 3	
BMV	PEG-coated quantum dots (QD)	8 nm	~ 32	*T* = 2	73
BMV	PEG-coated iron oxide nanoparticles	20.1 nm	~ 41.3	*T* > 3	124
CCMV	zinc phthalocyanine (ZnPcs)	895 g/mol per ZnPc (~ 160 ZnPcs)	~ 19	*T* = 1	102
CCMV	polymeric DNA amphiphiles (micelles)	10 nm	~ 20	*T* = 2	125
CCMV	polystyrene sulfonate (PSS)	38 kDa	~ 19 ~ 21	*T* = 1 *T* =2	98
CCMV	polystyrene sulfonate PSS	300-900 kDa, R_G 18-25 nm	~ 21-22	*T* = 2	94
CCMV	polystyrene sulfonate PSS	1900-3300 kDa R_G 36-42 nm	~ 27-28	*T* = 3	94
CCMV	MPS-PPV	R_G 26 nm	~ 20 nm	*T* = 1	102
CCMV	oligothymines (Tq), q = 40 thymine units	---	~ 19 nm	*T* = 1	99

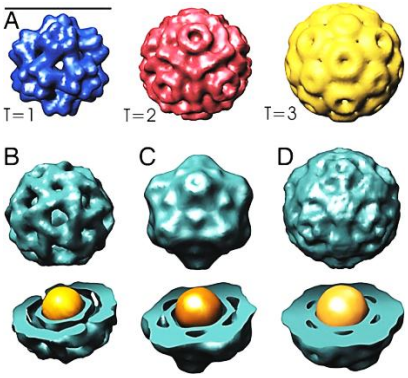

Figure 2.10. Encapsulation of Au-PEG of different core sizes in BMV. (A) Model of *T* = 1, 2 and 3 BMV cages. (B) *T* = 1 VLP filled with Au-PEG of 6 nm in diameter, (C) pseudo *T* = 2 VLP filled with Au-PEG of 9 nm in diameter and (D) *T* = 3 VLP filled with Au-PEG of 12 nm in diameter (adapted from reference 96). Copyright © 2007, National Academy of Sciences, U.S.A.

Template-induced clustering of spherical VLPs

The encapsulation of functional nanoparticles combined with the reversible clustering of hybrid assemblies has been explored extensively.[124] For example, surface interactions between the negatively charged exterior of virus particles and positively charged nanoparticles have been shown to induce the assembly of complex hierarchical structures. In this example, cationic gold nanoparticles functionalized with an amphiphilic ligand, were used to induce surface-surface clustering of individual CCMV, apoferritin or magnetoferritin particles.[125] Similarly, rod-like bacteriophages containing negatively charged gold nanoparticles were used to assemble well-organized monolayers of M13 bacteriophages.[126, 127]

In addition to clustering via interactions at the exterior of capsids, the clustering of several single capsids can be obtained in the presence of high molecular mass polymers. For example, encapsulation of ssRNA of 3000 nt in CCMV leads to the formation of single $T = 2$ or $T = 3$ virus-like assemblies.[128] Interestingly, encapsulation of ssRNA with more than 4500 nt resulted in clusters of two or more capsids whereby the RNA cargo was proposed to span across individual capsid assemblies (Figure 2.11).[98]

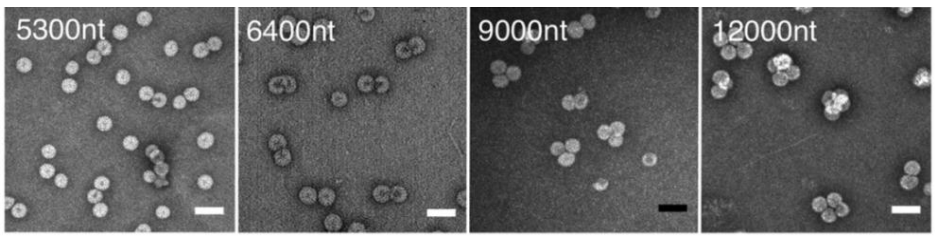

Figure 2.11. Negatively stained TEM micrographs of CCMV assemblies. Depending on the RNA length (5300 nt, 6400 nt, 9000 nt or 12000 nt), CCMV-VLP cluster formation can be observed, adapted from reference 98. Copyright © 20012, American Society for Microbiology.

Similar results were observed using synthetic cargo such as high molecular mass poly[(2-methoxy-5-propyloxy sulfonate)-phenyl-ene vinylene] (MPS-PPV) polymers, in which the extended length and flexibility of the polymer chains allows the polymer to span across multiple capsids.[102]
In a particular interesting example, controlled reversibly with UV light, clustering was shown using photosensitive dendrons.[129] Upon irradiation, important electrostatic interactions between the dendrons and the CCMV capsids were disrupted, triggering the clusters to dissociate back into individual capsids.

Template-induced rod-like assemblies

In very special cases, the rigidity of the template can be used to direct the virus-protein to assemble into a different morphology. In particular, tubular assemblies of CCMV with a length scale spanning several hundreds of nm have been reported upon encapsulation of double stranded DNA (dsDNA)-based polymers (Figure 2.12).[130, 131] In both cases, the rigidity of the dsDNA template directs the assembly of the normally spherical virus to form well-defined tubular structures.

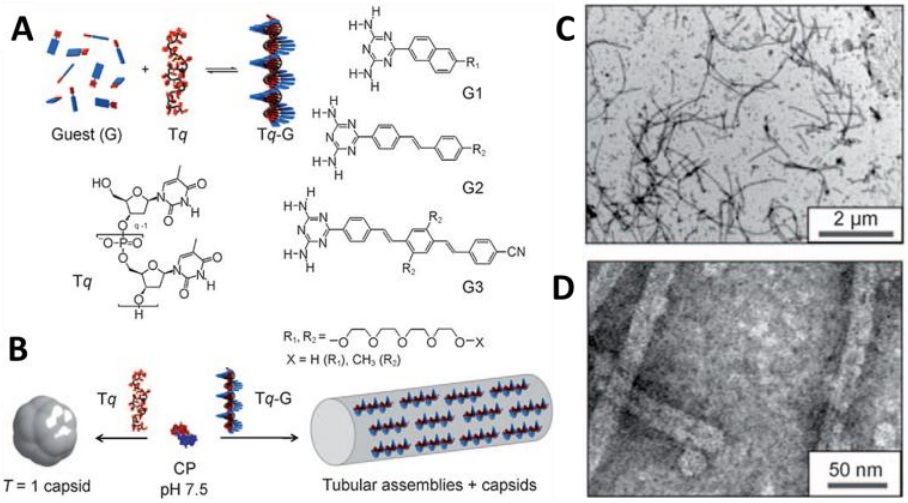

Figure 2.12. DNA-templated chromophore assemblies. (A) Schematic of Tq-G complex formation between single-stranded oligothymine (Tq), q is representing the number of thymine units and the guest molecules used for incorporation into the oligothymine sequence to mimic dsDNA. (B) Encapsulation of either single-stranded oligothymine, which resulted in *T* = 1 particles or Tq-G mimicking dsDNA, which resulted in tubular assemblies. (C and D) Negatively stained TEM micrographs of tubular structures (adapted from reference 130). Copyright © 20010, WILEY-VCH Verlag GmbH & Go. KGaA, Weinheim.

2.5.2 Effects of encapsulation on the properties of the template

Towards medical applications

While various templates have been used to induce the assembly of virus-like particles, at the same time, the interior of viruses provides a confined environment, which can greatly influence the physical, optical or chemical properties of the encapsulated cargo. This has distinct advantages, particularly in cases where solvent effects play an important role.[132] In an example, polymer-DNA amphiphiles were encapsulated into virus-like assemblies.[133] The combination of solvent shielding and high local concentration led to an increase in stability of the amphiphilic micelles upon dilution below their critical micelle concentration and demonstrated their potential applications in molecular imaging, targeted therapy and as drug delivery systems. In another example, the capsid of CCMV has been used for the encapsulation of Gd^{3+} complexes for potential applications in magnetic resonance imaging (MRI). In this case, the N-terminus of CCMV was genetically modified with a peptide sequence that can coordinate Gd^{3+}. The encapsulation and shielding of the Gd^{3+} center led to high local concentrations of Gd^{3+} with better Gd^{3+} binding and improved T1 and T2 relaxivity.[114] Similarly, Douglas and coworkers recently reported the functionalization of the exterior of the P22 capsid with Gd-DTPA-NCS (DTPA: diethylenetriaminepentacetate).[66] In both cases, the tethering of Gd complexes to virus-based assemblies leads to a significant increase in rotational correlation times over free Gd complexes. Apart from applications in MRI, CCMV has been used for the encapsulation of zinc phthalocyanine (ZnPc) for use in photodynamic therapy (PDT).[102] A detailed description of the PDT mechanism is already reported.[20, 134, 135] In this example, CCMV capsids filled with ZnPcs were internalized inside macrophage cells. Upon irradiation with red light, ZnPc produces reactive oxygen species, which induced cell death. However, further investigations towards cell uptake efficiency and immune response are needed before such assemblies would find applications in cancer cell therapeutics.

Tuning optical properties

In a somewhat related field, virus-based assemblies show much potential as model systems that mimic biological systems. Very recently, Douglas and coworkers reported the encapsulation of two fluorescent proteins, namely GFP and mCherry, in the bacteriophage P22. The co-localization of the two fluorescent proteins led to 5-fold increase in Fluorescence Resonance Energy Transfer (FRET) efficiency, and opens up opportunities to mimic *in vivo* conditions and "cell-like" crowding effects, in order to improve our understanding in how a living cell functions.[67] Similarly, mimics of natural light-harvesting assemblies were reported by Francis and coworkers, who exploited the hierarchical self-assembly properties of TMV that

were functionalized with fluorescent chromophores. Upon self-assembly of the modified TMV into hierarchical stacks, broad spectrum light could be collected with over 90% overall efficiency.[136] In a recent example, the group of Francis reported the encapsulation of gold nanoparticles within the MS2 bacteriophage combined with the external functionalization of the capsid assemblies with a DNA-coupled fluorophore (Figure 2.13).[137] Impressively, the distance between the fluorophore and the nanoparticle could be carefully tuned in order to enhance the fluorescence intensity. Although the authors focus on applications for metal-enhanced fluorescence, one can envision that such assemblies could be useful in biomedical applications.

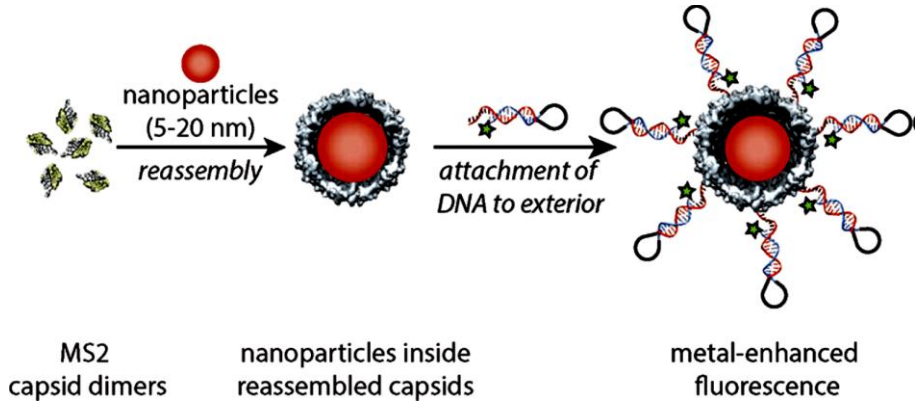

Figure 2.13. Encapsulation of DNA-modified gold nanoparticles inside MS2 viral capsids and the outer capsid modification with a fluorophore (adapted from reference 137). Copyright © 2013, American Chemical Society.

Influencing enzymatic activity

In recent years, there has been increasing interest to explore the role of organelles in Nature with the ultimate aim of replicating the complexity of the living cell using biosynthetic components (*i.e.* developing artificial organelles). In particular, the use of protein-based assemblies has shown great potential to study the influence of compartmentalization on enzyme activity. Douglas and coworkers genetically engineered the bacteriophage P22 to encapsulate 87 ± 3.5 homotetrameric β-glycosidase (CelB) unit or 249 ± 13 copies of alcohol dehydrogenase D (AdhD).[65] In another example, aspartate dipeptidase peptidase E (PepE), firefly luciferase (Luc) and a thermostable mutant of Luc(tsLuc) were encapsulated within Qβ bacteriophages.[56] Similarly, alkaline phosphatase (PhoA) was genetically modified with an acidic peptide tag for the encapsulation of, on average, 1.6 PhoA within the MS2 bacteriophage.[49] The acidic peptide tag provides an overall negatively charge on the enzyme cargo, which is then able to interact with the native positively charged MS2 coat proteins. This result in the formation of filled MS2 capsids. In

most cases, the encapsulation of multiple copies of the same enzyme inside bacteriophages revealed either very similar or a slight decrease in enzymatic activity compared to the free enzymes.[49, 56, 65]

In an opposite example, the encapsulation of *Pseudozyma antartica* lipase B (PalB) in CCMV showed an overall increased activity compared to free enzymes. Interestingly, although the encapsulation of 1.3, 2.0, 3.5 and 4.0 PalBs were reported, the largest increase in enzymatic activity was observed when only a single enzyme per capsid was present (Figure 2.14).[118]

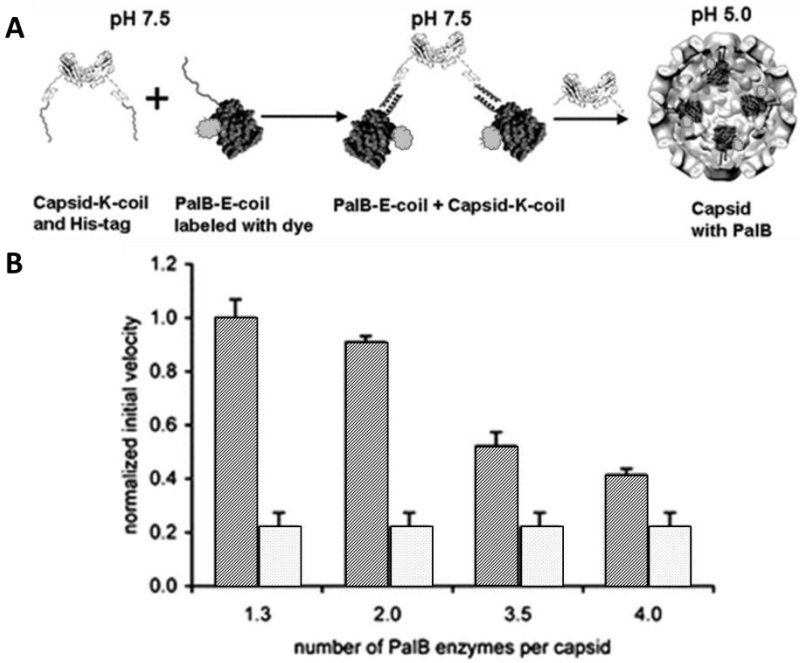

Figure 2.14. (A) Schematic representation of the encapsulation of lipase B (PalB) inside CCMV. Encapsulation of PalB inside CCMV was achieved by pre-forming the CCMV-PalB complex at pH 7.5 before inducing CCMV assembly at pH 5.0. (B) Normalized initial enzyme velocity rates of PalB encapsulated in CCMV (dark gray bars) compared to free PalB (light gray bars) (adapted from reference 118).

In general, there is still very little that is known about the influence of compartmentalization on enzymatic pathways and the physical environment inside protein cages. The encapsulation of individual enzyme types has been shown to be possible and demonstrates the future possibilities of including multiple-step enzyme reactions or enzyme cascades within protein assemblies. Further challenges lay in the ability to control the flux of substrates and products in and out of protein-based compartments in order to truly understand and mimic cellular organelles.

2.6 Concluding remarks

In summary, protein-based compartments have proven to be highly attractive scaffolds for the encapsulation of functional materials. The disassembly and reassembly pathways of many protein-based compartments have been identified, many of which are driven by either pH and/or ionic strength, and their ease of assembly offers a highly attractive and accessible means for scientists, for the formation of hybrid assemblies that are reversible yet highly mono-disperse. The diverse range of natural structures, from protein cages to bacteriophages to viruses, provides a seemingly endless source of protein building blocks that can be modified or functionalized by chemical or genetic means. In this chapter, different protein-based compartments and strategies to functionalize and fill these compartments have been reviewed.

Although there are currently many examples in the literature describing the encapsulation of polymers, inorganic complexes, micelles, proteins, enzymes, nanoparticles in protein-based (in particular virus-based) assemblies, this field of bionanotechnology continues to grow with the design and development of more complex assemblies. In recent years, the design of "smart" responsive compartments has shown much promise, in which protein assemblies are equipped with triggers that respond to an external stimulus such as light, temperature or pH, for applications in biomedicine, biomaterials and in opto-electronics. Similarly, the role of these assemblies as cargo delivery systems (viruses), storage proteins (ferritins) and catalytic compartments (metabolosomes) provokes widespread interest towards understanding how these assemblies evolved in Nature and how they can be manipulated and used by scientists for the creation of (bio)synthetic mimics.

2.7 References

1. A. H. Chen and P. A. Silver, *Trends Cell Biol*, 2012, 22, 662-670.
2. I. Budin and N. K. Devaraj, *J Am Chem Soc*, 2012, 134, 751-753.
3. M. Marguet, C. Bonduelle and S. Lecommandoux, *Chem Soc Rev*, 2013, 42, 512-529.
4. K. Letchford and H. Burt, *Eur J Pharm Biopharm*, 2007, 65, 259-269.
5. N. J. Turro, J. K. Barton and D. A. Tomalia, *Acc Chem Res*, 1991, 24, 332-340.
6. A. D. Bangham, *Bioessays*, 1995, 17, 1081-1088.
7. T. A. P. F. Doll, S. Raman, R. Dey and P. Burkhard, *J Roy Soc Interface*, 2013, 10.
8. S. Kim, Y. Shi, J. Y. Kim, K. Park and J.-X. Cheng, *Expert Opin Drug Deliv*, 2010, 7, 49-62.
9. T. O. Yeates, C. S. Crowley and S. Tanaka, *Annu Rev Biophys*, 2010, 39, 185-205.
10. V. P. Torchilin, *Pharm Res*, 2007, 24, 1-16.
11. M. Uchida, S. Kang, C. Reichhardt, K. Harlen and T. Douglas, *BBA-Gen Subjects*, 2010, 1800, 834-845.
12. A. Zeltins, *Mol Biotechnol*, 2013, 53, 92-107.
13. J. Parsons, S. Frank, D. Bhella, M. Liang, M. Prentice, D. Mulvihill and M. Warren, *Mol Cell*, 2010, 38, 305-315.
14. S. Cheng, Y. Liu, C. S. Crowley, T. O. Yeates and T. A. Bobik, *Bioessays*, 2008, 30, 1084-1095.
15. S. Frank, A. D. Lawrence, M. B. Prentice and M. J. Warren, *J Biotechnol*, 2013, 163, 273-279.
16. H. Yebenes, P. Mesa, I. G. Munoz, G. Montoya and J. M. Valpuesta, *Trends Biochem Sci*, 2011, 36, 424-432.
17. Y. Zhang and B. P. Orner, *Int J Mol Sci*, 2011, 12, 5406-5421.
18. M. Banach, K. Stąpor and I. Roterman, *Int J Mol Sci*, 2009, 10, 844-861.
19. L. Peng, Y. Fukao, F. Myouga, R. Motohashi, K. Shinozaki and T. Shikanai, *Plos Biology*, 2011, 9, e1001040.
20. D. K. Clare, D. Vasishtan, S. Stagg, J. Quispe, G. W. Farr, M. Topf, A. L. Horwich and H. R. Saibil, *Cell*, 2012, 149, 113-123.
21. D. K. Clare, P. J. Bakkes, H. van Heerikhuizen, S. M. van der Vies and H. R. Saibil, *Nature*, 2009, 457, 107-110.
22. F. U. Hartl, A. Bracher and M. Hayer-Hartl, *Nature*, 2011, 475, 324-332.
23. T. Tosha, R. K. Behera and E. C. Theil, *Inorg Chem*, 2012, 51, 11406-11411.
24. R. A. Grant, D. J. Filman, S. E. Finkel, R. Kolter and J. M. Hogle, *Nat Struct Biol*, 1998, 5, 294-303.
25. E. C. Theil, *Annu Rev Biochem*, 1987, 56, 289-315.

26. S. H. Banyard, D. K. Stammers and P. M. Harrison, *Nature*, 1978, 271, 282-284.
27. Z. Yang, X. Wang, H. Diao, J. Zhang, H. Li, H. Sun and Z. Guo, *Chem Commun*, 2007, 0, 3453-3455.
28. J. Swift, C. A. Butts, J. Cheung-Lau, V. Yerubandi and I. J. Dmochowski, *Langmuir*, 2009, 25, 5219-5225.
29. B. Zheng, M. Uenuma, K. Iwahori, N. Okamoto, M. Naito, Y. Ishikawa, Y. Uraoka and I. Yamashita, *Nanotechnology*, 2011, 22, 1-7.
30. B. Zheng, I. Yamashita, M. Uenuma, K. Iwahori, M. Kobayashi and Y. Uraoka, *Nanotechnology*, 2010, 21, 045305.
31. S. A. Bode, I. J. Minten, R. J. M. Nolte and J. J. L. M. Cornelissen, *Nanoscale*, 2011, 3, 2376-2389.
32. T. O. Yeates, C. A. Kerfeld, S. Heinhorst, G. C. Cannon and J. M. Shively, *Nat Rev Microbiol*, 2008, 6, 681-691.
33. J. L. Corchero and J. Cedano, *Microb Cell Fact*, 2011, 10, 1-8.
34. M. Badger and G. Price, *J Exp Bot*, 2003, 54, 609-622.
35. Y. Tsai, M. R. Sawaya, G. C. Cannon, F. Cai, E. B. Williams, S. Heinhorst, C. A. Kerfeld and T. O. Yeates, *Plos Biology*, 2007, 5, e144.
36. S. Tanaka, C. Kerfeld, M. Sawaya, F. Cai, S. Heinhorst, G. Cannon and T. Yeates, *Science*, 2008, 319, 1083-1086.
37. J. N. Kinney, S. D. Axen and C. A. Kerfeld, *Photosynth Res*, 2011, 109, 21-32.
38. M. F. Schmid, A. M. Paredes, H. A. Khant, F. Soyer, H. C. Aldrich, W. Chiu and J. M. Shively,*J Mol Biol*, 2006, 364, 526-535.
39. C. A. Kerfeld, M. R. Sawaya, S. Tanaka, C. V. Nguyen, M. Phillips, M. Beeby and T. O. Yeates, *Science*, 2005, 309, 936-938.
40. G. D. Havemann and T. A. Bobik, *J Bacteriol* 2003, 185, 5086-5095.
41. D. D. Sriramulu, M. Liang, D. Hernandez-Romero, E. Raux-Deery, H. Lunsdorf, J. B. Parsons, M. J. Warren and M. B. Prentice, *J Bacteriol*, 2008, 190, 4559-4567.
42. G. D. Havemann, E. M. Sampson and T. A. Bobik, *Journal of Bacteriol*, 2002, 184, 1253-1261.
43. M. Sutter, D. Boehringer, S. Gutmann, S. Gunther, D. Prangishvili, M. J. Loessner, K. O. Stetter, E. Weber-Ban and N. Ban, *Nat Struct Mol Biol*, 2008, 15, 939-947.
44. R. Rahmanpour and T. D. H. Bugg, *The FEBS journal*, 2013, 280, 2097-2104.
45. R. Rahmanpour and T. D. H.Bugg, *The FEBS journal*, 2013, 280, 2097-2104.
46. T. Chen and S. C. Glotzer, *Phys Rev E*, 2007, 75, 1-7.
47. C. Dika, C. Gantzer, A. Perrin and J. F. Duval, *Phys Chem Chem Phys*, 2013, 15, 5691-5700.
48. B. C. Bundy, M. J. Franciszkowicz and J. R. Swartz, *Biotechnol Bioeng*, 2008, 100, 28-37.

49. J. E. Glasgow, S. L. Capehart, M. B. Francis and D. Tullman-Ercek, *ACS Nano*, 2012, 6, 8658-8664.
50. A. de la Escosura, R. J. M. Nolte and J. J. L. M. Cornelissen, *J Mater Chem*, 2009, 19, 2274-2278.
51. R. Golmohammadi, K. Fridborg, M. Bundule, K. Valegård and L. Liljas, *Structure*, 1996, 4, 543-554.
52. K. Toropova, P. G. Stockley and N. A. Ranson, *J Mol Biol*, 2011, 408, 408-419.
53. P. G. Stockley, N. J. Stonehouse and K. Valegard, *Int J Biochem*, 1994, 26, 1249-1260.
54. C. E. Ashley, E. C. Carnes, G. K. Phillips, P. N. Durfee, M. D. Buley, C. A. Lino, D. P. Padilla, B. Phillips, M. B. Carter, C. L. Willman, C. J. Brinker, C. Caldeira Jdo, B. Chackerian, W. Wharton and D. S. Peabody, *ACS Nano*, 2011, 5, 5729-5745.
55. R. Olsthoorn and J. van Duin, in *eLS*, John Wiley & Sons, Ltd, 2001, 1-8.
56. J. D. Fiedler, S. D. Brown, J. L. Lau and M. G. Finn, *Angew Chem Int Ed*, 2010, 49, 9648-9651.
57. S. D. Brown, J. D. Fiedler and M. G. Finn, *Biochemistry*, 2009, 48, 11155-11157.
58. Z. Yin, M. Comellas-Aragones, S. Chowdhury, P. Bentley, K. Kaczanowska, L. BenMohamed, J. C. Gildersleeve, M. G. Finn and X. Huang, *ACS Chem Biol*, 2013, 8, 1253-1262.
59. J. Rumnieks and K. Tars, *Protein Sci*, 2011, 20, 1707-1712.
60. A. Kashiwagi and T. Yomo, *PLoS Genet*, 2011, 7, e1002188.
61. I. Cielens, V. Ose, I. Petrovskis, A. Strelnikova, R. Renhofa, T. Kozlovska and P. Pumpens, *FEBS Lett*, 2000, 482, 261-264.
62. J. D. Fiedler, C. Higginson, M. L. Hovlid, A. A. Kislukhin, A. Castillejos, F. Manzenrieder, M. G. Campbell, N. R. Voss, C. S. Potter, B. Carragher and M. G. Finn, *Biomacromolecules*, 2012, 13, 2339-2348.
63. K. N. Parent, R. Khayat, L. H. Tu, M. M. Suhanovsky, J. R. Cortines, C. M. Teschke, J. E. Johnson and T. S. Baker, *Structure*, 2010, 18, 390-401.
64. P. A. Thuman-Commike, B. Greene, J. A. Malinski, J. King and W. Chiu, *Biophys J*, 1998, 74, 559-568.
65. D. P. Patterson, P. E. Prevelige and T. Douglas, *ACS Nano*, 2012, 6, 5000-5009.
66. J. Lucon, S. Qazi, M. Uchida, G. J. Bedwell, B. LaFrance, P. E. Prevelige and T. Douglas, *Nat Chem*, 2012, 4, 781-788.
67. A. O'Neil, P. E. Prevelige, G. Basu and T. Douglas, *Biomacromolecules*, 2012, 13, 3902-3907.
68. G. A. Loset, B. Bogen and I. Sandlie, *PLoS One*, 2011, 6, e14702.

69. D. Stopar, R. B. Spruijt, C. J. Wolfs and M. A. Hemminga, *Biochim Biophys Acta*, 2003, 1611, 5-15.
70. L. Specthrie, E. Bullitt, K. Horiuchi, P. Model, M. Russel and L. Makowski, *J Mol Biol*, 1992, 228, 720-724.
71. Z. Liu, J. Qiao, Z. Niu and Q. Wang, *Chem Soc Rev*, 2012, 41, 6178-6194.
72. S. S. Sidhu, *Biomol Eng*, 2001, 18, 57-63.
73. S. K. Dixit, N. L. Goicochea, M. C. Daniel, A. Murali, L. Bronstein, M. De, B. Stein, V. M. Rotello, C. C. Kao and B. Dragnea, *Nano Lett*, 2006, 6, 1993-1999.
74. B. T. Tey, S. T. Ooi, K. C. Yong, M. Y. T. Ng, T. C. Ling and W. S. Tan, *Afr J Biotechnol*, 2009, 8, 268-273.
75. G. R. Souza, D. R. Christianson, F. I. Staquicini, M. G. Ozawa, E. Y. Snyder, R. L. Sidman, J. H. Miller, W. Arap and R. Pasqualini, *Proc Natl Acad Sci U.S.A.*, 2006, 103, 1215-1220.
76. Y. S. Nam, H. Park, A. P. Magyar, D. S. Yun, T. S. Pollom, Jr. and A. M. Belcher, *Nanoscale*, 2012, 4, 3405-3409.
77. D. Ghosh, Y. Lee, S. Thomas, A. G. Kohli, D. S. Yun, A. M. Belcher and K. A. Kelly, *Nat Nano*, 2012, 7, 677-682.
78. D. W. Domaille, J. H. Lee and J. N. Cha, *Chem Commun*, 2013, 49, 1759-1761.
79. X. Dang, H. Yi, M. H. Ham, J. Qi, D. S. Yun, R. Ladewski, M. S. Strano, P. T. Hammond and A. M. Belcher, *Nat Nanotechnol*, 2011, 6, 377-384.
80. S. Adkins, I. Kamenova, D. Achor and D. J. Lewandowski, *Plant Dis*, 2003, 87, 1190-1196.
81. C. M. Soto and B. R. Ratna, *Curr Opin Biotechnol*, 2010, 21, 426-438.
82. D. J. Hwang, I. M. Roberts and T. M. Wilson, *Proc Natl Acad Sci U.S.A*, 1994, 91, 9067-9071.
83. A. Mueller, A. Kadri, H. Jeske and C. Wege, *J Virol Methods*, 2010, 166, 77-85.
84. J. A. Lindbo, *BMC biotechnology*, 2007, 7, 52.
85. S. Kagale, S. Uzuhashi, M. Wigness, T. Bender, W. Yang, M. H. Borhan and K. Rozwadowski, *Scientific reports*, 2012, 2, 874.
86. M. Levy, O. Edelbaum and I. Sela, *Plant Physiol*, 2004, 135, 2392-2397.
87. F. C. Geiger, F. J. Eber, S. Eiben, A. Mueller, H. Jeske, J. P. Spatz and C. Wege, *Nanoscale*, 2013, 9, 3808-3816.
88. J. A. Speir, S. Munshi, G. J. Wang, T. S. Baker and J. E. Johnson, *Structure*, 1995, 3, 63-78.
89. J. B. Bancroft and E. Hiebert, *Virology*, 1967, 32, 354-&.
90. L. O. Liepold, J. Revis, M. Allen, L. Oltrogge, M. Young and T. Douglas, *Phys Biol*, 2005, 2, S166-S172.
91. L. Lavelle, J. P. Michel and M. Gingery, *J Virol Methods*, 2007, 146, 311-316.
92. A. Ali and M. J. Roossinck, *J Virol Methods*, 2007, 141, 84-86.

93. J. M. Fox, G. Wang, J. A. Speir, N. H. Olson, J. E. Johnson, T. S. Baker and M. J. Young, *Virology*, 1998, 244, 212-218.
94. Y. Hu, R. Zandi, A. Anavitarte, C. M. Knobler and W. M. Gelbart, *Biophys J*, 2008, 94, 1428-1436.
95. J. E. Johnson and J. A. Speir, *J Mol Biol*, 1997, 269, 665-675.
96. J. Sun, C. DuFort, M. C. Daniel, A. Murali, C. Chen, K. Gopinath, B. Stein, M. De, V. M. Rotello, A. Holzenburg, C. C. Kao and B. Dragnea, *Proc Natl Acad Sci U.S.A.*, 2007, 104, 1354-1359.
97. P. Singh, M. J. Gonzalez and M. Manchester, *Drug Develop Res*, 2006, 67, 23-41.
98. R. D. Cadena-Nava, Y. Hu, R. F. Garmann, B. Ng, A. N. Zelikin, C. M. Knobler and W. M. Gelbart, *J Phys Chem B*, 2011, 115, 2386-2391.
99. A. de la Escosura, P. G. A. Janssen, A. P. H. S. Schenning, R. J. M. Nolte and J. J. L. M. Cornelissen, *Angew Chem Int Ed*, 2010, 49, 5335-5338.
100. M. Comellas-Aragones, H. Engelkamp, V. I. Claessen, N. A. J. M. Sommerdijk, A. E. Rowan, P. C. Christianen, J. C. Maan, B. J. Verduin, J. J. L. M. Cornelissen and R. J. M. Nolte, *Nat Nanotechnol*, 2007, 2, 635-639.
101. F. D. Sikkema, M. Comellas-Aragones, R. G. Fokkink, B. J. Verduin, J. J. L. M. Cornelissen and R. J. M. Nolte, *Org Biomol Chem*, 2007, 5, 54-57.
102. M. Brasch, A. de la Escosura, Y. Ma, C. Uetrecht, A. J. R. Heck, T. Torres and J. J. L. M. Cornelissen, *J Am Chem Soc*, 2011, 133, 6878-6881.
103. D. Willits, X. Zhao, N. Olson, T. S. Baker, A. Zlotnick, J. E. Johnson, T. Douglas and M. J. Young, *Virology*, 2003, 306, 280-288.
104. F. D. Sikkema, M. Comellas-Aragones, R. G. Fokkink, B. J. M. Verduin, J. J. L. M. Cornelissen and R. J. M. Nolte, *Org Biomol Chem*, 2007, 5, 54-57.
105. D. Lindberg, M. de la Fuente Revenga and M. Widersten, *Biochemistry*, 2010, 49, 2297-2304.
106. M. De Angelis, M. Calasso, R. Di Cagno, S. Siragusa, F. Minervini and M. Gobbetti, *J Appl Microbiol*, 2010, 109, 1763-1774.
107. M. G. Mateu, *Protein Eng Des Sel*, 2011, 24, 53-63.
108. G. Jutz and A. Boker, *Polymer*, 2011, 52, 211-232.
109. A. A. Aljabali, G. P. Lomonossoff and D. J. Evans, *Biomacromolecules*, 2011, 12, 2723-2728.
110. M. Comellas-Aragones, A. de la Escosura, A. J. Dirks, A. van der Ham, A. Fuste-Cune, J. J. L. M. Cornelissen and R. J. M. Nolte, *Biomacromolecules*, 2009, 10, 3141-3147.
111. J. Tu, T. X. Wang, W. Shi, G. S. Wu, X. H. Tian, Y. H. Wang, D. T. Ge and L. Ren, *Biomaterials*, 2012, 33, 7903-7914.
112. A. A. Aljabali, J. E. Barclay, N. F. Steinmetz, G. P. Lomonossoff and D. J. Evans, *Nanoscale*, 2012, 4, 5640-5645.
113. L. A. Lee and Q. Wang, *Nanomedicine*, 2006, 2, 137-149.

114. M. Uchida, M. Klem, M. Allen, P. Suci, M. Flenniken, E. Gillitzer, Z. Varpness, L. Liepold, M. Young and T. Douglas, *Adv Mater*, 2007, 19, 1025 - 1042.
115. L. A. Lee, H. G. Nguyen and Q. Wang, *Org Biomol Chem*, 2011, 9, 6189-6195.
116. D. Cardinale, N. Carette and T. Michon, *Trends Biotechnol*, 2012, 30, 369-376.
117. I. J. Minten, R. J. M. Nolte and J. J. L. M. Cornelissen, *Macromol Biosci*, 2010, 10, 539-545.
118. I. J. Minten, V. I. Claessen, K. Blank, A. E. Rowan, R. J. M. Nolte and J. J. L. M. Cornelissen, *Chem Sci*, 2011, 2, 358-362.
119. I. J. Minten, L. J. Hendriks, R. J. M. Nolte and J. J. L. M. Cornelissen, *J Am Chem Soc*, 2009, 131, 17771-17773.
120. M. B. van Eldijk, J. C. Wang, I. J. Minten, C. Li, A. Zlotnick, R. J. M. Nolte, J. J. L. M. Cornelissen and J. C. van Hest, *J Am Chem Soc*, 2012, 134, 18506-18509.
121. A. Merzlyak, S. Indrakanti and S. W. Lee, *Nano Lett*, 2009, 9, 846-852.
122. A. J. Bernal and W. G. T. Willats, *Trends Plant Sci*, 2004, 9, 465-468.
123. J. P. Phelps, P. Dao, H. Jin and L. Rasochova, *J Biotechnol*, 2007, 128, 290-296.
124. A. de la Escosura, M. Verwegen, F. D. Sikkema, M. Comellas-Aragones, A. Kirilyuk, T. Rasing, R. J. Nolte and J. J. Cornelissen, *Chem Commun*, 2008, 1542-1544.
125. M. A. Kostiainen, P. Hiekkataipale, A. Laiho, V. Lemieux, J. Seitsonen, J. Ruokolainen and P. Ceci, *Nat Nano*, 2013, 8, 52-56.
126. G. R. Souza, E. Yonel-Gumruk, D. Fan, J. Easley, R. Rangel, L. Guzman-Rojas, J. H. Miller, W. Arap and R. Pasqualini, *PLoS One*, 2008, 3, e2242.
127. P. J. Yoo, K. T. Nam, J. Qi, S. K. Lee, J. Park, A. M. Belcher and P. T. Hammond, *Nat Mater*, 2006, 5, 234-240.
128. R. D. Cadena-Nava, M. Comas-Garcia, R. F. Garmann, A. L. N. Rao, C. M. Knobler and W. M. Gelbart, *J Virol*, 2012, 86, 3318-3326.
129. M. A. Kostiainen, P. Hiekkataipale, J. A. de la Torre, R. J. M. Nolte and J. J. L. M. Cornelissen, *J Mater Chem*, 2011, 21, 2112-2117.
130. A. de la Escosura, P. G. A. Janssen, A. P. H. J. Schenning, R. J. M. Nolte and J. J. L. M. Cornelissen, *Angew Chem Int Ed*, 2010, 49, 5335-5338.
131. Y. Xu, J. Ye, H. Liu, E. Cheng, Y. Yang, W. X. Wang, M. Zhao, D. Zhou, D. S. Liu and R. X. Fang, *Chem Commun*, 2008, 49-51.
132. N. F. Steinmetz, *Nanomedicine*, 2010, 6, 634-641.
133. M. Kwak, I. J. Minten, D. M. Anaya, A. J. Musser, M. Brasch, R. J. M. Nolte, K. Mullen, J. J. L. M. Cornelissen and A. Herrmann, *J Am Chem Soc*, 2010, 132, 7834-7835.
134. R. R. Allison and K. Moghissi, *Clin Endosc*, 2013, 46, 24-29.
135. C. A. Robertson, D. H. Evans and H. Abrahamse, *J Photochem Photobiol B*, 2009, 96, 1-8.

136. R. A. Miller, A. D. Presley and M. B. Francis, *J Am Chem Soc*, 2007, 129, 3104-3109.
137. S. L. Capehart, M. P. Coyle, J. E. Glasgow and M. B. Francis, *J Am Chem Soc*, 2013, 135, 3011-3016.

Chapter 3

Encapsulation of Phthalocyanine Supramolecular Stacks into Virus-Like Particles

Protein cages can be used as well-defined and monodisperse particles for the organization of external and internal material. Here, a method is described to induce the aggregation of zinc phthalocyanines (ZnPcs) inside virus like particles (VLPs), induced by their high local concentration. Some advantages of using VLPs include the low concentration of ZnPcs needed to induce aggregation in VLPs compared to bulk, the restricted volume inside the VLPs limits the aggregation size and length of ZnPcs and finally, the encapsulation of ZnPcs inside VLPs make them suitable for biomedical application such as photodynamic therapy (PDT). To encapsulate ZnPcs inside VLPs, water soluble ZnPcs were either incubated with virus coat protein dimers of the Cowpea Chlorotic Mottle Virus (CCMV) at pH 7.5, or incubated with the preformed empty capsid of CCMV at pH 5.0. Encapsulation at neutral pH led to the formation of ZnPc aggregates inside the VLPs, whereas encapsulation in the preformed CCMV capsid at pH 5.0 led to the formation of ZnPc dimers inside the VLPs. In both cases, the formation of aggregated ZnPc stacks, or the formation of dimers was followed spectroscopically. Furthermore, PDT studies on macrophage cells using the ZnPc-filled VLPs revealed a cell death efficiency of 92–95%.

This chapter is published:
M. Brasch, A. de la Escosura, Y. Ma, C. Uetrecht, A. R. Heck, T. Torres and J. J. L. M. Cornelissen; J Am Chem Soc; ***2011****; 133; 6878-6881*

3.1 Introduction

Light-absorbing organic molecules such as porphyrins (Pors) and phthalocyanines (Pcs) are widespread building blocks in materials science and nanotechnology.[1, 2] In particular, Pcs are highly robust and versatile chromophores that tend to aggregate and form stacks through π-π interactions, and have been used for applications in medicine, photonics, electronics, and energy conversion.[3-7] By means of controlling the size and long-range order of the Pc stacks, their optical properties can be modified and tuned. To achieve this ordering, viruses are highly attractive, monodisperse scaffolds for the organization of chemical moieties both in their inner cavities and on their exterior surfaces.[8-14] For example, the protein scaffold of rod-like viruses, such as the bacteriophage M13[15, 16] and the Tobacco Mosaic Virus (TMV),[17] or of icosahedral ones, such as the Hepatitis B Virus (HBV)[18] and the bacteriophage MS2,[19] have been decorated with Pors. However, in most cases, the virus coat proteins were genetically modified for the subsequent covalent[16-19] or non-covalent[15] coupling with the Por moieties. Cowpea Chlorotic Mottle Virus (CCMV) is an icosahedral plant virus with inner and outer diameters of 18 and 28 nm, respectively.[20, 21] The inner cavity of native CCMV is highly positively charged and accommodates the negatively charged RNA inside. At neutral pH and high ionic strength, the capsid disassembles into 90 identical virus coat protein (CP) dimers. After removal of the viral RNA and lowering the pH (to pH 5.0), the coat proteins can be reassembled into $T = 3$ virus-like particles (VLPs). Although the native virus forms $T = 3$ particles, smaller $T = 1$[22] capsids can be formed at pH 7.5 in the presence of polyanionic species.[23, 24] T represents the triangulation number, a geometrical parameter that characterizes icosahedral structures. $T = 1$ and $T = 3$ capsids are formed by 60 and 180 CP subunits, respectively.[21]

Here, the encapsulation of a water-soluble zinc phthalocyanine (ZnPc) into VLPs was investigated. The superior optical and electronic properties of Pcs combined with the biocompatible nature of VLP assemblies could be of potential use for biomedical applications, *i.e.* fluorescence imaging and photodynamic therapy.

3.2 Results and discussion

3.2.1 Aggregation behavior of metal Pc tetrasulfonic acid salt

The aggregation behavior of metallophthalocyanine derivatives has been well characterized and is known to be highly dependent on both concentration and solvent.[25] For example, at low concentration (10^{-7} – 10^{-4} M), water-soluble zinc phthalocyanine (ZnPc) (Figure 3.1A) partially aggregates in water and has an absorbance maximum at approximately λ = 635 nm. By comparison, dissolution in DMSO leads to the formation of non-aggregated ZnPc monomers, which subsequently causes a red-shift in the absorbance maximum to λ = 679 nm (Figure 3.1B).

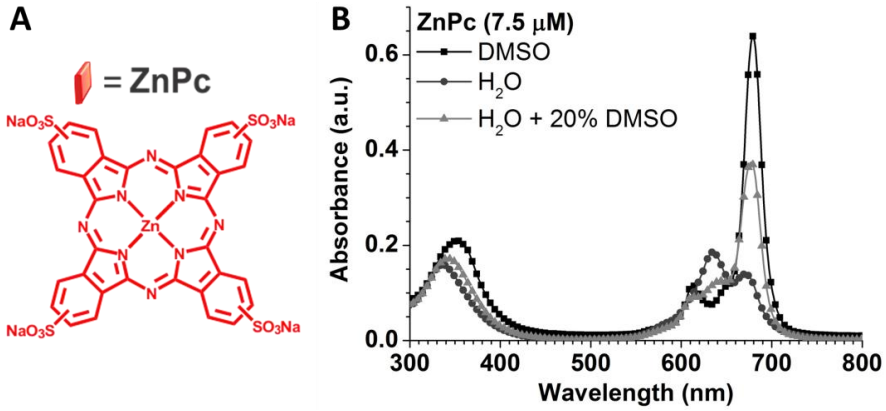

Figure 3.1. (A) Structure of the here used water-soluble zinc phthalocyanine (ZnPc) compound. (B) UV-visible absorbance spectra of zinc phthalocyanine (ZnPc) in different solvent conditions. At 7.5 µM, ZnPc exists as a monomer in DMSO and exhibits a maximum absorbance at λ = 679 nm whereas in H_2O, ZnPc aggregates and exhibits a maximum absorbance at λ = 635 nm. Addition of 20% DMSO partially breaks the aggregates.

To investigate the aggregation behavior of ZnPc under different aqueous conditions, the spectroscopic properties of ZnPc (10^{-5} – 0.10 mM) at various concentrations were studied in Tris-HCl (pH 7.5) and sodium acetate buffer (pH 5.0). In general, the formation of long zinc phthalocyanine arrangements (H aggregates) can be readily characterized by a concomitant blue-shift of the Q band in the absorbance spectrum.[2] In the case of zinc phthalocyanine, the formation of dimeric H aggregates was monitored by UV-visible spectroscopy at λ = 635 nm (Q band). Figure 3.2 shows the same trend for ZnPc in both Tris-Cl (pH 7.5) and sodium acetate buffer (pH 5.0) within the concentration range of 10^{-4} – 0.10 mM, suggesting that H aggregates do not form. The direct relationship between the ZnPc absorbance and concentration allowed for the determination of the ZnPc extinction coefficient at λ = 280 nm and λ = 635 nm (Figure 3.2E and

3.2F). The calibration curves obtained from non-encapsulated ZnPcs as well as native electrospray ionization mass spectroscopy (ESI-MS) were later used to estimate the number of ZnPc molecules in either T = 1 or T = 3 VLPs after encapsulation.

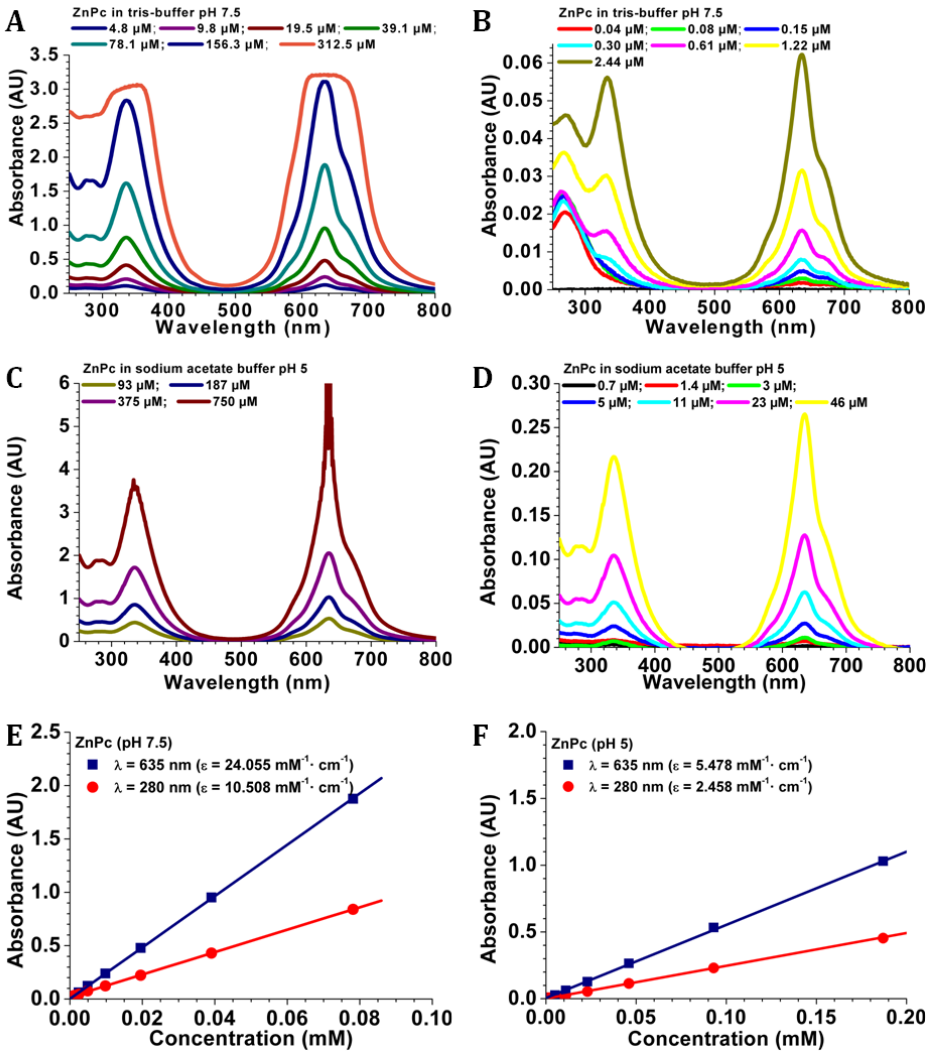

Figure 3.2. UV-visible absorbance spectra of ZnPc upon increasing concentration (A) 10^{-5} – 0.10 mM at pH 7.5, (B) 10^{-5} – 10^{-3} mM at pH 7.5, (C) 10^{-4} – 10^{-1} mM at pH 5.0, (D) 10^{-4} – 10^{-2} mM at pH 5.0. Beer-Lambert calibration curves monitoring at λ = 280 nm and λ = 635 nm at (E) pH 7.5, (F) pH 5.0.

The concentration-dependent aggregation of ZnPc was further confirmed by dynamic light scattering (DLS) studies in tris-HCl buffer at pH 7.5. At concentrations higher than 1 mM, large ZnPc aggregates (100 – 1000 nm in diameter) appeared to form, whereas at concentrations below 1 mM, aggregates of approximately 1 nm in diameter were observed (Figure 3.3).

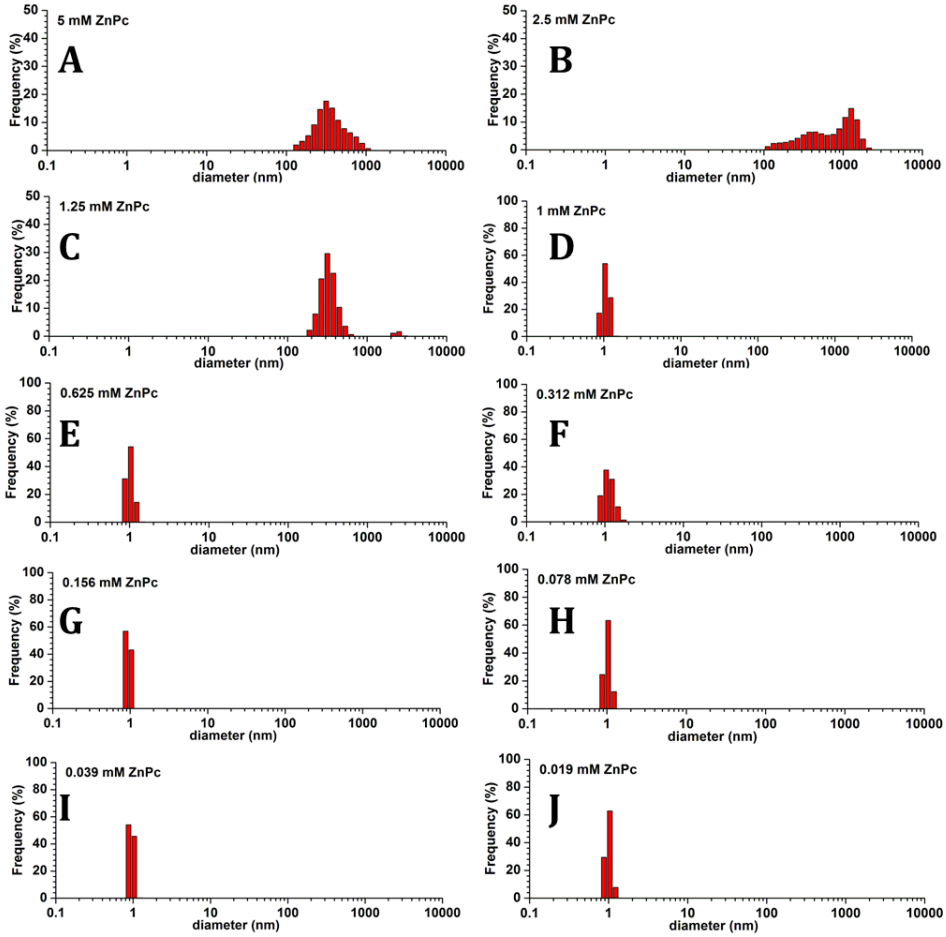

Figure 3.3. DLS measurements of ZnPc aggregates at (A) 5 mM, (B) 2.5 mM, (C) 1.25 mM, (D) 1 mM, (E) 0.625 mM, (F) 0.312 mM, (G) 0.156 mM, (H) 0.078 mM, (I) 0.039 mM and (J) 0.019 mM. †

† The data are represented as "Frequency (%)", which refers to the volume percentage as determined by the instrument.

3.2.2 Encapsulation of ZnPc inside VLPs

CCMV has been shown to form *T* = 1 particles at pH 7.5 in the presence of negatively charged cargos and empty *T* = 3 particles at pH 5.0. In order to study whether the VLP size can be used to induce and control aggregation of ZnPc, two different approaches were investigated. First, ZnPc and CP solutions (with final concentrations of [ZnPc] = 1 mM and [CP] = 0.2 mM) in Tris-HCl buffer (50 mM, 0.3 M NaCl, 1 mM DTT, pH 7.5) were mixed and incubated for 1 h at 4 °C (Figure 3.4).

Figure 3.4. Schematic representation of the encapsulation approach of ZnPcs into CCMV by mixing ZnPcs and CP at pH 7.5.

Two control samples based on empty *T* = 3 CCMV (pH 5) and unassembled CP (pH 7.5) were purified by size-exclusion chromatography (SEC), which showed elution peaks at 11.5 mL and 18.5 mL respectively (Figure 3.5A I-II). After incubation, ZnPc filled CCMV was purified by SEC, monitoring at λ = 260 nm and λ = 280 nm for the CCMV protein and at λ = 635 nm for ZnPc. SEC revealed two peaks at 13.0 mL and 18.5 mL. The shift in elution volume from 11.5 mL to 13.0 mL compared to the control sample was thought to be due to virus-like capsids that are smaller in diameter than empty *T* = 3 capsids (Figure 3.5 III). The strong absorbance at 635 nm also indicated that the virus-like particles were loaded with ZnPc. The particle size and morphology was confirmed by both Transmission Electron Microscopy (TEM) and DLS analyse, which confirmed *T* = 1 particles with an average diameter of 19 ± 2 nm (Figure 3.5B). Integration of the peak intensities from the SEC indicated approximately 71% assembly efficiency (*i.e.* 71% of the CP used formed *T* = 1 particles). Interestingly, the absorbance spectrum of ZnPc-CCMV showed a blue-shift of the ZnPc Q-band from 635 nm to 613 nm compared to the non-encapsulated ZnPc, indicating aggregation behaviour inside the VLPs (Figure 3.5C). As described in the previous section, the aggregation of free ZnPc was only observed at concentrations higher than 1 mM (Section 3.2.1). Based on the calibration curve, the local concentration of ZnPc within the VLPs was estimated to be 120 mM (Appendix). The unexpectedly high local concentration is attributed to the strong electrostatic interactions between the negatively charged ZnPc dimers and the positively charged N-terminus of CCMV. The high local concentration combined with the strong electrostatic interactions may enhance the aggregation behaviour of ZnPc when encapsulated in VLPs. Dialysis of ZnPc filled VLPs against fresh Tris-HCl buffer did not lead to any loss of ZnPc (by diffusion out of the VLP

pores), which also indicates that the ZnPc aggregates are highly stable (Figure 3.5A IV and 5C).

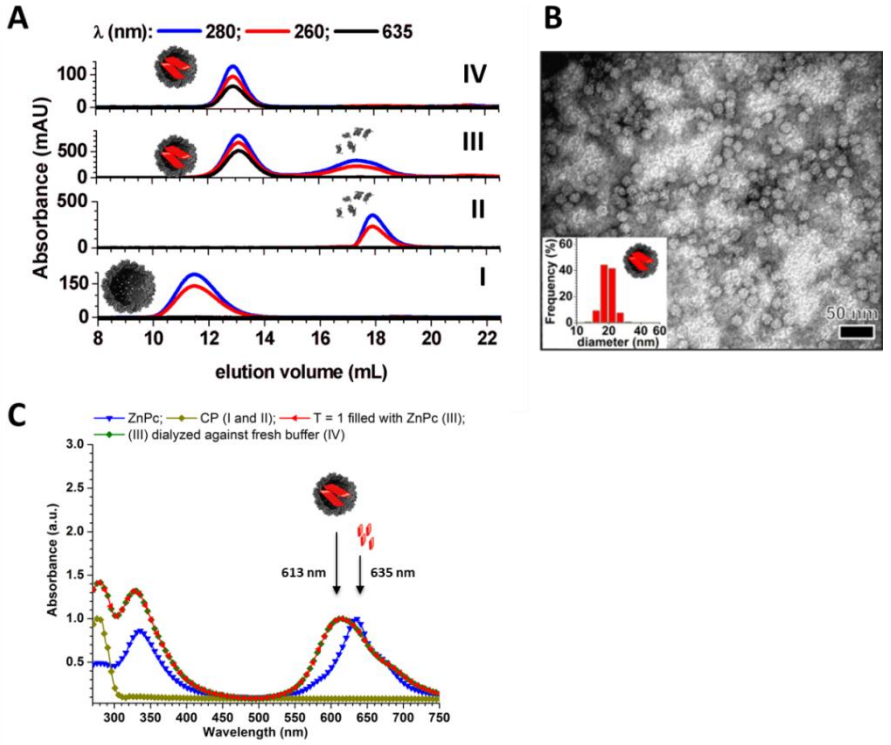

Figure 3.5 (A) Size exclusion chromatography of (I) empty *T* = 3 CCMV capsid (pH 5), (II) coat proteins (pH 7.5), (III) VLPs filled with ZnPcs (pH 7.5) and (IV) purified VLPs filled with ZnPcs after dialysis against fresh buffer. The red and blue lines represent protein specific UV-Vis absorbance at λ = 260 nm and 280 nm; λ = 635 nm represents the ZnPc specific UV-Vis absorbance. (B) TEM micrographs and DLS size distribution diagram (inset) of ZnPc containing *T* = 1 particles from the SEC fraction. (C) Normalized UV-Vis spectra of ZnPc, CP and SEC purified *T* = 1 VLPs filled with ZnPcs and dialysis of VLPs filled with ZnPcs against fresh buffer.

In the second encapsulation approach, a mixture of ZnPc (1 mM final concentration) and empty *T* = 3 capsids (0.23 mM final concentration) was incubated in 50 mM sodium acetate buffer, 1 M NaCl, 1 mM NaN_3, pH 5 for 1 h at 4 °C, to allow ZnPc to diffuse into the capsid through the capsid pores (Figure 3.6).

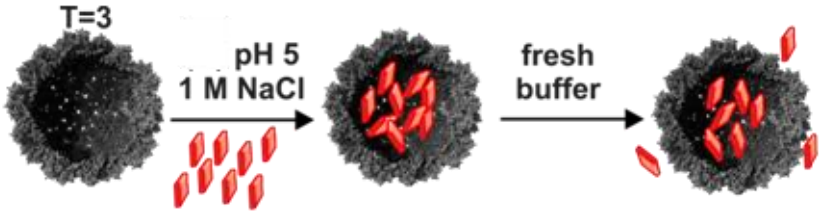

Figure 3.6. Schematic representation of the encapsulation approach of ZnPcs into empty preformed *T* = 3 CCMV capsids at pH 5.

Purification by size-exclusion chromatography showed a clear peak eluting at 11.5 mL, with an intense absorption at 635 nm, suggesting that the CCMV capsids were filled with ZnPcs (Figure 3.7A II). TEM and DLS analyses confirmed the presence of *T* = 3 particles (Figure 3.7B). The absorbance spectrum revealed a peak maximum centered around 635 nm, which is indicative of ZnPc dimers and suggests that, unlike *T = 1* particles, encapsulation inside *T* = 3 capsids does not induce ZnPc aggregation (Figure 3.7C). Dialysis against fresh acetate buffer showed that ZnPc diffuses out of the CCMV capsids (Figure 3.7A III and 3.7C), resulting in a substantial decrease in local concentration of ZnPc from 57 mM to 38 mM (based on UV-visible spectroscopy).

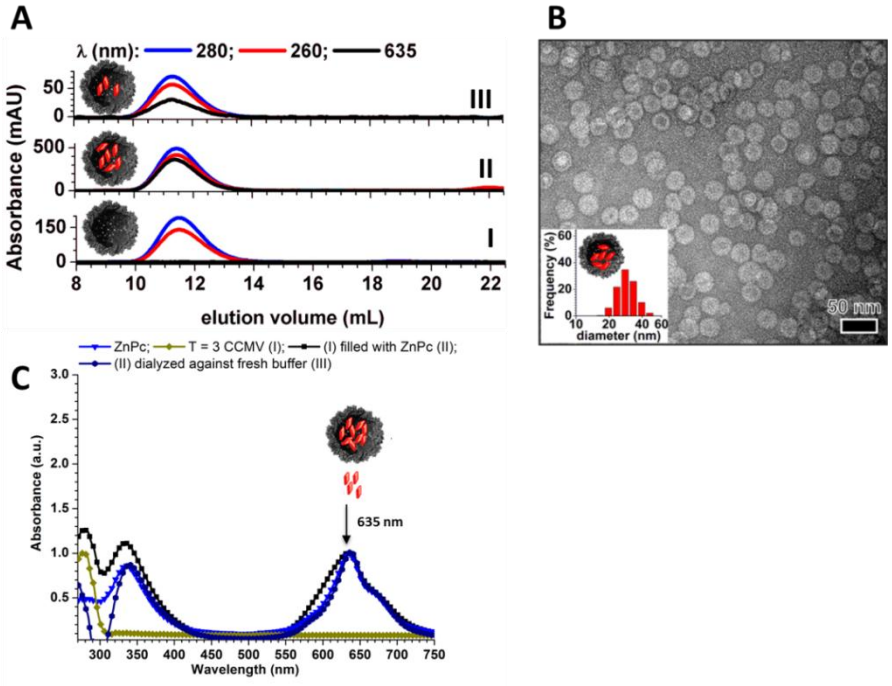

Figure 3.7. (A) Size exclusion chromatography of (I) empty *T* = 3 CCMV capsid (pH 5), (II) *T* = 3 CCMV capsid incubated with ZnPcs (pH 5) and (III) *T* = 3 VLPs filled with ZnPcs after dialysis against fresh buffer (pH 5). The red and blue line represent protein specific UV-Vis absorbance at λ = 260 nm and 280 nm; λ = 635 nm represents the ZnPc specific UV-Vis absorbance. (B) TEM micrographs and DLS size distribution diagram (inset) of ZnPc containing *T* = 3 particles from the SEC fraction. (C) Normalized UV-Vis spectra of ZnPc, *T* = 3 CCMV, SEC purified *T* = 3 VLPs filled with ZnPcs and dialysis of VLPs filled with ZnPcs against fresh buffer.

The absence of leaked ZnPc in the FPLC traces (Figure 3.7A) is caused by the interactions of the molecules with the SEC column under buffering conditions. Flushing the column with pure water after ZnPc loading resulted in a main elution peak at 28 mL (Figure 3.8).

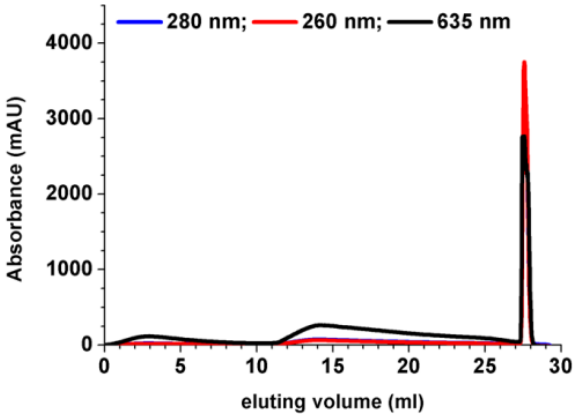

Figure 3.8. SEC chromatograms of ZnPc after flushing the column with pure water.

In the case of native CCMV, it is known that empty T = 3 particles normally disassemble into CP dimers at pH 7.5. Here this knowledge was used to induce a shape transition from T = 3 to T = 1 particles in order to prevent the leakage of ZnPcs from the particle interior (Figure 3.9). As it has been shown for the first encapsulation approach, where incubation of ZnPc with CCMV CP led to the formation of highly robust T = 1 VLPs and the high local concentration of encapsulated ZnPcs induced ZnPc aggregation, which prevented ZnPcs from leaking out form the interior of these T = 1 particles.

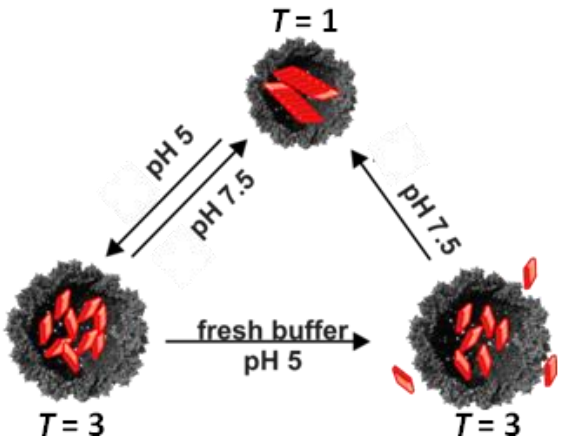

Figure 3.9. Schematic representation of the shape transition of T = 3 to T = 1 particles by dialysis from pH 5 to pH 7.5, as well as the attempt to transform T = 1 particles back to T = 3 particles.

Indeed, dialysis of the T = 3 particles filled with ZnPcs against Tris-HCl buffer (50 mM, 0.3 M NaCl, 1 mM DTT, pH 7.5) transformed the T = 3 particles into T = 1 particles (61%) and free CP (39%), as revealed by SEC, TEM and DLS (Figure 3.10A II, 3.10B and 3.10C, respectively).

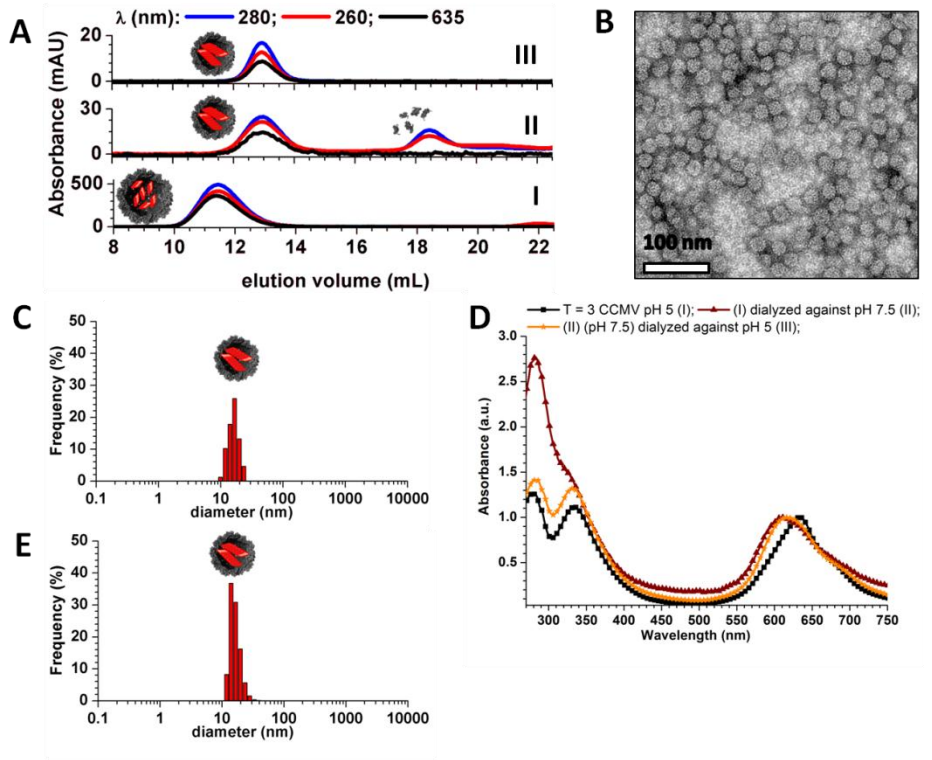

Figure 3.10. Size exclusion chromatography of (I) *T* = 3 CCMV capsid filled with ZnPcs (pH 5), (II) *T* = 3 VLPs filled with ZnPcs after dialysis against pH 7.5 and (III) dialysis of the later sample against fresh buffer (pH 5). The red and blue line represent protein specific UV-Vis absorbance at λ = 260 nm and 280 nm; λ = 635 nm represents the ZnPc specific UV-Vis absorbance. (B) TEM micrographs of the obtained *T* = 1 particles and (C) DLS size distribution diagram of the ZnPc containing *T* = 1 particles from the SEC fraction sample (II). (D) Normalized UV-Vis spectra of SEC purified samples (I, II and III). (E) DLS size distribution diagram of SEC purified samples (III) containing stable *T* = 1 particles at pH 5.

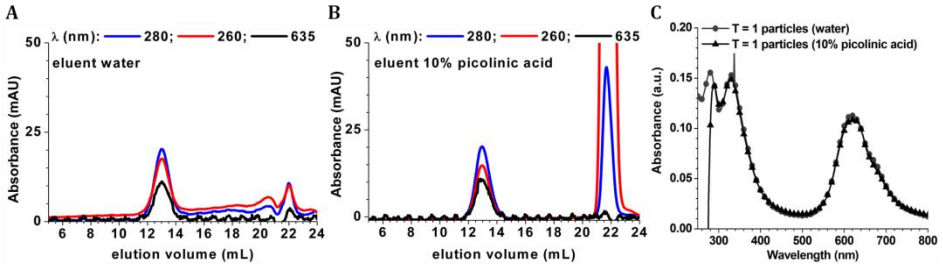

Figure 3.11. FPLC chromatograms of purified *T* = 1 CCMV capsids filled with ZnPcs after dialysis against (A) Milli-Q water and (B) 10% picolinic acid in water at pH 7.5 for 24h. (C) UV-Vis spectra showing the aggregation behavior of ZnPc in Sample 1. Water and picolinic acid are not able to disrupt the aggregation of ZnPc.

Upon dialysis to pH 7.5, the absorbance maximum of the ZnPc stacks was further blue-shifted to 613 nm, which is in line with the *T* = 1 ZnPc filled VLPs (Figure 3.10D). Interestingly, dialyzing back to pH 5 did not induce the reformation of *T* = 3 capsids (Figure 3.9, Figure 3.10A III and 3.10E), neither did dialyzing against Milli-Q water or addition of water-soluble pyridine derivatives (*e.g.*, 10% picolinic acid), which are generally used to disrupt the ZnPc aggregation by coordination to the zinc central atom of the macrocycle (Figure 3.11). This suggests that the stronger aggregation of ZnPc inside the *T* = 1 capsids involves different driving forces that direct their assembly and might be explained by the following argument. *T* = 3 capsids are thermodynamically stable at pH 5 and do not need a template for their assembly. Consequently, ZnPcs that diffuse in and out of the capsid do not increase the stability of the capsid nor are they needed for electrostatic charge compensation to form or stabilize the capsid further. As a result no strong driving forces are present to store the ZnPcs at the interior, giving no effective increase in the local concentration of ZnPcs and therefore no aggregation of ZnPcs which does occur at high local concentrations. On the contrary, electrostatic interactions between the CP and the cargo are dominant at pH 7.5.[26] The ZnPc stacks are then needed to template the formation of *T* = 1 capsids, and cannot diffuse out of the evidently very stable protein cage. Such presumed cooperative encapsulation / templated assembly process strongly promotes the aggregation of ZnPc at neutral pH.

3.2.3 Quantification of ZnPc molecules per capsid

The average number of ZnPc molecules and their concentration inside the capsids were determined by UV-visible spectroscopy based on the calibration curve of the free non-encapsulated ZnPc (Figure 3.2E). The concentration of ZnPc per capsid was estimated to be 0.12 M corresponding to 120 ZnPcs per capsid (Appendix). However, due to the significant hypsochromic shift for the ZnPc absorption, this approach is only an estimation. For a more accurate quantification of the number of ZnPc molecules per capsid, the sample was analyzed by native electrospray ionization mass spectrometry (ESI-MS).

3.2.3.1 Native electrospray ionization mass spectrometry (ESI-MS)

Based on native ESI-MS, an average number of 192 ± 20 ZnPc molecules per *T* = 1 capsid was obtained (Figure 3.12 and Table 3.1).[27] Using the equation z = 0.078 x $M^{0.5}$, *T* = 1 particles (M ~1.2 MDa), should contain (z) approximately 85 charges. At low acceleration voltage, a small amount of truncated CP dimers and the *T* = 1 particles around m/z 15,600 were detected, which is within the expected m/z of around 14,117 (Figure 3.12, bottom). Tandem MS was performed on selected mass to charge ratios (m/z) (Figure 3.12, grey bar). Charge stripping at medium

acceleration voltage (150 V) enables the mass determination for ZnPc filled VLPs. At high acceleration voltage (220 V, top), highly charged CP units are ionized from the capsids and appear at m/z 1,500. Similarly, the high mass species observed at m/z 18,200 corresponds to the capsid missing one monomer. Notably, the particles contained primarily the intact CP, which was not present in solution. This suggests that the assembly is less efficient for the truncated protein (Figure 3.12).

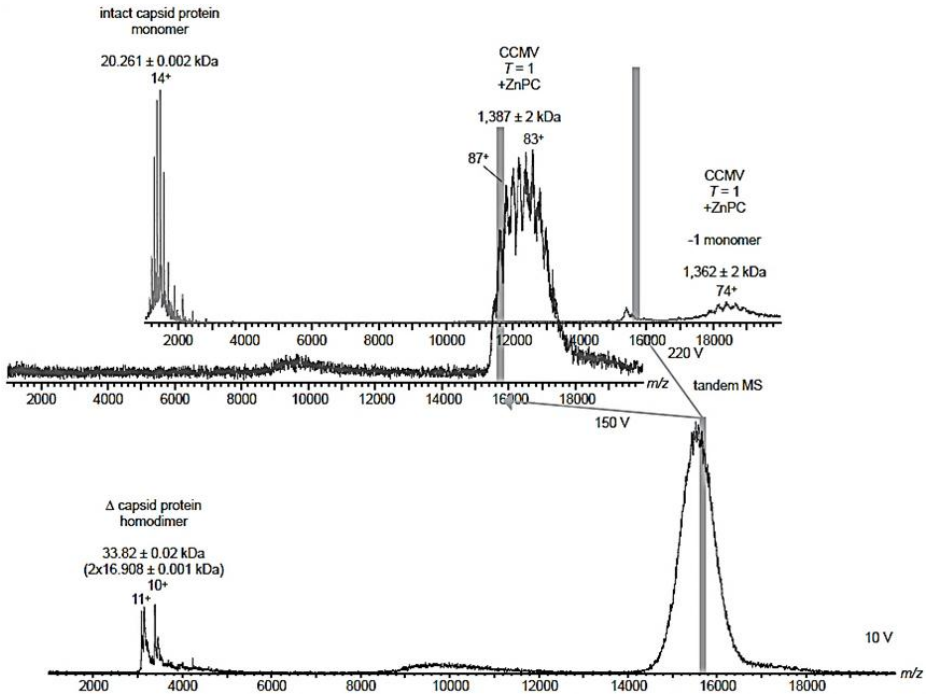

Figure 3.12. ESI-MS analysis of ZnPc-loaded *T* = 1 particles.

Table 3.1. ESI-MS analysis of ZnPc molecules per *T* = 1 particle.

Acceleration voltage	$M_{individual\ CP}$ / Da	$M_{capsid,\ calculated}$ / Da [1]	$M_{capsid,\ measured}$ / Da [2]	[2] - [1] = $M_{ZnPc\ incorporated}$ (# molecules) / Da
10 V	16,908 ± 1 (ΔCP)	1,014,480 (only ΔCP)	n.d.	n.d.
150 V (with selection)	n.d.	1,215,660*	1,387,000 ± 2000	~171,000 (192)
220 V (with selection)	20,261 ± 2	1,215,660*	1,382,000 ± 2000 (1,362,000 + 20,261)	~166,000 (186)

*The capsid masses were calculated with the full-length protein to determine the amount of ZnPc. Anionic ZnPc was assumed to be incorporated in the VLPs (892 Da).

3.2.4 VLPs loaded with ZnPc and their application in PDT

Pcs are promising candidates as photosensitizers for photodynamic therapy (PDT) of neoplastic and non-neoplastic diseases.[1] Two important requirements are 1) the transport of Pc to its intracellular target, and 2) the high local concentration of Pc for optimal photosensitizing effects. Both of these aspects can be effectively and efficiently met by encapsulating Pc molecules within virus-like particles. The virus capsid is intrinsically designed to deliver (nucleic acid) cargo to host cells, and can be readily functionalized on the surface to introduce targetability, making viruses promising candidates as delivery systems. Although preliminary experiments have shown that ZnPc filled $T = 3$ and $T = 1$ capsids could be taken up by macrophage cells, $T = 3$ particles are not as suitable, since they have been shown to rearrange and release part of the encapsulated ZnPc molecules into the medium. Subsequent irradiation between $\lambda = 620 - 660$ nm for 20 min induced almost complete death of 92 – 95% of cells, whereas in the non-illuminated area, the cells survived (Figure 3.13). The presence of dead cells was evaluated by staining with propidium iodide (PI), which intercalates into double-stranded nucleic acids. PI is excluded by viable cells but can penetrate the cell membrane of dying or dead cells. Dead cells are thus identified in the micrographs as they appear colored in red in the fluorescence images. The ZnPc induces a similar PDT effect (92%, Table 3.2) in the absence of CP (Figure 3.13C). In contrast, when irradiation took place in the absence of ZnPc and the CP, almost no dead cells (5%, Table 3.2) were observed (Figure 3.13D).

Table 3.2. Percentage of cells killed after the uptake of different types of particles.

	T=1		*T*=3		ZnPc		Blank	
	Trial 1	**Trial 2**	**Trial 1**	**Trial 2**	**Trial 1**	**Trial 2**	**Trial 1**	**Trial 2**
# of cells counted	170	751	296	579	292	612	359	889
% of dead cells	92.4%	92.5%	93.9%	95.9%	91.8%	92.6%	3.6%	6.1%
Average killing efficiency	92.5%		94.9%		92.2%		4.8%	

The suitability of ZnPc-loaded CCMV $T = 1$ particles to induce cell death, upon cellular uptake and subsequent irradiation has been proven by these experiments. An experimental confirmation of whether encapsulated or free ZnPc is the species responsible for cellular death could unfortunately not been obtained. The encapsulation of ZnPc presents, however, plenty of potential benefits for PDT *in vivo*. The photosensitizer biocompatibility may be improved during its transport through the organism. Moreover, our strategy could facilitate cellular targeting, and would certainly provide an increased local concentration. Future implementations are envisioned, such as the encapsulation of non-aggregated Pc

derivatives and the capsid functionalization with target-selective biocompatible polymers. Understanding how these factors would affect the assembly properties of the CP and the efficacy of the PDT response will be of fundamental importance in the route towards an efficient photosensitizer/vehicle system. Interestingly, the analogous copper derivative of ZnPc (tetrasulfonated CuPc) has been used to target G-quadruplexes and to selectively inhibit the elongation of telomers (*i.e.*, one of the causes of cell canceration) in the presence of dsDNA.[28] These Pc-containing VLPs may therefore be potentially useful for the inhibition of telomerase activity.

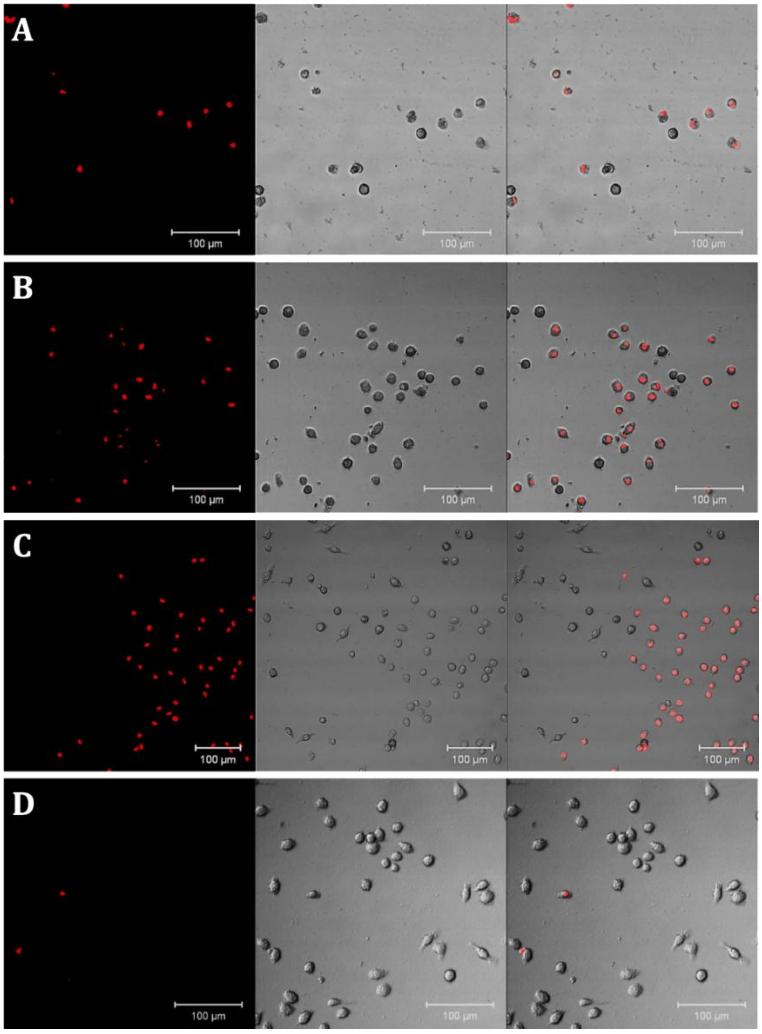

Figure3.13. Fluorescence microscopy of RAW 264.7 macrophage cells irradiated with a mercury lamp (excitation BP (bandpass filter) wavelengths of 620/60 nm) for 20 min, (A) in the presence of ZnPc-containing *T* = 1 capsids, (B) in the presence of ZnPc-containing *T* = 3 capsids, (C) in the presence of ZnPc and (D) in the absence of ZnPc and VLPs. Dead cells stained with PI appear in red. Left: Fluorescence microscopy images (excitation at 543 nm, emission recorded with a LP 560 filter); middle: transmission images; right: overlap of the other two images.

3.3 Conclusions

In summary, the presented data shows that the assembly of artificially loaded icosahedral protein cages is a complex process, with a delicate interplay between capsid protein and cargo. On one hand the formation of $T = 1$ particles at neutral pH is due to the presence of a negatively charged template. On the other hand, the high effective concentration resulting from the dye confinement leads to larger ZnPc aggregates, which in turn might be better templates. This cooperative association between protein assembly and ZnPc aggregation yields in the end a stable Pc-loaded protein nanocontainer inducing the formation of ZnPc aggregates at their interior.

Remarkably, ZnPc-filled $T = 1$ VLPs are stable after dialysis against other water based solvents in a pH range from 5.0 to 7.5, demonstrating the robust nature of such VLP-based assemblies. In contrast, ZnPc filled $T = 3$ VLPs are susceptible to loss of ZnPc cargo by diffusion through the pores of the capsid shell. Furthermore, ZnPc-filled $T = 3$ particles (at pH 5.0) are not stable upon dialysis to neutral pH 7.5 and instead rearrange into stable $T = 1$ particles filled with ZnPc.

Finally, ZnPc-filled virus-like assemblies can be used for PDT *invitro* with a cell death efficiency of 92-95% of the macrophages. This is a similar efficiency as obtained with ZnPc itself, but with the possibility to contain the PDT dye with surface functionality, for *e.g*. targeting and other drugs.

3.4 Acknowledgments

Dr. Andrés de la Escosura is gratefully acknowledged for the synthesis and characterization of the ZnPc as well as for the help and fruitful discussions. Many thanks go to Dr. Yujie Ma for performing the cell studies and for the help and discussions on this part. Dr. Charlotte Uetrecht is acknowledged for the help and performance of the ESI-MS studies.

3.5 Experimental

3.5.1 Materials

The purification of the CCMV virus, removal of its RNA and isolation of the CCMV coat protein (CP) were carried out according to literature procedures.[29, 30] The resulting viral CP were characterized by size exclusion chromatography (SEC) and UV-Vis spectroscopy. The ZnPc tetrasulfonic acid sodium salt was prepared according to literature procedures.[31]

3.5.2 Methods

General methods:
Size exclusion chromatography was performed using a Superose 6 10/100 GL (GE Healthcare) preparative column, eluting with either 50 mM Tris-HCl buffer, 0.3 M NaCl, 1 mM DTT at pH 7.5 or 50 mM NaOAc buffer, 1 M NaCl, 1 mM NaN_3 at pH 5.0. Buffers were prepared from ultrapure (Milli-Q) water. UV-visible spectra were recorded using a Perkin Elmer Lambda 850 UV spectrophotometer. ^{1}H NMR was recorded at room temperature using a Bruker 300 MHz spectrometer. Chemical shifts are given in ppm (δ) relative to tetramethylsilane. MALDI-TOF MS was performed using a Bruker ULTRAFLEX III spectrometer, using α-cyano-4-hydroxycinnamic acid as the matrix.

Encapsulation of ZnPc into CCMV T = 1 capsids (Sample 1):
From a stock solution of ZnPc (3 mM in 50 mM Tris-HCl buffer, 0.3 M NaCl, 1 mM DTT (pH 7.5), 133 µL of ZnPc were added to CCMV CP in the same buffer (0.4 mM, 182 µL). The final volume was made up to 400 µL with buffer. The resulting solution (1 mM ZnPc; 0.2 mM CP) was incubated for 1 h at 4 °C on a roller bank. After incubation, the sample containing ZnPc/CP as well as a reference solution (only CP) were purified and analyzed by SEC monitoring at λ = 260 nm, 280 nm and 635 nm. Fractions of 200 µL were collected, and those corresponding to ZnPc-containing *T* = 1 capsids were further analyzed by DLS, TEM and UV-visible spectroscopy.

Encapsulation of ZnPc into CCMV T = 3 capsids:
From a stock solution of ZnPc (3 mM in 50 mM sodium acetate buffer, 1 M NaCl, 1 mM NaN_3, pH 5), 100 µL of ZnPc were added to CCMV capsid solution in the same buffer (0.35 mM, 200 µL). The final volume was made up to 400 µL with buffer and the mixture was incubated for 1 h at 4 °C on a roller bank. After the incubation step, the sample containing ZnPc/CP as well as a reference solution (with only native CCMV capsid) were purified and analyzed by SEC, monitoring at λ = 260 nm, 280 nm and 635 nm. Fractions of 200 µL were collected, and those corresponding to ZnPc-containing *T* = 3 capsids were further analyzed by DLS, TEM and UV-visible spectroscopy.

Dialysis of Sample 1 against different solvents:
Sample 1 (200 µL) was dialyzed for 24 h against either 200 mL of 10% pyridine or 10% picolinic acid solutions in 50 mM Tris-HCl buffer, 0.3 M NaCl, 1 mM DTT, pH 7.5 or against Milli-Q water at 4 °C using 6-8 kDa MWCO dialysis membranes. The resulting samples were purified and analyzed by SEC and UV-visible spectroscopy.

Conversion of T = 3 containing ZnPc into T = 1 capsids:
Sample 2 (200 µL) was dialyzed for 24 h against 50 mM Tris-HCl buffer, 0.3 M NaCl, 1 mM DTT, pH 7.5 at 4°C using 6-8 kDa MWCO dialysis membranes. The resulting samples were purified and analyzed by both SEC and UV-visible spectroscopy.

Mass Spectrometry Studies:
Electrospray ionization (ESI) mass spectrometry (MS) measurements in the positive ion mode were performed on modified QTOF 1 and QTOF 2 instruments (Waters, UK; and MS Visions, the Netherlands).[32] To optimize the resolution and ion transmission, the backing pressure was increased to 10 mbar. The capillary and cone voltages were 1350 V and 150 V, respectively. In the collision cell, the pressure was 1.5 x 10^{-2} mbar with xenon as collision gas,[33] and the acceleration voltage was varied from 10 to 300 V. For tandem MS experiments, ions were selected according to m/z (mass to charge ratio) in the quadrupole preceding the collision cell. Capillaries for ESI were home-made from borosilicate glass tubes of 1.2 mm OD and 0.68 mm ID with filament (World Precision Instruments, USA) using a P-97 micropipette puller (Sutter Instruments, USA) and gold-coated using an Edwards Scancoat (Edwards Laboratories, USA) six Pirani 501 sputter coater. Capillary tips were opened on the sample cone of the instrument. Mass spectra were calibrated where necessary with cesium iodide and analyzed using Masslynx, ESIprot[34] and a program, LeastMass, recently developed in collaboration with the Department of Physics, National Dong Hwa University, Taiwan.[35] Buffer exchange of the ZnPc-loaded *T* = 1 CCMV particle solution to 200 mM ammonium acetate (pH 7.5) was carried out using centrifugal filter units at 13,000 g, 4 °C (5 kDa MWCO,

Vivaspin 500, Sartorius AG, Germany). The CCMV particles were analyzed at concentrations in the range of 8-16 μM, based on the monomer concentration.

Photo-toxicity studies in cells:
RAW 264.7 macrophages were grown in Dulbecco's modified Eagle's medium (DMEM) + 10% fetal bovine serum (FBS) + 1% penicillin, streptomycin solution (PS) at 37 °C. Approximately 10^{14} ZnPc-loaded virus-like particles in their corresponding buffer or approximately 10^{14} ZnPc molecules in pH 7.5 buffer were mixed with 10^3-10^4 seeded cells in 100 μL growth medium and incubated at 37 °C for more than 18 h. Afterwards the cells were washed three times with the medium to remove the excess of material and then resuspended in fresh medium. The washed cells were irradiated using a mercury lamp fitted with a filter cube (excitation BP wavelengths of 620/60) for 20 min. After incubation at 37 °C for ~ 20 h, propidium iodide (PI) was added to the cell culture and images were taken with a Zeiss LSM 510 confocal laser scanning system using a 543 nm HeNe laser with 10-times magnification.

Size-exclusion chromatography (SEC):
SEC was performed using the GE Healthcare FPLC Äkta purifier 900 combined with fraction collector Frac-950. Samples were purified over a preparative column superpose 6 10/100 GL (GE Healthcare) with a 24 mL bed volume. Samples were injected over a 100 μL injection loop.

Transmission Electron Microscopy (TEM):
The samples were examined in an analytical FEG-TEM (Phillips CM 30) operated at 300 kV acceleration voltages. For the sample preparation 5 μL of the desired sample were applied onto Formvar-carbon coated grids. After leaving the sample for 1 min, the excess of liquid was drained using a piece of filter paper. Uranyl acetate (5 μL, 1% w/v) was applied and the excess of liquid was drained after 20 seconds. The grid was dried for 30 mins at room temperature.

UV-Vis spectroscopy:
UV-Vis spectra were recorded on a Varian Cary 300 UV-Vis spectrometer, using a quartz cuvette with 3 mm path length.

Dynamic light scattering for ZnPc filled VLPs:
DLS measurements were obtained using 600 μL of sample. The size distribution of the capsids was determined by measuring their diameter for more than 80 counts unless otherwise stated. All samples were measured in triplicate. The data are presented as "Frequency (%)", which refers to the volume percentage as determined by the instrument.

3.6 Appendix

3.6.1 Appendix : Calculation of ZnPc molecules per capsid

Starting values measured by UV-VIS and extinctions coefficient (ε) for ZnPc:

A = ε · c · d, with c: concentration and d: path length of the cuvette

$A_{(T = 1 \text{ filled ZnPc @ 635 nm})}$: 0.0876 (only ZnPc absorbs in this region)

$A_{(T = 1 \text{ filled ZnPc @ 280 nm})}$: 0.1398 (CP and ZnPc absorb in this region)

$\varepsilon_{(\text{ZnPC @ 635 nm})}$: 24055 $\text{mol}^{-1} \cdot \text{l} \cdot \text{cm}^{-1}$, y-intercept: 0.00317

$\varepsilon_{(\text{CP @ 280 nm})}$: 10508 $\text{mol}^{-1} \cdot \text{l} \cdot \text{cm}^{-1}$, y-intercept: 0.01974

$\varepsilon_{(\text{CP @ 280 nm})}$: 24075 $\text{mol}^{-1} \cdot \text{l} \cdot \text{cm}^{-1}$,

Calculation of ZnPc overall concentration:

$$c_{(ZnPc)} = \frac{0.0876 - 0.00317}{24055 \text{ mol}^{-1} \cdot \text{l}} = 3.509 \cdot 10^{-6} M$$

Calculation of Absorbance @ 280 caused by ZnPc:

$$A_{(ZnPc \text{ @ } 280\ nm)} = 10508\ mol^{-1} \cdot \text{l} \cdot 3.509 \cdot 10^{-6} M + 0.01974 = 0.0566$$

Calculation of Absorbance @ 280 related to CP:

$$A_{(CP \text{ @ } 280\ nm)} = A_{(\text{T = 1 filled ZnPc @ 280 nm})} - A_{(ZnPc \text{ @ } 280\ nm)}$$

$$A_{(CP \text{ @ } 280\ nm)} = 0.1399 - 0.0566 = 0.0833$$

Calculation of T = 1 concentration:

$$c_{(CP)} = \frac{0.0833}{24075 \text{ mol}^{-1} \cdot \text{l} \cdot \text{cm}^{-1} \cdot 1 \text{ cm}} = 3.460 \cdot 10^{-6} M$$

$$c_{(T = 1)} = \frac{3.460 \cdot 10^{-6} \text{M}}{60} = 5.766 \cdot 10^{-8} \text{M}$$

Calculation of ZnPc aggregates (dimers) per T = 1 particle:

$$\frac{c_{(ZnPc)}}{c_{(T = 1)}} = \frac{3.509 \cdot 10^{-6} M}{5.766 \cdot 10^{-8} M} = \mathbf{60.8\ ZnPc\ dimers\ or\ 120\ monomers} \text{ per } T = 1$$

Volume of a $T = 1$ capsid:

$$V = \frac{4}{3} \cdot \pi \cdot r^3$$

$r_{(T=1)} = 7$ nm (inner radius)

$$V = \frac{4}{3} \cdot \pi \cdot (7 \cdot 10^{-8}\ \text{dm})^3 = 1439 \cdot 10^{-24}\ \text{l}$$

Local concentration caused by one molecule per $T = 1$ capsid:

N_A: $6.022 \cdot 10^{23}$ molecules per mol

$$n = \frac{\text{molecules}}{N_A}$$

$$n = \frac{1}{6.022 \cdot 10^{23}} = 0.166 \cdot 10^{-23}\ \text{mol}$$

$$\frac{n}{V} = \frac{0.166 \cdot 10^{-23}\ \text{mol}}{1439 \cdot 10^{-24}\ \text{l}} = 1.15\ \text{mM}$$

One molecule inside a $T = 1$ particle causes a concentration around 1 mM.

3.7 References

1. G. de la Torre, C. G. Claessens and T. Torres, *Chem Commun*, 2007, 2000-2015.
2. K. M. KIadish, K. M. Smith and R. Guilard, *Handbook of Porphyrin Science*, Singapore, 2010.
3. S. M. O'Flaherty, S. V. Hold, M. J. Cook, T. Torres, Y. Chen, M. Hanack and W. J. Blau, *Adv Mater*, 2003, 15, 19-32.
4. N. Kobayashi and C. C. Leznoff, *J Porphyr Phthalocya*, 2004, 08, 1015-1019.
5. G. Bottari, D. Olea, C. Gómez-Navarro, F. Zamora, J. Gómez-Herrero and T. Torres, *Angew Chem Int Ed*, 2008, 47, 2026-2031.
6. J. Jiang and D. K. P. Ng, *Acc Chem Res*, 2008, 42, 79-88.
7. G. Bottari, G. de la Torre, D. M. Guldi and T. Torres, *Chem Rev*, 2010, 110, 6768-6816.
8. Q. Wang, T. W. Lin, L. Tang, J. E. Johnson and M. G. Finn, *Angew Chem Int Ed*, 2002, 41, 459-462.
9. T. Douglas and M. Young, *Science*, 2006, 312, 873-875.
10. K. T. Nam, D.-W. Kim, P. J. Yoo, C.-Y. Chiang, N. Meethong, P. T. Hammond, Y.-M. Chiang and A. M. Belcher, *Science*, 2006, 312, 885-888.
11. M. Fischlechner and E. Donath, *Angew Chem Int Ed*, 2007, 46, 3184-3193.
12. V. M. Rotello, *J Mater Chem*, 2008, 18, 3739-3740.
13. A. de la Escosura, R. J. M. Nolte and J. J. L. M. Cornelissen, *J Mater Chem,* 2009, 19, 2274-2278.
14. M. A. Kostiainen, O. Kasyutich, J. J. L. M. Cornelissen and R. J. M. Nolte, *Nat Chem*, 2010, 2, 394-399.
15. L. M. Scolaro, M. A. Castriciano, A. Romeo, N. Micali, N. Angelini, C. Lo Passo and F. Felici, *J Am Chem Soc*, 2006, 128, 7446-7447.
16. Y. S. Nam, T. Shin, H. Park, A. P. Magyar, K. Choi, G. Fantner, K. A. Nelson and A. M. Belcher, *J Am Chem Soc*, 2010, 132, 1462-1463.
17. M. Endo, M. Fujitsuka and T. Majima, *Chem Eur J*, 2007, 13, 8660-8666.
18. D. E. Prasuhn Jr, J. Kuzelka, E. Strable, A. K. Udit, S.-H. Cho, G. C. Lander, J. D. Quispe, J. R. Diers, D. F. Bocian, C. Potter, B. Carragher and M. G. Finn, *Chemistry & Biology*, 2008, 15, 513-519.
19. N. Stephanopoulos, Z. M. Carrico and M. B. Francis, *Angew Chem Int Ed*, 2009, 48, 9498-9502.
20. J. A. Speir, S. Munshi, G. Wang, T. S. Baker and J. E. Johnson, *Structure*, 1995, 3, 63-78.
21. J. E. Johnson and J. A. Speir, *J Mol Biol*, 1997, 269, 665-675.
22. F. D. Sikkema, M. Comellas-Aragones, R. G. Fokkink, B. J. M. Verduin, J. J. L. M. Cornelissen and R. J. M. Nolte, *Org Biomol Chem*, 2007, 5, 54-57.

23. J. Tang, J. M. Johnson, K. A. Dryden, M. J. Young, A. Zlotnick and J. E. Johnson, *J Struct Biol*, 2006, 154, 59-67.
24. L. Lavelle, M. Gingery, M. Phillips, W. M. Gelbart, C. M. Knobler, R. D. Cadena-Nava, J. R. Vega-Acosta, L. A. Pinedo-Torres and J. Ruiz-Garcia, *J. Phys. Chem. B*, 2009, 113, 3813-3819.
25. T. Nyokong, *Coordin Chem Rev*, 2007, 251, 1707-1722.
26. K. Burns, S. Mukherjee, T. Keef, J. M. Johnson and A. Zlotnick, *Biomacromolecules*, 2009, 11, 439-442.
27. A. J. R. Heck, *Nat Meth*, 2008, 5, 927-933.
28. H. Yaku, T. Murashima, D. Miyoshi and N. Sugimoto, *Chem Commun*, 2010, 46, 5740-5742.
29. B. J. Verduin, *FEBS Lett*, 1974, 45, 50-54.
30. M. Comellas-Aragones, H. Engelkamp, V. I. Claessen, N. A. Sommerdijk, A. E. Rowan, P. C. Christianen, J. C. Maan, B. J. Verduin, J. J. Cornelissen and R. J. Nolte, *Nat Nanotechnol*, 2007, 2, 635-639.
31. V. M. Derkacheva, S. A. Mikhalenko, L. I. Soloveva, V. I. Alekseeva, L. E. Marinina, L. P. Savina, A. V. Butenin and E. A. Lukyanets, *Russ J Gen Chem+*, 2007, 77, 1117-1125.
32. R. H. van den Heuvel, E. van Duijn, H. Mazon, S. A. Synowsky, K. Lorenzen, C. Versluis, S. J. Brouns, D. Langridge, J. van der Oost, J. Hoyes and A. J. Heck, *Anal Chem*, 2006, 78, 7473-7483.
33. K. Lorenzen, C. Versluis, E. van Duijn, R. H. H. van den Heuvel and A. J. R. Heck, *Int J Mass Spectrom*, 2007, 268, 198-206.
34. R. Winkler, *Rapid Commun Mass Sp*, 2010, 24, 285-294.
35. Y. H. Tseng, C. Uetrecht, A. J. Heck and W. P. Peng, *Anal Chem*, 2011, 83, 1960-1968.

Chapter 4

Encapsulation of Enzyme Pathways in Protein Compartments

The ability to design and mimic bacterial microcompartments can provide valuable insight as to their role in Nature and how primitive organelles evolved to enhance metabolic efficiency. Inspired by Nature, we demonstrate the use of virus-like assemblies as model nanocompartments to investigate the effects of confinement on enzyme activity. The compartmentalization of a two-enzyme reaction pathway in virus-like assemblies led to an overall enhancement in catalytic efficiency, likely due to the reduced inter-enzyme distance and the restricted diffusion of substrate intermediates. We use viruses as a nanocompartment to show that the confinement of a two-enzyme reaction pathway leads to a significant enhancement in catalytic efficiency.

This chapter is submitted:
M. Brasch, R. M. Putri, M. S. T. Koay and J. J. L. M. Cornelissen; ***2013***

4.1 Introduction

Compartmentalization occurs in living cells and is a critical feature in order to ensure independent cellular reactions and transport, or to protect cells against toxic intermediates.[1] It occurs at several scales, from molecular reaction chambers, such as proteasomes, chaperons and ribosomes,[2] to eukaryotic organelles such as peroxisomes, lysosomes and mitochondria. Recently, protein-based microcompartments, named bacterial microcompartments (BMCs), have been discovered in prokaryotic cells. BMCs are large polyhedral shell-like structures composed entirely of proteins, with a diameter varying from 20-150 nm.[3, 4] Various types and amounts of enzymes can be encapsulated into BMCs. The earliest discovered BMC was the carboxysome, followed by metabolosomes and encapsulins.[4] Carboxysomes encapsulate two metabolic enzymes, carbonic anhydrase and ribulose biphosphate carboxylase monooxygenase (RuBisCo). Both enzymes are involved in the uptake mechanism of carbon dioxide (CO_2), resulting in an increase of the CO_2 fixation rate.[3-6] Pores within the protein shell presumably ensure restriction of non-charged molecules such as CO_2 and O_2, while negatively charged molecules such as substrates and products of RuBisCo can pass through.[4] Metabolosomes encapsulate enzymes which are involved in specific metabolic processes, *i.e.* ethanolamine utilization (Eut) and propanediol utilization (Pdu). In these cases compartmentalization ensures the restriction of toxic intermediates, such as reactive aldehydes to reduce cytotoxicity, while regulating the enzyme activity and increasing the reaction efficiency via substrate channeling.[5, 7] Until now, encapsulins are the smallest reported BMC with a diameter of 20-24 nm. They encapsulate either an iron-depending peroxidase or a protein related to the iron transporter ferritin. It is reported that encapsulins encase those proteins to either store ferrous ions or to prevent the formation and release of toxic intermediates in the same way as reported for carboxysomes and metabolosomes.[1] Formation of compartments around an enzyme has been found to lead to either a change of enzyme efficiency due to confinement effects, rate enhancement by substrate channeling, or protection of the cell from toxic intermediates or the enzyme against degradation.[1, 3-4, 6, 8-9] Consequently, there is a growing interest in mimicking the encapsulation of enzymes inside microcompartments using viral protein cages,[10-14] since they provide a reliable re-assembly mechanism and their size is comparable to the smaller BMCs. Viral protein cages represent a promising approach to perform multi-step reactions in a confined space, which is beneficial to gain more information about the influence of confinement effects in reaction rates, substrate exchange through protein compartments and their stability against environmental changes.[14-16] To date, researchers have investigated the encapsulation of multiple enzymes of the same species in different viral protein cages, such as bacteriophages Qβ,[13] P22[10] or MS2[14] and the cowpea chlorotic

mottle virus (CCMV),[11] to explore the influence of compartmentalization on the enzymatic activity of the encapsulated enzymes. Overall the encapsulation of multiple enzymes of the same species inside bacteriophages reveals very similar enzymatic activities compared to the free enzymes in solution.[10, 13, 14] In contrast, enzymes encapsulated in CCMV show an overall increased activity compared to free enzymes. In this case, it is remarkable that the largest increase in enzymatic activity was achieved when only a single enzyme per capsid was encased.[11] To the best of our knowledge no encapsulation of two different enzymes performing a multi-step or cascade reaction inside viral protein cages has been reported. Consequently, very little is known about the influence of compartmentalization on enzymatic cascades and the induced changes in either enzymatic activity or substrate channeling. Studying these effects is key to understand compartmentalized cascades such as the ones present in BMCs. To mimic the function of BMCs, we use CCMV as a model protein microcompartment to encapsulate two different enzymes within its interior, in order to 1) investigate whether substrate intermediates are entrapped inside, 2) to study the effects of confinement on enzyme activity and 3) to provide a general strategy for successful encapsulation of multiple enzymes of different types inside CCMV.

The CCMV capsid is composed of 180 identical coat proteins (CP) each 20 kDa, which self-assemble into icosahedral VLPs. Two different self-assembly strategies are possible. The first strategy to form VLPs is based on protein-protein interaction at low pH (5) and high ionic strength (I > 1 M). In this case the cargo does not need to provide any surface charges and gets randomly encapsulated. The assemblies resulting from this are a mixture of empty and filled VLPs. In the second strategy, the positively charged N-terminus of the CP assembles around negatively charged cargo and forms a smaller VLP (*i.e.* with an outer diameter of 18 nm) at pH 7.5 of 60 CPs. These assemblies are driven by ionic-charge compensation and result in VLPs that always encapsulate a cargo.[17-19] CCMV VLPs that are formed by ionic-charge compensation are highly stable against temperatures up to 65 °C and pH values between 5 and 7.5.[19, 20] Moreover, they present pores of 2 nm in diameter which allow substrate exchange with the surrounding solution.[18, 19] These qualities make CCMV VLPs suitable for material encapsulation, even for enzymes performing reactions at elevated temperature and a wide range of pH values.[21, 22]

We choose two different enzyme-DNA hybrids for the encapsulation into CCMV VLPs. The first enzyme-hybrid system (GOx-DNAzyme) consists of glucose oxidase (GOx) coupled to a DNAzyme. GOx is a 160 kDa dimeric protein with a diameter of 8 nm,[23] which catalyzes the oxidation of glucose to gluconic acid and hydrogen peroxide (H_2O_2) as a by-product.[2] The DNAzyme is a guanine-rich nucleic acid sequence, which in the presence of hemin folds into a supramolecular structure with biocatalytic activity, mimicking the well-known enzyme horseradish peroxidase (HRP).[24, 25] The DNAzyme catalyzes the decomposition of H_2O_2 in the

presence of an electron donor. One of the commonly used electron donors is 2,2-azinobis(3-ethylbenzothiozoline)-6-sulfonic acid ($ABTS^{2-}$), which turns from colorless to the green $ABTS^{\cdot-}$ radical, and is used for the quantification of H_2O_2 production in enzymatic reactions.[5, 26-28] The advantage of the GOx-DNAzyme-hybrid system is not only the decomposition of the side product H_2O_2, which can be followed by the oxidation of $ABTS^{2-}$ at λ = 410 nm, but also the release of the produced gluconic acid. The production of gluconic acid can be quantified by an additional cascade reaction involving two enzymes, gluconic kinase (GCK) and 6-phosphogluconate dehydrogenase (6-PGDH). The resulting NADPH formation can be used to quantify the amount of produced gluconic acid. The second hybrid system (GOx-GCK) consists of GOx coupled to gluconate kinase (GCK). GCK is a 38.8 kDa homodimeric protein and phosphorylates gluconic acid, produced by GOx, to D-gluconate-6-phosphate. The latter can diffuse into the bulk solution where 6-PGDH oxidizes it to ribulose-5-P involving the production of NADPH, which can be monitored at λ = 340 nm.[29-32] The advantage of this GOx-GCK-hybrid system is that the product of GOx can be directly passed to GCK without diffusion over the protein pores. In both presented enzyme-hybrid systems, the influence of enzyme ratios and/or substrate channeling in enzymatic multi-step reactions under compartmentalized condition can be investigated and provide a model system for natural microcompartments. A schematic model of our multi-enzyme nanoreactor and the multi-step reactions performed within is provided in Figure 4.1.

4.2 Results and discussion

4.2.1 Enzyme-hybrids system: (A) GOx-DNA, (B) GCK-DNA, (C) GOx-GCK

Different methods for the coupling of single stranded DNA (ssDNA) to enzymes are described in literature.[14, 33, 34] Those synthetic descriptions served as guideline in order to synthesize our two enzyme-DNA hybrid systems, GOx-DNAzyme and GOx-GCK as illustrated in Figure 4.2. First, lysine groups available at the outer surface of GOx or GCK (Figure 4.2A and 4.2B) were functionalized with a bifunctional linker (Sulfo-EMCS linker) containing a succinamide moiety, which reacts with amine groups, and a maleimide moiety, which reacts with thiol groups. Second, thiol-functionalized DNA sequences were added to either linker-functionalized enzyme to obtain DNA functionalized enzymes. For the first system, the GOx-DNAzyme-hybrid, a guanine-rich DNA sequence was chosen, which in the presence of hemin self-assembles into a supramolecular structure with biocatalytic activity, herein referred to as DNAzyme (Figure 4.2A). To prepare the second enzyme-DNA hybrid system a DNA sequence complementary to the DNAzyme sequence (csDNA) was chosen to functionalize GCK, the complementary hybridization of GOx-DNAzyme (Figure 4.2A) and GCK-csDNA (Figure 4.2B) leads to the GOx-GCK-hybrid (Figure 4.2C).

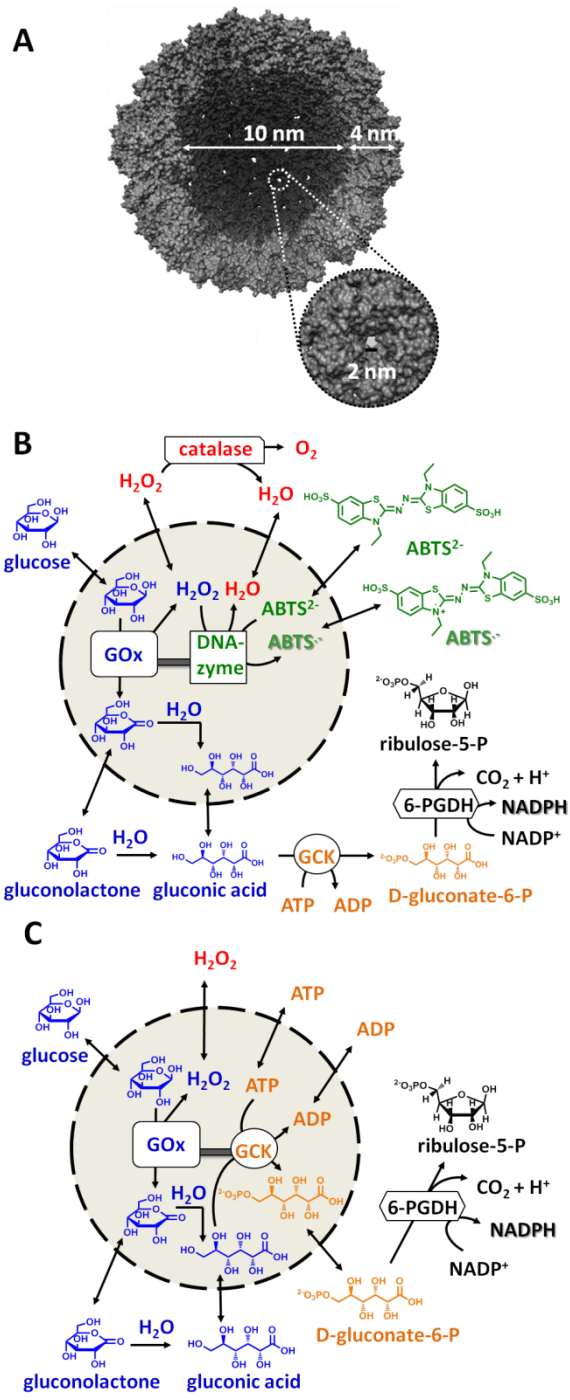

Figure 4.1. A model for the CCMV capsid and the schematic representation of the enzyme cascade reactions studied inside CCMV.

(A) Structural representation of the CCMV capsid, emphasizing the diameter of the interior, the shell wall and the pore.

(B) Schematic overview of the enzymatic cascade reaction by GOx-DNAzyme, which is composed of GOx (shown as a blue square), which is covalently functionalized with DNAzyme (shown as a green square). GOx oxidizes glucose to H2O2 and gluconolactone inside the CCMV capsid (represented as a black dashed line). H2O2 is either consumed at the interior by the DNAzyme, which catalyzes the oxidation of ABTS2- into ABTS−· (green pathway) or can diffuse out of the capsid and is subsequently consumed at the exterior by catalase (red pathway). The second intermediate, gluconolactone, spontaneously hydrolyzes to gluconic acid. Gluconic acid is then phosphorylated at the exterior of the CCMV capsid by GCK (in the presence of ATP) to form D-gluconate-6-P (orange pathway). The 6-PGDH then catalyzes the oxidative decarboxylation of D-gluconate-6-P to ribulose-5-P and CO2 with simultaneous reduction of NADP+ to NADPH (black pathway). The formation of both ABTS−· and NADPH can be followed spectroscopically to determine the apparent kinetic parameters.

(C) A model for the enzymatic cascade reaction performed by DNA functionalized GOx (blue), which is connected to csDNA functionalized GCK (orange) via hybridization (GOx-GCK). The enzymatic pathway for the conversion of glucose to D-gluconate-6-P occurs at the interior of the CCMV capsids whereas the conversion of D-gluconate-6-P into ribulose-5-P occurs at the exterior of the CCMV capsid.

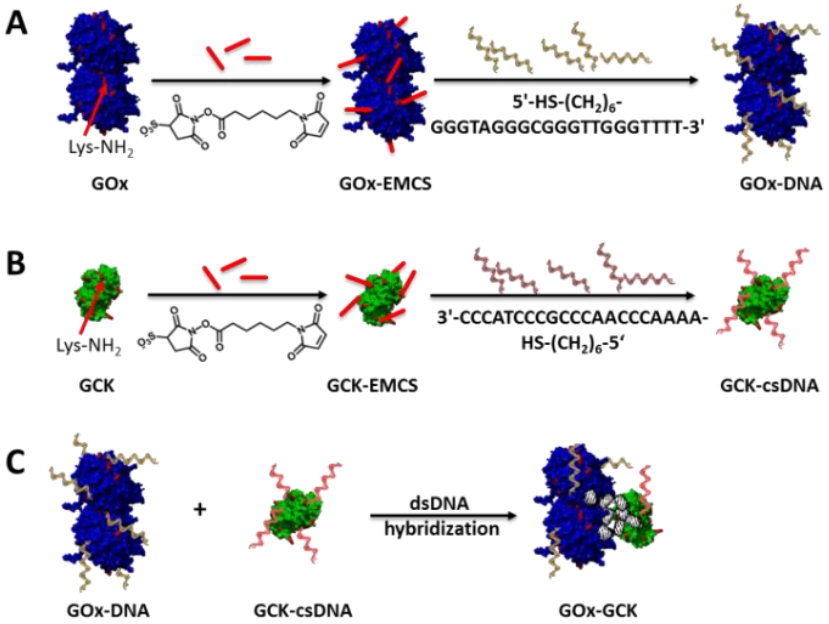

Figure 4.2. Schematic representation of the reaction scheme for the covalent coupling of (A) ssDNA to GOx leading to the formation of GOx-ssDNA, (B) the complementary csDNA to GCK leading to the formation of csDNA-GCK. (C) DNA hybridization of the two functionalized enzymes, GOx-ssDNA and csDNA-GCK leads to the formation of GOx-GCK.

The successful coupling of the DNA sequence to the enzymes of choice and the removal of excess GCK in the case of GOx-GCK hybrid formation was confirmed by gel analysis as illustrated in Figure 4.3. The first lane (A) in the SDS-PAGE gel shows three bands for the GOx-DNAzyme-hybrid, which can be identified as GOx in its dimeric (160 kDa) and monomeric (80 kDa) form. The second lane (B) in the SDS-PAGE-gel shows bands for monomeric (19.4 kDa) and dimeric (38.8 kDa) GCK. The third lane (C) shows two bands. The first band represents GOx and the second band represents monomeric GCK (Figure 4.3 (left), lane (A-C)). Since coomassie staining provides only reliable information about the presence of protein and not the presence of DNA, a 1% agarose gel was prepared, which allows the specific staining for DNA in the GOx-DNAzyme hybrid, GCK-csDNA and the GOx-GCK hybrid (Figure 4.3 (right), lanes (A-C)). In the first lane (A), successful functionalization of GOx with SH-DNAzyme was confirmed by the presence of two bands. The first band represented dimeric GOx and the second band monomeric GOx, both functionalized with DNAzyme. (Figure 4.3, lane (A)) The second lane shows the GCK functionalized with csDNA. The monomeric and dimeric form of functionalized GCK could not be resolved since they do not migrate into the agarose gel, presumably because of the charged compensation between GCK and DNA. However, the third lane (C) shows the hybridized GOx-DNAzyme and GCK-

csDNA, indicated by two bands. The bands migrate slower than the GOx-DNAzyme-hybrid and faster than the band assigned to GCK-csDNA, indicating the complex formation of GOx-GCK-hybrid. At this stage it could not be determined if 1 : 1 hybridization between GOx-DNAzyme and GCK-csDNA was achieved, because of the smeared appearance of the bands. Most importantly, all enzymes were successfully functionalized with the desired DNA sequence and the excess of DNA could be efficiently removed by repeated centrifugal filtration steps, otherwise a specific band for the DNA sequence would be present in the agarose gel as indicated in lane 4, containing only ssDNA of 21 nucleotides (Figure 4.3 (right), lane 4).

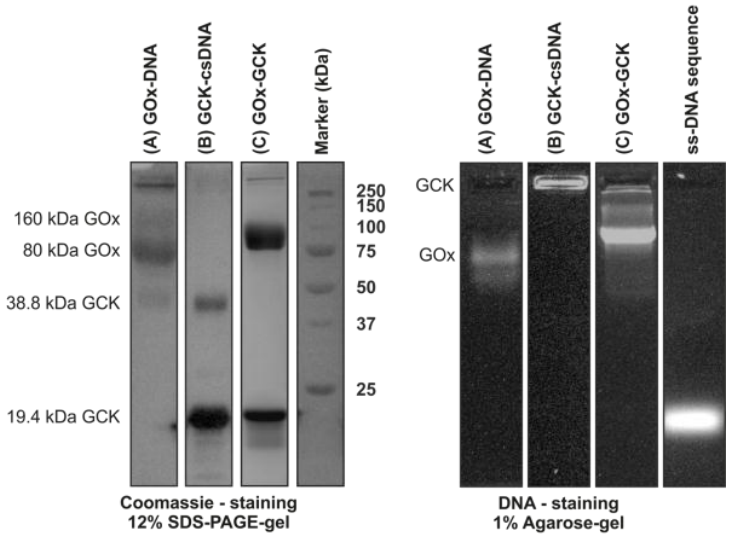

Figure 4.3. Gel analysis of enzyme-hybrids. Lane (A): GOx-DNAzyme-hybrid, lane (B): GCK-csDNA, lane (C): GOx-GCK-hybrid, lane 4: ss-DNA sequence. (left) 12% SDS-PAGE gel after coomassie staining and imaged under white light, (right) 1% Agarose gel after DNA-staining and imaged under UV-light.

4.2.2 Encapsulation of enzyme-hybrids: purification and characterization

The ssDNA has negative charges and can be used to trigger encapsulation (Figure 4.4A) or to functionalize enzymes via sulfo-NHS coupling. The attached DNA causes an overall negatively charged enzyme-hybrid surface, which interacts with the positively charged N-terminus of the CP. The electrostatic interaction results in an ionic-charge compensation, which induces the self-assembly process of CP around the negatively charged enzyme-DNA hybrid surface resulting in VLPs. This concept of protein encapsulation[14] was used in order to encapsulate GOx-DNAzyme-hybrid, GCK-csDNA and GOx-GCK-hybrid into CCMV VLPs as illustrated in Figure 4.4A – 4.4D, respectively.

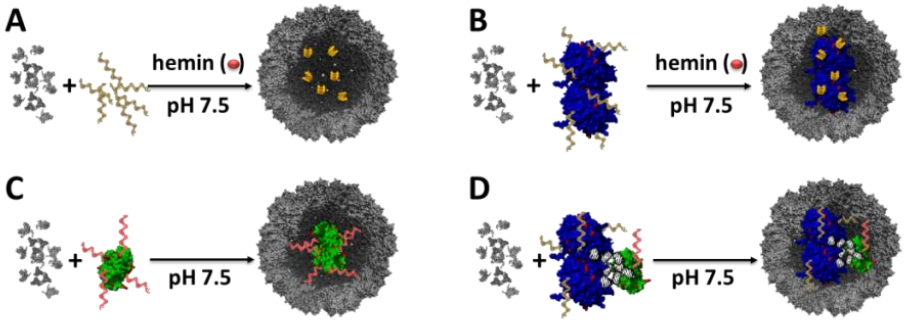

Figure 4.4. Encapsulation of enzyme-hybrid composed of up to two coupled biocatalysts inside CCMV capsids. Enzymes are chemically modified with negatively charged ssDNA tags, which induce the spontaneous self-assembly of CP into icosahedral capsids at pH 7.5, while enclosing the enzymes at their interior. Encapsulation of (A) ssDNAs, (B) GOx functionalized with ssDNA (GOx-DNA), (C) GCK functionalized with the complementary ssDNA (GCK-csDNA) or (D) GOx conjugated to GCK (GOx-GCK) via hybridization of the coupled ssDNA and csDNA, respectively. The ssDNA sequences fold in the presence of hemin into catalytic active DNAzymes.

The enzyme-filled CCMV capsids were purified by size-exclusion chromatography. The elution volume (12 mL), together with the absorbance ratio (260/280 nm) > 1, are characteristic features of intact CCMV capsids containing DNA-based cargoes (Figure 4.5A – 4.5D). Non-encapsulated material such as GOx elutes at 16 mL and GCK together with CP at 18 mL (Figure 4.5B – 4.5D). Negatively stained transmission electron microscopy (TEM) of the purified capsids showed well-defined $T = 1$ and $T = 2$ particles, as determined by the Casper-Klug triangulation (T) number,[35] confirming the morphology of the virus assemblies (Figure 4.5E – 4.5H). Further analysis by dynamic light scattering (DLS) also confirmed the assembly of intact CCMV capsids (Figure 4.5I – 4.5L).

Control experiments were performed to confirm the encapsulation of GOx-DNAzyme, GCK-csDNA and GOx-GCK into CCMV-capsids induced by the attached DNA tags. Therefore, non-functionalized GOx or GCK were incubated with CP at pH 7.5 and analyzed by FPLC. The chromatogram for GOx incubated with CP shows two elution peaks at 16 mL and 18 mL, which are assigned to GOx and CP, respectively (Figure 4.6A). The chromatogram for GCK and CP incubation shows only one elution peak at 18 mL (Figure 4.6B) assigned to GCK and CP. These results indicate that non-functionalized enzymes do not get encapsulated in a measurable amount.

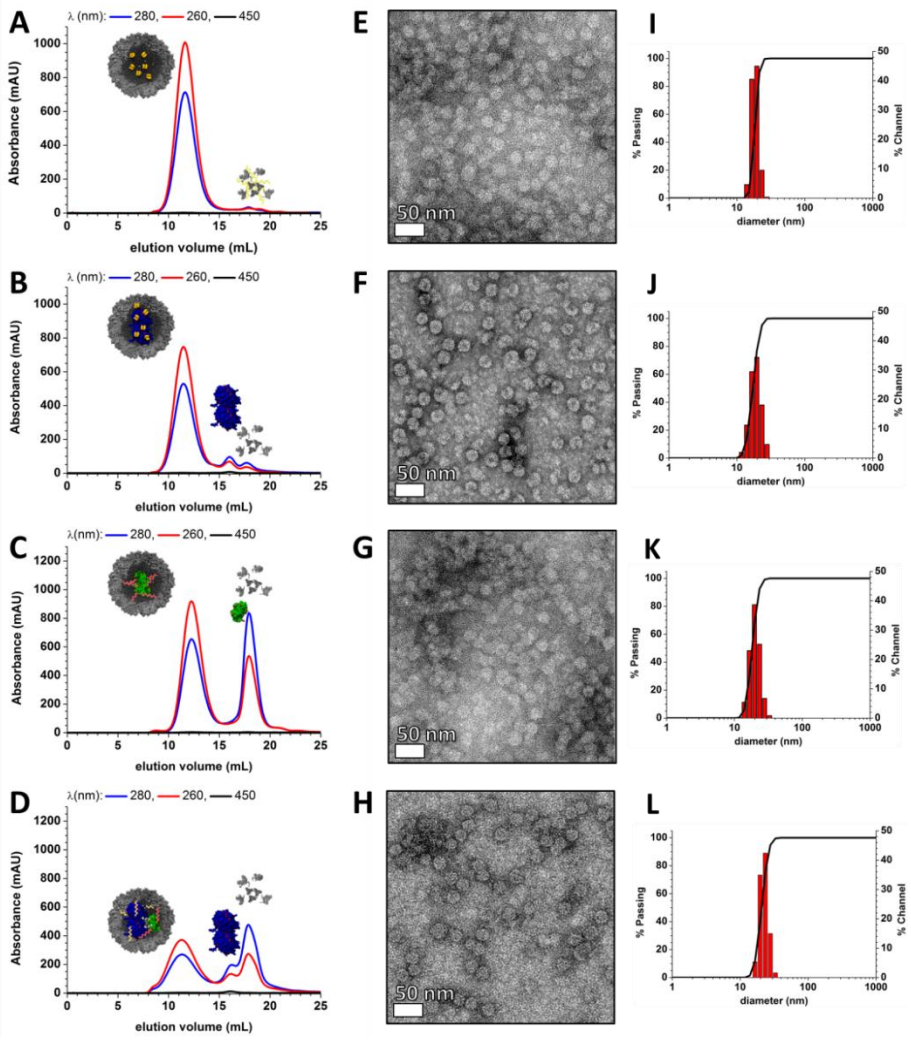

Figure 4.5. Characterization of encapsulated biocatalysts inside CCMV capsids by size-exclusion chromatography (SEC), transmission electron micrographs (TEM) and dynamic light scattering (DLS) of the corresponding purified materials. The eluting material was detected at λ = 280 nm, λ = 260 nm and λ = 450 nm, the strongest absorbance peaks representative for proteins, DNA and flavin molecules inside GOx, respectively. FPLC purification of intact CCMV capsids filled with (A) DNAzyme, (B) GOx-DNAzyme, (C) GCK-csDNA and (D) GOx-GCK eluting around 12 mL and their corresponding negatively stained transmission electron micrographs (E), (F), (G) and (H), respectively. Non-encapsulated GOx elutes at 16 mL and GCK together with CP at 18 mL. The DLS results confirm the intact CCMV capsids formation for (I) DNAzyme, (J) GOx-DNAzyme, (K) GCK-csDNA and (L) GOx-GCK, respectively.

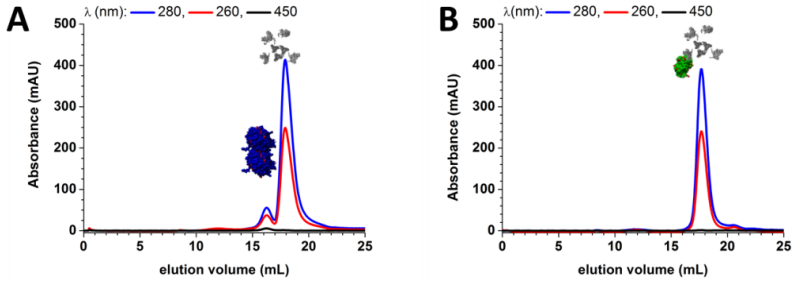

Figure 4.6. SEC-chromatograms of (A) a mixture of GOx and CP, eluting at 16 mL and 18 mL, respectively and (B) a mixture of GCK and CP, eluting both at 18 mL.

The concentrations of GOx, GCK and DNAzyme were estimated by UV-Vis spectroscopy, SDS-PAGE densitometry and western blot analysis (Appendix and Figure 4.7). For the western blot immunostaining, a mixture of primary antibodies against GOx and GCK was used. A HRP-linked secondary antibody was used to visualize the antibody binding by chemiluminescence. The analysis of the obtained images proved the co-existence of both enzymes GOx and GCK in GOx-GCK-hybrid filled VLPs, visualized by two bands, assigned to GOx and GCK, respectively and is illustrated in Figure 4.7A, lane D. These findings are supported by comparing the observed band with bands of further samples containing a mixture of non-functionalized GOx and non-functionalized, encapsulated GOx-DNAzyme or GCK-csDNA and a mixture of GOx-DNAzyme with GCK-csDNA (Figure 4.7A). Lane A showed two bands, where the upper band represents non-functionalized GOx (1 µM) and the lower non-functionalized GCK (1 µM). In lane B a single band is visible, assigned to GOx, since no other enzymes are present in this sample. Lane C shows a single band, which indicates the presence of GCK in the formed GCK-csDNA VLPs. The last sample, a mixture of both GOx-DNAzyme and GCK-csDNA, is represented in lane E and showed four bands. The upper indicates GOx and the lowest GCK, while the bands in the middle might refer to non-functionalized GOx, when compared to the band obtained for non-functionalized GOx and GCK-csDNA as previously observed for non-encapsulated GCK-csDNA analysis (Figure 4.3, lane B, left)). Another explanation for those bands might as well be different states of hybridization between GOx-DNAzyme and GCK-csDNA, since the excess of non-hybridized GCK-csDNA was successfully removed by repeated centrifugal filtration, as described in Section 4.2.1. The image of the western-blot analysis reveals further information about the ratio of the incorporated enzymes by comparing the band intensities. While an equal amount of GOx to GCK was achieved for the solution containing non-encapsulated and non-functionalized enzymes (lane A), a higher concentration of GOx-DNAzyme compared to GCK-csDNA is present in both, encapsulated (lane D) and non-encapsulated GOx-GCK-hybrid samples (lane E). The detection of CP by immunostaining was unsuccessful, since CP did not transfer from the SDS-PAGE gel to the polyvinylidene fluoride

(PVDF) membrane as illustrated by subsequently coomassie-staining of the SDS-PAGE gel. A single band around 20 kDa was detected characteristic for CP staying on the SDS-PAGE gel (Figure 4.7B).
In summary, the presented results show so far three different achievements. First, the successful functionalization of two enzymes, GOx and GCK, with a short DNA sequence of 21 nucleotides, second, the hybridization of those two enzymes into an enzyme complex GOx-GCK and third, the successful encapsulation of either GOx-DNAzyme-hybrid or GOx-GCK-hybrid into VLPs, driven by the DNA attached to the enzymes.

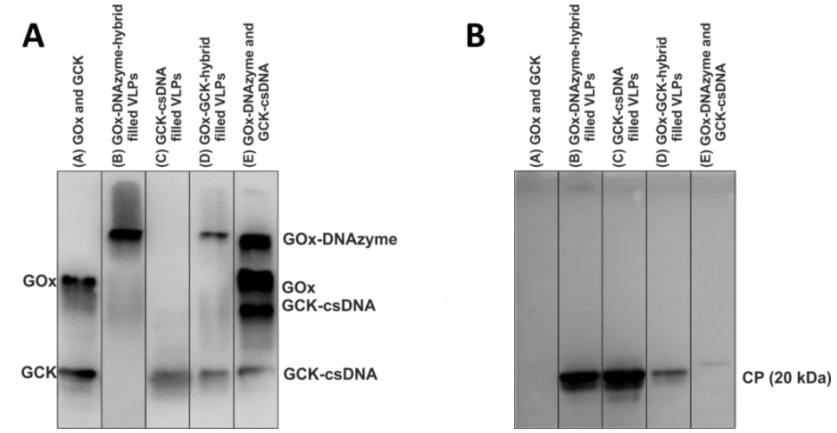

Figure 4.7. (A) western-blot with immunostaining by incubating the PVDF membrane first with a mixture of primary antibodies against GOx and GCK. The detection of the primary antibodies was realized by the incubation with HRP-linked secondary antibody, which catalyzes a chemiluminescent reaction. (B) Coomassie-staining of the SDS-PAGE gel after the transfer onto PVDF membrane, showing still CP.

4.2.3 Kinetics of encapsulated metabolic pathways

To prove the permeability of the capsid for the substrates involved in the metabolic pathway performed by the GOx-DNAzyme system, we encapsulated the DNAzyme while keeping the GOx in the outer medium. In this way, both H_2O_2 and ABTS must cross the capsid barrier to reach the DNAzyme and participate in the production of $ABTS^{\cdot-}$. In order to examine the effect of confinement on the reaction rate of this construction we measured the production of $ABTS^{\cdot-}$ in time for systems where either the DNAzyme or the full pathway composed of GOx-DNAzyme is confined. The apparent kinetic parameters, $K_{M,app.}$ and $V_{max,app.}$ were determined using Michaelis-Menten analysis. The system with confined DNAzyme showed similar $K_{M,app.}$ and $k_{cat,app.}$ values compared to the system with non-confined DNAzyme, indicating that neither the diffusion of the substrate nor the confinement influence the reaction rates. However, when the full pathway is confined, the $K_{M,app.}$ value increases by about a factor of 2, compared to non-

confined GOx-DNAzyme. This increase is most likely caused by the protein shell acting as a diffusion barrier for glucose. In addition, the apparent turn-over rate ($k_{cat,app.}$) of the confined GOx-DNAzyme system was twice as high as the $k_{cat,app.}$ of the non-confined system (Figure 4.8A). This can be expected because the frequency of collision with surrounding molecules is much higher under crowded conditions and these collisions favor the formation of product resulting in an enhancement of the forward reaction rate $k_{cat,app.}$.[36] There is the remaining question of whether the H_2O_2 is consumed faster at the interior than it can diffuse out of the capsid. To test this possibility, we added the enzyme catalase to a solution of encapsulated GOx-DNAzyme. We observed that the production of $ABTS^{-\cdot}$ was almost completely suppressed, which suggest that a large fraction of H_2O_2 can escape out of the capsid before it is consumed by the DNAzyme (Figure 9).
The excess of H_2O_2 can degrade the hemin and consequently inactivate the catalytic activity of the DNAzyme, which then results in a lower production of $ABTS^{-\cdot}$ and influences the $K_{M,app.}$ and $k_{cat,app}$ parameters.
To avoid this situation, we followed the formation of gluconolactone, a different product of GOx, by the action of two auxiliary enzymes (GCK and 6-PGDH), that eventually produce NADPH, which can be monitored spectroscopically. Both auxiliary enzymes possess high affinities to their substrates. The reported K_M value for GCK is 0.02 mM[37] and for 6-PGDH is 0.01 mM.[25] To test the permeability of the capsid for the product gluconolactone, we encapsulated GOx-DNA while keeping GCK and 6-PGDH in the bulk solution. In order for NADPH to form in this system, glucose must enter the protein cage and gluconolactone has to diffuse out (Figure 4.1B). We analyzed the kinetic parameters to study the influence of confined and crowded conditions on these encapsulated enzymes. The values of $K_{M.app.}$ and $k_{cat.app}$ for the encapsulated GOx-DNA system exceed the corresponding values for the non-confined GOx-DNA system by a factor of 3 and 2.6, respectively. Additionally, $K_{M,app.}$ and $k_{cat,app.}$ increase by a factor of 2 for non-confined GOx-DNA when compared to non-confined native GOx (Figure 4.8B). These results show that confined and crowded conditions improves the catalytic turn-over number but decrease the substrate affinity, which is most likely caused by the diffusion of the substrate through a crowded environment formed by multiple DNA tags around the enzyme and the interior of the protein shell itself. Furthermore, the effective concentration of enzymes and substances increases inside the confinement of a protein cage and therefore the kinetics change, likely due to more collision events. To study the influence of a crowded environment on the kinetics, we reduced the amount of DNA-tags coupled to the enzymes. Subsequently, the kinetics of three different systems were studied, 1) confined GCK-csDNA in the presence of non-confined GOx and 6-PGDH, 2) confined GOx-DNA in the presence of non-confined GCK and 6-PGDH and 3) confined GOx in the presence of confined GCK and non-confined 6-PGDH.

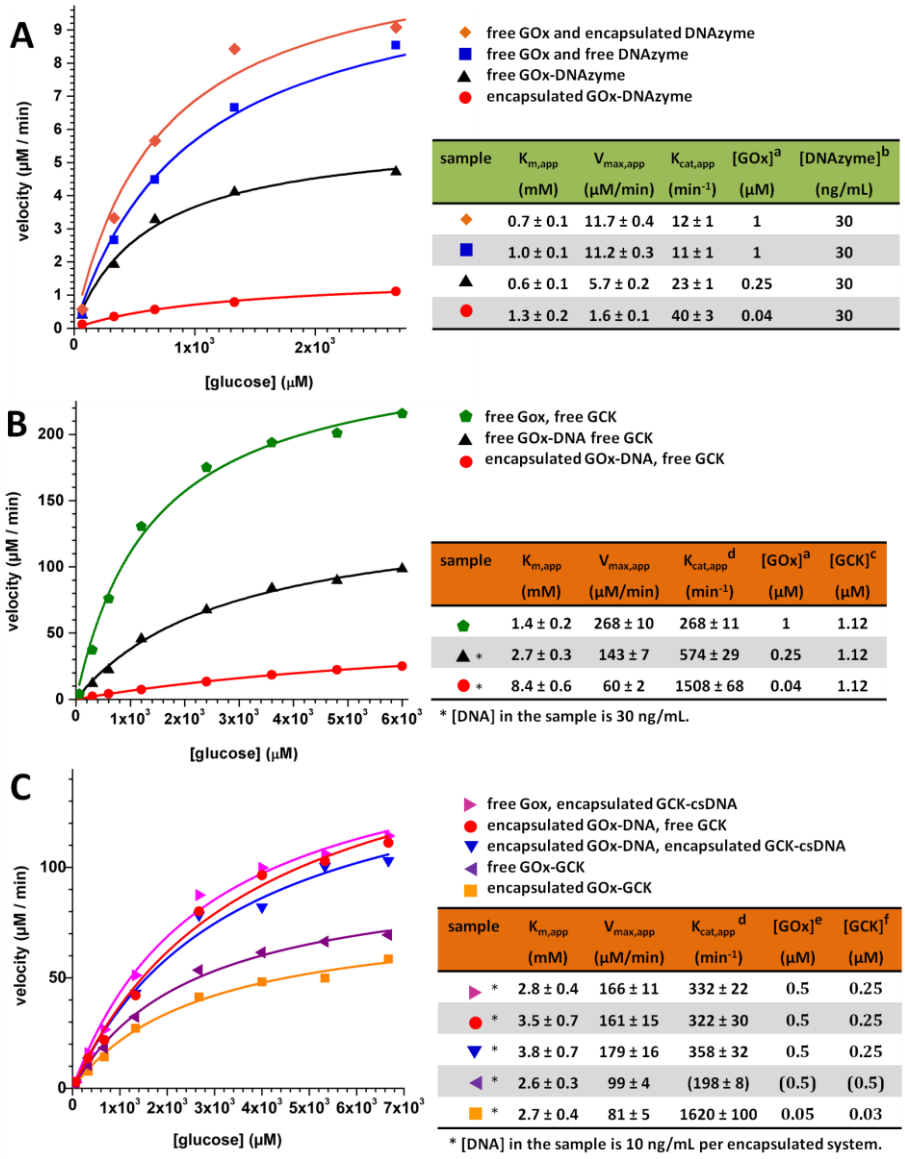

sample	$K_{m,app}$ (mM)	$V_{max,app}$ (μM/min)	$K_{cat,app}$ (min^{-1})	[GOx][a] (μM)	[DNAzyme][b] (ng/mL)
◆	0.7 ± 0.1	11.7 ± 0.4	12 ± 1	1	30
■	1.0 ± 0.1	11.2 ± 0.3	11 ± 1	1	30
▲	0.6 ± 0.1	5.7 ± 0.2	23 ± 1	0.25	30
●	1.3 ± 0.2	1.6 ± 0.1	40 ± 3	0.04	30

sample	$K_{m,app}$ (mM)	$V_{max,app}$ (μM/min)	$K_{cat,app}$[d] (min^{-1})	[GOx][a] (μM)	[GCK][c] (μM)
⬟	1.4 ± 0.2	268 ± 10	268 ± 11	1	1.12
▲ *	2.7 ± 0.3	143 ± 7	574 ± 29	0.25	1.12
● *	8.4 ± 0.6	60 ± 2	1508 ± 68	0.04	1.12

* [DNA] in the sample is 30 ng/mL.

sample	$K_{m,app}$ (mM)	$V_{max,app}$ (μM/min)	$K_{cat,app}$[d] (min^{-1})	[GOx][e] (μM)	[GCK][f] (μM)
▶ *	2.8 ± 0.4	166 ± 11	332 ± 22	0.5	0.25
● *	3.5 ± 0.7	161 ± 15	322 ± 30	0.5	0.25
▼ *	3.8 ± 0.7	179 ± 16	358 ± 32	0.5	0.25
◀ *	2.6 ± 0.3	99 ± 4	(198 ± 8)	(0.5)	(0.5)
■ *	2.7 ± 0.4	81 ± 5	1620 ± 100	0.05	0.03

* [DNA] in the sample is 10 ng/mL per encapsulated system.

Figure 4.8. Kinetics of glucose conversion measured by either ABTS and/or NADPH in the presence of CCMV capsid filled with one enzyme or two different enzymes, which are involved in the metabolic pathway of glucose. Solid curves show the best fit using the Michaelis-Menten equation. The apparent parameters for KM, Vmax and kcat are shown in the table beside the plots. The concentrations of GOx and DNAzyme were estimated by UV-Vis spectroscopy,a,b SDS-PAGE densitometry analysisa and western blot.e,f The Kcat,app. is calculated using [GOx] values.d (A) Kinetics of glucose conversions measured by ABTS assay in the presence of free GOx and encapsulated DNAzyme (◆), free GOx and free DNAzyme (■), free GOx-DNAzyme (▲) or encapsulated GOx-DNAzyme (●). (B) Kinetics of glucose conversions measured by NADPH assay in the presence of free GOx (⬟), free GOx-DNAzyme (▲) or encapsulated GOx-DNAzyme (●). (C) Kinetics of glucose conversions measured by NADPH assay in the presence of free GOx and encapsulated GCK-csDNA (▶), encapsulated GOx-DNA and free GCK (●), encapsulated GOx-DNA and encapsulated GCK-csDNA (▼), free GOx-GCK (◀) or encapsulated GOx-GCK (■).

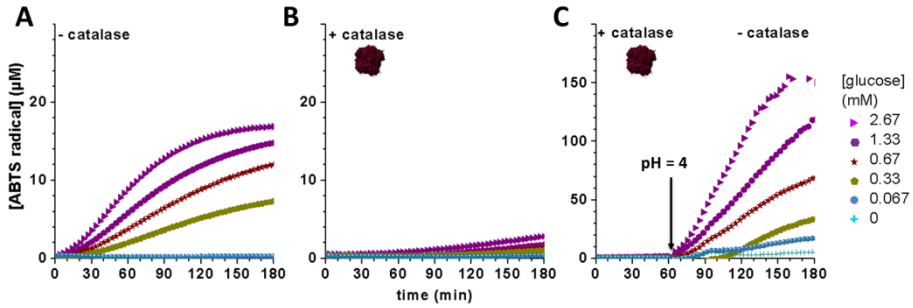

Figure 4.9. Monitoring the formation of ABTS radical at λ = 410 nm over 3h as a result of the production of H_2O_2 at different glucose concentration catalyzed by encapsulated GOx-DNAzyme. (A) Consumption of H_2O_2 at the capsid interior by the DNAzyme, which catalyzes the oxidation of $ABTS^{2-}$ into ABTS radical. (B) Consumption of H_2O_2 at the capsid exterior by catalase. (C) Consumption of H_2O_2 by the internal DNAzyme after inactivation of the external catalase, by reducing the pH from 7.5 to pH 5.

In all these systems the substrate for either GOx or GCK must penetrate through the capsid shell to get converted at the interior of the capsid while the resulting product must escape out to be available for the next enzyme in the cascade reaction. The $K_{M,app.}$ and $k_{cat,app.}$ values for all three systems are quite similar to each other (Figure 4.8C). However, the $K_{M,app.}$ and $k_{cat,app}$ of the GOx-DNA confined system , which presents a larger amount of DNA tags per GOx, (Figure 4.8B) are 2.4 and 4.6 times lower, respectively. This shows that a crowded medium indeed influences the diffusion of the substrates and consequently the kinetic parameters. Finally, we encapsulated both enzymes GOx-GCK inside CCMV-capsid, while keeping the third enzyme, 6-PGDH, in the bulk medium. This experiment allowed us to investigate if the productivity of a confined metabolic pathway increases when the distance between the enzymes is minimized. The $K_{M,app.}$ was found to be similar, whereas $k_{cat,app.}$ was found to be about 5-times higher when compared to the results obtained for the confined single enzymes systems, functionalized with a minimum amount of DNA-tags (Figure 4.8C). These results confirm that a reduced distance between two enzymes of the same metabolic cascade, realized by confinement, indeed enhances the productivity. This can be explained by direct consumption of the intermediate of the first enzymes by the second enzyme without crossing the capsid shell, which otherwise would influence the kinetics as shown earlier. Moreover, the confinement causes a higher effective concentration of substrates, intermediates and enzymes resulting in presumably more collisions between them and favors the formation of product resulting in an enhanced forward reaction rate, which has been seen before for the GOx-DNAzyme pathway involving the ABTS production.

4.3 Conclusions

The controlled encapsulation of two different enzyme cascades, GOx-DNAzyme and GOx-GCK, inside virus-like capsids is reported. These capsids filled with enzymes involved in a enzymatic pathway serve as a model system for cellular microcompartments. The formation of either ABTS radicals or NADPH prove not only that the enzymes are active at the interior of CCMV-capsids but also that all substrates, intermediates and products involved in the metabolic pathway can diffuse freely in an out. The small volume of CCMV-capsids leads to a higher effective concentration of enzymes and substrates, enhancing their productivity compared to non-confined enzyme cascades. The capsids shell and the DNA-tags, which are attached to the enzymes, represent a diffusion barrier, which affects the substrate binding affinity but does not retain substrates, metabolic intermediates nor products at the interior, and these observations differs from results reported for BMCs. By decreasing the amount of DNA-tags attached to the enzymes, the binding affinity for the substrate was increased, proving the influence of crowded environments towards kinetic parameters. The enzymatic pathway benefits from compartmentalization, because the confinement of the enzymes and their substrates results not only in an increase in their local concentrations but also in the ability to consume the metabolic intermediates before they escape through the protein barrier into the outer medium. This might lower the presence of toxic intermediates in the bulk solution. Interfering or competing pathways can be avoided when metabolic intermediates are consumed at the capsid interior. Consequently, confining metabolic pathways into microcompartments by using chemical or engineered based methods might improve the performance of pathways and may provide fundamental information about the efficiency of metabolic reactions inside living cells as well as the need of confinement. Moreover, we demonstrated an effective strategy of using complementary ssDNA for the controlled encapsulation of two enzymes in virus-like assemblies.

4.4 Acknowledgments

Rindia Maharani Putri, M.Sc is gratefully acknowledged for her consistent and reliable work, for fruitful discussions and support, without her input it would not be possible to achieve such a huge amount of data in such short time. Dr. Alberto Gomez-Casado is also gratefully acknowledged for voluntary fruitful discussions, explanations and advices in the interpretations of some results.

4.5 Experimental

4.5.1 Materials

The bifunctional cross-linker sulfo-EMCS (N-[ε-maleimidocaproyloxy] sulfosuccinimide ester) was purchased from Pierce. Oligonucleotides were synthesized by eurofins MWG Operaton. The sequences of the oligomers are for the DNAzyme: 5'-HS-$(CH2)_6$-GGGTAGGGCGGGTTGGGTTTT-3' and for the csDNA: 5'-HS-$(CH2)_6$-AAAACCCAACCCGCCCTACCC-3'. D-Gluconate/D-Glucono-δ-lactone assay was purchased from Megazyme and contain amongst others the following chemicals: nicotinamide-adenine dinucleotide phosphate ($NADP^+$), adenosine-5'-triphosphate (ATP), gluconate kinase (GCK) and 6-phosphogluconate dehydrogenase (6-PGDH). All other chemicals, including glucose oxidase (GOx from *Aspergillus niger*), catalase (from bovine liver), ABTS (2,2′-Azino-bis(3-ethylbenzothiazoline-6-sulfonic acid) diammonium salt), PBS buffer (phosphate buffered saline (0.138 M NaCl, 0.0027 M KCl, pH 7.4)), salts and solvents were purchased from Sigma-Aldrich or Fluka and used as received unless explicitly noted. A hemin (5 mM) stock solution was prepared in DMSO and stored in the dark at 4 °C. The substrates (glucose, mannose, galactose, ABTS and catalase) were dissolved in 50 mM Tris-HCl buffer containing 100 mM KCl at pH 7.5. Gel loading dye (6x) from BioLabs New England contains 2.5 % Ficoll 400, 11 mM EDTA, 3.3 mM Tris-HCl, 0.017 % SDS, 0.015 % bromophenol blue, pH 8.0. The purification and characterization of the Cowpea Chlorotic Mottle Virus (CCMV), the removal of its RNA and the isolation of the coat protein (CP) were carried out according to literature procedures.[18] Water was purified and deionized (MQ water, resistivity of 18.2 $M\Omega cm^{-1}$). The buffer was adjusted with 1 M NaOH or 5 mM HCl to the desired pH. All reactions were carried out at room temperature unless stated otherwise.

4.5.2 Methods

Size-exclusion chromatography (SEC):

SEC was performed using GE Healthcare FPLC Äkta purifier 900 combined with fraction collector Frac-950. Samples were purified over a preparative column

superose 6 10/100 GL (GE Healthcare) with a 24 mL bed volume. Samples were injected over a 500 µL injection loop.

Transmission Electron Microscopy (TEM):
The samples were examined in an analytical FEG-TEM (Phillips CM 30) operated at 300 kV acceleration voltages. For the sample preparation 5 µL of the desired sample were applied onto Formvar-carbon coated grids. After 1 min, the excess of liquid was drained using a piece of filter paper. Uranyl acetate (5 µL, 1% w/v) was added and the excess of liquid was drained after 20 sec. The grid was dried for 30 min at room temperature.

UV-Vis spectroscopy:
UV-Vis spectra were recorded on a Varian Cary 300 UV-Vis spectrometer by using a quartz cuvette with 3 mm path length. Absorbance measurements related to ABTS or Gluconic-acid assays were performed in a 96 well plate (greiner, flat-bottom, transparent) using a Tecan i-control infinite 200 PRO microplate reader.

SDS-PAGE:
Samples (10 µL) were mixed with 2x samples buffer (10 µL, 125 mM Tris-HCl, 20% (v/v) glycerol, 5% SDS, 0.02% bromophenol blue, pH 6.8 and 10% β-mercaptoethanol) and heated at 99 °C for 10 min. Samples were separated on a SDS-Page gel containing 6% stacking gel and a 12% resolving gel using a constant current of 100 V for approximately 2 h. Gels were stained with coomassie blue or silver staining. Images were taken on a ISOGEN Life Science ULTIMA 10 si instrument and imaged using ProXima AQ-4 software.

Agarose gel:
A 20 µl aliquot of sample was mixed with 4 µL gel loading dye and loaded into a 1% agarose gel (w/v) in electrophoresis buffer (40 mM Tris, 20 mM acetic acid, 1 mM EDTA, pH 7.6). The samples were electrophoresed at 4 °C for 90 min at 80 V in a horizontal gel apparatus (peolab). The samples were then stained in a Bio-safe™ Coomassie G-250 stain solution and visualized on a ISOGEN Life Science ULTIMA 10 si instrument and imaged using ProXima AQ-4 software.

Western blot:
The specific antibodys for GOx and GCK are commercially available. GCK rabbit antibody was obtained from NeoCorp and glucose oxidase antibody from ScienceVision. Both antibodies were diluted 5000 times. The assay were performed as commonly described in literature, for example online by CHEMICON INTERNATIONAL, Introduction to antibodies 2nd edition.

Preparation of GOx-DNAzyme-hybrid:
DNA (100 µM) was dissolved in PBS (10 mM, pH 7.4) containing additional DTT (2 mM). The solution was incubated for 3 h at RT to reduce any disulfide groups to thiol groups. The excess of DTT was removed by exchanging the solution 6 times against PBS buffer using Amicon Ultra centrifugal filters (10K MWCO). To test if all DTT was successfully removed, 20 µL Ni(II)-sulfate (100 µM) were added to 10 µL filtrate, a transparent color indicates a DTT free solution, whereas a brown-yellow color indicates DTT contamination, in which case the exchanging of PBS was repeated. To prepare a cross-linker modified GOx, a solution of GOx (2 µM) and sulfo-EMCS (100 µM) in PBS (10 mM, pH 7.4) was incubated for 1 h at RT. The excess of sulfo-EMCS was removed by exchanging the solution 5 times against PBS buffer using Amicon Ultra centrifugal filters (30K MWCO). Modified GOx (2 µM) was mixed with thiolated-DNAyzme (100 µM) in a 2:1 (v/v) ratio and incubated for 1 h at RT (stored at 4 °C overnight, if necessary). The excess of DNA was removed by exchanging the solution 6 times against PBS buffer using Amicon Ultra centrifugal filters (30K MWCO). The filtrates were tested for DNA contamination by measuring the specific UV-Vis absorbance for DNA at λ = 260 nm. Only if no signal at λ = 260 nm was observed the removal of uncoupled DNAzyme was completed. Before the GOx-DNAzyme was used for further experiments, the PBS buffer was exchanged against Tris-HCl buffer (50 mM, NaCl (100 mM), $MgCl_2$ (10 mM), DTT (0.2 mM), pH 7.5).

Preparation of GCK-csDNA:
csDNA (100 µM) was dissolved in PBS (10 mM, pH 7.4) containing additional DTT (2 mM). The solution was incubated for 3 h at RT to reduce any disulfide groups to thiol groups. The excess of DTT was removed by exchanging the solution 6x against PBS buffer using Amicon Ultra centrifugal filters (10K MWCO). To test if all DTT was successfully removed, 20 µL Ni(II)-sulfate (100 µM) were added to 10 µL filtrate, a transparent color indicates a DTT free solution, whereas a brown-yellow color indicates DTT contamination, in which case the exchanging of PBS was repeated. To prepare a cross-linker modified GCK, a solution of GCK (1 mL) and sulfo-EMCS (100 µM) in PBS (10 mM, pH 7.4) was incubated for 1 h at RT. The excess of sulfo-EMCS was removed by exchanging the solution 5 times against PBS buffer using Amicon Ultra centrifugal filters (30K MWCO). Modified GCK was mixed with thiolated-DNAyzme (100 µM) in a 2:1 (v/v) ratio and incubated for 1 h at RT (stored at 4 °C overnight, if necessary). The excess of DNA was removed by exchanging the solution 6x against PBS buffer using Amicon Ultra centrifugal filters (30K MWCO). The filtrates were tested for DNA contamination by measuring the specific UV-Vis absorbance for DNA at λ = 260 nm. Only if no signal at λ = 260 nm was observed the removal of uncoupled csDNA was completed. Before the GCK-

csDNA was used for further experiments, the PBS buffer was exchanged against Tris-HCl buffer (50 mM, NaCl (100 mM), $MgCl_2$ (10 mM), DTT (0.2 mM), pH 7.5).

Preparation of GOx-GCK-hybrid:
Purified GOx-DNAzyme and GCK-csDNA were mixed in a 1 : 1 (v/v) ratio and incubated at 27 °C for 1h and subsequently cooled down to 20 °C to induce hybridization between the two complementary DNA strands. The excess of GCK-csDNA was removed by repetitive centrifugal filtration using Amicon Ultra centrifugal filter (50K MWCO). The successful removal of excess of GCK-csDNA or non-functionalized GCK was followed by absorbance measurements at 280 nm. Only when no signal at 260 nm in the filtration was observed the purification was finished and the supernatant used for further experiments. Before the GOx-GCK-hybrid was used for further experiments, the PBS buffer was exchanged against Tris-HCl buffer (50 mM, NaCl (100 mM), $MgCl_2$ (10 mM), DTT (0.2 mM), pH 7.5).

Encapsulated DNAzyme, GOx-DNAzyme, GCK-csDNA and GOx-GCK in virus-like particles (VLPs):
Capsid protein was dialyzed against assembly buffer (Tris-HCl (250 mM), NaCl (500 mM), $MgCl_2$ (50 mM), DTT (1 mM) pH 7.5) to obtain dimeric coat proteins (CP) (500 µM). In order to encapsulate DNAzyme, GOx-DNAzyme, GCK-csDNA and GOx-GCK into VPLs, the PBS buffers of DNAzyme, GOx-DNAzyme, GCK-csDNA and GOx-GCK were exchanged against MQ using Amicon Ultra centrifugal filters (30K or 10K MWCO) before DNAzyme, GOx-DNAzyme, GCK-csDNA and GOx-GCK and CP (assembly buffer) were mixed in a 4:1 (v/v) ratio and incubated for 2h at 4 °C. DNAzyme, GOx-DNAzyme, GCK-csDNA and GOx-GCK loaded VLPs were then purified by size-exclusion chromatography (SEC) over a superose 6 10/100 GL (GE Healthcare) column with 24 mL bed volume and 500 µL injection volume at RT. A 5x diluted assembly buffer was used as elution buffer (Tris-HCl (50 mM), NaCl (100 mM), $MgCl_2$ (10 mM), DTT (0.5 mM) pH 7.5). The GOx-DNA loaded VLPs as well as the DNAzyme loaded VLPs were eluted at 12.5 mL by a flow rate of 0.8 mL/min. Fractions corresponding to DNAzyme, GOx-DNAzyme, GCK-csDNA and GOx-GCK loaded VLPs were combined and used for analysis by SDS-Page, Agarose and Western blot as well as for further experiments, such as kinetic studies in nanoconfinement.

Kinetic data of free or encapsulated coupled and non-coupled GOx-DNAzymes in the presence or absence of catalase: ABTS assay
Substrate solutions containing various substrates concentrations (0-1 M of glucose, mannose or galactose) and ABTS (4 mM) or ABTS (4 mM) / catalase (10 µM) were incubated for 3 h at RT. Separately, four different enzyme solutions were prepared and incubated at RT for 2 h. The enzyme solution contains either (1) free

GOx-DNAzyme (30 µL), (2) encapsulated GOx-DNAzyme (30 µL) and hemin (30 µL, 5 µM) or (3) free DNAzyme (30 µL), (4) encapsulated DNAzyme (30 µL), GOx (15 µL, 1 µM) and hemin (15 µL, 10 µM). The reaction was started by adding 120 µL of substrate to 60 µL enzyme solution. Fast after initiation, the conversion of ABTS to $ABTS^{\cdot+}$ radical cation was followed by recording the absorbance at λ = 410 nm in intervals of 100 sec at 27 °C over 2 h. The activity of free and encapsulated GOx-DNAzyme were tested for all three substrates, whereas the activity of free and encapsulated DNAzyme in the presence of GOx were only tested for glucose as substrate. Additionally, the activities of all four enzymes solutions, which contained glucose as substrate, were tested in the presence of catalase. All experiments were compared with a control experiment (background) composed of the same volume of hemin, substrate solutions, ABTS or ABTS/catalase.

Reactivation of free or encapsulated coupled and non-coupled GOx-DNAzymes in the presents of catalase: ABTS assay

Substrate solutions containing various glucose concentrations (0-1 M) and ABTS (4 mM) or ABTS (4 mM) / catalase (10 µM) were incubated for 3 h at RT. Separately, two different enzyme solutions were prepared and incubated at RT for 2 h. The enzyme solution contains either (1) free GOx-DNAzyme (30 µL) or (2) encapsulated GOx-DNAzyme (30 µL) with hemin (30 µL, 5 µM). The reaction was started by adding 120 µL of substrate to 60 µL enzyme solution. Immediately after initiation, the conversion of ABTS to $ABTS^{\cdot+}$ radical cation was followed by recording the absorbance at λ = 410 nm in intervals of 100 seconds at 27 °C over 1 h. Catalase containing samples do not show any signal at λ = 410 nm, because most of the produced H_2O_2 is consumed by the catalase and is no longer available for the DNAzyme. In order to inactivate the catalase the pH of the assay was droped to pH 3-4 by adding a few drops of gluconic acid solution (2 M) after 1h recording. The pH of the used gluconic acid solution was adjusted before with acetic acid to pH 2-3. After the inactivation of catalase the conversion of ABTS to $ABTS^{\cdot+}$ radical cation was followed for 2 h longer. All experiments were compared with a control experiment (background) composed of the same volume of hemin, substrate solutions, ABTS or ABTS/catalase.

Kinetic data of free or encapsulated coupled and non-coupled GOx-DNAzymes: Gluconic-acid assay.

Substrate solutions, containing various glucose concentrations (0-1 M, 180 µl) and 3 µL GCK (365 U/ml) were prepared. Separately, four different enzyme solutions were prepared and incubated at RT for 2h. The enzyme solution contains either (1) free GOx-DNAzyme (30 µL), (2) encapsulated GOx-DNAzyme (30 µL) and hemin (30 µL, 5 µM) or (3) free DNAzyme (30 µL), (4) encapsulated DNAzyme (30 µL), GOx (15 µL, 1 µM) and hemin (15 µL, 10 µM). Additionally 2 µL 6-PGDH (55 U/mL) and 20 µl of a solution containing $NADP^+$ (16.1 mM) and ATP (69.4 mM) at pH 7.5

were added to all enzyme solution. The reaction was started by adding 120 µL of substrate solution to 82 µL enzyme solution. Immediately after initiation, the formation of reduced NADPH was followed by recording the absorbance at λ = 340 nm in intervals of 100 sec at 27 °C. All experiments were compared with a control experiment (background) composed of the same volume of hemin and substrate solutions.

Kinetic data of free or encapsulated coupled and non-coupled GOx-GCK: Gluconic-acid assay.

Substrate solutions containing various glucose concentrations (0-1 M, 180 µL) were prepared. Separately, six different enzyme solutions were prepared and incubated at RT for 2 h. The enzyme solution contains either (1) free GOx-GCK (60 µL), (2) encapsulated GOx-GCK (60 µL), (3) free GOx (30 µL) and free GCK (30 µL), (4) encapsulated GOx (30 µL) and encapsulated GCK (30 µL), (5) free GOx (30 µL) and encapsulated GCK (30 µL) and (6) encapsulated GOx (30 µL) and free GOx (30 µL). Additionally 2 µl 6-PGDH (55 U/mL) and 20 µL of a solution containing $NADP^+$ (16.1 mM) and ATP (69.4 mM) at pH 7.5 were added to all enzyme solution. The reaction was started by adding 120 µL of substrate solution to 82 µL enzyme aolution. Immediately after initiation, the formation of reduced NADPH was followed by recording the absorbance at λ = 340 nm in intervals of 100 sec at 27 °C. All experiments were compared with a control experiment (background) composed of the same volume of hemin and substrate solutions.

Data treatment

First, the corresponding control experiments were subtracted from the raw data of the experiments. Second, the absorbance values of $ABTS^{\cdot+}$ (λ = 410 nm) or NADPH (λ = 340 nm) were converted into concentration values of $ABTS^{\cdot+}$ or NADPH and plotted against the time and last, the velocity (v (µM/min)) was determined. Therefore, the plots ([$ABTS^{\cdot+}$ or NADPH] vs. time were first smoothed by using the Savitzky-Golay method and then differentiated to identify the slope maxima representing the velocity value. The velocity values were multiplied by a dilution factor (DF) related to the enzyme (GOx) as well as with a proportionality factor (p) of ABTS to substrate consumption. The corrected modified velocity data were then used to determine the kinetic parameters (maximum velocity ($V_{max,app}$) and apparent Michaelis-Menten constant, ($K_{m,app}$)), both by direct fits of Michaelis-Menten equation and by Eadie-Hoftsee plot using OriginPro 8.6 software (OriginLab Corp. Northampton, MA, USA) which does linear and nonlinear regression. The catalytic constant ($k_{cat,app}$) was determined by dividing $V_{max,app}$ with the enzyme concentration [E]. The enzyme concentration was estimated by SDS-PAGE and UV-Vis spectroscopy.

Example of $V_{max,app}$, $K_{m,app}$ and $k_{cat,app}$ calculations:

(1) Concentration (µM): Abs($ABTS^{\cdot+}$ or NADPH) = c · d · ε

ε: extinction coefficients of $ABTS^{\cdot+}$ (ε_{410nm} = 36000 $M^{-1} \cdot cm^{-1}$) or NADPH (ε_{340nm} = 6300 $M^{-1} \cdot cm^{-1}$)[2] , Abs: absorbance of $ABTS^{\cdot+}$ or of NADPH, d: 0.5 cm path length of filled well-plate.

(2) Velocity (µM/min): y-axis: [$ABTS^{\cdot+}$ or NADPH]; x-axis: time

velocity (ν (µM/min)): [$ABTS^{\cdot+}$ (µM) or NADPH (µM)] = ν (µM/min) · time (min)

(3) Taking dilution factors (DF) of enzyme (GOx) and proportionality (p) of substrates into consideration: v_0 (µM/min) = ν (µM/min) · DF · p ;

$$(v = -\frac{d[Glu]}{dt} = \frac{1}{2}\,\frac{d[ABTS]}{dt}\ or\ \frac{d[ABTS]}{dt})$$

(4) Plot to determine $V_{max,app}$ *and* $K_{m,app}$*:* v_0 (µM/min) vs. [substrate] (µM)

(5) Fitting of data set with non-linear curve fit (Michaelis-Menten equation):

$v_0 = \frac{V_{max,app} \cdot [S]}{K_{m,app} + [S]}$; with $K_{m,app}$ (µM) and $V_{max,app}$ (µM/min)

(6) $k_{cat,app}$ (1/min) = $V_{max,app}$ (µM/min) / [GOx] (µM)

4.6 Appendix

4.6.1 Appendix: Determining the GOx concentration in GOx-DNAzyme

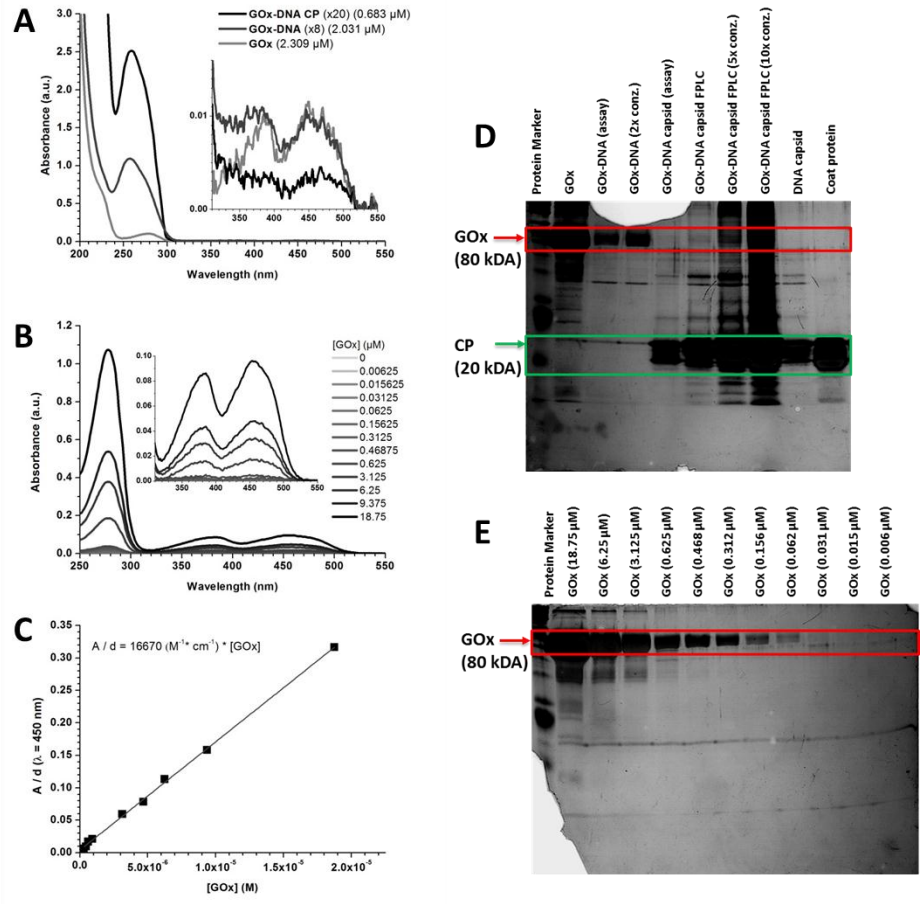

Appendix. Estimation of the overall GOx concentration by UV-Vis spectroscopy for GOx, GOx-DNA and GOx-DNA filled VLPs (A) with calibration line for GOx (B and C) and by SDS-PAGE densitometry for GOx, GOx-DNA and GOx-DNA filled VLPs (D) with calibration line for GOx (E).

4.7 References

1. M. Sutter, D. Boehringer, S. Gutmann, S. Gunther, D. Prangishvili, M. Loessner, K. Stetter, E. Weber-Ban and N. Ban, *Nat Struct Mol Biol*, 2008, 15, 939 - 947.
2. C. Wang, Z. H. Sheng, J. Ouyang, J. J. Xu, H. Y. Chen and X. H. Xia, *Chem Phys Chem*, 2012, 13, 762-768.
3. S. Cheng, Y. Liu, C. S. Crowley, T. O. Yeates and T. A. Bobik, *Bioessays*, 2008, 30, 1084-1095.
4. J. L. Corchero and J. Cedano, *Microb Cell Fact*, 2011, 10, 92.
5. S. Frank, A. D. Lawrence, M. B. Prentice and M. J. Warren, *J Biotechnol,* 2013, 163, 273-279.
6. G. Cannon, C. Bradburne, H. Aldrich, S. Baker, S. Heinhorst and J. Shively, *Appl Environ Microbiol*, 2001, 67, 5351 - 5361.
7. D. D. Sriramulu, M. Liang, D. Hernandez-Romero, E. Raux-Deery, H. Lunsdorf, J. B. Parsons, M. J. Warren and M. B. Prentice, *J Bacteriol*, 2008, 190, 4559-4567.
8. C. M. Agapakis, P. M. Boyle and P. A. Silver, *Nat Chem Biol*, 2012, 8, 527-535.
9. F. Mayer, *FEMS Microbiol Rev*, 1993, 10, 327-345.
10. D. P. Patterson, P. E. Prevelige and T. Douglas, *ACS Nano*, 2012, 6, 5000-5009.
11. I. J. Minten, V. I. Claessen, K. Blank, A. E. Rowan, R. J. M. Nolte and J. J. L. M. Cornelissen, *Chem Sci*, 2011, 2, 358-362.
12. S. A. Bode, I. J. Minten, R. J. M. Nolte and J. J. L. M. Cornelissen, *Nanoscale*, 2011, 3, 2376-2389.
13. J. D. Fiedler, S. D. Brown, J. L. Lau and M. G. Finn, *Angew Chem Int Ed*, 2010, 49, 9648-9651.
14. J. E. Glasgow, S. L. Capehart, M. B. Francis and D. Tullman-Ercek, *ACS Nano*, 2012, 6, 8658-8664.
15. R. J. Conrado, T. J. Mansell, J. D. Varner and M. P. DeLisa, *Metab Eng*, 2007, 9, 355-363.
16. K. Renggli, P. Baumann, K. Langowska, O. Onaca, N. Bruns and W. Meier, *Adv Funct Mater*, 2011, 21, 1241-1259.
17. L. Lavelle, J.-P. Michel and M. Gingery, *J Virol Methods*, 2007, 146, 311-316.
18. F. D. Sikkema, M. Comellas-Aragones, R. G. Fokkink, B. J. Verduin, J. J. L. M. Cornelissen and R. J. M. Nolte, *Org Biomol Chem*, 2007, 5, 54-57.
19. M. Brasch, A. de la Escosura, Y. Ma, C. Uetrecht, A. J. R. Heck, T. Torres and J. J. L. M. Cornelissen, *J Am Chem Soc*, 2011, 133, 6878-6881.
20. D. Willits, X. Zhao, N. Olson, T. S. Baker, A. Zlotnick, J. E. Johnson, T. Douglas and M. J. Young, *Virology*, 2003, 306, 280-288.

21. D. Lindberg, M. de la Fuente Revenga and M. Widersten, *Biochemistry*, 2010, 49, 2297-2304.
22. M. De Angelis, M. Calasso, R. Di Cagno, S. Siragusa, F. Minervini and M. Gobbetti, *J Appl Microbiol*, 2010, 109, 1763-1774.
23. R. Wilson and A. P. F. Turner, *Biosens Bioelectron*, 1992, 7, 165-185.
24. M. Zhang, H. Li, M. Deng, X. Weng, H. Ma, S. Feng, Y. Zhou and X. Zhou, *Chem Biodivers*, 2012, 9, 170-180.
25. T. Li, S. Dong and E. Wang, *Chem Asian J*, 2009, 4, 918-922.
26. S. M. Jia, X. F. Liu, D. M. Kong and H. X. Shen, *Biosens Bioelectron*, 2012, 35, 407-412.
27. Y. Yuan, R. Yuan, Y. Chai, Y. Zhuo, X. Ye, X. Gan and L. Bai, *Chem Commun* 2012, 48, 4621-4623.
28. X. Yang, C. Fang, H. Mei, T. Chang, Z. Cao and D. Shangguan, *Chem Eur J*, 2011, 17, 14475-14484.
29. B. Rauch, J. Pahlke, P. Schweiger and U. Deppenmeier, *Appl Microbiol Biotechnol*, 2010, 88, 711-718.
30. X. Cetó, F. Céspedes, J. Capdevila and M. del Valle, *Talanta*, 2011, 85, 1207-1212.
31. L. Kraft, G. A. Sprenger and Y. Lindqvist, *J Mol Biol*, 2002, 318, 1057-1069.
32. Z. Zhu, C. Momeu, M. Zakhartsev and U. Schwaneberg, *Biosens Bioelectron*, 2006, 21, 2046-2051.
33. M. You, R. W. Wang, X. Zhang, Y. Chen, K. Wang, L. Peng and W. Tan, *ACS Nano*, 2011, 5, 10090-10095.
34. B. Shlyahovsky, D. Li, E. Katz and I. Willner, *Biosens Bioelectron*, 2007, 22, 2570-2576.
35. J. E. Johnson and J. A. Speir, *J Mol Biol*, 1997, 269, 665-675.
36. M. G. S. Norris and N. Malys, *Biochem Biophys Res Commun*, 2011, 405, 388-392.
37. H. Izu, O. Adachi and M. Yamada, *FEBS Lett*, 1996, 394, 14-16.

Chapter 5

Molecular Weight Sensitive Encapsulation of a Conjugated Polyelectrolyte in Virus-like Protein Structures

In this chapter the encapsulation of a conjugated polyelectrolyte poly[(2-methoxy-5-propyloxy sulfonate)-phenyl-ene vinylene] (MPS-PPV) into Cowpea Chlorotic Mottle Virus (CCMV) capsids is studied. To achieve maximal shielding of the polymer from the outer environment CCMV coat proteins encapsulate the MPS-PPV polymer either in single virus-like particles (VLPs) or in aggregates with more than two VLPs. In the latter case, high molecular mass and an extended MPS-PPV chain conformation seem to be the reason for the formation of aggregates composed of VLPs.

This chapter is published:
M. Brasch and J. J. L. M. Cornelissen; Chem Commum; ***2012****; 48; 1446-1448*

5.1 Introduction

Biomolecules that self-assemble into precisely shaped containers with a defined size are of growing interest in nanotechnology. In particular, viruses represent some of the most diverse, robust yet adaptable nanoparticles found in nature. The self-assembly of the virus capsid proteins protects its contents from extreme surroundings (*e.g.* pH and temperature) and ensures highly efficient delivery of its cargo. Devoid of their native DNA, virus-like particles (VLPs) are composed of virus coat proteins that assemble into empty non-infectious capsids.[1-3] VLPs have been used to encapsulate biomaterials, such as proteins[4-8] or enzymes,[9] as well as synthetic materials, *e.g.* micelles[10] or anionic polymers.[11, 12] While the virus shell often retains its native spherical morphology, the VLP size can be dictated by the encapsulated cargo material. Cowpea Chlorotic Mottle Virus (CCMV) is one exceptional example that exhibits the ability to self-assemble into either spherical or rod-like structures.[13] CCMV is an icosahedral virus that is composed of 180 identical coat proteins. Under defined conditions of pH and ionic strength, CCMV self-assembles either into empty native spherical capsids with an external diameter of 27 nm or in the presence of polyanionic materials, such as negatively charged polymers, into artificial spherical or tubular structures with an external diameter of 18 – 27 nm.[3] This chapter describes the use of conjugated polymers as template to induce assembly of CCMV into different hierarchical architectures. In particular, the extended or coiled nature of a conjugated, rod-like polyelectrolyte, poly[(2-methoxy-5-propyloxy sulfonate)-phenyl-ene vinylene] (MPS-PPV) (R_g = 26 nm)[14] was investigated to determine if the polymer backbone could direct CCMV assembly into a rod-like structure. Such structures have been reported in the past for DNA[15-17] and could potentially lead to different polymer arrangements (*e.g.* the polymer chain can be encapsulated either in its stretched or its coiled state) and therefore may exhibit unique optical properties.

5.2 Results and discussion

5.2.1 Characterization of non-encapsulated MPS-PPV polymer

The bare non-encapsulated MPS-PPV polymer (purchased from Sigma Aldrich, 0.25 wt. % in H_2O) was analyzed by size-exclusion chromatography and UV-Vis Spectroscopy to obtain more information about its polydispersity and the optical properties. The MPS-PPV polymer elutes between 7-10 mL, based on the characteristic π-electron transitions of MPS-PPV at λ = 440 nm, 370 nm and 295 nm (Figure 5.1).[18-20]

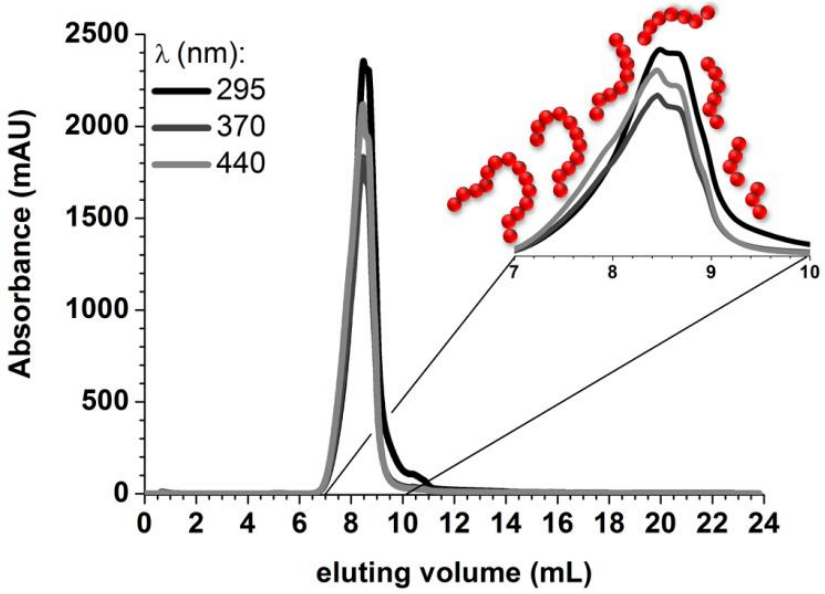

Figure 5.1. Size-exclusion chromatogram of non-encapsulated MPS-PPV. Inset: schematic representation illustrating that high molecular mass polymers elute at low elution volumes, whereas low molecular mass polymers elute at high elution volumes.

Although the MPS-PPV polymer eluted as a single peak, each isolated fraction was expected to contain a different ratio of high-to-low molecular mass polymer which enabled studies of the individual optical properties. The higher molecular mass polymer shows a characteristic absorbance maximum at λ = 440 nm whereas the low molecular mass polymer exhibits an absorbance maximum at λ = 370 nm. Therefore, the peak ratio of optical density (440) / O.D. (370) gives a good indication of the relative amounts of short or long polymer chains and can be used to estimate the polymer composition in each fraction. As expected, the initial fraction volumes (7.1 mL – 8.5 mL) exhibited a higher absorbance at λ = 440 nm

compared to λ = 370 nm, indicating that higher molecular mass species elute earlier. In the elution range (8.5 mL – 9.5 mL), the absorbance at λ = 440 nm gradually decreased until the absorbance at λ = 370 nm reached the same intensity, indicating the elution of shorter MPS-PPV chains (Figure 5.2).

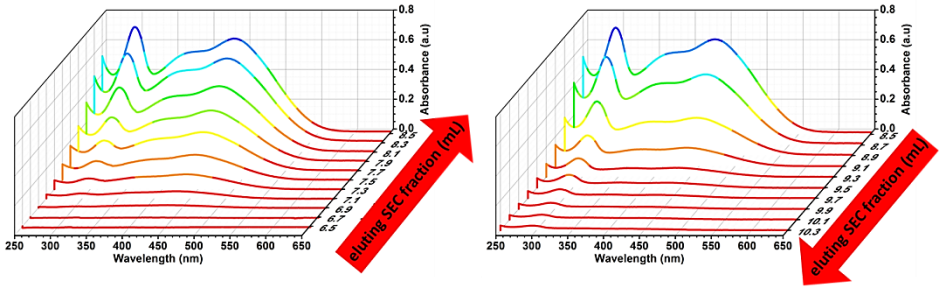

Figure 5.2. UV-visible absorbance spectra of size-exclusion chromatography (SEC) purified MPS-PPV fractions. In the left graph the absorbance spectra of the SEC fractions ranging from 6.5 to 8.5 mL are plotted and in the right graph the absorbance spectra of the SEC fractions ranging from 8.5 – 10.3 mL. Depending on the SEC fractions containing different molecular mass of MPS-PPV a different ratio of the absorbance maxima are visible. The different colors only represent the peak intensity caused by higher concentrated samples.

While the peak ratio of O.D. (440) / O.D. (370) correlated to the relative amounts of short or long polymer chains, the relative peak intensity at λ = 295 nm also provided information about the polymer length. By comparison of the relative peak ratios at O.D. (295) / O.D. (440) or O.D. (295) / O.D. (370), it was found that a relative ratio below 1.5 indicated higher molecular mass chains, whereas a relative ratio above 1.5 indicated shorter chains (Figure 5.3).

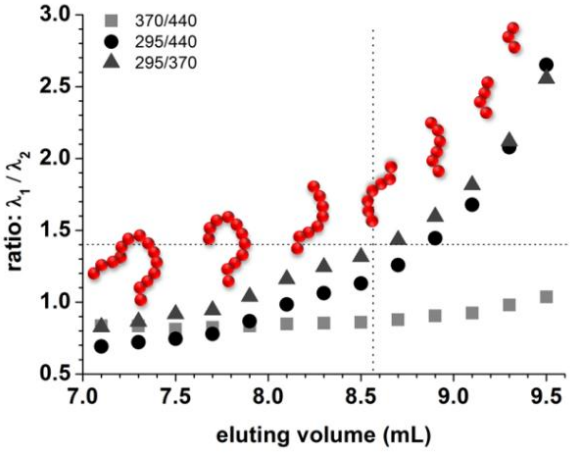

Figure 5.3. Plot of the relative absorbance ratios for MPS-PPV (λ = 295 nm, 440 nm or λ = 370 nm) as a function of the elution volume as determined by size-exclusion chromatography.

5.2.2 Characterization of different VLPs morphologies encapsulating MPS-PPV

The native CCMV is composed of 180 identical virus coat protein (CP) subunits, which assemble around the RNA to form a T = 3 icosahedral capsid with an external diameter of 27 nm. Devoid of its native RNA, the CCMV capsid can be disassembled into CP dimers (at pH 7.5 and an ionic strength higher than 0.3 M) and then reassembled in the presence of negatively charged materials to form T = 1 VLPs with an average external diameter of 18 nm.[3, 10, 21] In this chapter, the encapsulation of MPS-PPV in VLPs at pH 7.5 not only led to single T = 1 VLPs (herein referred to as free particles, FP) but also to clusters of more than two T = 1 VLPs (herein referred to as aggregated particles, AP) and is illustrated in Figure 5.4. To understand which parameters control the formation of FP or AP, the nature of these assemblies was investigated further to determine whether the molecular weight of the polymer dictates the particle size and whether this process can be controlled.

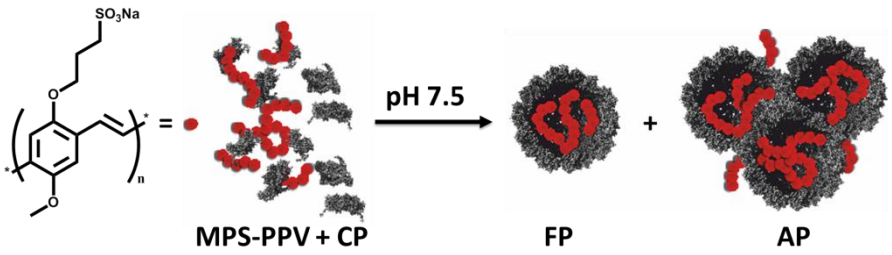

Figure 5.4. Schematic representation for the template-directed assembly of MPS-PPV into either free CCMV particles (FP) or aggregated CCMV particles (AP).

To investigate the influence of MPS-PPV towards FP or AP assembly and whether adjusting the template-to-protein ratio could control the two different assembly pathways, two sets of experiments were performed. In the first set of experiments, the concentration of MPS-PPV was kept constant while varying the concentration of CP. A series of encapsulation studies was performed in the presence of MPS-PPV (100 μg/mL) and various CP concentrations (100-5000 μg/mL). Upon encapsulation, the samples were purified by size-exclusion chromatography (SEC), monitoring at λ = 451 nm for the MPS-PPV, and λ = 260, 280 nm for the virus protein. Three elution peaks at 8.5 mL, 12.5 mL and 18.5 mL were resolved (monitoring at all three wavelengths), indicating the successful encapsulation of the polymer in VLPs (Figure 5.5A). Transmission electron microscopy (TEM) measurements were performed to determine the morphology of the assemblies corresponding to the fractions at 8.5 mL and 12.5 mL. TEM revealed clustered,

chain-like AP and individual T = 1 VLPs for the fractions at 8.5 and 12.5 mL, respectively (Figure 5.6). The relative elution volume for each fraction is consistent with their apparent molecular masses and all VLPs were within the expected size range of T = 1 particles (18 nm in diameter) based on TEM. The third peak at V = 18.5 mL corresponds to unassembled, dimeric CP. Furthermore, increasing the concentration of CP did not result in the exclusive formation of FP. In all samples both species, AP and FP, were found (Figure 5.5A).

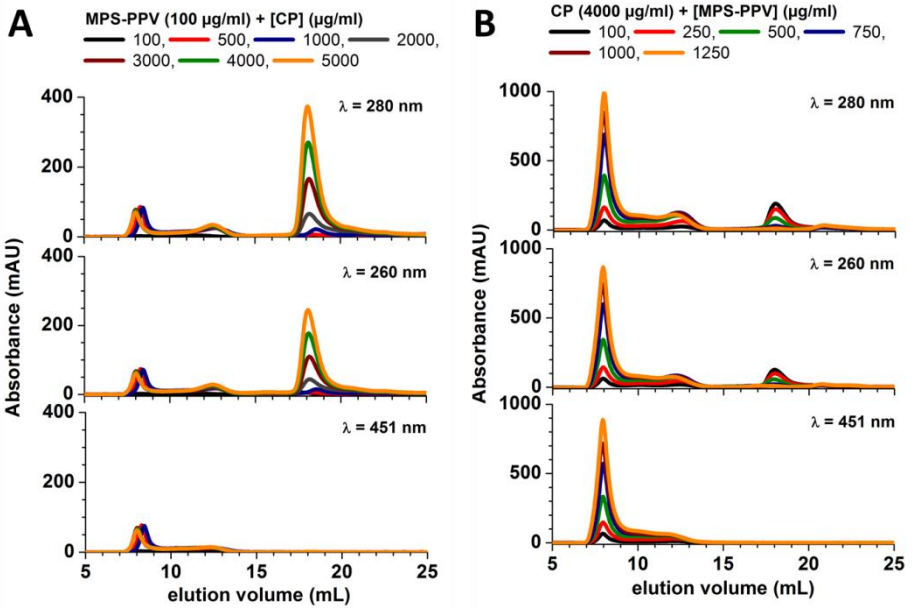

Figure 5.5. Size-exclusion chromatography for the encapsulation of MPS-PPV in CCMV in the presence of (A) MPS-PPV (100 µg/mL) and increasing CP concentration, (B) CP (4000 µg/mL) and increasing MPS-PPV concentration, monitoring at λ = 260 nm; λ = 280 nm (CP) and λ = 451 nm (MPS-PPV).

The relative ratios of AP, FP and CP were determined by integrating the size exclusion chromatograms at λ = 280 nm, since both the polymer and the CP absorb at this wavelength. The integrated areas were plotted as a function of CP concentration (Figure 5.7). At very low CP concentration (100 µg/mL), more FP are observed whereas at higher CP concentration, more AP are observed. Nevertheless, in both cases, the ratio between AP (■) and FP (●) formation approach a constant value, which is independent of CP concentration, indicating that all polymer material is encapsulated, leaving the excess of unassembled, dimeric CP (▲).

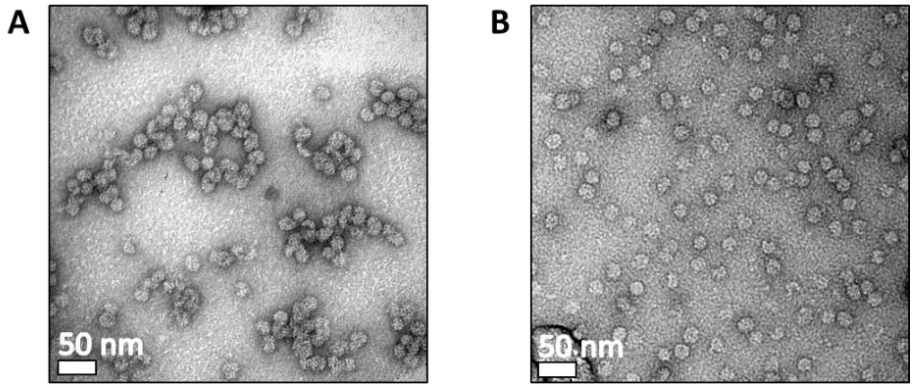

Figure 5.6. Transmission Electron Microscopy images of the purified fractions of (A) AP and (B) FP.

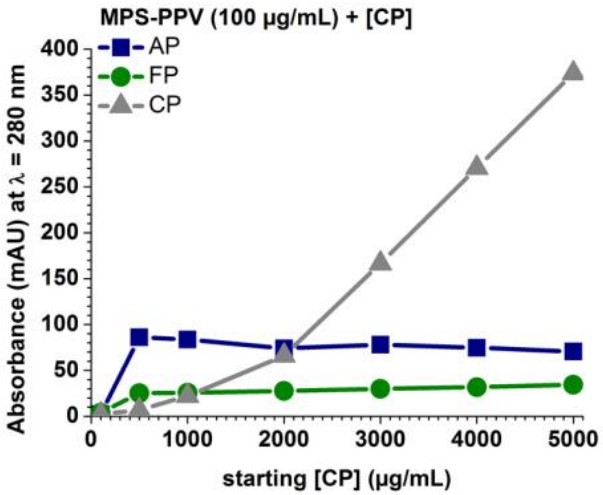

Figure 5.7. Relative ratios of AP, FP and excess CP as a function of CP concentration. The relative ratios were determined by integration of the size exclusion chromatograms at λ = 280 nm.

The higher yield of FP formation at low CP concentration suggests that FP formation is more favorable at limiting CP concentrations (*i.e.* under conditions where there is insufficient CP to encapsulate all the polymer material). However, in the presence of excess CP, more specifically five times excess of CP, the entire polymer material is encapsulated either into FP or AP. In particular, low molecular mass polymers appear to be preferentially encapsulated in FP to form well-defined, individual protein assemblies. By comparison, AP contain excess of high molecular mass polymers, composed of protein shell assemblies that appear to be linked by extended polymer chains spanning from one particle into the next. To

study the stability of FP and AP, both species were isolated and analyzed again by SEC after 30 days (Figure 5.8). However no clear shift in equilibrium was observed between FP and AP, suggesting that both species form highly stable morphological assemblies.

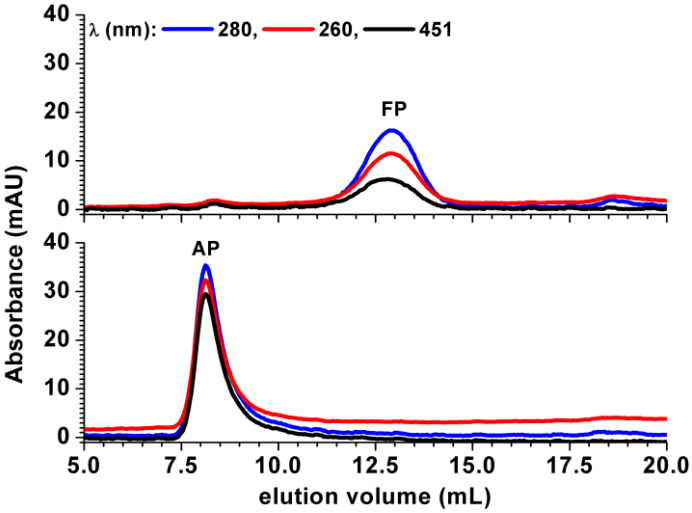

Figure 5.8. Time-course studies by size-exclusion chromatography of FP (top) and AP (bottom) show that the particles are stable and remain intact after 30 days.

Since a protein : polymer ratio of 5 : 1 was found to be optimal to encapsulate the entire polymer, further investigations were conducted to study how these assemblies behave under conditions of limited CP and conditions whereby the protein : polymer ratio is less than 5 : 1. For these studies, a series of samples containing CP (4000 µg/mL) and various concentration of MPS-PPV, varied from 25 µg/mL to 1250 µg/mL was prepard.†

Quantitative analysis by size-exclusion chromatography showed that the formation of AP continuously increases with increasing polymer concentration whereas FP formation increases until an optimal polymer concentration of 500 µg/mL (Figure 5.9). This suggests that at this polymer concentration there is insufficient CP available to encapsulate the entire polymer material into either FP or AP. Overall, it appears that CP initially encapsulates polymer material with low molecular mass (preferentially forming FP), before encapsulating higher molecular mass polymer to form the less favorable AP.

† The ratio between MPS-PPV and CP concentration overlaps with the previous series of samples and serves as an internal control to ensure first that the entire polymer is either encapsulated in FP or AP as long as the CP concentration is at least 5 times higher than the polymer concentration and second, that the previous observed phenomena are not depending on the concentrations of the compounds to each other, but rather on the ratio of the concentrations between CP and MPS-PPV.

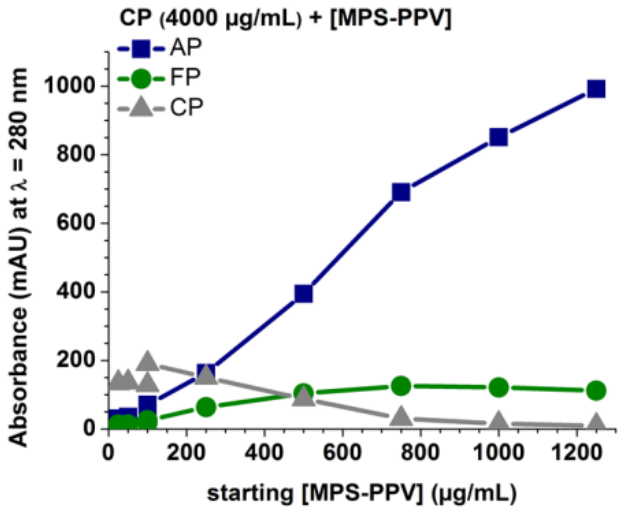

Figure 5.9. Absolute values of each species, AP, FP and CP calculated from the SEC data (λ = 280 nm). Samples containing CP (4000 µg/mL) and various [MPS-PPV].

Overall, these results indicate that the most efficient ratio for complete encapsulation of MPS-PPV into FP and AP is approximately 1 µg/mL MPS-PPV to 5 µg/mL CP. However, the exact mechanism of this complex assembly behavior still remains unclear. Given that both species are stable over a period of at least 30 days, the formation of thermodynamically stable species is suggested.

5.2.3 Spectroscopic analysis of purified FP and AP

Purified FP and AP containing MPS-PPV were characterized by UV-visible spectroscopy. As for the non-encapsulated polymer, the characteristic absorbance peaks at λ = 440 nm, 370 nm and 295 nm were detected for both FP and AP species, confirming the presence of the MPS-PPV polymer (Figure 5.10). For FP, the absorbance spectra shows two bands of equal intensity (A_{370} = A_{440}), which is consistent with the presence of low molecular mass MPS-PPV polymer whereas, the absorbance spectra for AP shows two bands with A_{440} > $A_{370,}$ which is consistent with the presence of high molecular mass polymer. Overall, this indicates that FP contains shorter MPV-PPS polymer fragments compared to AP, which is in agreement with TEM measurements which showed individual T = 1 particles in FP and clustered particles in AP.

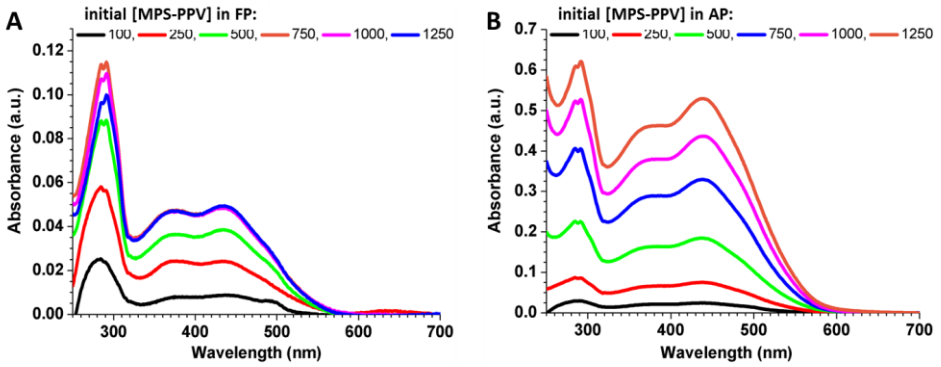

Figure 5.10. UV-visible spectra of purified (A) FP and (B) AP encapsulated MPS-PPV.

For encapsulated MPS-PPV, a significant difference in relative ratios of O.D. (295) / O.D. (440) and O.D. (295) / O.D. (370) was observed for AP and FP. For O.D. (295) / O.D. (440), a ratio of approximately 1.2–1.4 was found for AP, whereas for FP this ratio was between 2.0–2.4 (Figure 5.11). Overall, these results show that the different ratios in absorbance are related to the relative molecular weight, and moreover, confirms that FP predominantly contains low molecular mass polymer compared to the AP.

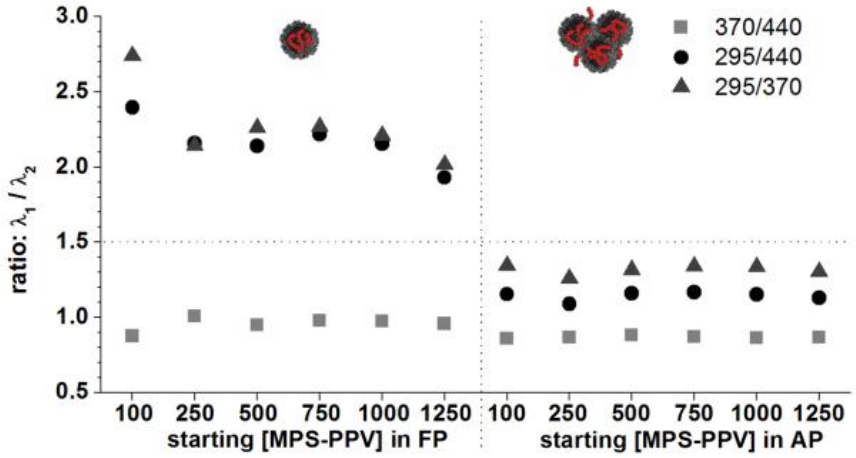

Figure 5.11. The absorbance ratio of FP compared to AP at λ = 295/440 nm or 295/370 nm as a function of different MPS-PPV concentrations. The estimated error in the data is < 5%.

5.2.4 Conformation of MPS-PPV in FP and AP

The conformation of MPS-PPV chains has been reported to vary from extended (*i.e.* more conjugated) to coiled structures, depending on the environment.[22-28] The two conformations can be distinguished by their fluorescence emission spectra, which show a blue-shift for the coiled structure compared to that of extended structures. To study whether the chains of MPS-PPV are extended or coiled inside AP and FP, the emission spectra were measured showing signals centered at λ = 560 nm and 535 nm, respectively (Figure 5.12A and B).

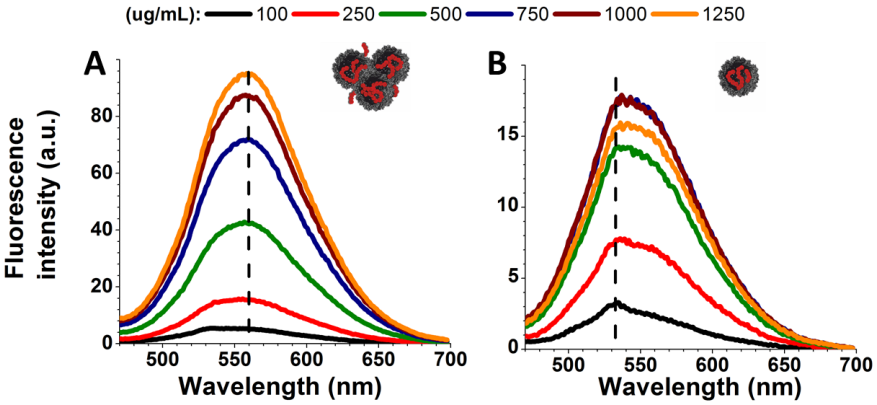

Figure 5.12. Fluorescence emission spectra of MPS-PPV encapsulated in CCMV as (A) AP and (B) FP.

The observed blue-shift towards λ = 535 nm confirmed that the MPS-PPV polymer adopts a more coiled conformation within FP. Together with TEM and DLS (Figure 5.3A and Appendix A1, respectively), this suggests that MPS-PPV is likely to be fully encapsulated inside individual particles. By comparison, the AP particles appear to accommodate more stretched polymer chains, as indicated by the fluorescence emission maximum at λ = 560 nm. This suggests that the polymer chains extend through the protein shell, leading to exposure of polymer to the external environment. This is also consistent with TEM and DLS measurements (Figure 5.3B and Appendix A2, respectively), which indicate average diameters of AP to be between 20-120 nm.

In the case of AP, since the MPS-PPV polymer is partially exposed to solvent, it was expected that the polymer backbone should be more accessible to small molecules (such as fluorescence quenchers), compared to MPS-PPV that is fully encapsulated in FP. To test this, the fluorescence spectra of AP and FP were measured in the presence of methyl viologen (MV^{2+}) (Figure 5.13A and B, respectively).[29, 30]

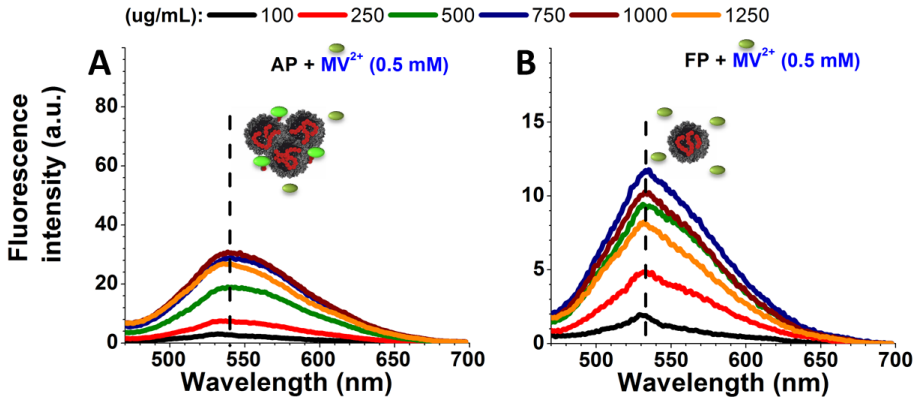

Figure 5.13. Fluorescence emission spectra of MPS-PPV encapsulated as (A) AP and (B) FP in the presence of methyl viologen (MV^{2+}). Excitation wavelength λ_{ex} = 451 nm.

The optimal amount of the small fluorescence quencher (MV^{2+}) was found to be approximately 0.5 mM and was determined by adding different concentrations of quencher to different concentrations of non-encapsulated MPS-PPV (Appendix B). Upon addition of MV^{2+} to AP, the fluorescence emission was quenched ~70% and a blue-shift to λ = 535 nm was observed (Figure 5.13A). However, addition of MV^{2+} to FP shows a decreased quenching efficiency (~25%) and no blue-shift (Figure 5.13B). This confirms that the MPS-PPV polymer is more accessible to small quenching molecules, such as MV^{2+}, in the case of AP but is substantially less accessible in FP, in which the entire MPS-PPV is encapsulated inside. This can be quantified by the Stern-Volmer fluorescence quenching constant (K_{SV}),[31] which provides information about the quenching rates. Here, K_{SV} was determined to be $2 \cdot 10^6$ M^{-1} and $1 \cdot 10^6$ M^{-1} for AP and FP, respectively. The K_{SV} for free MPS-PPV is approximately $2.7 \cdot 10^7$ M^{-1} (Figure 5.14). In both cases, this also confirms that the polymer is still partially protected from small molecules such as MV^{2+}, since both K_{SV} values (for AP and FP) are 10 times lower than the K_{SV} value for free MPS-PPV.[11] It is possible that AP also encapsulates some shorter MPS-PPV polymer chains, which are fully protected from the outside environment and are not quenched by MV^{2+} present in solution. Upon fluorescence quenching of the extended polymer chains by external MV^{2+}, the fluorescence signal from shorter encapsulated polymer chains remains unaffected and hence causes a blue-shift in the fluorescence emission spectra of AP. Whether a dynamic or static quenching process occurs could not be determined, it is expected that a dynamic quenching process would show a concentration-dependent change in both the emission intensity and fluorescence lifetime. In contrast, static quenching would only exhibit a decrease in fluorescence emission spectra upon increasing the quencher concentration whereas the lifetime would be expected to remain unaffected since the unassociated fluorophores still emit.

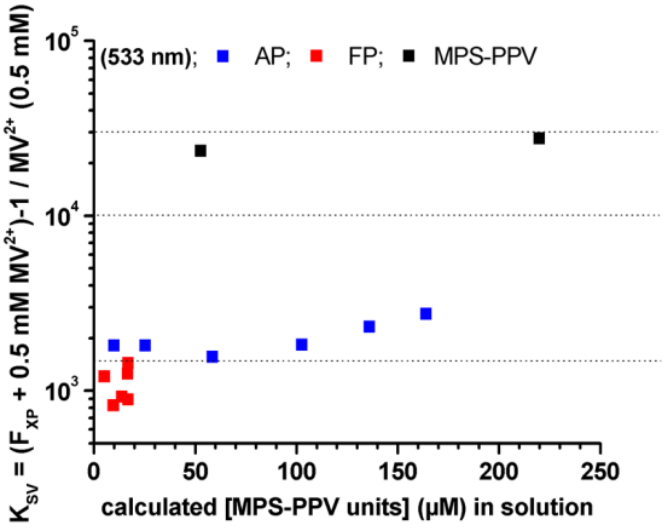

Figure 5.14. Stern-Volmer plot for quenching of the fluorescence of MPS-PPV (repeating units) encapsulated in AP and FP and for non-encapsulated MPS-PPV.

5.3 Conclusions

Here, it is shown that highly conjugated rigid polymers, such as MPS-PPV, can be encapsulated into VLPs. However, in contrast to the expected template-driven assembly, MPS-PPV encapsulation appears to be directed by a virus-driven process, leading to the formation of individual free particles (FP) and clustered aggregated particles (AP) instead of rod-like assemblies. Based on the spectroscopic analyses, FPs are derived from the encapsulation of coiled-up, shorter MPS-PPV polymer chains whereas AP accommodates more extended polymers of higher molecular mass. The delicate interplay between polymer conformation and capsid protein assembly results in an unexpected selection of molecular weight distributions, where longer conjugated MPS-PPV chains cannot sufficiently coil to be accommodated in a single VLP. This does not result in a morphology change of the protein assembly (*e.g.* from spheres to rods),[15-17] but instead leads to the clustering of VLPs. This is further evidenced by fluorescence quenching studies, whereby methyl viologen was shown to efficiently quench the fluorescence of AP due to the presence of more solvent-exposed MPS-PPV polymer chains. Although there are spectroscopic differences in the polymer conjugation length in AP and FP, VLP assembly does not influence the polymer structure substantially (unlike DNA-chromophore hybrid materials).[17] The controlled encapsulation of guest materials in VLPs is of great interest for applications in bionanomedicine. In particular, understanding the size and morphology of VLPs is of importance since cellular uptake is dependent on the particle size[32] and its surface chemistry.[2]

5.4 Acknowledgments

Dr. Alberto Gomez-Casado is gratefully acknowledged for his help and fruitful discussions.

5.5 Experimental

5.5.1 Materials

The growth and purification of the native CCMV virus, including the removal of RNA and isolation of the coat protein (CP) were performed according to literature procedures.[9] The purity of the CCMV virus CP was confirmed by size exclusion chromatography (SEC), SDS-PAGE and UV-Vis spectroscopy. Poly[5-methoxy-2-(3-sulfopropoxy)-1,4-phenylenevinylene] potassium salt solution (MPS-PPV) 0.25 wt. % in H_2O was purchased from Sigma Aldrich and used without further purification. All chemicals used for the preparation of buffers were of analytical grade quality and all buffers were prepared in ultrapure (Milli-Q) water.

5.5.2 Methods

Encapsulation of MPS-PPV into CCMV:
Different concentrations of MPS-PPV (stock solution: 2500 µg/mL) were prepared in 50 mM Tris-HCl buffer, 0.3 M NaCl, 1 mM DTT (pH 7.5) and a solution of the CP (8 mg/mL) in the same buffer was added. The resulting solutions were incubated for 1 h at 4 °C on a roller bank to ensure mixing. After incubation, the samples (including a reference containing only CP) were purified and analyzed at room temperature by size exclusion chromatography (100 µL injection volume), monitoring at λ = 260, 280 nm and 451 nm. 200 µL fractions were collected and those corresponding to AP, FP or CP were further analyzed by TEM, UV-Vis spectroscopy, DLS and fluorescence spectroscopy.

Size-exclusion chromatography (SEC):
SEC was performed using the following buffers: 50 mM Tris-HCl, 0.3 M NaCl and 1 mM DTT (pH 7.5) and the GE Healthcare FPLC Äkta purifier 900 combined with fraction collector Frac-950. Samples were injected into a 100 µL injection loop and purified over a preparative column Superose 6 10/100 GL (GE Healthcare) with a 24 mL bed volume. UV-Vis spectra were recorded using a Perkin Elmer Lambda 850 UV spectrophotometer.

Transmission Electron Microscopy (TEM):
All TEM samples were examined using an analytical FEG-TEM (Phillips CM 30) operated at 300 kV acceleration voltage. For sample preparation, 5 µL of protein sample were applied onto Formvar-carbon coated grids. After depositing, the

sample was left to incubate for 1 min before removing the excess liquid using a piece of filter paper. Uranyl acetate (5 μL, 1% w/v) was deposited on the carbon grid and the excess liquid was removed after 20 sec. The grid was left to dry for 30 min at room temperature.

UV-Vis spectroscopy:
UV-Vis spectra were recorded on a Varian Cary 300 UV-Vis spectrometer by using a quartz cuvette with 3 mm path length.

Fluorescence measurements:
Fluorescence spectra were recorded on a Perkin Elmer LS55 Fluorescence spectrometer by using a quartz cuvette with 3 mm path length.

Dynamic light scattering (DLS):
A cell inside the DLS-setup was filled with 600 μL of solution containing either AP or FP. All DLS measurements were performed on a particle analyser Zetatrac UIT autotitrator from Anaspec. Samples were measured and the size distribution of the capsids was determined by measuring their diameter for more than 80 counts, unless otherwise stated.

5.6 Appendix

5.6.1 Appendix A: DLS of AP and FP after size exclusion purification

DLS results show that the size distribution of AP and FP does not vary with MPS-PPV concentration (in the range of 100 – 1250 µg/mL). In all measurements, the diameter of APs ranged from 20 – 120 nm (Figure A1) whereas FP were 10 – 30 nm (Figure A2).

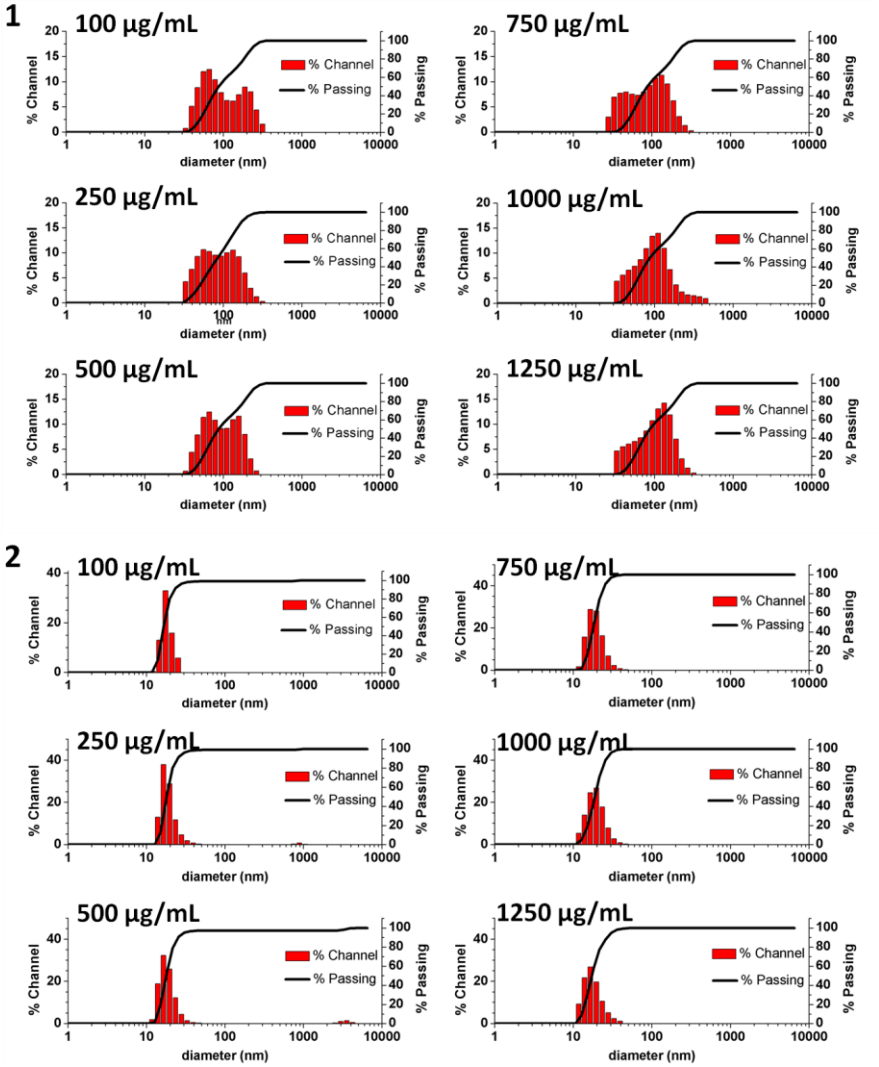

Appendix A. Dynamic light scattering (DLS) measurements of purified (1) AP and (2) FP after size-exclusion chromatography (based on a starting [MPS-PPV] = 100-1250 µg/mL). Note: the measuring range of the instrument is divided into fixed "channels" or particle sizes. Particle sizes were identified on the x-scale (in nm).

5.6.2 Appendix B: Quenching studies of MPS-PPV with MV^{2+}

Fluorescence emission spectra of MPS-PPV (concentration range from 12.5 µg/mL to 625 µg/mL) were recorded after the addition of the fluorescence quencher, methyl viologen (MV^{2+}) (Figure B1). The fluorescence emission intensity of MPS-PPV was quenched almost 90% in the presence of 0.5×10^{-6} M MV^{2+}, followed by a blue shift in the emission spectra from 560 nm to 512.5 nm (Figure B2). Plot of fluorescence intensity at 533 nm (a.u.) vs. [MPS-PPV] (µg/mL). Different concentrations of MV^{2+} were added to show the most efficient quenching of MPS-PPV. A concentration of 0.5×10^{-3} M MV^{2+} shows the highest efficiency and was used for all further quenching studies.

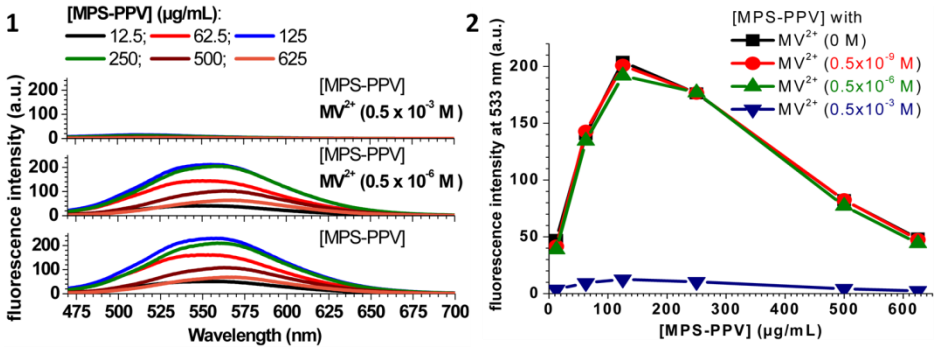

Appendix B. (1) Emission spectra of MPS-PPV after adding different concentration of MV^{2+} (2) Plot of [MPS-PPV] (µg/mL) vs. fluorescence intensity at 533 nm (a.u.)

5.7 References

1. T. Douglas and M. Young, *Science*, 2006, **312**, 873 - 875.
2. J. K. Pokorski and N. F. Steinmetz, *Mol Pharm*, 2011, **8**, 29-43.
3. L. Lavelle, J.-P. Michel and M. Gingery, *J Virol Methods*, 2007, **146**, 311-316.
4. J. D. Fiedler, S. D. Brown, J. L. Lau and M. G. Finn, *Angew Chem Int Ed*, 2010, **49**, 9648-9651.
5. I. J. Minten, V. I. Claessen, K. Blank, A. E. Rowan, R. J. M. Nolte and J. J. L. M. Cornelissen, *Chem Sci*, 2011, **2**, 358-362.
6. I. J. Minten, L. J. Hendriks, R. J. M. Nolte and J. J. L. M. Cornelissen, *J Am Chem Soc*, 2009, **131**, 17771-17773.
7. B. Wörsdörfer, K. J. Woycechowsky and D. Hilvert, *Science*, 2011, **331**, 589-592.
8. A. O'Neil, C. Reichhardt, B. Johnson, P. E. Prevelige and T. Douglas, *Angew Chem Int Ed*, 2011, **50**, 7425-7428.
9. M. Comellas-Aragones, H. Engelkamp, V. I. Claessen, N. A. Sommerdijk, A. E. Rowan, P. C. Christianen, J. C. Maan, B. J. Verduin, J. J. L. M. Cornelissen and R. J. M. Nolte, *Nat Nanotechnol*, 2007, **2**, 635-639.
10. M. Kwak, I. J. Minten, D. M. Anaya, A. J. Musser, M. Brasch, R. J. M. Nolte, K. Mullen, J. J. L. M. Cornelissen and A. Herrmann, *J Am Chem Soc*, 2010, **132**, 7834-7835.
11. R. D. Cadena-Nava, Y. Hu, R. F. Garmann, B. Ng, A. N. Zelikin, C. M. Knobler and W. M. Gelbart, *J Phys Chem B*, 2011, **115**, 2386-2391.
12. F. D. Sikkema, M. Comellas-Aragones, R. G. Fokkink, B. J. Verduin, J. J. L. M. Cornelissen and R. J. M. Nolte, *Org Biomol Chem*, 2007, **5**, 54-57.
13. L. Lavelle, M. Gingery, M. Phillips, W. M. Gelbart, C. M. Knobler, R. D. Cadena-Nava, J. R. Vega-Acosta, L. A. Pinedo-Torres and J. Ruiz-Garcia, *J Phys Chem B*, 2009, **113**, 3813-3819.
14. S. A. Bode, I. J. Minten, R. J. M. Nolte and J. J. L. M. Cornelissen, *Nanoscale*, 2011, **3**, 2376-2389.
15. S. Mukherjee, C. M. Pfeifer, J. M. Johnson, J. Liu and A. Zlotnick, *J Am Chem Soc*, 2006, **128**, 2538-2539.
16. K. Burns, S. Mukherjee, T. Keef, J. M. Johnson and A. Zlotnick, *Biomacromolecules*, 2010, **11**, 439-442.
17. A. de la Escosura, P. G. Janssen, A. P. Schenning, R. J. M. Nolte and J. J. L. M. Cornelissen, *Angew Chem Int Ed*, 2010, **49**, 5335-5338.
18. A. Kohler, D. A. dos Santos, D. Beljonne, Z. Shuai, J. L. Bredas, A. B. Holmes, A. Kraus, K. Mullen and R. H. Friend, *Nature*, 1998, **392**, 903-906.
19. Z. Gu, Q.-D. Shen, J. Zhang, C.-Z. Yang and Y.-J. Bao, *J Appl Polym Sci*, 2006, **100**, 2930-2936.
20. K. Liu, Y. Li, L. Hong and M. Yang, *Sensor Actuat B-Chem*, 2008, **129**, 24-29.

21. J. A. Speir and J. E. Johnson, *Curr Opin Struc Biol*, 2012, **22**, 65-71.
22. Y.-G. Chen, D. Zhao, Z.-K. He and X.-P. Ai, *Spectrochim Acta A*, 2007, **66**, 448-452.
23. E. Ji, D. G. Whitten and K. S. Schanze, *Langmuir*, 2011, **27**, 1565-1568.
24. E. Ji, D. Wu and K. S. Schanze, *Langmuir*, 2010, **26**, 14427-14429.
25. H. Jiang, X. Zhao and K. S. Schanze, *Langmuir*, 2006, **22**, 5541-5543.
26. A. T. Ngo and G. Cosa, *Langmuir*, 2009, **26**, 6746-6754.
27. L. Chen, D. W. McBranch, H.-L. Wang, R. Helgeson, F. Wudl and D. G. Whitten, *PNAS*, 1999, **96**, 12287-12292.
28. A. D. Smith, C. K.-F. Shen, S. T. Roberts, R. Helgeson and B. J. Schwartz, *Res Chem Intermediat*, 2007, **33**, 125-142.
29. J. Dalvi-Malhotra and L. Chen, *J Phys Chem B*, 2005, **109**, 3873-3878.
30. S. J. Dwight, B. S. Gaylord, J. W. Hong and G. C. Bazan, *J Am Chem Soc*, 2004, **126**, 16850-16859.
31. C. Tan, E. Atas, J. G. Müller, M. R. Pinto, V. D. Kleiman and K. S. Schanze, *J Am Chem Soc*, 2004, **126**, 13685-13694.
32. M. Brasch, A. de la Escosura, Y. Ma, C. Uetrecht, A. J. R. Heck, T. Torres and J. J. L. M. Cornelissen, *J Am Chem Soc*, 2011, **133**, 6878-6881.

Chapter 6

Photo-Triggered Cargo Release from Virus-like Assemblies

There has been tremendous progress in the development of responsive polymers that are programmed to respond to an external stimulus such as light, pH and temperature. The unique combination of molecular packaging followed by slow, controlled release of molecular cargo is of particular importance for self-healing materials and the controlled release of drugs. While much focus and progress remains centered around synthetic carriers, viruses and virus-like particles can be considered ideal cargo carriers as they are intrinsically designed to package, protect and deliver nucleic acid cargo to host cells. In this chapter the encapsulation of a stimuli-responsive self-immolative polymer within virus-like assemblies of Cowpea Chlorotic Mottle Virus is described. Upon photo-irradiation, the self-immolative polymer undergoes a head-to-tail depolymerization into its monomeric subunits, resulting in the release of molecular cargo. It is proposed that the liberated monomers are small enough to diffuse through the pores of the virus capsid shell and offer an alternative strategy for the controlled loading and unloading of molecular cargo using viruses as cargo carriers.

This chapter is published:
M. Brasch, I. K. Voets, M. S. T. Koay and J. J. L. M. Cornelissen; Faraday Discuss; ***2013****; Accepted Manuscript: Phototriggered cargo release from virus-like assemblies.*

6.1 Introduction

Molecular cargo carriers such as nanoparticles,[1] polymersomes,[2-4] colloids[5] and lipid vesicles[6] have been of growing interest for applications in nanomedicine.[7, 8] More recently, "triggerable" self-immolative carriers which respond to external stimuli such as light,[9-12] pH,[10] and heat, have been developed for the controlled release of drugs for "smart" biomaterials and hydrogels.[13] Amongst the platforms of synthetic carriers, the use of viruses as a vehicle for the controlled release of molecular cargo has remained largely unexplored. Viruses and virus-like particles (VLPs) are ideal alternatives as cargo carriers as they are intrinsically designed to package, protect and deliver nucleic acid cargo to host cells. The capsids of non-enveloped viruses are composed of multiple coat proteins that bear N-terminal arginine (and lysine) rich motifs (ARMs) that provide important electrostatic interactions necessary for the packaging of viral RNA. In some cases, the viral genome can be replaced by another negatively-charged template to form stable virus-like assemblies. A well-studied example is the virus capsid of the Cowpea Chlorotic Mottle Virus (CCMV). CCMV is an icosahedral plant virus that undergoes reversible self-assembly to form virus-like particles of 28 nm or smaller 18 nm diameter assemblies, as a function of pH and ionic strength. In the absence of its native RNA, CCMV serves as an attractive scaffold and has been subsequently used for the encapsulation of various functional materials.[14-17]

In this chapter, the encapsulation of a stimuli-responsive self-immolative polymer (SIP) inside CCMV virus-like assemblies is investigated. Upon photo-irradiation, the SIP head group is cleaved which initiates its irreversible depolymerization into its monomeric building blocks (Figure 6.1, box). The released monomers are then thought to be able to diffuse out of the pores of the CCMV capsid,[18] and serve as a model for the controlled release of molecular cargo from the inner cavity (Figure 6.1). Furthermore, it is also of interest to investigate the disruption of the template of assembled VLPs and the resulting consequences for the VLP shell.

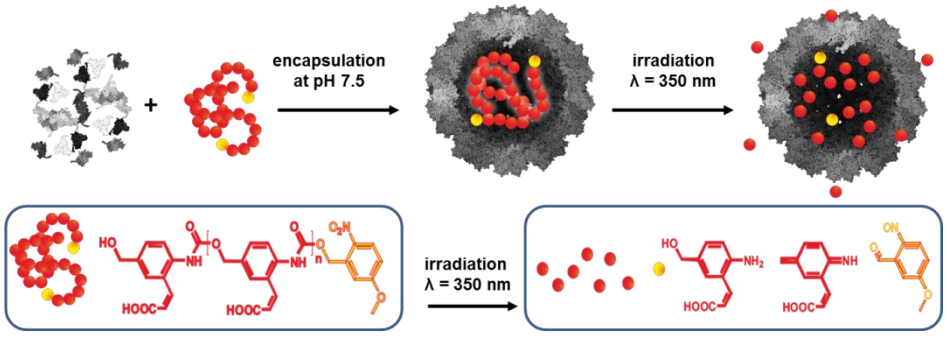

Figure 6.1. Schematic representation of the encapsulation of the self-immolative polymer (SIP) within Cowpea Chlorotic Mottle Virus (CCMV). Upon photo-irradiation, the encapsulated SIP undergoes a head-to-tail depolymerization to form monomeric fragments, leading to the release of molecular cargo from the inner cavity of CCMV.

6.2 Results and discussion

A diverse range of SIP structures has been reported, including alternation of the backbone monomer, positively and negatively charged side groups attached to the monomers, or differences in the trigger groups which response to enzymatic,[19, 20] acid, basic[10] and light stimuli.[9, 11, 12] The selected SIP used in this study is composed of multiple negatively charged monomers and a photo labile group as the stimulus-responsive trigger. The removal of the trigger upon light irradiation induces a spontaneous decarboxylation, resulting in the release of the trigger itself, *i.e.* 5-methoxy-2-nitrobenzyl alcohol, multiple monomers, *i.e.* azaquinone-methide, and carbon dioxide. Although the negatively-charged SIP used in this chapter is quite similar to one already reported in literature,[19] the disassembly of the SIP was characterized and studied independently since the backbone structure of the SIP was modified slightly and all studies were performed in aqueous buffer solution rather than in organic solvents, as reported in literature.

6.2.1 Characterization of self-immolative polymer (SIP)

The polymer, previously prepared by Sagi *et al.*,[19] was characterized by NMR spectroscopy. Three relevant signals can be distinguished in the ^{1}H-NMR spectrum. The first peak at 3.8 ppm represents three protons assigned to the methoxy group of the photolabile trigger, the second peak at 4.4 ppm represents around 2 protons assigned to the last monomer in the SIP chain and the third peak at 9.5 ppm is assigned to the amide proton in the repeating monomer unit. However the labile protons in an alcohol group (-OH) or amine groups (-NH_2 or -NH-) do not have specific chemical shifts, their chemical shift depends on the concentration, solvent and temperature. In a D_2O exchange experiment the protons assigned to the amide groups are exchanged by deuterium and the corresponding peaks disappear in the ^{1}H-NMR spectra. The latter is a significant proof that indeed the peak at 9.5 ppm results from the amide proton in the SIP structure (Appendix 1A). The integration of the areas of the three peak and the comparison of their values to each other allow an estimation of an average chain length of 22 monomers for the SIP (Figure 6.2).

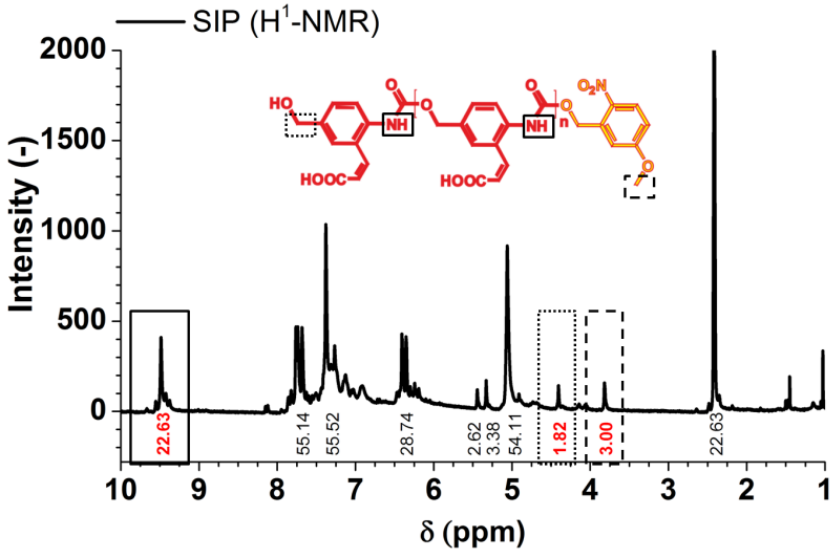

Figure 6.2. ^{1}H-NMR stectrum of SIP revealing an average of 22 monomers per SIP chain.

The ESI-mass spectra and the MALDI spectra showed different chain lengths for SIP composed of 6 to 20 monomers per chain with a m/z of 1688 and 4735 respectively (Figure 6.3A and B, respectively). The latter is in agreement with the estimated average of 20 monomers per chain found by NMR studies (Figure 6.2).

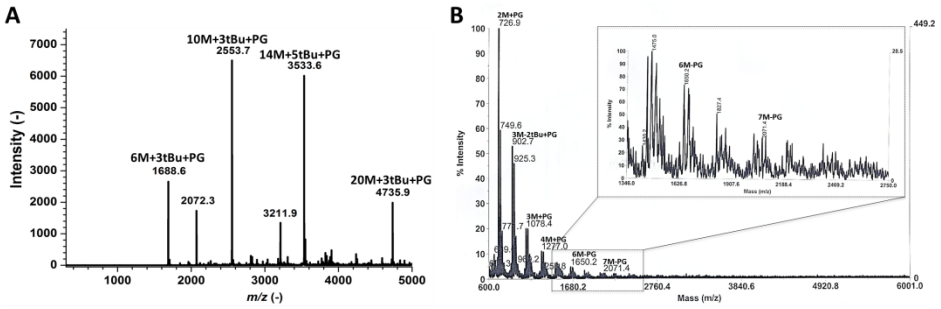

Figure 6.3. (A) ESI-mass spectrum and (B) MALDI-mass spectrum of SIP show different chain length composed of 6 to 20 monomers.

The detection of shorter SIP chains in the MALDI experiments might be caused by the sample preparation and measurement itself, which can cause fragmentation of the polymer chains. Nevertheless, in all fragments the additional mass of 182 g/mol assigned to the photo labile trigger was present when assuming a mass of 218 g/mol per SIP monomer, 57 g/mol per tert-butyl residue and 23 g/mol for the sodium addent.

6.2.2 Depolymerization of SIP after removal of photolabile trigger

The self-immolative polymer used in these studies is composed of multiple negatively charged monomers and a photolabile 5-methoxy-2-nitrobenzyl alcohol head group as the stimuli-responsive trigger. Upon irradiation, the SIP head group is cleaved via a single-photon process, initiating the depolymerization into azaquinone methide intermediates[19] with the concomitant release of CO_2 (Figure 6.4).[11, 21] The azaquinone intermediate subsequently reacts further with a nucleophile to form the stable monomer. The depolymerization upon irradiation reaction was monitored by ^{1}H-NMR spectroscopy by following the changes in selected chemical shifts, assigned to the aromatic region and the amide group in the SIP (Figure 6.4).

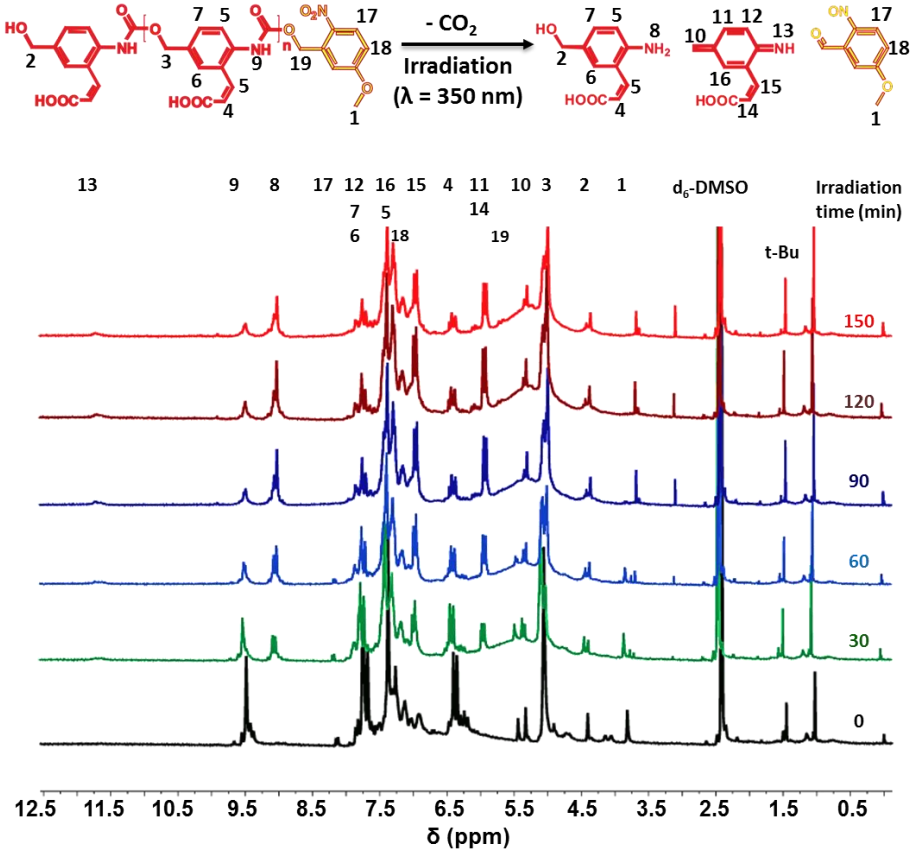

Figure 6.4. ^{1}H-NMR spectra of SIP before and during irradiation. Structural changes during the irradiation at 330-400 nm for 2.5 h are depicted in the different spectra taken every 30 min.

The depolymerization reaction was probed initially in DMSO-d_6 by irradiation at λ = 330-440 nm for 2.5 h and sampling every 30 min. Clear shifts of the signals at δ = 9.5 ppm towards δ = 9.0 ppm (NH protons 9 and NH_2 protons 8 in Figure 6.4, respectively) are observed. This was further confirmed by amide H-D exchange upon addition of D_2O for the longest irradiation time of 150 min (Appendix 1B). The signals around δ = 7.5 ppm (likely protons 5-7, Figure 6.4) clearly decreased in intensity, while around δ = 6.0 ppm new signals (likely 11, 12 and 16, Figure 6.4) emerged. Based on the ^{1}H-NMR spectroscopy the majority of the changes occurred within 90 min.

The signal at 9.5 ppm, however which is representative for the amine group does not disappear completely and indicates a non-complete depolymerization of SIP chains into inactive monomers but also shorter SIP chains such as inactive dimers. It is speculated that the latter reaction can occur when the alcohol group (-OH) from the inactive monomer reacts with the active intermediate during the disassembly process measured in DMSO. However, this reaction might be suppressed when the disassembly process is carried out in a more polar solvent such as aqueous buffer solutions.

Since the acrylic acid side chains in the self-immolative monomer units contribute not only to the water solubility of the SIP, but also can provide a fluorescent chromophore through conjugation with the aromatic amine, the depolymerization process was monitored in aqueous solutions by both UV-Vis and fluorescence spectroscopy. The SIP was dissolved in tris-HCl buffer at pH 7.5 and irradiated for 90 min. During this period samples were taken and analyzed by UV-Vis and fluorescence spectroscopy. The non-irradiated solution showed an absorbance peak around λ = 270 nm, which is assigned to the self-immolative monomer units and a shoulder around λ = 345 nm corresponding to the trigger group, 5-methoxy-2-nitrobenzyl alcohol.[11] After irradiation, the peak at λ = 270 nm disappeared suggesting the depolymerization of SIP (Figure 6.5A). The trends in the optical spectra are summarized in Figure 6.5B for λ = 270 nm and λ = 350 nm. Tentatively, we can assign the spectral behavior at λ = 270 nm by release of the monomers (decreasing absorption) and at λ = 350 nm by the increasing concentration of the released nitroaromatic photocleavable group. Visually, the depolymerization was observed as a color change (Figure 6.5C), with a concomitant change in solubility, *i.e.* the irradiated samples for 60 min and 90 min showed a pellet after centrifugation and a clear almost colorless supernatant (Figure 6.5C). According to Figure 6.5B the majority of the absorbance λ = 270 nm is to the same level already after 15 mins.

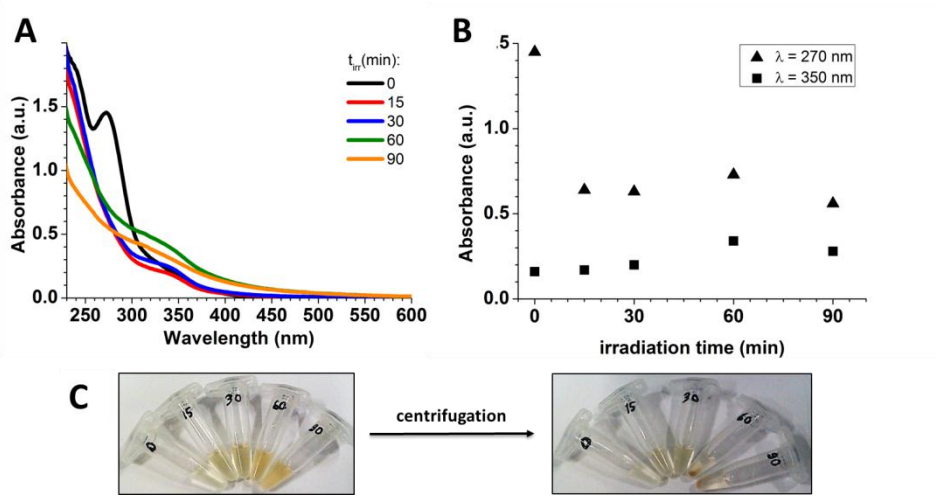

Figure 6.5. (A) UV-Vis absorbance spectra of the depolymerization process of SIP during light irradiation. (B) Absorption at λ = 270 nm (triangles) and at λ = 350 nm (squares) as function of irradiation times. (C) Color change of SIP solution during irradiation before (left) and after (right) centrifugation.

The monomer absorption at λ = 270 nm substantially decreased in the used buffer solution, which makes these fragments unsuited to follow the depolymerization reaction by fluorescence spectroscopy at an excitation wavelength of λ = 270 nm. The release of the nitroaromatic photocleavable group was monitored with this technique using an excitation wavelength of λ = 345 nm (Figure 6.6).

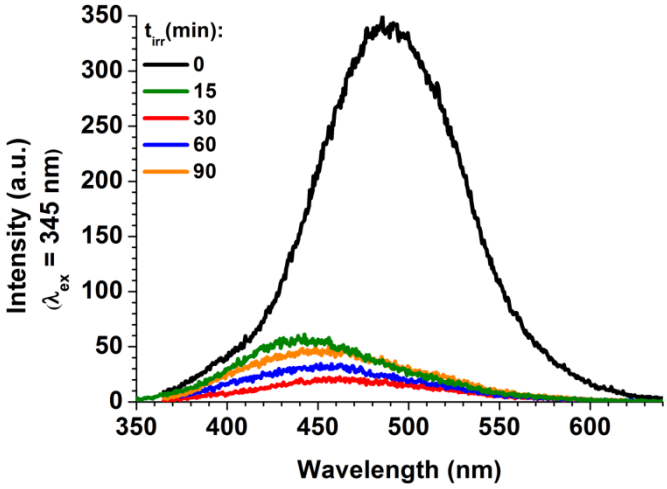

Figure 6.6. Fluorescence emission spectra of SIP irradiated for 0, 15, 30, 60 and 90 min using an excitation wavelength of λ = 345 nm.

After 15 min of irradiation the intensity of the signal at λ = 490 nm decreases to 15%. The intensity of the signal decreases even further when the sample is irradiated for 30 min. An even longer irradiation time (up to 90 min) leads to insignificant changes in the fluorescence intensity of SIP. Note that the emission spectra of samples irradiated for 60 and 90 min are taken from the supernatant after the centrifugation step. This result in a minor increase in the emission spectra compared to the spectra of 30 min irradiation and originates from soluble SIP fragments composed of multiple monomers, because the monomer is insoluble under the measured condition (Figure 6.6). Based on the presented data, it is clear that the SIP depolymerizes upon irradiation at λ = 350 nm into smaller, albeit not all well-defined, fragments.

6.2.3 VLPs filled with SIP

To study the controlled release of cargo from virus-like particles upon photo-irradiation, the negatively charged SIP was encapsulated in CCMV. For the formation of SIP-filled CCMV, the SIP polymer was solubilized in the assembly buffer at pH 7.5 and subsequently added to CCMV coat proteins in a 1:4 (v/v) ratio and allowed to incubate overnight (see experimental). After purification of SIP-CCMV by size-exclusion chromatography, the depolymerization was triggered by irradiation at λ = 350 nm and monitored using steady-state fluorescence spectroscopy by following the release of the nitroaromatic photocleavable group (Figure 6.1). Prior to irradiation, the self-immolative polymer exhibits an emission peak centered at λ = 490 nm, due to the aromatic backbone of the polymer (Figure 6.7A). Prior to irradiation, the fluorescence emission of the carbamate groups in the self-immolative polymer is quenched, however, upon head-to-tail depolymerization, the liberation of the monomer as the free amine leads to restored fluorescence emission.[18, 21, 22] In our case, we observe a significant decrease in fluorescence emission intensity after irradiation for 15 min and the emission maximum is slightly blue-shifted towards λ = 470 nm. Prolonged irradiation for 90 min leads to a further 10 nm spectral shift towards the blue region. Although we observe significant fluorescence quenching, it is possible that during SIP depolymerization, some azaquinone methide intermediates react with the ARMs of the CCMV coat protein that are present inside the virus-like capsid. Nevertheless, a significant change in SIP fluorescence was observed upon photo-irradiation, indicating cleavage of the photo-triggerable group and subsequent depolymerization of the self-immolative polymer. After 90 min irradiation, no change in fluorescence emission is observed, suggesting that the depolymerization reaction is complete.[10, 19-22]

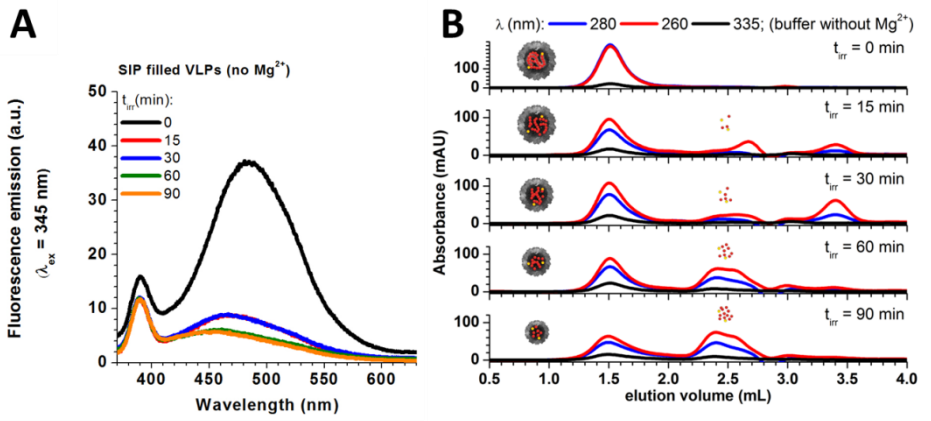

Figure 6.7. (A) Fluorescence emission spectra of SIP-CCMV upon increasing irradiation time (t_{irr} = 0, 15, 30, 60, 90 min). (B) Size-exclusion chromatography of SIP-CCMV shows changes in elution profile upon increasing irradiation time as monitored at λ = 260 nm, 280 nm and λ = 335 nm.

To confirm that depolymerization of SIP does indeed occur, and to determine whether photo-irradiation of SIP-CCMV also triggers the disassembly of CCMV, size-exclusion chromatography was performed at various time intervals (t_{irr} = 0, 15, 30, 60, 90 min), monitoring at λ = 260, 280 nm and λ = 350 nm for CCMV protein and the photo-triggerable group of SIP, respectively. In all cases a major peak at 1.5 mL was observed, which is characteristic for T = 1 CCMV particles and strongly suggests that CCMV does not disassemble during SIP depolymerization (Figure 6.7B). Free, unassembled CCMV coat proteins typically elute at 18.5 mL (Appendix 3). However, the absorbance peak intensity at 1.5 mL decreases upon increasing irradiation, with the concomitant appearance of additional elution peaks at > 2.2 mL (note: for clarity, the absorbance scale for the non-irradiated (t_{irr} = 0 min) samples is off-set compared to the irradiated samples). The peaks at > 2.2 mL exhibit a dominant absorbance at λ = 260 (compared to 280 nm) and also a weak absorbance at λ = 350 nm. The absorbance characteristics suggest that the peaks at > 2.2 mL should be attributed to SIP-based material being released from the CCMV particles rather than CCMV coat proteins, since CCMV typically exhibits a dominant absorbance peak at 280 nm compared to 260 nm. After irradiation for 90 min, the elution profile remains unchanged, indicating that the depolymerization is complete and no additional SIP fragments are released from the CCMV particles. This is also consistent with the fluorescence measurements, which showed no change in emission spectrum after 90 min of irradiation.

While size-exclusion chromatography indicated that the CCMV particles remain intact, the resolution of separation is insufficient to detect small changes in size and shape of the CCMV particles. Electrophoretic mobility shift assay (EMSA) is a

quantitative technique that is often used to study protein-DNA interactions. This technique has been shown to be useful for studying the mobility of virus-like particles, since the migration is determined by molecular weight and the apparent three-dimensional shape.[23] Here, EMSA was used to study relative changes in CCMV shape and molecular weight upon irradiation. Since the CCMV particle formation is highly dependent on the molecular cargo inside,[14] it was anticipated that the loss of SIP fragments may be accompanied by morphological changes of the CCMV particles. As expected, there is a distinct shift in CCMV migration upon increasing irradiation times, indicating a gradual change in size of the CCMV particles as SIP fragments are released (Figure 6.8A). Dynamic light scattering (DLS) further confirmed a shift from $T = 1$ particles (18 nm) to smaller particles of approximately 10 – 14 nm in size upon increasing irradiation time (Figure 6.8B).

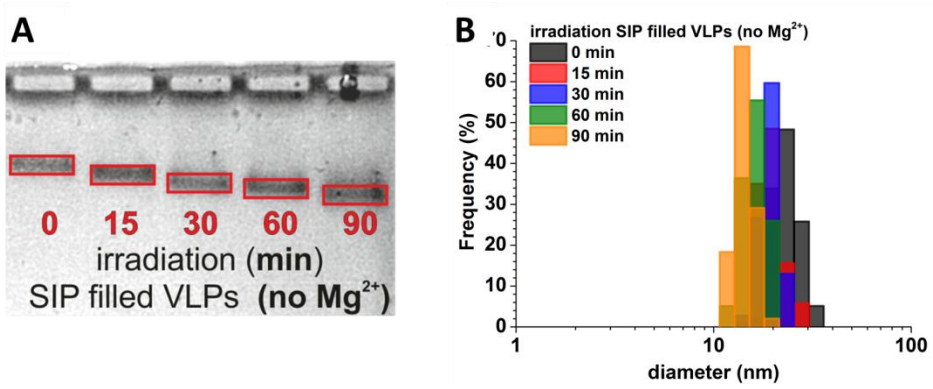

Figure 6.8. Electrophoretic mobility shift assay of SIP-CCMV upon increasing irradiation time and (B) dynamic light scattering shows the average particle size decreases upon increasing irradiation time.

In a comparative study, SIP-CCMV was prepared and irradiated in the presence of 10 mM Mg^{2+}. Previous studies have shown that divalent ions, such as Ca^{2+}, can bind to the pores of the native CCMV and have been implicated to induce contraction and/or stabilization of the capsid shell.[18, 24] Here, we investigated whether Mg^{2+} can also stabilize the SIP-CCMV capsid during depolymerization and whether the presence of Mg^{2+} impairs cargo release. In the presence of Mg^{2+} ions the encapsulation of SIP into CCMV was more effective than in the presence of Ca^{2+} ions. Therefore, SIP-CCMV in the presence of 10 mM Mg^{2+} was irradiated for 0, 15, 30, 60 and 90 min and purified by size-exclusion chromatography (Figure 6.9). No significant differences were observed between the elution profiles in the presence and absence of 10 mM Mg^{2+}, however, the peak at 2.2 mL appears to be less dominant in the presence of 10 mM Mg^{2+} (at t_{irr} = 15 min), suggesting there may be subtle differences in cargo release in the absence and presence of Mg^{2+}.

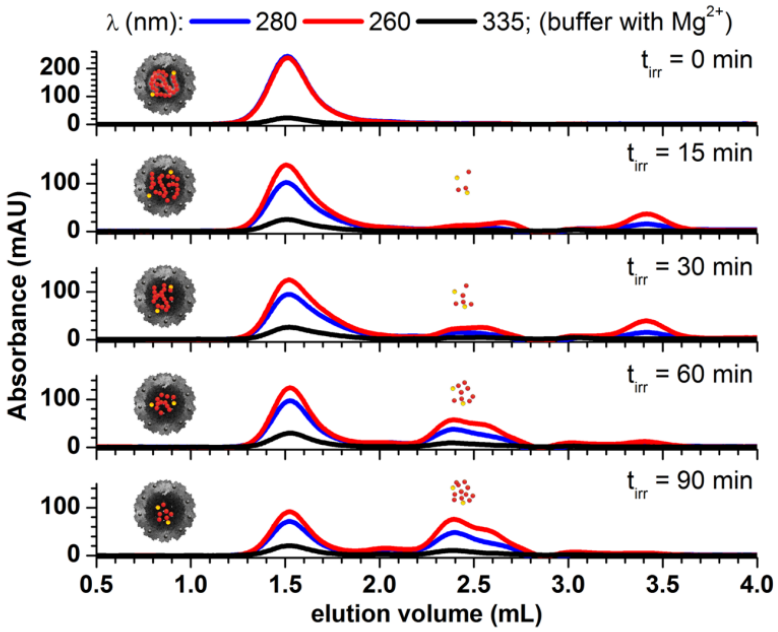

Figure 6.9. Size-exclusion chromatography of SIP-CCMV in the presence of Mg^{2+} ions showing changes in elution profile upon increasing irradiation time as monitored at λ = 260 nm, 280 nm and λ = 335 nm.

The size-exclusive chromatography profiles of Mg^{2+}-poor and Mg^{2+} enriched SIP CCMV were very similar, DLS and EMSA studies revealed clear differences in their hydrodynamic size as a function of irradiation time. The size of SIP CCMV in the presence of 10 mM Mg^{2+} remains approximately constant irrespective of the irradiation time (Figure 6.10A and 6.10B, respectively). Overall, these studies indicate that Mg^{2+} does indeed stabilize the CCMV capsid during cargo release.

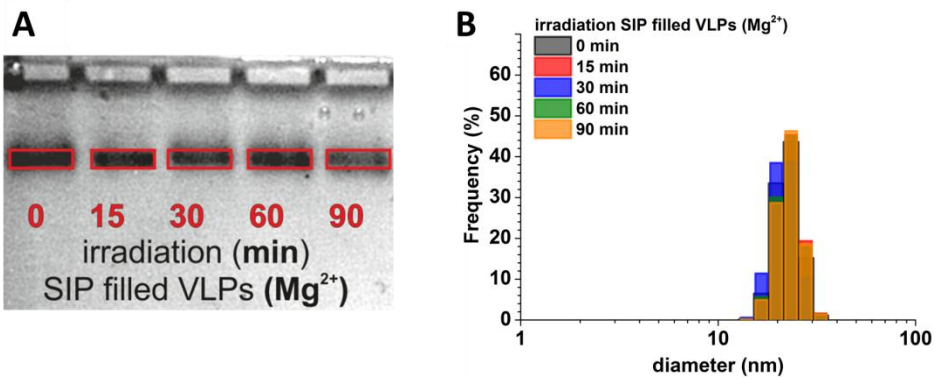

Figure 6.10. In the presence of Mg^{2+} ions, (A) electrophoretic mobility shift assay of SIP-CCMV upon increasing irradiation time and (B) dynamic light scattering shows that the average particle size remains unaltered upon increasing irradiation time.

To probe changes in CCMV size and morphology, Transmission Electron Microscopy (TEM) was performed at different stages of photo-irradiation, both in the absence and presence of Mg^{2+} ions (Figure 6.11A and 6.11B). For SIP-CCMV in the absence of Mg^{2+} ions, spherical particles with a diameter of 19 ± 2 nm were observed prior to irradiation. However, the size and morphology of CCMV particles changes significantly upon increasing irradiation time. Irregularly shaped assemblies with a diameter of 11 ± 1 nm are visible after 90 min of irradiation. Although the CCMV particles appear to stay intact and do not disassemble, they are significantly smaller than expected for T = 1 particles. This strongly suggests that the CCMV shell undergoes morphological changes during cargo release in line with MD simulations reported by Arkhipov *et al*. showing that empty virus capsids tend to be smaller than their filled counterparts.[25]

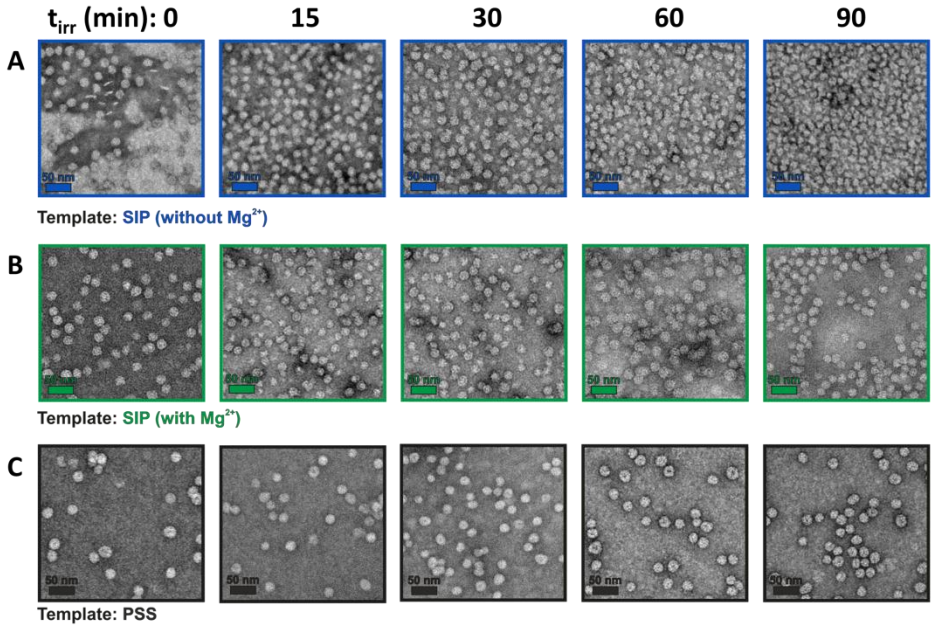

Figure 6.11. Negative-stained TEM of SIP-filled CCMV in the (A) absence or (B) presence of Mg^{2+} ions and (C) PSS filled CCMV. TEM studies show that SIP-CCMV particles undergo morphological changes in the absence of Mg^{2+} upon increased irradiation.

In addition, irradiation for 90 min appears to induce aggregation of SIP-CCMV in the absence of Mg^{2+}, which may be attributed to reduction in the net surface charge, which reduces their colloidal stability.[26,27] In contrast, SIP-CCMV in the presence of Mg^{2+} ions remained unaffected upon increasing irradiation time, which is highly consistent with both DLS and EMSA and strongly suggests that Mg^{2+} does indeed stabilize the CCMV capsid during cargo release.

As an additional control, the non-photoresponsive polymer polystyrene sulfonate (PSS) was encapsulated into CCMV to form presumably pseudo T = 2 particles based on their size (for full characterization, see Appendix 3).[28] As expected, in the absence of Mg^{2+}, PSS-CCMV showed particles that remained intact upon prolonged irradiation as determined by DLS and TEM analysis (Appendix 3B and Figure 6.11 C, respectively). This further confirms that irradiation of CCMV alone does not induce particle shrinkage or aggregation. Image analysis of the electron micrographs revealed a distinct relationship between the dimensions of Mg^{2+}-free SIP-CCMV and irradiation time (Figure 6.12A).

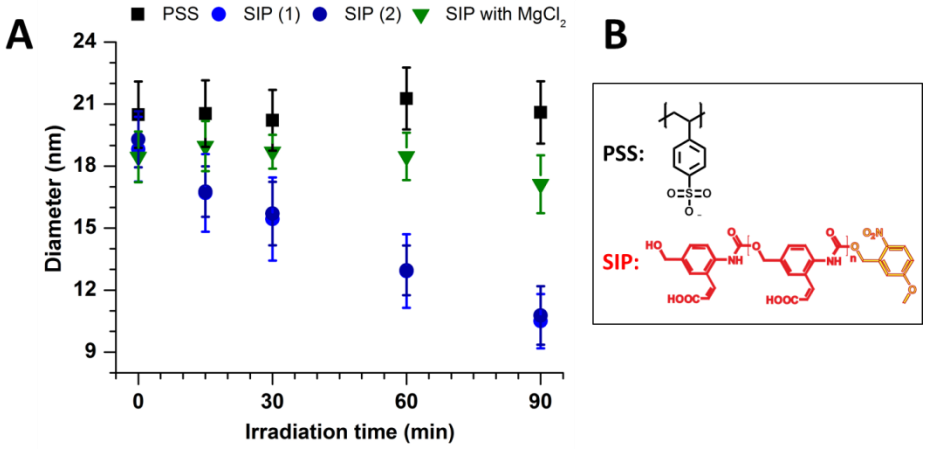

Figure 6.12. (A) Plot of the average CCMV particle diameter as a function of irradiation time for SIP-CCMV in the absence (blue circles, measured in duplo) and presence (green triangles) of Mg^{2+} ions. As a non-photoresponsive control, PSS-CCMV particles were irradiated and analysed (black squares). The particle diameters were estimated by TEM and the distribution value is calculated from an average of 300 particles. (B) Structures of the self-immolative polymer (SIP) and polystyrene sulfonate (PSS) used in these studies.

The stabilizing effect of Mg^{2+} on the capsid structure of SIP-CCMV capsids undergoing phototriggered cargo release is corroborated by small angle X-ray scattering measurements carried out on samples with and without Mg^{2+} irradiated for 0, 30, 60 and 90 min (Figure 6.13A and 6.13B, respectively). While UV irradiation has no discernible effect on the SAXS profiles in the presence of Mg^{2+} depicted in Figure 6.13A, a close inspection of Figure 6.13B reveals that both the position (q_*) and depth ($I(q_*)$) of the first form factor oscillation depend on t_{irr} in the absence of Mg^{2+}. Both q_* and $I(q_*)$ increase with increasing t_{irr}, indicating that SIP-CCMV capsids decrease in size and become structurally less well defined upon increasing irradiation time in the absence of Mg^{2+} (Table 6.1). Moreover, a non-negligible upturn appears in the low q regime of SAXS profiles collected after prolonged irradiation of samples without Mg^{2+}, which is indicative of VLP aggregation (Figure 6.13B). Notice that neither a Guinier analysis nor an inverse

Fourier transform analysis clearly revealed the subtle morphological changes in the VLP structure reflected in the first form factor oscillation (Appendix 5 Figure 1). The pair distance distribution functions, PDDFs (Figure 6.13C and 6.13D), and radii of gyration, R_g, extracted from these analyses appear virtually independent of t_{irr} and Mg^{2+} concentration (Appendix 5, Figure 1, Table 2). It appears that the small and local changes in VLP structure, which are visible in the high q regime of the SAXS profiles, significantly decreased its hydrodynamic dimensions while the overall static dimensions remained virtually unaffected. In summary, in line with the DLS and TEM results the SAXS experiments suggest that, in the absence of divalent Mg^{2+} ions, CCMV capsids undergo a subtle morphological reorganization upon cargo release, which leads to particle aggregation. This phenomenon is attenuated in the presence of Mg^{2+} ions, suggesting that these may stabilize the CCMV capsid during cargo release.

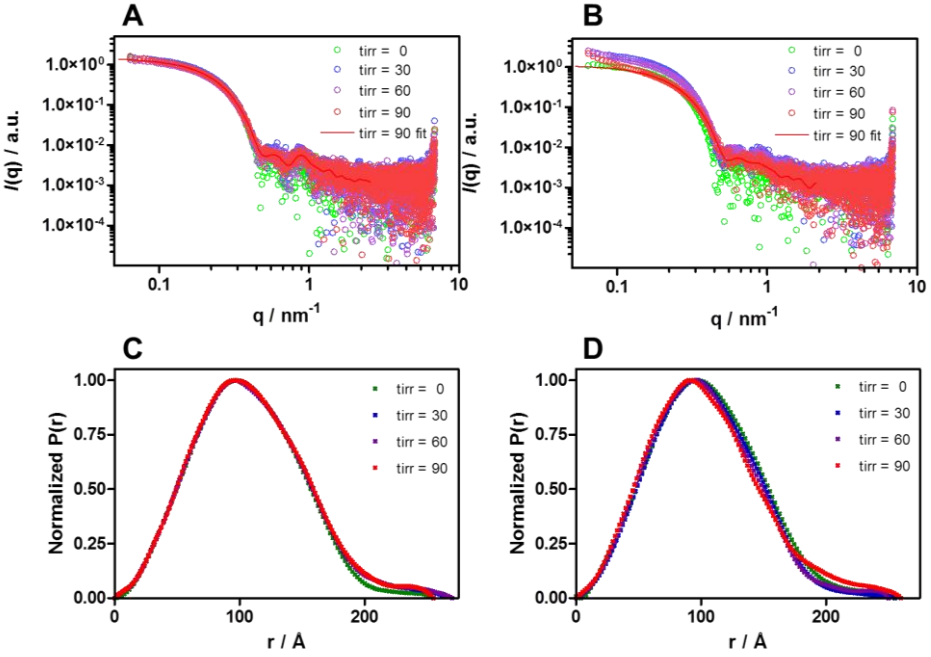

Figure 6.13. (A) SAXS profiles and (B) pair distance distribution functions for SIP-CCMV irradiated for t = 0, 30, 60 and 90 min in the presence of Mg^{2+} compared to the corresponding (C) SAXS profiles and (D) pair distance distribution functions for SIP-CCMV irradiated for t = 0, 30, 60 and 90 min in the absence of Mg^{2+}. Full SAXS analyses can be found in the Appendix 5.

Table 6.1. VLP dimensions obtained from the position of the first form factor minimum under the spherical approximation, *i.e.*, $q^*R = 4.49$.

	without Mg^{2+}		*with* Mg^{2+}	
t_{irr} (min)	q^* (nm^{-1})	R *(nm)*	q^* (nm^{-1})	R *(nm)*
0	0.049±0.001	9.1±0.3	0.049±0.001	9.2±0.1
30	0.049±0.001	9.1±0.2	0.049±0.001	9.1±0.1
60	0.052±0.000	8.6±0.0	0.050±0.001	9.0±0.1
90	0.054±0.001	8.3±0.1	0.050±0.000	9.0±0.1

6.3 Conclusions

We report the encapsulation and release of a stimuli-responsive self-immolative polymer (SIP) within CCMV virus-like assemblies. Upon irradiation, the SIP depolymerizes into monomeric subunits, which are small enough to diffuse through the pores of the CCMV capsid shell. Interestingly, in the absence of Mg^{2+} ions, the liberation of SIP monomers from CCMV also induces a morphological change in the virus-like assemblies, which was confirmed by electrophoretic mobility shift assay, DLS, TEM and SAXS measurements. Furthermore, this phenomenon of capsid "shrinkage" can be attenuated by addition of Mg^{2+}, which can stabilize native virus capsid assemblies. The presence of Mg^{2+} does not significantly perturb SIP depolymerization nor prevent the release of SIP monomers from the CCMV capsid but merely stabilizes the CCMV capsid during cargo release. In both scenarios, we show the slow release of molecular cargo from virus-like assemblies upon activation of an external stimulus. While pH and divalent-ion concentration have been shown to effectively control the infusion and release of molecules in similar viruses,[29] the use of an external stimulus, such as light, is highly attractive since it allows for the controlled, non-invasive release of molecular cargo from virus-based cargo carriers.

6.4 Acknowledgments

Dr. Ilja Voets is gratefully acknowledged for her help and fruitful discussions regarding SAXS measurements. Many thanks go to Xandra de Peuter, B.Sc. for her help and support in the polymer synthesis. Dr. Inge Minten and Prof. Roeland Nolte are gratefully acknowledged for invaluable discussions. The Swiss Light Source (SLS) at the Paul Scherrer Institute (PSI, Villigen, Switzerland) is gratefully acknowledged for beam time.

6.5 Experimental

6.5.1 Materials

All moisture-sensitive reactions were carried out under an argon atmosphere at room temperature unless stated otherwise. All starting material and chemicals, including salts and solvents were purchased from Sigma-Aldrich or Fluka and used as received unless explicitly noted. All compounds used for the preparation of buffers were of analytical quality. Water was purified and deionized (MQ water, resistivity of 18.2 $M\Omega cm^{-1}$). The buffer was adjusted with 1 M NaOH or 5 mM HCl to the desired pH.

Buffer solutions: Assembly buffer A (ABA) was prepared as followed: 50 mM Tris-HCl, 300 mM NaCl, 1 mM DTT, pH 7.5. Assembly buffer B (ABB) was prepared as followed: 50 mM Tris-HCl, 300 mM NaCl, 1 mM DTT, 10 mM $MgCl_2$, pH 7.5. Electrophoresis buffer: 0.1 M sodium acetate, 1 mM EDTA, pH 6.

Synthesis of self-immolative polymer (SIP): The synthesis, including detailed procedures, synthetic schemes and full characterization of all compounds presented in the chapter, is described in the section 6.5.2 – 6.5.3. The monomer unit (**5**) and the polymer albeit with a different head group was synthesized according to literature procedure.[19]

Polystyrene sulfonate (PSS): Polystyrene sulfonate was purchased from Sigma-Aldrich as a powder with an average molecular weight of 70000 g/mol.

Cowpea Chlorotic Mottle Virus purification: The purification and characterization of the Cowpea Chlorotic Mottle Virus (CCMV), the removal of its RNA and the isolation of the coat protein (CP) were carried out according to literature procedures.[30, 31]

6.5.2 Synthesis of SIP – Monomer

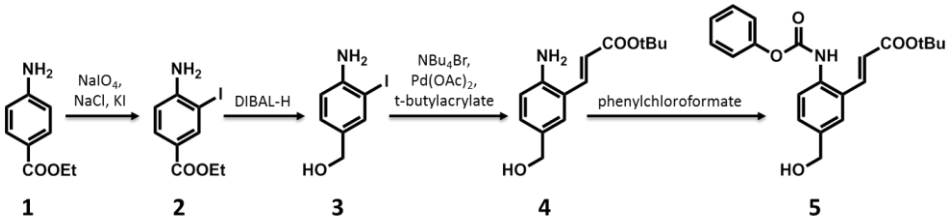

Scheme 6.1. Overview of the monomer synthesis.

Synthesis of compound 2

Compound **2** was prepared following the procedure from reference 19. Commercially available ethyl-4 amino benzoate (7.67 g, 46 mmol) was dissolved in 100 mL of AcOH : H_2O (50 : 50, v/v). $NaIO_4$ (10.01 g, 47mmol), NaCl (5.52 g, 94 mmol) and KI (7.77 g, 47 mmol) were added sequentially. The reaction mixture was stirred at room temperature overnight. The mixture was then diluted with EtOAc and washed three times with brine, two times with a saturated solution of $Na_2S_2O_3$ and finally three times with a saturated solution of $NaHCO_3$. The organic layer was dried over $MgSO_4$, the solvent removed under reduced pressure and the crude product purified by column chromatography on silica gel (EtOAc:Hex 30:70) to give **2** (4.58 g, 34%) as a beige powder. The purification was monitored by TLC (EtOAc:Hex 30:70).

^{1}H-NMR (300 MHz, $CDCl_3$): δ=8.33 (1H, d, J=0 Hz), 7.80 (1H, d, J=4.5 Hz), 7.26 (chloroform), 6.68 (1H, d, J=4.5 Hz), 4.51 (2H, s), 4.28 (2H, q, J=4.5 Hz), 1.31 (3H, t, J=3 Hz).

MS (ES+): m/z: 290.97 [M] (calculated), 292 [M + H^+] (found)
TLC: EtOAc:Hex 30:70, R_f (**2**) = 0.53

Synthesis of compound 3 (see reference 19)

Compound **2** (1.97 g, 68 mmol) was dissolved in dry THF (20 mL) and the solution was cooled to 0 °C under an Ar atmosphere, by means of an ice bath. DIBAL-H (1.0 M solution in THF) (21 mL, 21 mmol) was added drop wise over 30 min until a bright yellow solution was obtained and the reaction was stirred at room temperature for 20 min. The progress of the reaction was monitored by TLC (EtOAc : Hex, 40 : 60 v/v). After consumption of **2**, the excess DIBAL-H was quenched by addition of MeOH (40 mL), THF (20 ml) and celite (2.0 g). A white solid was obtained, after adding MeOH and the solution turned colorless. The mixture was then stirred for 1 hour and the formed white solid filtered off. The residue on the filter was washed with THF (20 mL), in order to extract the maximal

amount of absorbed product. The clear and colorless filtrates were combined and the solvent removed under reduced pressure, which yielded a yellow oil. This oil was dried under vacuum for 30 to 60 min and gave an orange solid. TLC (EtOAc:Hex 40:60) indicated that only one product was formed, which was different from the starting material, compound **2**. The formation and purity of **3** (1.3 g, 77%) as an orange powder was confirmed by ^{1}H-NMR, MALDI MS and TLC.

^{1}H-NMR (300 MHz, $CDCl_3$): δ=7.65 (1H, s), 7.25 (chloroform), 7.13 (1H, d, J=3 Hz), 6.71 (1H, d, J=3 Hz), 4.51 (2H, d, J=3 Hz), 4.10 (2H, s), 3.72 (THF/ethanol residue), 1.55 (water residue), 1.24 (ethanol residue).

MS (ES+): m/z: 248.97 [M] (calculated), 250 [M + H^+] (found)
TLC: EtOAc:Hex 40:60, R_f(**3**) = 0.22

Synthesis of compound 4 (see reference 19)

Compound **3** (2.0 g, 8 mmol) was dissolved in dry DMF (20 mL) under an argon atmosphere. $Pd(OAc)_2$ (90 mg, 0.4 mmol), K_2CO_3 (5.8 g, 42 mmol), Bu_4NBr (3.2 g, 10 mmol) and tert-butylacrylate (2.6 mL, 12 mmol) were added. The reaction mixture was then heated to 60 °C, stirring for 1.5 h, during which the reaction progress was monitored by TLC (EtOAc:Hex, 40:60 v/v) until it was completed. After cooling to room temperature, the mixture was diluted with EtOAc, washed three times with brine and the organic layer was dried over Na_2SO_4. The solvent was removed under reduced pressure and the fluorescent products were separated by column chromatography on silica gel (pure EtOAc). ^{1}H-NMR indicated that the product was present, but that also side products had formed. To yield compound **4**, column chromatography was performed a second time with ethyl acetate and hexane as solvent (EtOAc:Hex 30:70). Compound **4** (0.70 g, 35%) was purified as a yellow oil and gave a yellow/green fluorescent color when irradiated with an UV-light (wavelength 366 nm).

^{1}H-NMR (300 MHz, $CDCl_3$): δ=7.67 (1H, d, J= 9 Hz), 7.37 (1H, s), 7.26 (chloroform), 6,67 (1H,d, J= 4.5 Hz), 6.28 (1H, d, J= 7.5 Hz), 4.55 (2H, d, J= 3 Hz), 4.11 (ethyl acetate residue), 3.95 (2H, s), 2.04 (ethyl acetate residue), 1.56 (water residue), 1.48 (10H, d, J=7.5 Hz), 1.23 (hexane/ethyl acetate residue), 0.86 (hexane residue).

MS (ES+): m/z: 249.3 [M] (calculated), 250 [M + H^+] (found)
TLC: EtOAc:Hex 50:50, R_f (**4**) = 0.44

Synthesis of compound 5 (see reference 19)

Compound **4** (0.70 g, 28 mmol) was suspended in a 15 mL mixture of THF : saturated $NaHCO_3$: H_2O (ratio 2:2:1 v/v/v) and phenylchloroformate (0.50 mL, 40

mmol) was added drop wise over 5 min. The reaction was followed by TLC (EtOAc:Hex 30:70). The mixture was diluted with EtOAc and was washed two times with a saturated NH_4Cl solution. The solvents were removed under reduced pressure. The crude product was purified by column chromatography on silica gel (EtOAc : Hex, 30 : 70 v/v), after which it was dried under vacuum. This yielded compound **5** as a yellow solid (0.60 g, 16 mmol).

^{1}H-NMR (300 MHz, $CDCl_3$): δ=7.79 (2H, d, J = 7.5 Hz), 7.56 (1H, s), 7,37 (1H, d, J = 4.5 Hz), 7,26 (chloroform), 7.20 (3H, d, J = 3 Hz), 6.38 (1H, d, J = 7.5 Hz), 4.69 (2H, s), 1.71 (2H, s), 1.52 (9H, s, tert-butyl groups).

MS (ES+): m/z: 369.2 [M] (calculated), 370.3 M + H^+] (found)
TLC: EtOAc:Hex 50:50, R_f (**5**) = 0.44

6.5.3 Synthesis of SIP – Polymer

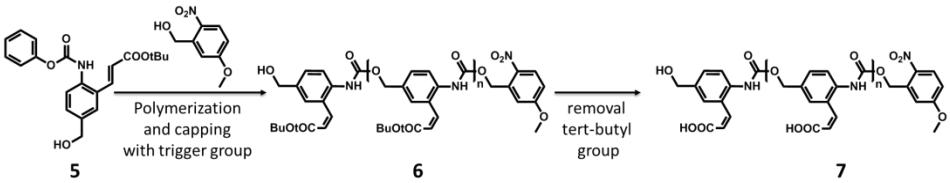

Scheme 6.2. Overview of the polymerization and deprotection of the protected carboxylic acids.

Synthesis of compound 6

Compound **5** (0.30 g, 8 mmol) and DBTL (12 µL, 0.02 mmol) were dissolved in dry toluene (800 µL, 7.51 mmol), after which the solution was heated to 110 °C under Ar atmosphere. The reaction mixture was stirred for 20 min, then the capping alcohol, 5-methoxy-2-nitrobenzyl alcohol (0.15 g, 0.8 mmol) was added to the reaction mixture. After 30 min of stirring, the mixture was cooled down to room temperature in 35 min. The polymer was precipitated by adding MeOH, filtered and dried under reduced pressure.

MS (MALDI): m/z: 2071.4 [7 monomers + trigger group + H^+], Matrix: DHB/H_2O

Synthesis of compound 7

Method 1: Compound **6** (0.10 g) was dissolved in a 1:1 mixture of TFA (1 mL) and DCM (1 mL). The reaction mixture was stirred for 30 min, after which the solvents were removed under reduced pressure. This method lead to incomplete deprotection of the tert-butyl groups for this reason a more vigorous method was used.

Method 2: Compound **6** (0.10 g) was dissolved in a 95:5 mixture of TFA (2.9 mL) and DCM (0.15 mL). The reaction mixture was stirred for 90 min, after which the solvents were removed under reduced pressure.

^{1}H-NMR (300 MHz, $CDCl_3$) first measurement: δ= 9.57 (23H, s), 7.77 (55H, d + s, J = 4.5 Hz), 7.46 (55 H, s), 6.44 (29H, d, J = 7.5 Hz), 5.14 (54H, s), 4.49 (2H, s), 3.90 (3H, s), 2.50 (DMSO), 1.53 (53H, s, tert-butylgroups), 1.11 (tert-butylalcohol)

^{1}H-NMR (300 MHz, $CDCl_3$) second measurement: δ= 9.57 (22H, s), 7.77 (51H, d + s, J = 4.5 Hz), 7.46 (51 H, s), 6.44 (22H, d, J = 7.5 Hz), 5.14 (51H, s), 4.49 (2H, s), 3.90 (3H, s), 3,35 (water residue), 2.50 (DMSO), 1.53 (1H, s, tert-butylgroups).

Highest mass in MS (ES+): m/z: 4897 [21 monomers + trigger group + 2x t-Bu] MS Highest mass in (MALDI) m/z: 1844 [7 monomers + trigger group + 2x t-Bu], Matrix: DHB/ACN/H_2O

6.5.4 Methods

General methods: FPLC chromatograms were performed using either ABA or ABB. Buffers were prepared from ultrapure (Milli-Q) water. UV-Vis spectra were recorded using a Perkin Elmer Lambda 850 UV spectrophotometer. ^{1}H NMR spectra were recorded at room temperature with a Bruker 500 MHz spectrometer. Chemical shifts are given in parts per million (ppm) relative to tetramethylsilane. MALDI-TOF MS was performed with a Bruker ULTRAFLEX III spectrometer, utilizing α-cyano-4-hydroxycinnamic acid as the matrix.

Size-exclusion chromatography: Size-exclusion chromatography (SEC) was performed using GE Healthcare FPLC Äkta purifier 900 combined with fraction collector Frac-950. Samples were purified by SEC using the buffer ABA or ABB. The SEC column superose 6 10/100 GL (GE Healthcare), 24 mL bed volume and 500 µL injection volume was used for preparative purposes and superose 6 PC 3.2/30, 2.4 mL bed volume and 100 µL injection volume was used for analytic purposes.

Irradiation of self-immolative polymer or polystyrene sulfonate samples: Irradiation of solutions containing SIP, PSS or virus like particles were performed at 4 °C using Honle UV technology equipped with a bluepoint 2 easy cure UV lamp (UVA radiation intensity of 330-400 nm; 4,500 mW/cm^2) further described as high intensity glass fiber optic UV lamp.

UV-Vis spectroscopy: UV-Vis spectra were recorded on a Varian Cary 300 UV-Vis spectrometer using a quartz cuvette with 1 cm path length.

Fluorescence spectroscopy: Fluorescence spectra were recorded on a Perkin Elmer LS 55 fluorescence spectrometer using a quartz cuvette with 1 cm path length. The emission spectra of SIP were measured upon excitation at λ = 270 nm.

Transmission Electron Microscopy (TEM): The samples were examined in an analytical FEG-TEM (Phillips CM 30) operated at 300 kV acceleration voltages. For the sample preparation 5 µL of the desired sample was applied onto Formvar-carbon coated grids. After 1 min, the excess of liquid was drained using a piece of filter paper. Uranyl acetate (5 µL, 1% w/v) was applied and the excess of liquid was drained after 20 seconds. The grid was dried for 30 min at room temperature.

Dynamic light scattering for VLPs filled with SIP or PSS: A cell inside the DLS-setup was filled with 600 µL of solution containing VLPs filled with SIP or PSS. The size distribution of the capsids was determined by measuring their diameter for more than 80 counts unless otherwise stated. All samples were measured three times. The data are presented as "Frequency (%)", which refers to the volume percentage as determined by the instrument.

Encapsulation and SEC experiments of self-immolative polymer (SIP) or polystyrene sulfonate (PSS) into VLPs: For the encapsulation of SIP into virus like particles, a solution of 100 µL SIP in ABA (2.5 mg SIP, 20 µL DMSO, 2 mL ABA) was added to a solution of 400 µL CP (150 µM) in either ABA or ABB. For the encapsulation of PSS into virus like particles, a solution of 100 µL PSS in ABA (2 mg PSS, 2 mL ABA) was added to a solution of 400 µL CP (150 µM) in ABA. The resulting SIP-CP or PSS-CP mixture was incubated over night at 4 °C on a roller bank to allow the formation of VLPs.
The samples obtained from the encapsulation mixture were purified and characterized by SEC. Therefore 500 µL of the crude mixture were injected on the preparative SEC column at room temperature and monitored by using UV detection at λ = 280 nm and λ = 260 nm, to monitor the absorbance values of coat protein, SIP or PSS and at λ = 335 nm, to monitor the absorbance values only for SIP. The elution buffer for the SEC experiments was identical to the encapsulation buffer. Fractions of 200 µL were collected and those corresponding to CCMV capsid containing SIP or PSS, were further analyzed by TEM, UV-Vis spectroscopy, fluorescence spectroscopy, gel retardation assay, DLS and SAXS.

Irradiation experiments of SEC purified VLPs containing SIP or PSS: All irradiation experiments were performed at 4 °C using a high intensity glass fiber optic UV lamp with a wavelength of 330-400 nm. A solution of SIP or a solution of SEC purified VLPs containing SIP or PSS were irradiated for 15, 30, 60, and 90 min. After each irradiation step 200 µL of the sample were removed for further characterization methods.

Gel retardation assay to visualize different particle sizes: Encapsulation reactions of CCMV coat proteins (CP) with SIP or PSS were performed in buffer ABA or ABB and purified with SEC as mentioned earlier. The SEC purified VLPs containing SIP were irradiated in different time intervals at 4 °C (15, 30, 60, 90 min). After irradiation the samples were directly used for the gel retardation assay without prior SEC purification. A 10 µL aliquot of each irradiation interval was mixed with 2 µL of 100% glycerol (RNAse-, DNAse and protease-free) and loaded into a 1% agarose gel in electrophoresis buffer. The samples were electrophoresed at 4 °C for 90 min at 70 V in a horizontal gel apparatus (peolab). The samples were then stained in a Bio-safe™ Coomassie G-250 Stain solution and visualized on a ISOGEN Life Science ULTIMA 10 si instrument and imaged using ProXima AQ-4 as software.

Small angle x-ray scattering (SAXS) analysis of SIP-CCMV capsids: Small angle X-ray scattering experiments were performed at the cSAXS beamline of the Swiss Light Source at the Paul Scherrer Institute in Villigen, Switzerland, operating at 12.4 keV. The scattering intensity was measured as a function of the momentum transfer vector $q = (4\pi/\lambda)\sin(\theta/2)$, where $\lambda = 0.1$ nm is the radiation wavelength and θ is the scattering angle. A single sample-to-detector distance of 2 m was used to cover a q-range of $0.064 < q < 6.9$ nm^{-1}. Samples were measured at room temperature in a polycarbonate (ENKI, KI-Beam) flow through capillary with a diameter of $d = 2$ mm. Two-dimensional SAXS patterns were collected using 240 frames of 0.25 s per sample and azimuthally averaged to obtain one dimensional SAXS profiles provided that no signs of radiation damage were apparent. The final CCMV scattering curves were obtained after subtraction of the background scattering profiles of the buffer and polycarbonate cell.

6.6 Appendices

6.6.1 Appendix 1: ^{1}H-NMR spectra of SIP before and after D_2O exchange, measured in D_2O

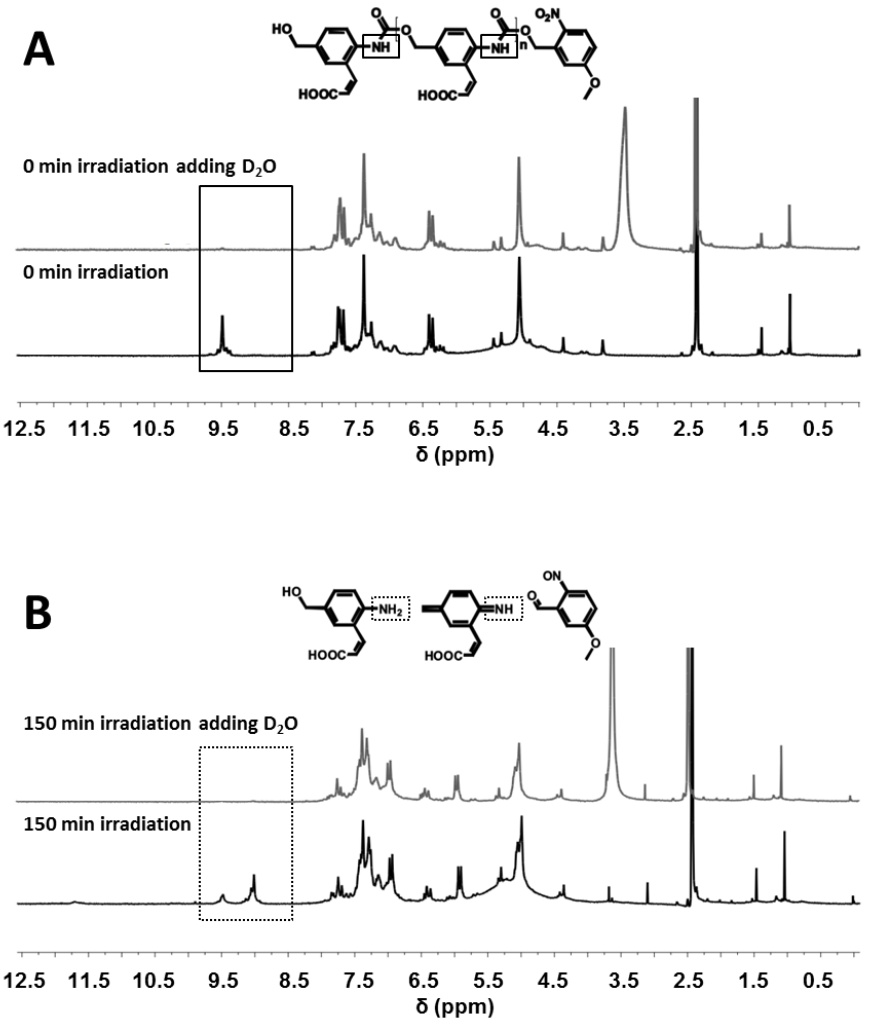

Appendix 1. ^{1}H-NMR spectra of SIP before and after D_2O exchange. (A) ^{1}H-NMR before irradiation of SIP and (B) after 150 min irradiation of SIP. In both cases the proton peaks representing amine or amide groups disappear after D_2O exchange.

6.6.2 Appendix 2: ^{1}H-NMR spectra of SIP irradiated for 60 min in D_2O, measured in D_2O

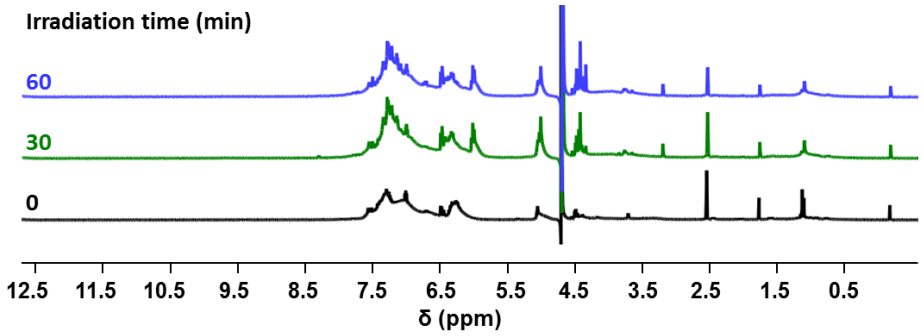

Appendix 2. Water suppression ^{1}H-NMR data of SIP after 0, 30 and 60 min irradiation measured in D_2O at 600 MHz.

6.6.3 Appendix 3: SEC chromatogram of coat protein only

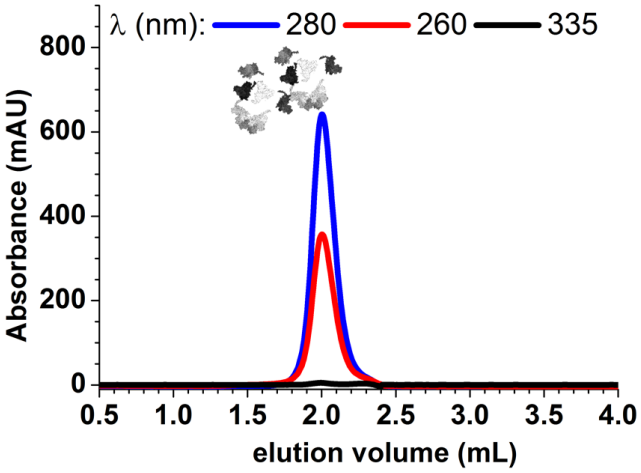

Appendix 3. Size-exclusion chromatography for unassembled CCMV coat proteins shows a single peak at 2.0 mL

6.6.4 Appendix 4: VLPs filled with PSS

The non-photoresponsive polymer polystyrene sulfonate (PSS) was encapsulated into CCMV and subsequently purified by size exclusion chromatography. To confirm that the irradiation time of PSS-CCMV does not have any influence of the capsid morphology size-exclusion chromatography was performed at various time intervals (t_{irr} = 0, 15, 30, 60 and 90 min). Similar to SIP-CCMV, the eluting material was monitored at λ = 260 and λ = 280, both are specific wavelengths for CCMV

protein and PSS. Although the third wavelength (λ = 335 nm) was monitored for the photo-triggerable group of SIP, here we monitored the absorbance at this wavelength as a control to confirm that neither CCMV nor PSS absorb at this wavelength. In all cases, a single peak at 1.3 mL was observed, which is characteristic for pseudo T = 2 particles. These results show that irradiation does not inherently cause the partial disassembly of CCMV nor does it initiate cargo loss (Appendix 4A). Dynamic light scattering measurements were performed on purified PSS-CCMV and confirm the presence of spherical particles with an average diameter around 22 nm (Appendix 4B). Upon irradiation, the average particle size remained unaffected.

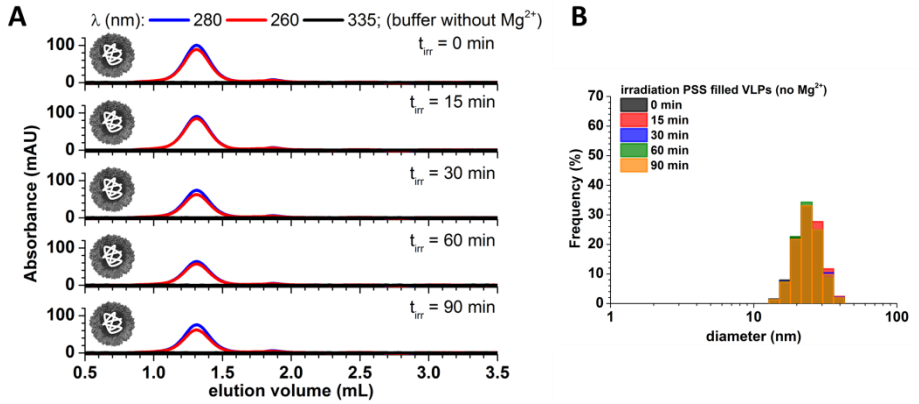

Appendix 4. (A) Size-exclusion chromatography of polystyrene sulfonate (PSS) filled CCMV at various irradiation times (t_{irr} = 0, 15, 30, 60 and 90 min) without Mg^{2+} ions. The absorbance was monitored at λ = 260 nm, 280 nm for the CCMV protein and λ = 335 nm to confirm that lack of a photo-triggerable group (*i.e.* negative control) (B) Dynamic light scattering of PSS-CCMV shows the average particle size remains unaffected upon increasing irradiation time.

6.6.5 Appendix 5: Small angle X-ray scattering experiments on SIP filled CCMV

Small angle X-ray scattering (SAXS) experiments were carried out on samples irradiated for 0, 30, 60, and 90 min with and without Mg^{2+} to corroborate the changes in CCMV size and morphology observed by transmission electron microscopy experiments reported in the main text. Each experiment was carried out in triplicate and representative SAXS profiles are depicted in Appendix 5 Figures 2 and 3. First, a Guinier approximation (Equation 1) was used to extract the radius of gyration, R_g, as a function of irradiation time and Mg^{2+} content (Appendix 5 Table 1) from the slope of the linear portion in the Guinier plots shown in Appendix 5 Figure 1.

$$I = I(O)e^{\frac{-q^2R_g^2}{3}} \qquad \text{Equation 1}$$

Notice that we expanded the used q-range beyond $qR_g < 1$, which is the regime in which the Guinier approximation is strictly valid, to include sufficient data points to determine R_g accurately.

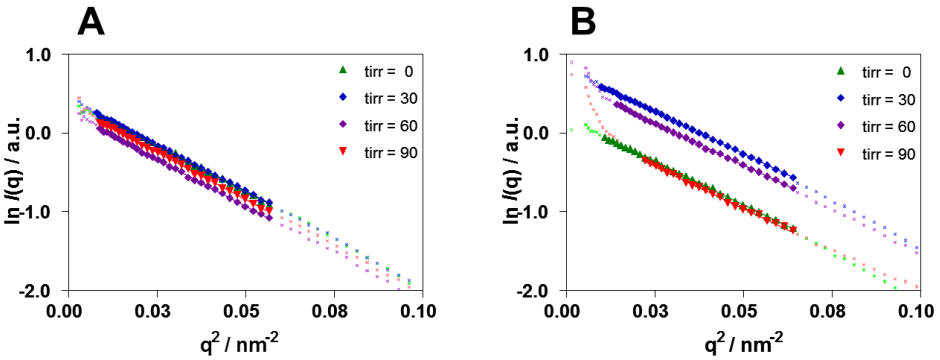

Appendix 5 Figure 1. Guinier plots for SIP-CCMV in the (A) presence of Mg^{2+} and (B) absence of Mg^{2+} upon increasing irradiation time.

Appendix 5 Table 1. Radius of gyration, R_g obtained from a Guinier analysis of the experimental data shown in Figure S4 using the q-range as tabulated, namely $q_{min} \leq q \leq q_{max}$

		without $MgCl_2$		*with $MgCl_2$*		
t_{irr} (min)	R_g (nm)	q_{min} (nm^{-1})	q_{max} (nm^{-1})	R_g (nm)	q_{min} (nm^{-1})	q_{max} (nm^{-1})
0	8.30 ± 0.03	0.09	0.25	8.3 ± 0.03	0.09	0.24
30	8.00 ± 0.02	0.09	0.25	8.3 ± 0.04	0.09	0.24
60	7.97 ± 0.03	0.11	0.25	8.4 ± 0.01	0.09	0.24
90	8.02 ± 0.01	0.15	0.25	8.4 ± 0.02	0.09	0.24

Subsequently, we performed an inverse Fourier transform (IFT) analysis (Appendix 5 Figure 2 and 3) to compute the pair distance distribution functions (PDDFs) given in Figure 13 in the main text, and from these extract R_g as presented in Appendix 5 Table 2 according to Equation 2.

$$R_g^2 = \frac{\int P(r) r^2 dr}{2 \int P(r) dr} \qquad \text{Equation 2}$$

The maximum linear dimension (D_{max}) was set to approximately $3*R_g$ and adjusted to maximize the goodness of fit (Appendix 5 Figures 2 and 3). The PDDF was set to zero at r = 0 nm and approaches zero at D_{max}.

Appendix 5 Table 2. Radius of gyration, R_g, obtained from an inverse Fourier transform analysis using a maximum linear dimension, D_{max}, as indicated. Fits to the experimental data are shown in Appendix 5 Figure 2 and 3, the PDDFs are plotted in Figure 6.13.

	without Mg^{2+}		*with Mg^{2+}*	
t_{irr} (min)	R_g (nm)	D_{max} *(nm)*	R_g (nm)	D_{max} *(nm)*
0	7.9 ± 0.0	25.4 ± 0.2	8.1 ± 0.0	25.3 ± 0.8
30	7.8 ± 0.1	25.5 ± 0.0	8.2 ± 0.1	26.5 ± 0.9
60	7.8 ± 0.0	25.0 ± 0.0	8.3 ± 0.0	26.8 ± 0.4
90	8.0 ± 0.1	25.7 ± 0.3	8.3 ± 0.1	26.5 ± 1.7

Clearly, the Guinier analysis and the IFT yield very similar values for R_g, which are fairly constant irrespective of irradiation time and Mg^{2+} concentration (compare the values in Appendix 4 Table 1 and 2). The shape of the PDDFs resembles that of rather homogeneous, spherical objects. In a subsequent data analysis step, we therefore assumed that we can describe the VLPs are homogeneous spheres and estimate their average size, R, from the first form factor minimum according to, q^*R = 4.49 (Table 6.1 in the main text). This analysis reveals a decrease in VLP size upon an increase in t_{irr} in the absence of Mg^{2+}. By contrast, VLP size is virtually t_{irr} independent in the presence of Mg^{2+}. These findings are further supported by a form factor analysis of the experimental data in the entire q-range measured employing a model for a homogeneous sphere yielding values for the average sphere radius tabulated in Appendix 5 Table 3.

Appendix 5 Table 3. VLP dimensions obtained from a form factor analysis using a form factor for a homogeneous sphere.

	without Mg^{2+}	*with Mg^{2+}*
t_{irr} (min)	R *(nm)*	R *(nm)*
0	9.2 ± 0.1	9.2 ± 0.2
30	8.9 ± 0.3	9.3 ± 0.2
60	8.7 ± 0.1	9.4 ± 0.1
90	8.2 ± 0.3	9.3 ± 0.2

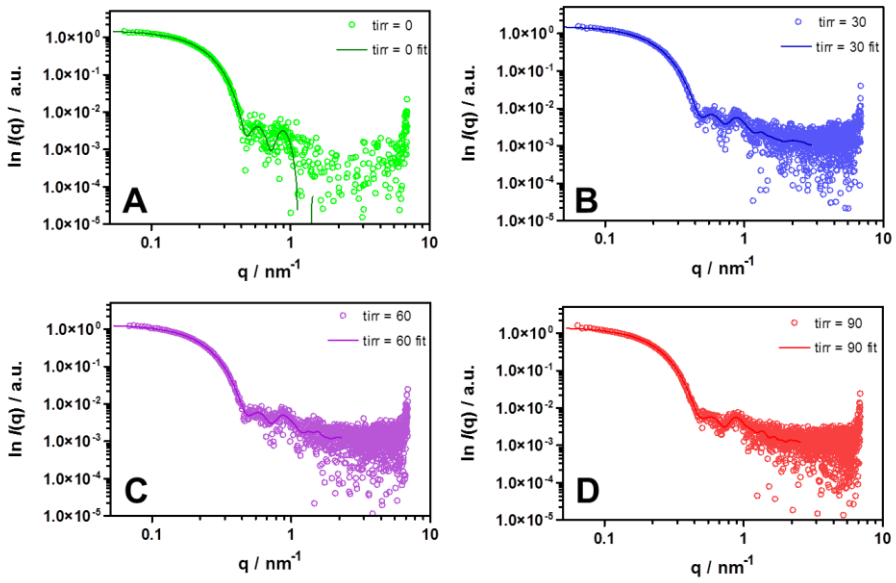

Appendix 5 Figure 2. Inverse Fourier Transform (IFT) analysis for SIP-CCMV in the presence of Mg^{2+} at irradiation times (A) 0 mins, (B) 30 mins, (C) 60 mins, (D) 90 mins.

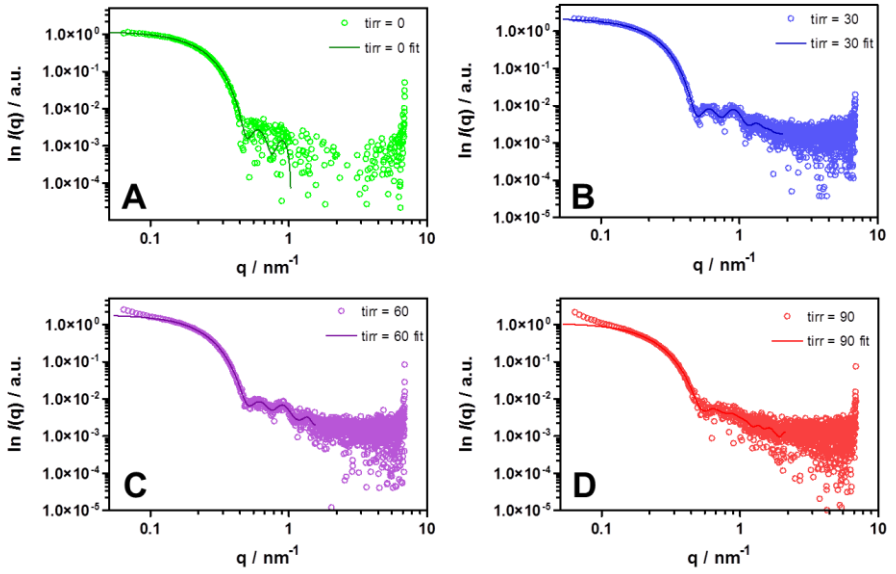

Appendix 5 Figure 3. Inverse Fourier Transform (IFT) analysis for SIP-CCMV in the absence of Mg^{2+} at irradiation times (A) 0 mins, (B) 30 mins, (C) 60 mins, (D) 90 mins.

6.7 References

1. W. H. De Jong and P. J. Borm, *Int J Nanomedicine*, 2008, **3**, 133-149.
2. J. V. Georgieva, R. P. Brinkhuis, K. Stojanov, C. A. G. M. Weijers, H. Zuilhof, F. P. J. T. Rutjes, D. Hoekstra, J. C. M. van Hest and I. S. Zuhorn, *Angew Chem Int Ed*, 2012, **51**, 8339-8342.
3. F. Meng, Z. Zhong and J. Feijen, *Biomacromolecules*, 2009, **10**, 197-209.
4. D. A. Christian, S. Cai, D. M. Bowen, Y. Kim, J. D. Pajerowski and D. E. Discher, *Eur J Pharm Biopharm*, 2009, **71**, 463-474.
5. D. Cunliffe, A. Kirby and C. Alexander, *Adv Drug Deliv Rev*, 2005, **57**, 1836-1853.
6. G. Cevc, *Adv Drug Deliv Rev*, 2004, **56**, 675-711.
7. N. Ohtake, K. Niikura, T. Suzuki, K. Nagakawa, S. Mikuni, Y. Matsuo, M. Kinjo, H. Sawa and K. Ijiro, *Chem Bio Chem*, 2010, **11**, 959-962.
8. P. Walde, K. Cosentino, H. Engel and P. Stano, *Chem Bio Chem*, 2010, **11**, 848-865.
9. A. P. Esser-Kahn, S. A. Odom, N. R. Sottos, S. R. White and J. S. Moore, *Macromolecules*, 2011, **44**, 5539-5553.
10. A. P. Esser-Kahn, N. R. Sottos, S. R. White and J. S. Moore, *J Am Chem Soc*, 2010, **132**, 10266-10268.
11. N. Fomina, C. McFearin, M. Sermsakdi, O. Edigin and A. Almutairi, *J Am Chem Soc*, 2010, **132**, 9540-9542.
12. A. D. Wong, M. A. DeWit and E. R. Gillies, *Adv Drug Deliv Rev*, 2012, **64**, 1031-1045.
13. C. A. Blencowe, A. T. Russell, F. Greco, W. Hayes and D. W. Thornthwaite, *Polym Chem*, 2011, **2**, 773-790.
14. R. D. Cadena-Nava, Y. Hu, R. F. Garmann, B. Ng, A. N. Zelikin, C. M. Knobler and W. M. Gelbart, *J Phys Chem B*, 2011, **115**, 2386-2391.
15. M. B. van Eldijk, J. C. Y. Wang, I. J. Minten, C. Li, A. Zlotnick, R. J. M. Nolte, J. J. L. M. Cornelissen and J. C. M. van Hest, *J Am Chem Soc*, 2012, **134**, 18506-18509.
16. Q. Wang, E. Kaltgrad, T. W. Lin, J. E. Johnson and M. G. Finn, *Chem Biol*, 2002, **9**, 805-811.
17. N. F. Steinmetz, T. Lin, G. P. Lomonossoff and J. E. Johnson, *Curr Top Microbiol*, 2009, **327**, 23-58.
18. J. A. Speir, S. Munshi, G. Wang, T. S. Baker and J. E. Johnson, *Structure*, 1995, **3**, 63-78.
19. A. Sagi, R. Weinstain, N. Karton and D. Shabat, *J Am Chem Soc*, 2008, **130**, 5434-5435.
20. R. Weinstain, P. S. Baran and D. Shabat, *Bioconjug Chem*, 2009, **20**, 1783-1791.

21. I. Aujard, C. Benbrahim, M. Gouget, O. Ruel, J. B. Baudin, P. Neveu and L. Jullien, *Chem-Eur J*, 2006, **12**, 6865-6879.
22. F. D. Sikkema, M. Comellas-Aragones, R. G. Fokkink, B. J. M. Verduin, J. J. L. M. Cornelissen and R. J. M. Nolte, *Org Biomol Chem*, 2007, **5**, 54-57.
23. J. M. Johnson, D. A. Willits, M. J. Young and A. Zlotnick, *J Mol Biol*, 2004, **335**, 455-464.
24. R. Konecny, J. Trylska, F. Tama, D. Zhang, N. A. Baker, C. L. Brooks, 3rd and J. A. McCammon, *Biopolymers*, 2006, **82**, 106-120.
25. A. Arkhipov, P. L. Freddolino and K. Schulten, *Structure*, 2006, **14**, 1767-1777.
26. S. Corezzi, D. Fioretto and F. Sciortino, *Soft Matter*, 2012, **8**, 11207-11216.
27. A. Ebrahim-Habibi, D. Morshedi, N. Rezaei-Ghaleh, M. Sabbaghian and M. Nemat-Gorgani, *J Iran Chem Soc*, 2010, **7**, 521-544.
28. Y. Hu, R. Zandi, A. Anavitarte, C. M. Knobler and W. M. Gelbart, *Biophysical J*, 2008, **94**, 1428-1436.
29. L. Loo, R. H. Guenther, S. A. Lommel and S. Franzen, *Chem Commun*, 2008, 88-90.
30. M. Comellas-Aragones, H. Engelkamp, V. I. Claessen, N. A. J. M. Sommerdijk, A. E. Rowan, P. C. Christianen, J. C. Maan, B. J. Verduin, J. J. L. M. Cornelissen and R. J. M. Nolte, *Nat Nanotechnol*, 2007, **2**, 635-639.
31. B. J. Verduin, *FEBS Lett*, 1974, **45**, 50-54.

Chapter 7

Supramolecular Stacks as Scaffolds for Virus Protein Assembly

The excellent luminescent and self-assembly properties of platinum(II) complexes have gained significant attention in recent years. In this chapter, assemblies of an anionic Pt(II) complex and a neutral Pt(II) complex were used to direct the self-assembly of Cowpea Chlorotic Mottle Virus (CCMV). Different morphologies of protein aggregates were observed, depending on the nature of the complex, the Pt(II) concentration and equilibration time. Increasing the concentration of the anionic Pt(II) complexes led to the preferential formation of protein assemblies with a rod-like morphology, while encapsulation of neutral Pt(II) complexes led to the formation of spherical CCMV assemblies. This is the first example that shows that the self-assembly of small metal-organic complexes into supramolecular stacks can be used to direct the assembly of native spherical viruses into different morphologies. The unique combination of highly luminescent Pt(II) assemblies encased in a protective protein shell opens up new possibilities for applications in biomolecular imaging and molecular optics.

*Manuscript in preparation (**2013**)*

7.1 Introduction

Luminescent square-planar platinum (II) complexes that emit light in the visible region (400-700 nm) have attracted much interest in the fields of optoelectronics,[1-3] organic light-emitting diodes (OLEDs),[4] chemical sensors and biomedical imaging. Their intrinsic tendency to form metal–metal and/or ligand–ligand interactions has been used to promote aggregated Pt(II) states, which significantly enhances their already excellent photophysical properties. More recently, Pt(II) complexes have been used in the self-assembly of nanoparticles,[5] rod- and sheet-like aggregates[6] and fibers.[7] While Pt(II) complexes are promising candidates for applications in materials science, one of their major limitations in biomedical applications is their inherent cytotoxicity.[8, 9] Since the cytotoxicity of Pt(II) complexes is related to both its chemical structure and cellular uptake efficiency (*i.e.* higher cellular uptakes leads to higher cytotoxicity),[10] the introduction of protective groups has been shown to be highly effective in reducing the cytotoxic effects of the Pt(II) core. While most strategies focus on modifying the ligand side-chain, an alternative approach is to encapsulate such materials inside viruses and virus-like particles (VLPs).

Composed of viral RNA (or DNA) and an outer protein coat shell that self-assembles around its genetic material, viruses are designed by nature to encapsulate, protect and deliver molecular cargo into cells.[11] The protein shell is often composed of multiple copies of the same protein and the self-assembly process is driven by electrostatic interactions between the positively charged N-terminus of individual virus coat proteins and the negatively charged phosphate backbone of the viral RNA/DNA.[12] In some cases, the viral RNA/DNA can be replaced with non-nucleic acid (negatively charged) cargo. A broad range of functional materials including polymers, nanoparticles, micelles and small molecules have been used as templates to drive the self-assembly of virus-like structures for applications in nanotechnolgy.[13] One of the most studied viruses is the Cowpea Chlorotic Mottle Virus (CCMV).[14] By controlling the pH and ionic strength, CCMV can be reversibly disassembled into virus coat protein dimers and reassembled into virus-like particles. At pH 7.5, only filled particles with a diameter of 28 nm (T = 3), 22 nm ("T = 2") or 18 nm (T = 1) can be assembled, whereas filled and empty particles of 28 nm (T = 1) in diameter occur at pH 5.0.[15, 16] As described in Chapter 2, depending on the rigidity of the molecular cargo, spherical or rod-like CCMV assemblies can be obtained.[12, 17] While rigid (covalent) polymer- or DNA-based scaffolds have been used to assemble rod-like structures, the use of supramolecular templates that self-assemble via non-covalent interactions into highly ordered structures has not been investigated. In this chapter, the encapsulation of two different Pt(II) complexes that self-assemble into supramolecular structures, into CCMV architectures was studied. The

encapsulation of supramolecular Pt(II) structures in virus-based assemblies could open up new opportunities for applications in biomolecular imaging.

7.2 Results and discussion

The synthesis and photophysical studies of both Pt(II) complexes (anionic Pt-Tet-SO_4 (C1) and neutral Pt-Tet-TEG2 (C2)) were performed by Dr. Naveen Kumar Allampally at Westfälische Wilhelms University Münster, Germany (Figure 7.1). The general synthetic procedure and photophysical properties of analogous Pt(II) complexes are described in literature.[7] Here, the encapsulation and characterization of these Pt(II) complexes in CCMV-CP assemblies are described.

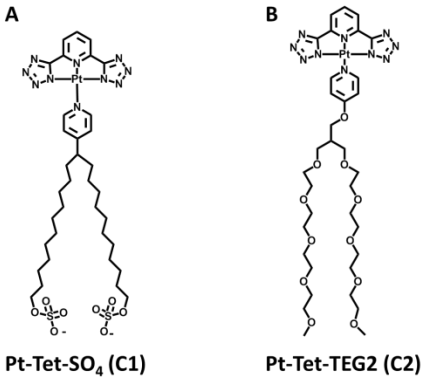

Figure 7.1. Schematic representation of Pt(II) complexes. Structure of (A) Pt-Tet-SO4 (C1) and of (B) Pt-Tet-TEG2 (C2).

7.2.1 Self-assembly of anionic Pt-Tet-SO_4 complex (C1)

The self-assembly of the anionic square-planar Pt(II) coordination complex composed of a dianionic tridentate ligand (2,6 *bis*-tetrazole-5-yl-pyridine) and an ancillary pyridine ligand functionalized with a two-pendant arm alkyl sulfate (herein referred to as the Pt-Tet-SO_4 complex (C1)) was investigated in aqueous buffer. It was anticipated that the strong tendency of the square-planar Pt(II) core to undergo π-π stacking and metal – metal interactions, in combination with the amphiphilic nature of the ancillary ligand induces their self-assembly into supramolecular nanowires or nanoparticles. The distance between the Pt(II) center and the sulfate group at the end of the ancillary ligand was estimated to be 2.2 nm and the full length of the C1 monomer is approximately 2.7 nm (Figure 7.2A and B). Pt-Tet-SO_4 (C1) (8 mM) was dissolved in 50 mM Tris-HCl buffer, 300 mM NaCl, 10 mM $MgCl_2$ and 1 mM DTT (pH 7.5) and equilibrated overnight at 24 °C, with slow agitation. Transmission electron microscopy (TEM) analysis showed the formation of fiber-like assemblies (so-called nanowires), with an average diameter of 13 ± 2 nm (Figure 7.2C and D). Although some nanoparticles of the same

diameter were also observed, the fiber-like structures appeared to be dominant. Because of their dimensions, aggregates of C1 seen suitable templates for CCMV assembly.

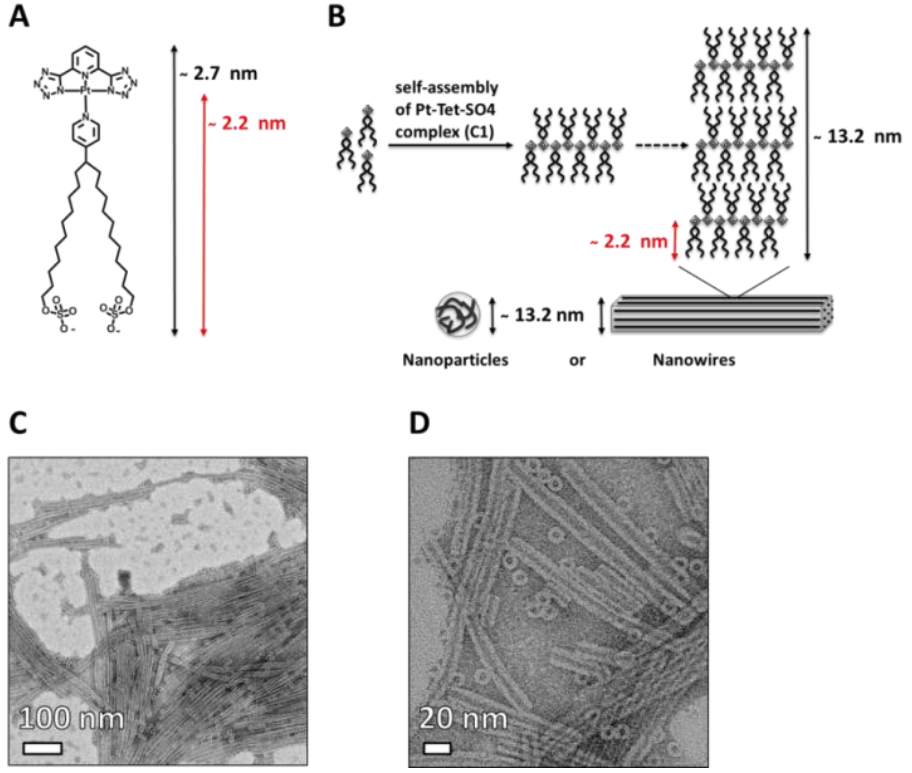

Figure 7.2. (A) Chemical structure of anionic Pt-Tet-SO_4 monomer (C1), (B) Schematic representation of the presumed self-assembly behavior of C1 in solution, (C and D) TEM micrograph of C1 solubilized in 50 mM Tris-HCl buffer (pH 7.5).

7.2.2 Encapsulation of the anionic Pt-Tet-SO_4 complex inside CCMV capsids

To study the entrapment of C1 aggregates, C1 was dissolved at various concentrations and encapsulated in CCMV at two different time intervals, fast addition (t = 0 min) and delayed (t = 12 h). C1 was dissolved at increasing concentrations of 2 mM, 4 mM and 8 mM in 50 mM Tris-HCl buffer, 300 mM NaCl, 10 mM $MgCl_2$ and 1 mM DTT (pH 7.5). A solution of CCMV coat proteins (CPs) (400 µM) was added at 0 min and 12 h after dissolution of C1 in a 1:1 volume ratio. Since the C1 complexes are also required to self-assemble, the different equilibration times (t = 0 min or t = 12 h) were expected to lead to different C1 aggregation states. At t = 0 min, the entrapment of C1 complexes in CCMV would inhibit or "freeze" the self-assembly of the initial C1 architectures, whereas at t = 12 h, entrapment of the equilibrated "aggregated" state was anticipated. To

monitor this presumed kinetic vs. thermodynamic entrapment, samples from both the fast addition and delayed addition of C1 (at increasing C1 concentration and a constant concentration of CPs) were first allowed to incubate for 2 h at 4 °C after mixing before purification by size-exclusion chromatography (Figure 7.3), monitoring at λ = 280 nm and λ = 260 nm for CPs and λ = 430 nm for the C1 complex. The elution volume (1 – 1.5 mL) in combination with the absorbance ratio (260 nm/280 nm > 1) are characteristic features of intact CCMV assemblies. Interestingly, in all cases of fast addition, the elution peak between 1 – 1.5 mL was very broad and asymmetrical and particularly in the presence of 4 mM of C1, the appearance of two overlapping peaks was apparent, which is indicative of a mixture of two or more different morphologies (Figure 7.2A, C and E). In contrast, the elution peak between 1 – 1.5 mL after delayed addition showed a sharp edge at 1 mL before tailing off towards higher elution volumes (Figure 7.2G, I and K). The sharp edge at 1 mL is atypical of spherical CCMV assemblies and may indicate a different morphology. Due to their differences in surface area and morphology, it is thought that rod-like CCMV assemblies elute mainly at 1 – 1.2 mL, while spherical CCMV assemblies elute at 1.2 – 1.5 mL. In all cases, the elution volumes between 1.8 – 2.6 mL and 4 – 4.4 mL are characteristic for non-encapsulated C1 aggregates or monomeric C1 complexes, respectively (Appendix A).

Fractions eluting between 1 – 1.5 mL were collected and analyzed by TEM. In the case of the fast addition of C1 to CPs, TEM confirmed a mixture of spherical and rod-like CCMV assemblies. Interestingly, upon increasing C1 concentrations, an increase in rod-like CCMV assemblies was observed compared to the formation of spherical CCMV assemblies (Figure 7.3, A - F). In contrast, samples prepared by the delayed addition of C1 at increasing concentrations showed predominantly rod-like assemblies with a negligible amount of spherical CCMV assemblies in all cases (Figure 7.3, G - L).

The average diameter of both rod-like and spherical CCMV assemblies is 23 ± 2 nm, which provides an inner cavity of ca. 16 nm. A C1 aggregate constructed from a bi- or multilayer of amphiphiles is expected to fit this dimension (Figure 7.2B).

Based on TEM studies, the average diameter of both rod-like and spherical CCMV assemblies was estimated to be 23 ± 2 nm. However, the particle length distribution of CCMV assemblies varied significantly for the conditions used as shown in Figure 7.4. This suggests, that the self-assembly of Pt(II) complexes is slow compared to the encapsulation process. Longer assembly times of the C1 (*i.e.* 12 h) are needed in order to achieve larger aggregates of Pt(II), which leads then to rod-like CCMV assemblies with length up to 400 nm. The cumulative frequency (%) of the obtained CCMV assemblies can be found in Appendix B.

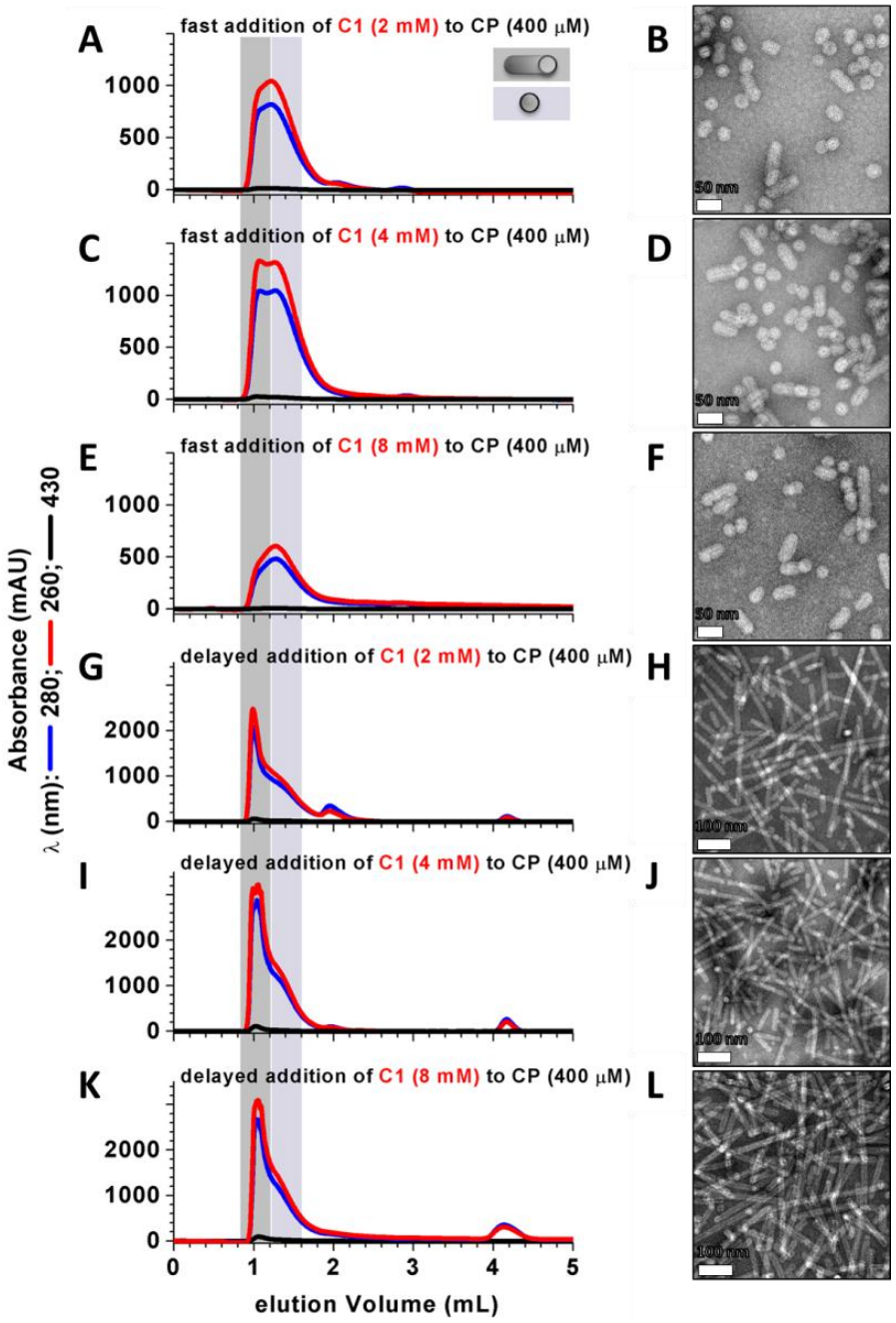

Figure 7.3. Size-exclusion chromatography and the corresponding negatively stained TEM micrographs upon 1) fast addition of CCMV-CPs o C1 at (A) 2 mM, (C) 4 mM and (E) 8 mM and 2) delayed addition after 12 h of CPs to C1 at (G) 2 mM, (I) 4 mM and (K) 8 mM. For size exclusion chromatography, the eluting material was monitored at λ = 280 nm and λ = 260 nm (corresponding to CCMV-CPs) and at λ = 430 nm (corresponding to C1 complexes).

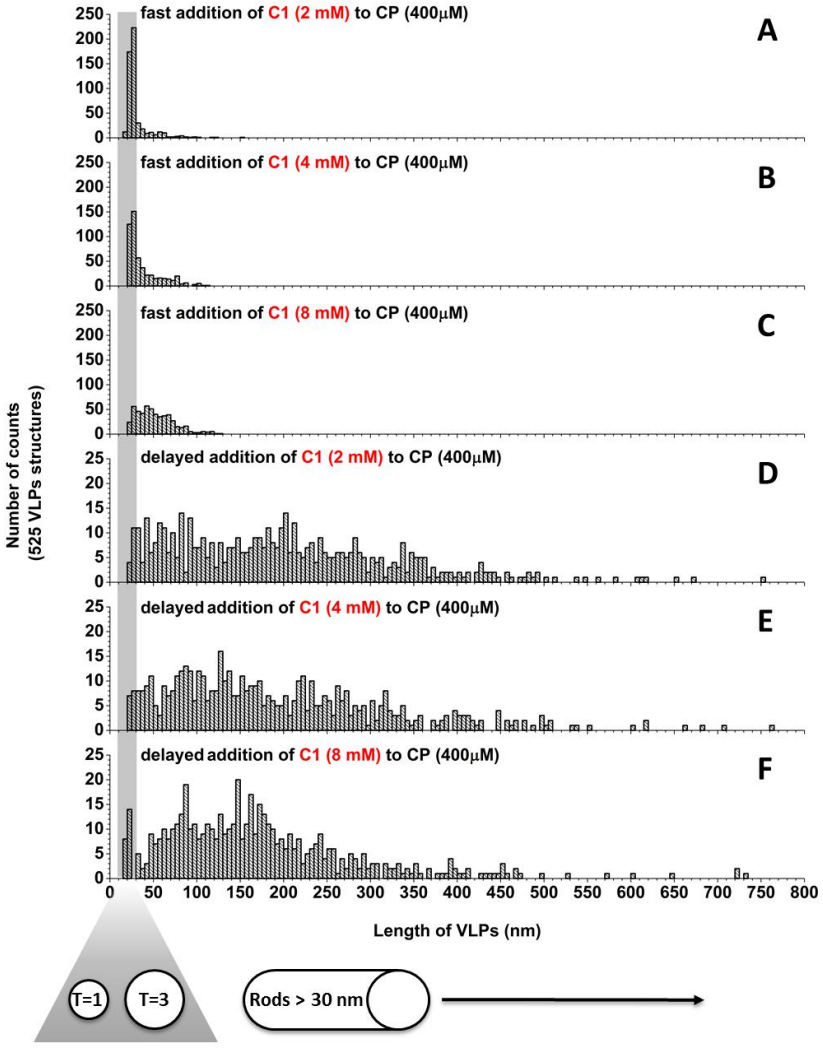

Figure 7.4. The size distribution of C1 assemblies upon fast encapsulation by CCMV at (A) 2 mM, (B) 4 mM and(C) 8 mM, and delayed encapsulation by CCMV at (D) 2 mM, (E), 4 mM and (F) 8 mM.

In the case of the fast addition, increasing the C1 concentration led to an increase in rod-like assemblies, with an average length below 100 nm (Figure 7.4 A - C and Appendix B). By comparison, the rod-like CCMV-CP assemblies obtained by delayed addition showed average lengths greatly exceeding 100 nm (Figure 7.4 D - F and Appendix B). Interestingly, the fast addition led to a narrow length distribution of CCMV-CP assemblies whereas delayed addition led to a broad length distribution, despite the prolonged pre-equilibration of C1 complexes prior to CCMV encapsulation. Here, the final morphologies of the CCMV-CP assemblies

appear to capture the different kinetic and thermodynamic aggregation states of C1, from small molecular aggregates to large stacked architectures.

7.2.3 Self-assembly of neutral Pt-Tet-TEG2 complex (C2)

The encapsulation of a neutral Pt-Tet-TEG2 complex (C2) in CCMV was also studied. The structural design of C2 is similar to C1 and differs only in the ancillary ligand, which bears a two pendant TEG arm instead of the alkylsulfate of C1. The overall size of the C2 monomer is slightly larger than that of C1, with an estimated length spanning 3 nm and a tail-to-tail distance between the Pt and the methyl end group of approximately 2.5 nm (Figure 7.5A). As described in the previous section for C1, C2 (8 mM) was dissolved in 50 mM Tris-HCl buffer, 300 mM NaCl, 10 mM $MgCl_2$, 1 mM DTT (pH 7.5) and equilibrated for overnight at 24 °C, with slow agitation. Unlike the C1 complex, which assembled into fiber-like structures, TEM of C2 showed the formation of large aggregates (Figure 7.5C and D). Because of their dimensions, aggregates of C2 seemed suitable templates for CCMV assembly.

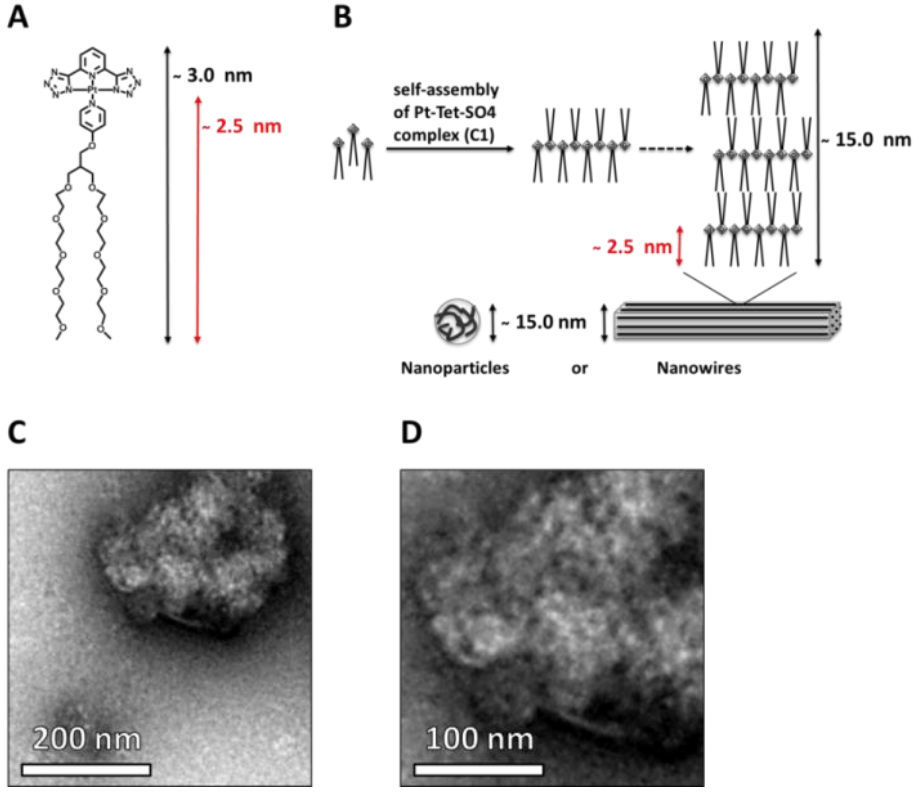

Figure 7.5. (A) Chemical structure of neutral Pt-Tet-TEG2 monomer (C2). (B) Schematic representation of presumable self-assembly of C2 in solution, (C and D) TEM micrograph of C2 solubilized in 50 mM Tris-HCl buffer (pH 7.5).

7.2.4 Encapsulation of neutral Pt-Tet-TEG2 complex inside CCMV capsids

C2 complexes were encapsulated in CCMV at various concentrations and different incubation times, *i.e.* after fast addition (t = 0 min) and delayed addition (t = 12 h), under the exact same conditions as described for the encapsulation of C1. The mixures were purified by size-exclusion chromatography, which revealed a peak characteristic for CCMV assemblies at 1.1 – 1.5 mL, and strongly suggests that CCMV is able to encapsulate C2 aggregates. Upon fast addition of C2 to CPs, the elution peak is asymmetrical and a clear shift in the elution volumes from 0.9 – 1.2 mL to 1.1 – 1.5 mL is observed upon increasing C2 concentration (Figure 7.6A, C, E). Similar to C1 encapsulation, the elution volume at 0.9 – 1.2 mL is indicative of rod-like CCMV based assemblies and the asymmetry suggests a mixture of morphological assemblies. To study the morphology of the assemblies, the SEC fractions (0.9 – 1.5 mL) were collected and analyzed by TEM (Figure 7.5). Systematic studies by TEM revealed the formation of rod-like assemblies at low C2 concentrations (2 mM), which shifted to mainly spherical CCMV structures at high C2 concentrations (8 mM) (Figure 7.6B, D, F).

After delayed addition, the size-exclusion chromatograms showed a symmetrical peak with an elution volume of 1.1 – 1.5 mL, which strongly implies that the CCMV assemblies are very similar for all three cases (Figure 7.6G, I, K). TEM analysis showed the exclusive formation of spherical-like assemblies, independent of C2 concentration (Figure 7.6H, J and L).

In an opposite trend to the one observed for C1, fast addition (t = 0 min) led to a broader distribution in assembly length and size (Figure 7.7A - C) whereas delayed addition (t = 12 h) of C2 to CPs led to the exclusive formation of spherical CCMV assemblies, independently of the concentration of C2. The average diameter of 22 ± 5 nm suggests the formation of *pseudo T* = 2 CCMV capsids (Figure 7.7D - F). The cumulative frequency (%) of the obtained CCMV assemblies can be found in Appendix D.

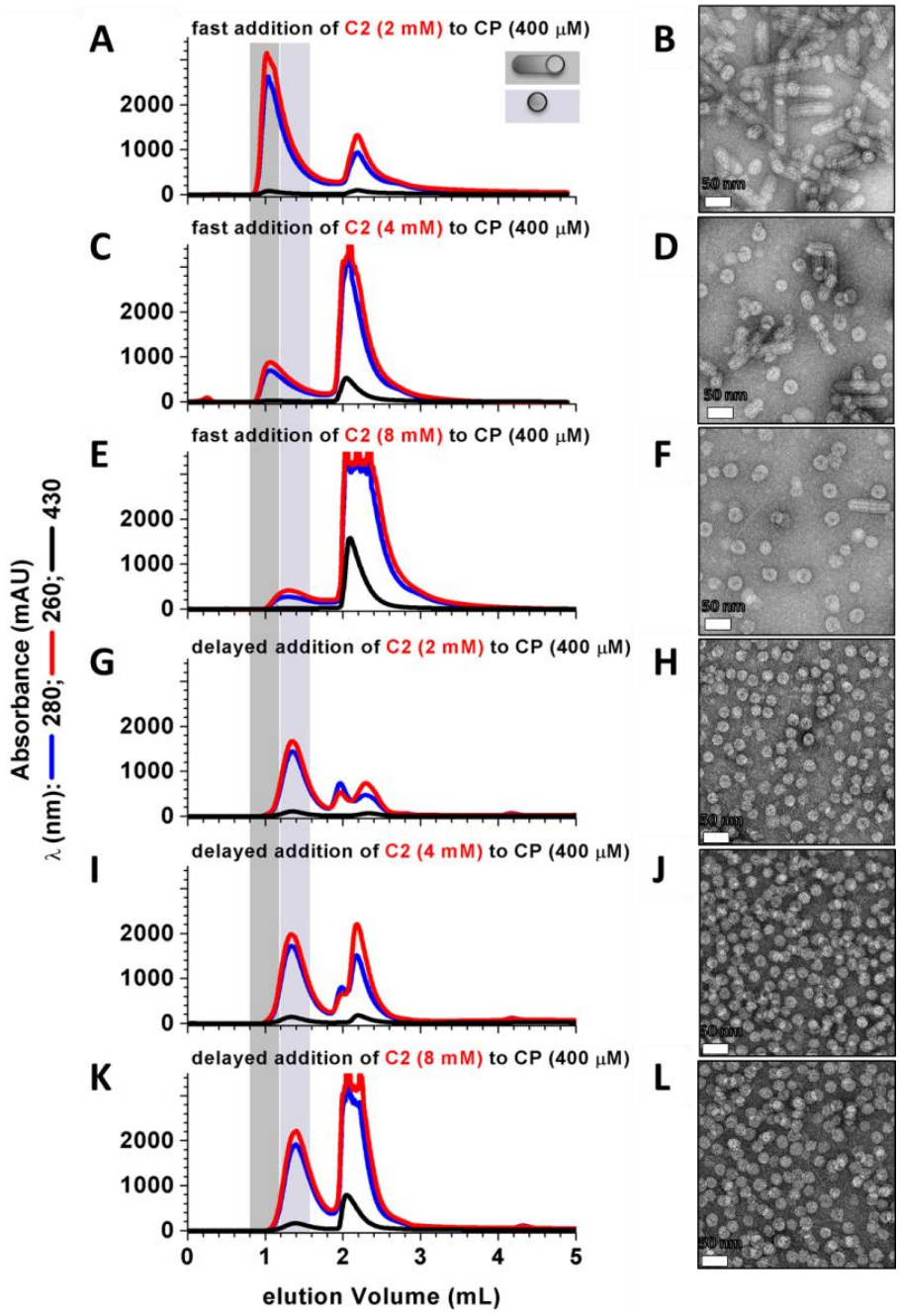

Figure 7.6. Size-exclusion chromatography and the corresponding negatively stained TEM micrographs upon 1) fast addition of CPs to C2 at (A) 2 mM, (C) 4 mM and (E) 8 mM and 2) delayed addition of CPs to C2 at (G) 2 mM, (I) 4 mM and (K) 8 mM. For size exclusion chromatography, the eluting material was monitored at λ = 280 nm and λ = 260 nm (corresponding to CPs) and at λ = 430 nm (corresponding to C2 complexes).

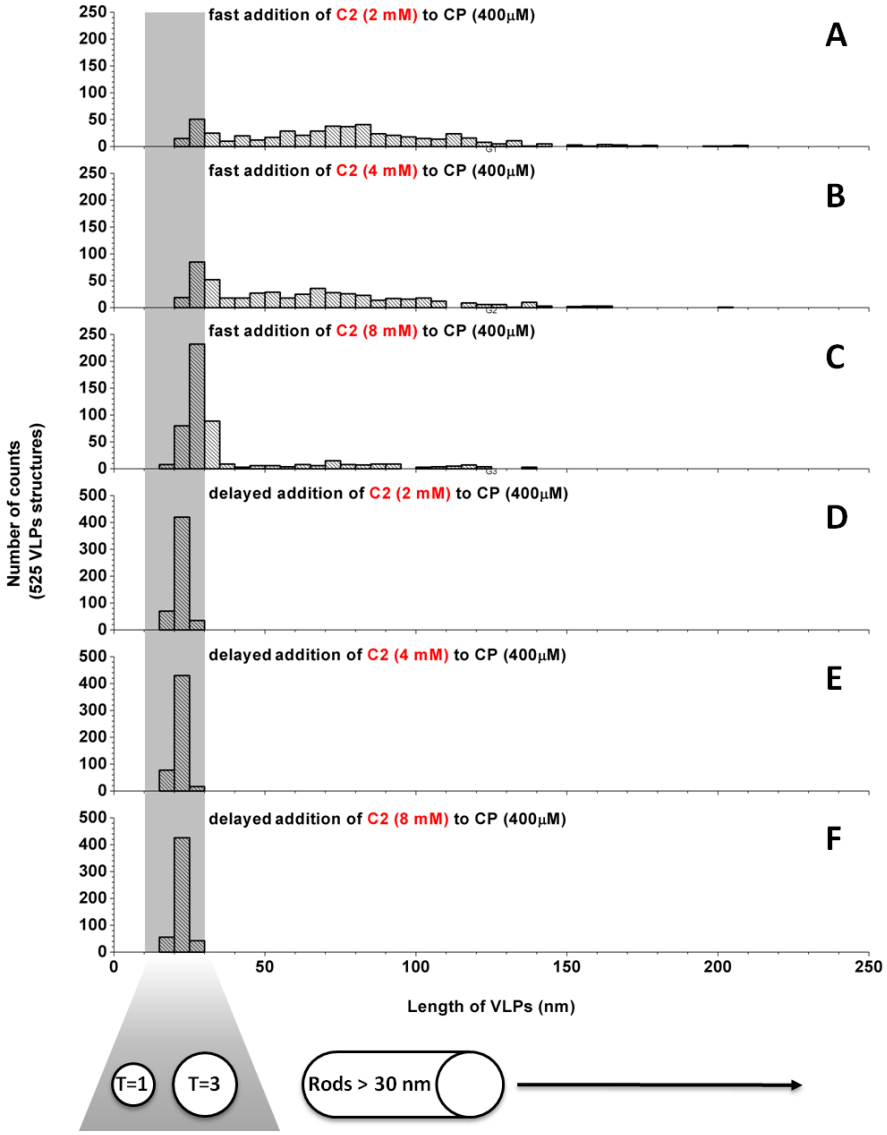

Figure 7.7. Size distribution histograms based on TEM of CCMV assemblies encapsulating C2 upon fast addition at (A) 2 mM, (B) 4 mM, (C) 8 mM and delayed addition at (D) 2 mM, (E) 4 mM, (F) 8 mM.

The encapsulation of C2 in CCMV was highly unexpected since, unlike C1 which is anionic, C2 is a neutral complex. In most cases reported in the literature, the encapsulation of functional materials (synthetic and biological) has always been based on the assumption that the electrostatic interactions between an anionic template and the cationic N-terminus of CPs are essential to drive the self-

assembly process. Although there are few examples reported in the literature, in which nearly neutral templates were encapsulated into bromomosaic virus (BMV),[18, 19] the encapsulation of small neutral metal-organic templates in CCMV has not been reported before. It is also striking that the fast addition of the neutral C2 complex (t = 0 min) led to the formation of rod-like assemblies whereas the delayed addition leads to the formation of spherical assemblies. It is proposed that the rod-like assemblies are formed upon encapsulation of the semi-crystalline state of C2, rather than the solubilized C2 complex. During solubilization of the C2 complex in buffer, it was observed that C2 was much less readily soluble compared to the C1 complex. Since C2 is less soluble, the fast addition of CCMV-CP to C2 may result in the encapsulation of non-solubilized semi-crystalline C2 material. Upon delayed addition, in which the C2 complex is incubated for 12 h, the C2 complex is fully solubilized in buffer, leading to spherical assemblies. More experiments, however, are needed to verify this hypothesis.

7.2.5 Detection and quantification of Pt in C1 and C2 based CCMV-CP assemblies

In order to determine the chemical composition of the different CCMV-CP assemblies, high-angle annular dark-field scanning transmission electron microscopy (HAADF-STEM) in combination with energy dispersive X-ray analysis (EDX) were performed in collaboration with Dr. Christian Kübel and Prof. Luisa De Cola at the Karlsruhe Institute for Technology (Germany). HAADF-STEM is a particularly sensitive technique used for the detection and quantification of heavy metal elements such as Pt. HAADF-STEM analysis of CCMV-CP assemblies encapsulating C1 at 1 mM and 4 mM confirmed the presence of rod-like assemblies (Figure 7.8). Interestingly, the lack of intensity contrast inside the rod-like assemblies suggests that Pt is not filling the protein shell completely. This is rather unexpected since CCMV-CPs requires the Pt(II) stacks as a rigid template in order to assemble into rod-like structures. Nevertheless, while Pt could not be detected by HAADF-STEM, EDX analysis confirmed the presence of Pt, C, O, Mg, Na, Si, S and Cl in the CCMV-CP assemblies encapsulating C1. To confirm the unexpectedly low Pt concentration, further measurements and analysis are still in progress.

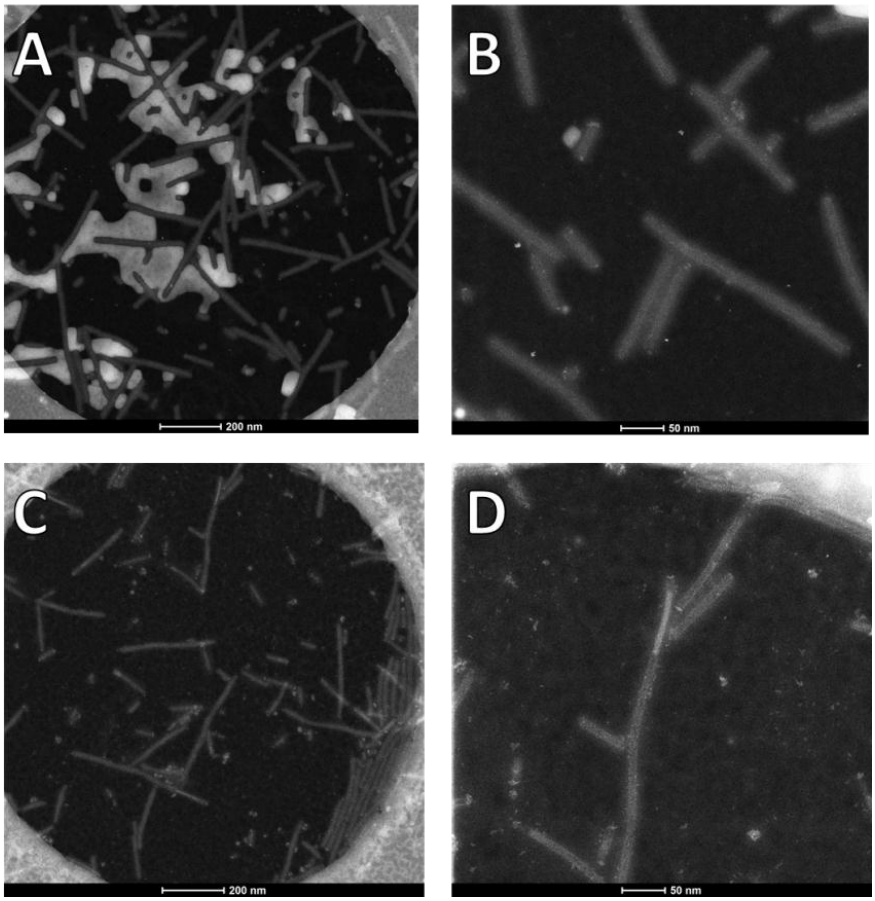

Figure 7.8. Unstained HAADF-STEM images of CCMV-CP assemblies encapsulating C1 at (A and B) 1 mM or (C and D) 4 mM.

In contrast to the C1 complex, HAADF-STEM images of CCMV-CP assemblies encapsulating C2 at 1 mM and 4 mM clearly show the Pt distribution inside the spherical CCMV-CP assemblies (Figure 7.9). The bright clusters originate from individual Pt complexes that are randomly oriented and distributed inside the protein shell (Figure 7.8B), and subsequent negative staining was performed to confirm that the CCMV-CP assemblies were still intact (Figure 7.9C and 7.8D). At higher concentrations, a faint white region surrounding the bright clusters is evident and is due to the protein shell (Figure 7.9E and F). This not only confirms that the CCMV-CP assemblies remain spherical and intact, but also clearly shows the encapsulation and localization of Pt inside the capsid assemblies. Furthermore, the size of the assemblies was estimated to be 22 – 25 nm in diameter, which is consistent with the TEM analysis described in the previous section. EDX analysis

further confirmed the presence of Pt, C, N, O, Si, S, Cl and Cu in the CCMV-CP assemblies encapsulating C2.

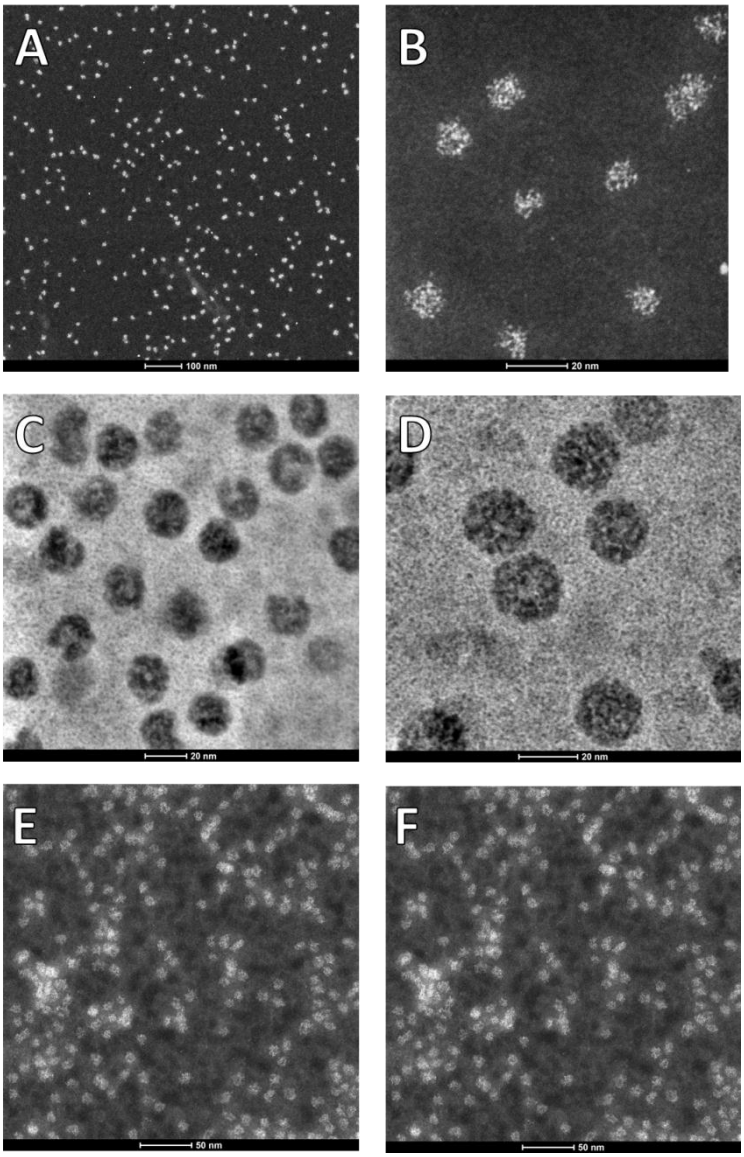

Figure 7.9. HAADF-STEM images of CCMV capsid assemblies encapsulating C2 at (A and B) 1 mM, unstained (C and D) 1 mM, stained, and (E and F) 4 mM, unstained.

7.3 Conclusions

Here, the encapsulation of different supramolecular aggregated states of anionic and neutral Pt(II) complexes in CCMV was investigated. Depending on the concentration and incubation time, rod-like or spherical structures were obtained. In the case of the anionic Pt(II) complex (C1), the entrapment of aggregates initially formed from C1 (at t = 0 mins), led to spherical CCMV assemblies, whereas pre-equilibration of the Pt(II) complexes (t = 12 h) prior to encapsulation led to rod-like CCMV assemblies. The opposite trend for the neutral Pt(II) complex (C2) was observed, which initially formed rod-like assemblies after fast addition (t = 0 min) and spherical CCMV assemblies after pre-equilibration (*i.e.* 12 h). In both C1 and C2 complexes, the presence of Pt encapsulated in the CCMV assemblies was confirmed by HAADF-STEM and EDX, however, further quantification of the Pt content in these assemblies is still in progress. Interesting photophysical properties are expected from the formed assemblies, which will be the subject of future studies. Overall, the unique combination of highly luminescent Pt(II) assemblies encased in a protective protein shell, as described here, opens up new possibilities for the use of Pt complexes in biomedical applications. Not only is the cytotoxic nature of Pt(II) expected to be reduced but the protective and stabilizing protein shell could be modified for improved (or targeted) cell uptake efficiency.

7.4 Acknowledgments

Dr. Naveen Kumar Allampally is gratefully acknowledged for the synthesis of the two compounds Pt-Tet-SO_4 (C1) and Pt-Tet-TEG2 (C2). Dr. Cristian A. Strassert and Prof. Luisa De Cola from Westfälische Wilhelms Universität Münster (Münster, Germany) are gratefully acknowledged for fruitful collaboration and the invaluable discussions throughout this project. Dr. Christian Kübel from the Karlsruhe Institute for Technology (Karlsruhe, Germany) is gratefully acknowledged for the HAADF-STEM and EDX analysis of encapsulated CCMV Pt(II) assemblies.

7.5 Experimental

7.5.1 Materials

The growth and purification of the native CCMV virus, including the removal of RNA and isolation of the coat protein (CP) were performed according to literature procedures.[22] The purity of the CCMV-CP was confirmed by size-exclusion chromatography (SEC), SDS-PAGE and UV-Vis spectroscopy. The anionic Pt-Tet-SO_4 complex (C1) and the neutral Pt-Tet-TEG2 complex (C2) were synthesized and characterized by the group of Prof. Luisa De Cola, Westfälische Wilhelms-Universität Münster, Germany. All chemicals used for the preparation of buffers were of analytical grade quality and all buffers were prepared in ultrapure (Milli-Q) water.

7.5.2 Methods

Encapsulation of anionic Pt-Tet-SO_4 complex (C1) or neutral Pt-Tet-TEG2 complex (C2) into CCMV:
Different concentrations of C1 or C2 (2 mM, 4 mM and 8 mM) were prepared in 50 mM Tris-HCl buffer, 300 mM NaCl, 10 mM $MgCl_2$, 1 mM DTT (pH 7.5). Two different encapsulation strategies were used. In the first strategy, CP (400 µM) were added immediately upon dissolution of the C1 or C2 complex (fast addition, t = 0 min) whereas in the second strategy, C1 or C2 were allowed to pre-equilibrate for 12 h, before addition of CP (delayed addition, t = 12 h). In both cases, the Pt(II) - CP mixtures were allowed to incubate for 2 h at 4 °C on a roller bank to ensure mixing. After incubation, the samples (including a reference containing only C1 or C2 complex) were purified by size-exclusion chromatography, monitoring at λ = 260 nm, λ = 280 nm (corresponding to CCMV–CP absorbance) and λ = 430 nm (corresponding to C1 or C2 absorbance). Individual fractions were collected (60 µL) and those corresponding to CCMV capsid assemblies were further analyzed by TEM.

Size-exclusion chromatography:
Size exclusion chromatography was performed using the following buffers: 50 mM Tris-HCl, 0.3 M NaCl, 1 mM DTT and 10 mM $MgCl_2$ (pH 7.5) and the GE Healthcare FPLC Äkta purifier 900 combined with fraction collector Frac-950. Samples were injected into a 100 μL injection loop and purified over an analytic column Superose 6 10/100 GL (GE Healthcare) with a 2.4 mL bed volume. UV-Vis spectra were recorded using a Perkin Elmer Lambda 850 UV spectrophotometer.

Transmission Electron Microscopy (TEM):
All TEM samples were examined using an analytical FEG-TEM (Phillips CM 30) operated at 300 kV acceleration voltage. For each sample, 5 μL of purified C1 and C2 CCMV assemblies were applied onto Formvar-carbon coated grids. The sample was left to incubate for 30 s before removing the excess liquid using a piece of filter paper. Uranyl acetate (5 μL, 1% w/v) was deposited on the carbon grid and the excess liquid was removed after 20 s. The grid was left to dry for 30 min at room temperature.

High-angle annular dark-field scanning transmission electron microscopy (HAADF-STEM) and energy dispersive X-ray analysis (EDX):
TEM analysis was performed using an image corrected FEI Titan 80-300 operated at 300kV in STEM mode at the Karlsruhe Institute of Technology, Germany. The Titan is equipped with an EDAX s-UTW EDX detector and a Gatan Tridiem 963 post-column energy filter. Samples were prepared on commercially available TEM grids on nominally 2-3 nm thick carbon support film (Quantifoil) by depositing the suspension on the grids for 30 s, rinsing them with deionized water and drying them in air.

7.6 Appendices

7.6.1 Appendix A: Size-exclusion chromatography of Pt-Tet-SO_4 complex (C1)

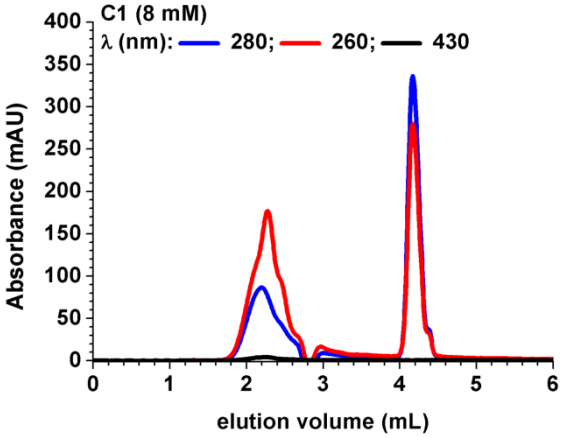

Appendix A. Size-exclusion chromatogram of the anionic C1 complex (8 mM), monitoring at 260 nm, 280 nm and 430 nm. The elution peaks at 2 – 2.8 mL and at 4 – 4.4 mL are characteristic of C1 aggregation or monomeric C1, respectively.

7.6.2 Appendix B: Cumulative frequency (%) of CCMV assemblies encapsulating Pt-Tet-SO_4 complex (C1)

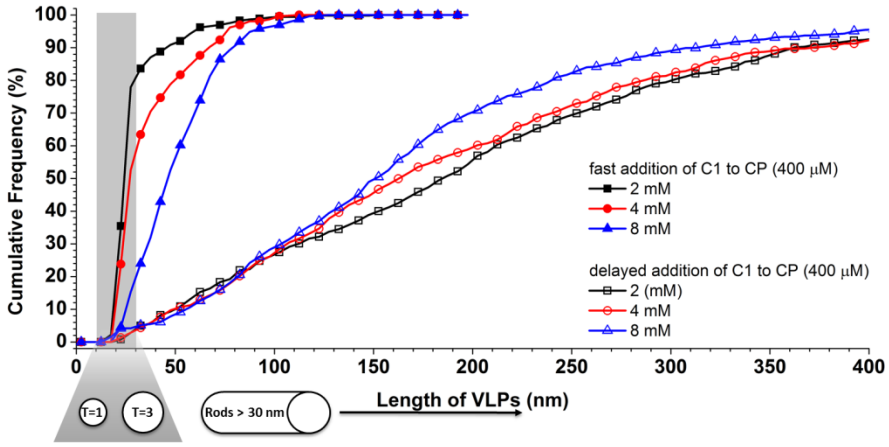

Appendix B. Cumulative frequency (%) distribution of CCMV assemblies at different C1 concentrations (2 mM, 4 mM and 8 mM) upon fast addition (t = 0 min) and delayed addition (t = 12 h) .

7.6.3 Appendix C: Size-exclusion chromatography of Pt-Tet-TEG2 complex (C2)

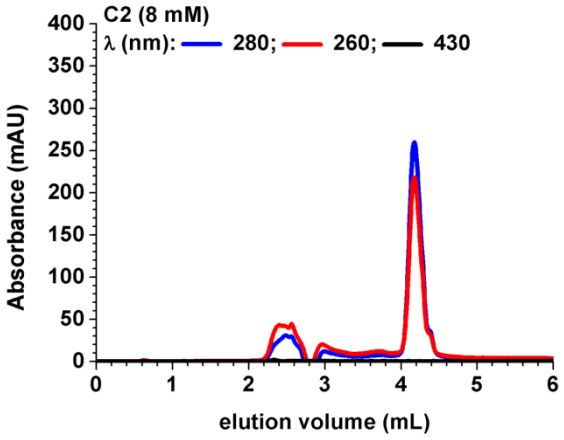

Appendix C. Size-exclusion chromatogram of the neutral C2 complex (8 mM), monitoring at 260 nm, 280 nm and 430 nm. The elution peaks at 2 – 2.8 mL and at 4 – 4.4 mL are characteristic of C2 aggregation or monomeric C2, respectively.

7.6.4 Appendix D: Cumulative frequency (%) of CCMV assemblies encapsulating Pt-Tet-TEG2 complex (C2)

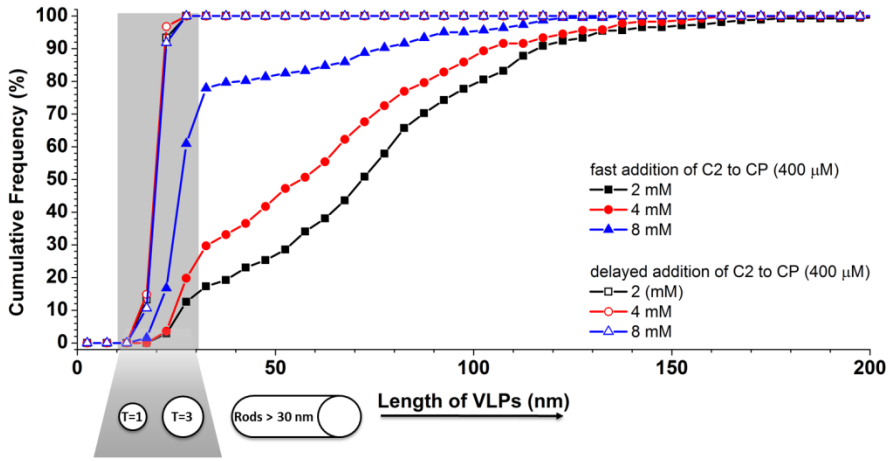

Appendix D. Cumulative frequency (%) distribution of CCMV assemblies at different C2 concentrations (2 mM, 4 mM and 8 mM) upon fast addition (t = 0 min) and delayed addition (t = 12 h).

7.7 References

1. X. Li, Y. Liu, J. Luo, Z. Zhang, D. Shi, Q. Chen, Y. Wang, J. He, J. Li, G. Lei and W. Zhu, *Dalton Trans*, 2012, **41**, 2972-2978.
2. J. Luo, Y. Liu, D. Shi, Y. Wang, Z. Zhang, J. Yu, G. Lei, Q. Chen, J. Li, X. Deng and W. Zhu, *Dalton T*rans, 2012, **41**, 1074-1081.
3. J. Luo, Y. Liu, Q. Chen, D. Shi, Y. Huang, J. Yu, Y. Wang, Z. Zhang, G. Lei and W. Zhu, *Dalton Trans*, 2013, **42**, 1231-1237.
4. Z. He, W.-Y. Wong, X. Yu, H.-S. Kwok and Z. Lin, *Inorg Chem*, 2006, **45**, 10922-10937.
5. K. Kuroiwa, N. Oda and N. Kimizuka, *Sci Technol Adv Mater*, 2006, **7**, 629-634.
6. N. J. Liu, B. Y. Wang, W. S. Liu and W. F. Bu, *J Mater Chem C*, 2013, **1**, 1130-1136.
7. N. K. Allampally, C. A. Strassert and L. De Cola, *Dalton Trans*, 2012, **41**, 13132-13137.
8. I. Eryazici, C. N. Moorefield and G. R. Newkome, *Chem Rev*, 2008, **108**, 1834-1895.
9. A. Divsalar, A. A. Saboury, L. Ahadi, E. Zemanatiyar and H. Mansouri-Torshizi, *Bmb Rep*, 2010, **43**, 766-771.
10. Q. Zhao, C. Huang and F. Li, *Chem Soc Rev*, 2011, **40**, 2508-2524.
11. L. Lavelle, J. P. Michel and M. Gingery, *J Virol Methods*, 2007, **146**, 311-316.
12. A. de la Escosura, P. G. A. Janssen, A. P. H. J. Schenning, R. J. M. Nolte and J. J. L. M. Cornelissen, *Angew Chem Int Ed*, 2010, **49**, 5335-5338.
13. S. A. Bode, I. J. Minten, R. J. M. Nolte and J. J. L. M. Cornelissen, *Nanoscale*, 2011, **3**, 2376-2389.
14. A. Zlotnick, R. Aldrich, J. M. Johnson, P. Ceres and M. J. Young, *Virology*, 2000, **277**, 450-456.
15. L. O. Liepold, J. Revis, M. Allen, L. Oltrogge, M. Young and T. Douglas, *Phys Biol*, 2005, **2**, S166-S172.
16. R. D. Cadena-Nava, Y. Hu, R. F. Garmann, B. Ng, A. N. Zelikin, C. M. Knobler and W. M. Gelbart, *J Phys Chem B*, 2011, **115**, 2386-2391.
17. B. C. Ng, S. T. Chan, J. Lin and S. H. Tolbert, *ACS Nano*, 2011, **5**, 7730-7738.
18. I. Tsvetkova, C. Chen, S. Rana, C. C. Kao, V. M. Rotello and B. Dragnea, *Soft Matter*, 2012, **8**, 4571-4577.
19. M.-C. Daniel, I. B. Tsvetkova, Z. T. Quinkert, A. Murali, M. De, V. M. Rotello, C. C. Kao and B. Dragnea, *ACS Nano*, 2010, **4**, 3853-3860.
20. F. E. Alemdaroglu, N. C. Alemdaroglu, P. Langguth and A. Herrmann, *Macromol Rapid Commun*, 2008, **29**, 326-329.
21. D. B. Chithrani, *Mol Membr Biol*, 2010, **27**, 299-311.

22. M. Comellas-Aragones, H. Engelkamp, V. I. Claessen, N. A. J. M. Sommerdijk, A. E. Rowan, P. C. Christianen, J. C. Maan, B. J. Verduin, J. J. L. M. Cornelissen and R. J. M. Nolte, *Nat Nanotechnol*, 2007, **2**, 635-639.

Summary

The design and engineering of biological building blocks that self-assemble into highly ordered, well-defined structures is of growing interest for applications in nanotechnology. For applications in biomedicine and drug delivery, the design of biomolecular cargo carriers has largely focused on either lipid-based assemblies (vesicles and micelles) or protein-based assemblies (cage-like proteins and virus-based assemblies). Owing to their reversible assembly, stability, monodispersity and biocompatibility, viruses are highly attractive candidates and have consequently received much attention. The outer shell of viruses is composed of multiple copies of identical virus coat proteins that can be modified by chemical or genetic means for enhanced functionality or molecular targeting, and their self-assembly can be controlled by tuning the pH or ionic conditions. Based on virus coat proteins, the term "virus-like particle" has been used to describe protein-based entities that resemble the size and morphology of native viruses but lack their natural genomic cargo. Viruses and virus-like particles have since been used for the encapsulation of a broad range of functional materials. Yet, there is still a lack in knowledge in the factors which drive the self-assembly process to occur.

The aim of this thesis was to investigate and understand the interplay between the molecular template and the virus coat protein of Cowpea Chlorotic Mottle Virus (CCMV), in particular, how to control and direct the self-assembly of viruses. The central theme of this thesis is based on the template-directed self-assembly of viruses, with a particular emphasis on the topics described in Chapter 2 in relation to viruses and functional cargo. The first two experimental Chapters, 3 and 4 described the controlled assembly of highly monodisperse virus-like particles (using light-absorbing phthalocyanines and DNA-enzyme hybrids), Chapters 5 deals with template induced clustering of CCMV resulting (using a conjugated polyelectrolyte) and Chapter 6 described structural changes in the CCMV shell upon cargo release in the absent of Mg^{2+} ions (using a photo-responsive self-immolative polymer) and finally in Chapter 7 the tunable morphology of CCMV from spherical to rod-like assemblies (using two different platinum(II) complexes) is investigated.

The results presented in this thesis provide a detailed, systematic study of the role of the molecular template in directing virus self-assembly and sheds new insights towards the design of the next generation of functional hybrid materials.

Samenvatting

Het ontwerpen en creëren van biologische bouwstenen die zichzelf rangschikken in sterk geordende, precieze structuren is voor de nanotechnologie van steeds groter wordende interesse. Voor toepassingen in bio-medicijnen en medicijn afgifte ligt de focus voor het ontwerp van bio-moleculaire medicijn dragers hoofdzakelijk op vet gebaseerde assemblages (vesicles en micellen) en eiwit assemblages (kooi-achtige eiwitten en virus capside). Virus kapsels in het bijzonder worden veel onderzocht omdat ze erg stabiel zijn, maar ook reversibel kunnen assembleren, een constante grootte hebben en zeer biocompatibel zijn. Deze virus kapsels zijn opgebouwd uit vele kopieën van identieke capside eiwitten waarvan de zelf assemblage met pH en ionische condities gestuurd kan worden. Ook kunnen deze kapsels op genetische en chemische wijze aangepast kunnen worden om een vergrote functionaliteit of gerichtheid te verkrijgen. Deeltjes die geen virussen zijn, maar wel gebaseerd zijn op de kapsel eiwitten en qua grootte en vorm op de oorspronkelijke virussen lijken worden virus-achtige deeltjes (Engels: virus-like particles) genoemd. Virussen en virus-achtige deeltjes zijn veelvuldig gebruikt om een breed spectrum aan functionele materialen te omkapselen. Desalniettemin is er weinig kennis over de factoren die het zelf assembleren, al dan niet om lading heen, sturen.

Het doel van deze thesis was het onderzoeken en het verkrijgen van een beter begrip van het complexe samenspel tussen de moleculaire template en de kapsel eiwitten van het virus CCMV (Engels: Cowpea Chlorotic Mottle Virus) in het vormen van het kapsel en specifiek hoe de kapselvorming gestuurd kan worden. Het centrale thema van deze thesis is de template gestuurde zelf assemblage van virussen, met de nadruk op de onderwerpen beschreven in hoofdstuk 2. In hoofdstuk 3 en 4 wordt de gecontroleerde assemblage van zeer monodisperse virus-achtige deeltjes beschreven, in hoofdstuk 3 met behulp van licht absorberende phthalocyanides en in hoofdstuk 4 met DNA-enzym hybride deeltjes. Daarna wordt er gekeken naar het template gedreven clusteren van de virus-achtige deeltjes met behulp van, in hoofdstuk 5, een geconjugeerde polyelektrolyt en, in hoofdstuk 6, een foto-degradeerbare polymeer. Als laatste wordt er in hoofdstuk 7 gekeken naar de stuurbaarheid van de morfologie, van op CCMV gebaseerde virus-achtige deeltjes, tussen bollen en staven door midden van platina(II) complexen.

De in deze thesis gepresenteerde resultaten geven een gedetailleerde en systematische studie van de rol van moleculaire templates in het sturen van de virus zelf assemblage. Deze resultaten geven nieuwe inzichten die van belang zullen zijn bij het ontwerpen van de volgende generatie functionele hybride materialen.

Acknowledgments

Four years ago, I started as the first PhD student in the Biomolecular Nanotechnology group and while it has been challenging, it has certainly been an unforgettable experience. In my last words, I would like to take the opportunity to thank all the people who have contributed to this work.

First and foremost, **Jeroen** thank you for the opportunity be a part of your new and exciting group and for the freedom, independence and trust you gave me to develop into a successful researcher, I have undoubtedly learnt a lot during this time.

I would also like to sincerely thank my committee members: **Dr. A. de la Escosura Navazo, Prof. J. Huskens, Prof. D. N. Reinhoudt, Prof. R. J. M. Nolte, Prof. D. Hilvert, and Prof. S. J. G. Lemay** for reading my manuscript.

About two years into my PhD, Melissa arrived and I requested that her to be my co-supervisor. **Melissa**, I will be always impressed by your incredible working hours, your enthusiasm and patience with people. I would really like to thank you for giving me the chance to collaborate with so many different international groups, the corrections of my manuscripts and my entire thesis, but most of all for your open door and ear when things got difficult.

Many thanks to **Pascal**: we first at the Max Planck Institute in Dortmund where you supervised me during my Bachelor project. Afterwards, you offered me the chance to do my Masters project here at the University of Twente to broaden my experience working in a foreign country and gave me the opportunity to improve my English. Without you and this opportunity, I would not be here. **Arancha**, I will never forget our first day. Pascal introduced us and I could not speak a word of English to you or anybody in the lab. I would like to thank you for your enthusiasm, great supervision, support and patience during the whole project and also for teaching me so many different techniques, methods and for teaching me how to be an independent and critical researcher. **Jurriaan**, thank you for letting me to do my Masters thesis in your huge Molecular Nanofabrication (MnF) research team. In addition, I would like to thank you for your always-honest suggestions and feedback during our joint MnF/BNT colloquia during the last four years. I also would like to thank **Natalie** for her suggestions and chats during my PhD time. It is amazing to see that you joined our group around 2 years ago and now you have already your own research team, which doubled the size of the BNT group. Although you just had a baby, I admire that you always found the time to encourage and help your own students and us. I would also like to express my gratitude to **Tibor**, **Wim** and **Aldrik** for all the discussions and chats during

conferences and general meetings. Many thanks also go to our technicians, **Richard**, **Regine**, **Marcel**, **Bianca** and **Tieme** for taking care of our research equipment, measuring samples and for providing their organization and support. Many thanks also to our secretaries, **Izabel** and **Nicole**, thank you for all your help in scheduling meetings, keeping things organized and for keeping deadlines as deadlines. I would thank the other PhD students in my group that joined shortly after me. **Rik**, thanks for driving to conferences and also for driving so often to Nijmegen at the beginning of our PhD times to isolate our proteins. I have never met a person before that is so incredibly happy on the dance floor, thanks for making the time in the lab a joyful experience. **Anne** and **Martijn,** thanks for discussion and support in meetings, conferences and the time in the lab. Although we become friends quite late during our PhDs, I would like to thank **Jealemy** for her time, support and honest suggestions during the last year together. I think we did a great job and achieved quite nice results in short time. Huge thanks also to **Yujie** and **Wies** for your help and support with the cell experiments but also for your friendship.

During these years I had the chance to collaborate with so many different people from other universities: **Andrès (UAM, Spain)**, **Ilja (TU/e)**, **Inge (RU)**, **Minsoek**, **Jan**, **Agnieszka and Prof. Andreas Herrmann (RUG)**, **Joost**, **Charlotte, Prof. Albert Heck (UU)**, **Naveen**, **Linda**, **Christian**, **Prof. Luisa de Cola (WWU-Münster).** I would like to thank you all for your useful discussions, support and help correcting manuscripts. Special thanks go to **Jordi** for your friendship and support during the last years, I enjoyed so much our game evenings, BBQs, the first times we went out for beers, your open ears and honest advice when things got bumpy. I wish you the best for your future and hopefully we will stay in contact. **Pieter**, vielen, vielen Dank für deine Hilfe und Unterstützung vom ersten Tag an als ich in Enschede angekommen bin. Insbesondere für die ganzen BBQ und Aktivitäten auserhalb vom Labor, für das aufpassen auf unser Haus in den Sommermonaten und nicht zu vergesses deine Hilfe und Übersetzung bei unserem letzten Umzug und anderen Dokumenten. Ich hoffe das wir in Kontakt bleiben und ihr beide bei eurem nächsten Skiurlaub mal vorbeischaut. **Shu Han**, **Carmen**, **Carlo** and **Kim** thank you a lot for the daily fun in the lab, dinners and your support during the last years. **Sarah,** vielen, vielen lieben Dank für deine Hilfe und die vielen Kleinigkeiten, die du zwischendurch für mich erledigt hast und wenn es nur war, dir Zeit zu nehme für ein Gespräch zwischendurch. Ich bin mir sicher, du wirst deinen Weg gehen und hoffe dass, du am Ende glücklich bist mit allem was du erreichst, bitte behalte deine positive Einstellung.

Many thanks also to the members of MNF/BNT for the good times in the lab, during lunch, in the office, outside of working hours and for the help in so many different ways: **Supitchaya, Raquel, Chengfen, Bettina, Jenny, Shirish, Rick,**

Tom, Roberto, Angel, Oya, Albert, Francesca, Mudassir, Nicolai, Vijay, Jasper, Erhan, Rianne, Emanuela, Rajesh, Tushar, Alejandro, Laura and **Fabian**.

Many thanks also to my Masters student, **Rindia**, for her contribution to my PhD research. I enjoyed a lot supervising you and I am happy that you will come back to start your PhD under a similar topic. I wish you all the best but I am sure you will succeed. Many thanks also to my Bachelor students, **Xandra** and **Hermann**, it was a great experience to supervise you both and I wish you both all the best. I would also like to thank **Sven** for being my paranimf but also for the good times and help outside of working hours. **Maarten**, you joined our group just recently and although we don't have any research related project in common, you voluntarily corrected my entire thesis and did so, in great detail. This impressed me a lot and many thanks for your huge help and the comments.

One of my biggest thank you goes to **Raluca**, you became one of my best friends during my time in Enschede. You are an amazing person and I admire you so much how you tackle all the challenges in life and research by always keeping the deadlines and positive thoughts. So many thanks for all the dinners, sport and game evenings. Also for your never-ending help with research questions, correcting my thesis, with moving from house to house, taking care of our garden, having always an open ear and simply your friendship. I hope you will start soon your own research line and we will stay in contact for sure.

Almost done, I would like to especially thank my family for their never-ending support and the education they allowed and encouraged me to have. **Jessica**, es ist schwer in Worten zu fassen, was es heißt, eine Zwillingsschwester wie dich zu haben. Ich danke dir so sehr für deine endlose Hilfe, Unterstützung, Gespräche und dein offenes Ohr. Es wäre mir ohne dich unmöglich gewesen hier zu sein und meinen Doktor Titel zu erlangen. Es wird mir sehr schwer fallen dich nicht mehr in meiner direkten Nähe zu haben. Liebe(r) **Mama** und **Papa**, auch euch möchte ich von Herzen für euren Beistand, Unterstützung und Erziehung danken. Ich danke euch für die Möglichkeit, meine Ausbildung im Nachbarland vorzusetzen und für euer Vertrauen und immer währende Hilfe in den letzten Jahren. Weiterhin möchte ich meinen Großeltern danken - insbesondere meiner Oma Hannelore, die letztes Jahr ebenfalls verstorben ist. **Markus** auch Dir möchte ich danken für deine Ratschläge, Hilfe und vor allem das bereitstellen der Bilder für das Deckblatt. Ich bewundere dich, wie du es schaffst aus jeder Situation das Positiv zu sehen und so viel Begeisterung an den Tag legst. Bitte behalte das immer bei. Pass auf meine Schwester auf.

Finally I would like to express my greatest THANK YOU to my boyfriend and his family. Although we could barely communicate in the beginning, they integrated me in their lives and gave me a new place to stay, to relax and to gain always fresh energy. **Alberto**, thank you not only for making my life so much better during and after work but also for your endless patience, support and help during the last years. Especially for doing such an amazing job in supervising me and correcting my manuscripts and thesis "voluntarily". **Maria**, **Mari** y **Antonio** muchas gracias por vuestra y apoyo. No solo por las estupendas vacaciones y la comida, sino tambien por aceptarme en la familia.

List of publications

- **M. Brasch**, M.S. T. Koay and J.J.L.M. Cornelissen; Synthetic Biology, *Volume 1*, **2013.**

- **M. Brasch**, i. K. Voets, M. S. T. Koay and J. J. L. M. Cornelissen; Phototriggered cargo release form virus-like assemblies; Faraday Discuss, **2013.**

- A. Gonzalez-Campo, **M. Brasch**, D. Uhlenheuer, A. Gomez-Casado, L. Yang; L. Brunsveld, J. Huskens, P. Jonkheijm; Supramolecularly Oriented Immobilization of Proteins Using Cucurbit[8]uril; Langmuir, 47, 16364 – 16371, **2012.**

- **M. Brasch**, J.J.L.M. Cornelissen; Relative size selection of a conjugated polyelectrolyte in virus-like protein structures; Chem Commun, 48, 1446-1448, **2012.**

- **M. Brasch**, A. de La Escosura, Y. Ma, C. Uetrecht, A.J.R. Heck, T. Torres, J.J.L.M. Cornelissen; Encapsulation of phthalocyanine supramolecular stacks into virus-like particles; J Am Chem Soc, 133, 6878 – 6881, **2011.**

- M. Kwak, I. J. Minten, D.- M. Anaya, A. J. Musser, **M. Brasch**, R. J. M. Nolte, K. Müllen, J.J.L.M. Cornelissen, A. Hermann; Virus-like Particles Templated by DNA Micelles: A General Method for Loading Virus Nanocarriers; J Am Chem Soc, 132, 7834-7835, **2010.**

Publications in preparation

- **M. Brasch**, R.M. Putri, M.S. T. Koay and J.J.L.M. Cornelissen; Enzymatic cascade reaction in virus-like particles; (submitted), **2013**

- V. Barsegov, O. Kononova, J. Snijder, **M. Brasch**, J. J. L. M. Cornelissen, K. A. Marx, W. H. Roos; Structural Transitions and Energy Landscape for Cowpea Chlorotic Mottle Virus Capsid mechanics from nanomanipulation in vitro and in silico; (submitted), **2013**

- D. Luquea, A. de la Escosura, J. Snijderc, **M. Brasch**, J.L. Carrascosa, G.J.L. Wuite, W.H. Roos, A.J.R. Hecke, J.J L.M. Cornelissen, T. Torres and J.R. Castóna; Structure and Mechanical Properties of Phthalocyanine-Loaded Virus-Like Particles: Optically Active Hollow Nanospheres in a Protein Cage; (submitted), **2013**

- J. Galindo Millán, **M. Brasch**, E. Anaya-Plaza, A. de la Escosura, A.H. Velders, D.N. Reinhoudt, T. Torres, M.S. T. Koay and J.J.L.M. Cornelissen; Self-Assembly Triggered by Self-Assembly: Optically Active, Paramagnetic Micelles Encapsulated in Protein Cage Nanoparticles; (submitted), **2013**

- **M. Brasch**, N.K. Allampally, L. Stegemann, C.A. Strassert, M.S. T. Koay, L. De Cola and J.J.L.M. Cornelissen; Amphiphilic molecules templating protein assembly: spheres to rods; (in preparation), **2013**

About the Author

Melanie Brasch was born on the 6th of June of 1984, in Wuppertal, Germany. She studied chemical biology at the University of Dortmund, where she received her Bachelor degree in 2007. During her bachelor project she worked on the immobilization of biomolecules onto surfaces using photochemistry under the supervision of Prof. Herbert Waldmann at the MPI Institute Dortmund. She continued her studies in biochemistry at the Ruhr University of Bochum in Germany and graduated in July 2009, where she received her Master with a thesis entitled: "Cucurbituril mediated protein immobilization". The practical work was carried out in the group of Prof. Jurriaan Huskens at the Department of Supramolecular Chemistry & Nanofabrication of the University of Twente in The Netherlands. Since September 2009 she continued in Twente as a Ph.D. student in the Biomolecular Nanotechnology group of Prof. Jeroen Cornelissen under the supervision of Dr. Melissa Koay. The aim of her project was to control the stability and morphology of protein complexes by changing the properties of the polyelectrolyte cargo materials. The results of this research are presented in this thesis.